The Pennsylvania State University

The Graduate School

College of Earth and Mineral Sciences

A FIRST-PRINCIPLES STUDY OF STACKING FAULTS AND LONG PERIODIC STACKING ORDER STRUCTURES IN MG AND MG ALLOYS

A Dissertation in

Materials Science and Engineering

by

Yi Wang

Submitted in Partial Fulfillment
of the Requirements
for the Degree of
Doctor of Philosophy

December 2013

The dissertation of Yi Wang was reviewed and approved* by the following:

Zi-Kui Liu
Professor of Materials Science and Engineering
Dissertation Advisor
Chair of Committee

Long-Qing Chen
Professor of Materials Science and Engineering

Jorge O. Sofo
Professor of Materials Science and Engineering and Physics

Suveen N. Mathaudhu
Program Officer – Synthesis and Processing
Materials Science Division, U.S. Army Research Office
Adjunct Assistant Professor of Materials Science and Engineering
North Carolina State University
Special Member

Suzanne Mohney
Professor of Materials Science and Engineering and Electrical Engineering
Associate Head for Graduate Studies
Department of Materials Science and Engineering

*Signatures are on file in the Graduate School

ABSTRACT

Since the main challenges in developing Mg alloys are to increase their strength, ductility, as well as stability at high temperatures, it is crucial to understand the fundamental properties which affect their mechanical properties. Formation of stacking faults is fundamental in deformation of materials with the hcp structure such as Mg and Ti alloys, affecting core structures and the mobility of dislocations, twinnability and ductility, and creep rate. Moreover, long periodic stacking order (LPSO) structures, such as 6H, 10H, 14H, 18R and 24R, play significant roles in enhancing the mechanical properties of Mg alloys and have been largely investigated separately.

In the present work, contributions of stacking faults, LPSOs and alloying elements to the formation energy, elastic, electronic and phonon properties of Mg and Mg alloys are investigated through the first-principles calculations.

In pure Mg, the connections among stacking faults and LPSOs are discussed. Three typical basal-plane stacking faults, i.e. growth fault (I1), deformation fault (I2) and extrinsic fault (EF), are investigated, showing that the stacking fault energy increases in the order of I1 < I2 < EF. Moreover, through the electron localization morphology, electronic structures of these three stacking faults are revealed in terms of deformation electron density ($\Delta\rho$) and electron localization function (ELF). These results yield a quantitative description of charge transfer between atoms in and out of the stacking faults. We also obtain a brief physical correlation between stacking fault energy and the difference of $\Delta\rho$ and ELF between the fault planes and the non-fault planes.

Furthermore, through detailed investigations of deformation electron density, we show that the electron structures of 10H, 14H, 18R and 24R LPSO structures in Mg originate from those of deformation stacking faults in Mg, and their formation energies can be scaled with respect to formation energy and the number of layers of deformation stacking faults, while the electron structure and formation energy of the 6H LPSO structure are between those of deformation and growth stacking faults. The simulated images of high resolution transmission electron microscopy compare well with experimental observed ones. In the end, effects of fault layers in SFs and LPSOs on the local phonon density of states and vibrational entropy are discussed together with their specific electronic structures.

In the binary Mg-X alloys, contributions of 17 alloying elements to the energy and the bond structure of growth, deformation and extrinsic faults are investigated. In view of electron localization morphology, the bonding structure of Mg around the fault plane can be recognized as the HCP-FCC transformations in short-range. Together with the specific electron structure of each alloying element, it has been confirmed that bond strength of the fault planes are strengthened by FCC-Al and HCP-Zn since tetrahedrons around alloying elements have more electron density. Taking Gd and Y as examples, their interactions with faults layers of 6H and 10H LPSO are presented in view of excess energy and deformation electron density. It has been determined that (i) with the addition of Gd and Y, the excess energy of 6H and 10H can be decreased significantly, indicating that the formability of 6H and 10H LPSO will be increased in Mg-10RE (wt %) alloys; (ii) Gd and Y prefer to occupy the position in fault layers of Mg-10RE with 6H and 10H

LPSOs; (iii) since the excess energy will be close to and smaller than that of the pure, the atomic array model can be used in Mg-10Y with 6H and 10H LPSOs, while the atomic cluster model can be used in Mg-10Gd with 6H and 10H LPSO and (iv) the bond strength of the basal plane characterized by $\Delta\rho$ is strengthened around the RE effect zone, while that of prismatic and pyramidal planes will be weakened caused by the electron redistributions effected by the contributions of RE and LPSOs.

In the ternary Mg-TM-RE alloys, contributions of alloying elements and fault layers to the energy, electronic structure and elastic properties of 6H and 10H LPSOs are discussed through our proposed atomic array/cluster model. In the view of excess energy, the energetic favorable configurations of the 6H LPSO in $Mg_{98}Zn_2$, $Mg_{98}Y_2$ and $Mg_{97}Zn_1Y_2$ (at %) have been estimated via first-principles calculations. Through the formation of an atomic array of Y forming with Zn occupying its 1st nearest neighbor, the ductility of $Mg_{97}Zn_1Y_2$ will be increased and the ratio of B/G is increased from 1.95 of Mg to 2.09. According to the energetic favorable structure of Mg-10Gd with 6H and 10H LPSOs, effect of TM elements, such as Zn and Zr, on their formability in Mg-10Gd-TM alloys has been estimated. With the addition of Zn and Zr, the excess energy of the 6H and 10H LPSOs can be decreased significantly when forming the cluster between the TM and Gd, indicating the formability of 6H and 10H will be increased in Mg-Gd-Zr and Mg-Gd-Zn alloys. Thus, with the addition of TMs into Mg alloys with LPSOs, the excess energy will be reduced to make the structure more stable than Mg alloy without TM. In view of the deformation electron density and electron localization function, the strengthen mechanism of alloying elements in the Mg alloy is that the basal plane of Mg

is strengthened due to the formation of stronger chemical bond between the atomic array and Mg matrix. With the addition of TMs into Mg alloys with LPSOs, the excess energy will be reduced to make the structure more stable than that of without the TM in the Mg alloy.

This work enables quantitative investigations of effects of alloying elements on the properties of Mg alloys. The understanding of stacking faults and LPSO structures in Mg enables future quantitative investigations of effects of alloying elements on properties of LPSO structures and Mg alloys.

TABLE OF CONTENTS

LIST OF FIGURES

LIST OF TABLES

ACKNOWLEDGEMENTS

I would like to thank the following people and institutions for their help and support to make this possible:

Dr. Zi-Kui Liu and Dr. Xi Dong Hui for providing me the great opportunity to be an exchange student from University of Science and Technology Beijing to the Pennsylvania State University, whose enthusiasms and knowledge in academic research always motivates me to aim higher in order to build a solid foundation in computational material science;

Dr. Long Qing Chen, Dr. Suzanne Mohney, Dr. Jorge O. Sofo and Dr. Suveen N. Mathaudhu for their time, suggestions and encouragements during serving on my thesis committee;

Dr. Laszlo J. Kecskes and Dr. Kristopher A. Darling for their valuable comments and suggestions in improving my capability to successfully finish objectives in the project;

Dr. Shun Li Shang, Dr. Yi Wang, and all the other members in Phase Research Lab for their patient guidance during my research;

The U.S. Army Research Laboratory for funding the work on Mg alloys (Project No. W911NF-08-2-0);

The China Scholarship Council for awarding the scholarship (File No. [2008]3072) to support my partial stipend in United States for 48 month;

Finally, I would like to express my special thanks to my parents, Mrs. Xiu Ying Ge and Mr. Xiu Liang Wang, for their unconditional love and support. I am especially grateful to my wife Yan Liu for her endless love, support and understanding. I want to thank my son Enze Wang and my daughter Enjia Wang for bringing me daily a happy life. Special thank you to my older sister Jing Wang and parents in-law Mrs. Dong Xue Gu and Mr. Xiu Er Liu for their great support.

Chapter 1 Introduction

Motivation

With a density that is two-thirds of aluminum or one-quarter of steel, Mg alloys become potential structural materials for vehicles to improve fuel economy and reduce emissions [1]. Since the main challenges in developing Mg alloys are to increase their strength, ductility, as well as stability at high temperatures [2, 3], it is crucial to understand the determinate factors that control their mechanical properties. It is worth mentioning that the stacking fault energy, γ_{sf}, is a key parameter to model a vast number of phenomena relating to structure and dislocation formed by slip process [4]. For instance, (i) γ_{sf} is crucial to describe the core structure and the mobility of the dislocations [5-7], since the distance between dissociate partials determined by the value of γ_{sf} [7-9] and the mobility of the dislocations is also dominated partially by γ_{sf} [6, 7]; (ii) the reduction of γ_{sf} could enhance the twinnability of the material [10] and decrease the twinning stress, which is essential to increase the ductility [11-13]; and (iii) the steady-state creep rate can be reduced with lower γ_{sf} [14, 15]. The focus of this work is to study the basal-plane stacking fault energy of hcp Mg due to the effects of alloying elements.

It was found that the basal plane of hexagonal close packed (hcp) structure is the most primary slip plane indicated by texture type of $\{0001\}<11\bar{2}0>$ [6, 16-19], which

can result in an intrinsic stacking fault. At atomic level, the stacking sequence of an ideal hcp metal could be ...ABABABAB... with A, B, (and C, see below) being different {0001} planes, while the growth fault (I1) is formed by removing an A plane above a B plane, and then shearing the remaining planes above the B plane by $1/3[1\bar{1}00]$ resulting in ...ABAḂCBCB... ; the deformation fault (I2) can be formed directly by shearing the hcp lattice by the displacement $1/3[1\bar{1}00]$, resulting in ...ABAḂĊACA... [6, 18]; and the extrinsic fault (EF) is generated by inserting an extra C plane into the ideal hcp structure, resulting in ...ABAḂĊȦBAB..., where fault layers are marked with a dot. Previous calculations for a series of hcp metals of Be, Co, Hf, Mg, Re, Ru, Sc, Ti, Y and Zr showed that the I1 stacking fault energy is considerably lower than the I2 stacking fault energy, with the latter even smaller than that of extrinsic fault [20-22]. However, these observations have not been clearly explained in the literature.

In recent years, Mg-RE alloys with excellent mechanical properties have been obtained through combining the fine grain size, the precipitates, and the long period stacking order (LPSO) structures. Transition metals (TM) together with rare earth elements (RE) play an important role in the formation of LPSOs in the high strength Mg-TM-RE alloys. Table 1.1 and Table 1.2 list the tensile strength and compressive strength of some classical Mg alloys with LPSOs. For instance, the tensile yield strength and the elongation of $Mg_{97}Y_2Zn_1$ (at %) alloy with the 6H LPSO structure produced by rapid solidification can reach 610 MPa and 4.8%, respectively, with grain sizes in the range of 100 nm to 150 nm [23]. When the grain size of Mg matrix is about 330 nm, the tensile yield strength and the elongation become 400 MPa and 2%, respectively [24]. The yield

tensile strength of Mg-14Gd-0.5Zr (wt %) is 445 MPa at room temperature. The yield tensile strength and elongation of Mg-8.2Gd-3.8Y-1Zn-0.4Zr alloy with 14H LPSO are 426 MPa and 4.5% at room temperature. It is commonly accepted that fine precipitates or local clustering of solute atoms together with different types of LPSO structures, including 6H, 10H, 14H, 18R and 24R, contribute to the strengthen of Mg alloys [25-34]. Works focusing on the segregating behavior of alloying elements are important to optimize the microstructure and to improve the mechanical properties of Mg alloys [30, 33, 35-40]. In the development of advanced Mg-Zn-Y alloys with good performance, effect of LPSOs and their enrichment of alloying elements on the electronic structure and the elastic properties of Mg remain ambiguous. Particularly, the segregation behavior of the alloying elements and their contributions on the formability and the electronic structures of 6H LPSOs have not been reported in binary and multicomponents systems.

The schematically descriptions of the present work together with the description of the development of Mg alloys reported in literature are presented in Figure 1.1. It can be seen that alloying elements are used to influence a wide variety of properties of Mg alloys, both to increase the manufacturability and the product properties. According to the demands on the development of Mg alloys, different directions are applied to classify Mg alloys into high creep resistant alloy, high ductile alloy, and high strength alloy and so on. In the development of advanced Mg alloy, there are many factors to be considered, i.e., molten metal reactivity, castability, grain structure control, mechanical properties, corrosion properties, physical properties, formability, weldability etc. In this work, crystal structure optimization through forming stacking faults and long periodic

stacking order structures are investigated in efforts to improve mechanical properties of Mg alloys.

Objectives

The goals of the project are to investigate the contributions of stacking faults, LPSOs and alloying element to the formation energy, elastic, electronic and phonon properties of Mg and Mg alloys through first-principles calculations.

The organization of this dissertation is as following:

In Chapter 2, computational methodologies yielding the energies of stacking faults and LPSOs, characterizing their electronic structures and presenting their effect on the phonon and elastic properties of Mg and Mg alloys are introduced. Different models for the arrangement of alloying elements in LPSOs of Mg alloys are compared.

In Chapter 3, formation energy, electronic and phonon properties of growth, deformation and extrinsic faults in Mg are discussed. Contributions of fault layers in stacking faults to the local phonon density of states and Debye temperatures are discussed together with their specific electronic structures.

In Chapter 4, effect of alloying elements on the formation energy, electronic and elastic properties of stacking faults in binary Mg-X alloys are described. Contributions of 17 alloying elements to the energy and the bond structure of growth, deformation and extrinsic fault are investigated.

In Chapter 5, formation energy, electronic and phonon properties of 6H, 10H, 14H, 18R and 24R LPSOs in Mg are studied. In the view of deformation electron density, connections among stacking faults and LPSOs are revealed. Local phonon density of states and Debye temperatures affect by fault layers of LPSOs are discussed together with their specific electronic structures.

In Chapter 6, effects of alloying element (X=TM and RE) on the total energy and electronic property of 6H and 10H LPSOs in binary Mg-X alloys are discussed. Taking Gd and Y as examples, their interactions with faults layers of 6H and 10H LPSO are discussed in views of excess energy and deformation electron density. Energetic favorable configurations of Mg-10RE with 6H and 10H are estimated and extended in the study of ternary Mg alloys.

In Chapter 7, interactions between TM (TM=Zn and Zr) and RE (RE=Y and Gd) in 6H and 10H LPSOs of Mg-TM-RE alloys are estimated efficiently through the proposed atomic array model and atomic cluster model. The predicted energetic favorable crystal structure matches well with the experimental observations reported in the literature. The possible strengthen mechanism of Mg alloy by alloying elements is discussed in view of deformation electron density.

Chapter 8 summarizes the contribution of the present work in understanding the stacking faults and long periodic stacking order structures in Mg alloys and discusses the future work.

Table 1.1. Tensile strength and elongation of Mg alloys with LPSOs

Alloy		Tensile Strength			Temp K	LPSO	Ref
		UTS MPa	YTS MPa	El %			
RE=Y	$Mg_{97}Zn_1Y_2$ (at %)	-	610	4.8	573	6H	[23]
		-	564	6.7	623	6H	[23]
		-	490	7.4	673	6H	[23]
	$Mg_{98.5}Zn_{0.5}Y_1$	-	200	-	RT	14H 18R	[26]
	$Mg_{95.5}Zn_{1.5}Y_3$	-	260	-	RT	14H 18R	[26]
	$Mg_{93.96}Zn_2Y_4Sr_{0.04}$	226	-	4.6	RT	18R	[41]
	$Mg_{87}Zn_4RY_9$	353	265	9.7	293	6H	[30]
		247	204	29.2	593	6H	[30]
RE=Gd	$Mg_{91.5}Al_{3.5}Gd_5$	-	-	-	-	18R	[42]
	$Mg_{97}Zn_1RE_2$	391±19	356±17.5	6±3	RT	6H	[25]
		334±12	301±9	8±4	473	6H	[25]
	$Mg_{96.5}Zn_1Gd_{2.5}$	-	345	6.9	RT	14H	[31]
	Mg-14Gd-0.5Zr (wt%)	482	445	2.0	RT	-	[43]
RE=Gd, Y **TM**=Zn, Zr	Mg-17.4Gd-1.1Zn -0.6Zr (wt%)	390	280	7.5	473	-	[44]
	Mg-8.2Gd-3.8Y-1Zn-0.4Zr (wt%)	517	426	4.5	RT	14H	[45]
	Mg-1.8Gd-1.8Y-0.7Zn-0.2Zr	542	473	8	RT	-	[46]
	Mg-12Gd-1.9Y-0.69Zr (wt%)	400	360	5	RT	-	[47]
	Mg-8.2Gd-3.8Y-1Zn-0.4Zr (wt%)	373	313	6.4	RT	14H	[48]
	GDZ732 (Mg-6.5Gd-2.5Dy-1.8Zn, wt%)	392	295	6.1	RT	14H	[49]
		247	152	12.0	523	14H	[49]
	Mg-8.3Gd-1.12Dy-0.38Zr (wt%)	355	261	3.8	RT	-	[50]
		230	174	7.4	523	-	[50]
		157	82	25.1	573	-	[50]
No-RE **TM**=Mn, Zn	AZ91 (Mg-9Al-1Zn-0.2Mn, wt%)	329±3	256±5	2.2± 0.8	RT	-	[51]
	AXM4303 (Mg-4Al-3Ca-0.3Mn, wt%)	349	331	8.2	RT	-	[52]
	AXM4303 (Mg-3.6Al-3.4Ca-0.3Mn, wt%)	413	409	8	RT	*	[53]
	AXM4304 (Mg-3.6Al-3.3Ca-0.4Mn, wt%)	420	410	5.6	RT	-	[54]

Table 1.2. Compressive strength and elongation of Mg alloys with LPSO

Alloy	Compressive Strength			Volume percentage of LPSO %	LPSO	Ref
	US MPa	YS MPa	El %			
$Mg_{77}Cu_{12}Y_6Zn_5$	1203	841	2.45	Vf=6%	6H	[35]
$Mg_{81}Cu_{9.3}Y_{4.7}Zn_5$	1163		18.5	Vf=48%	6H	[35]
$Mg_{83}Cu_8Y_4Zn_5$	942		15.4	Vf=66%	6H	[35]
AXM4303 (Mg-4Al-3Ca-0.3Mn, wt%)	472	285	9.5	-	-	[52]

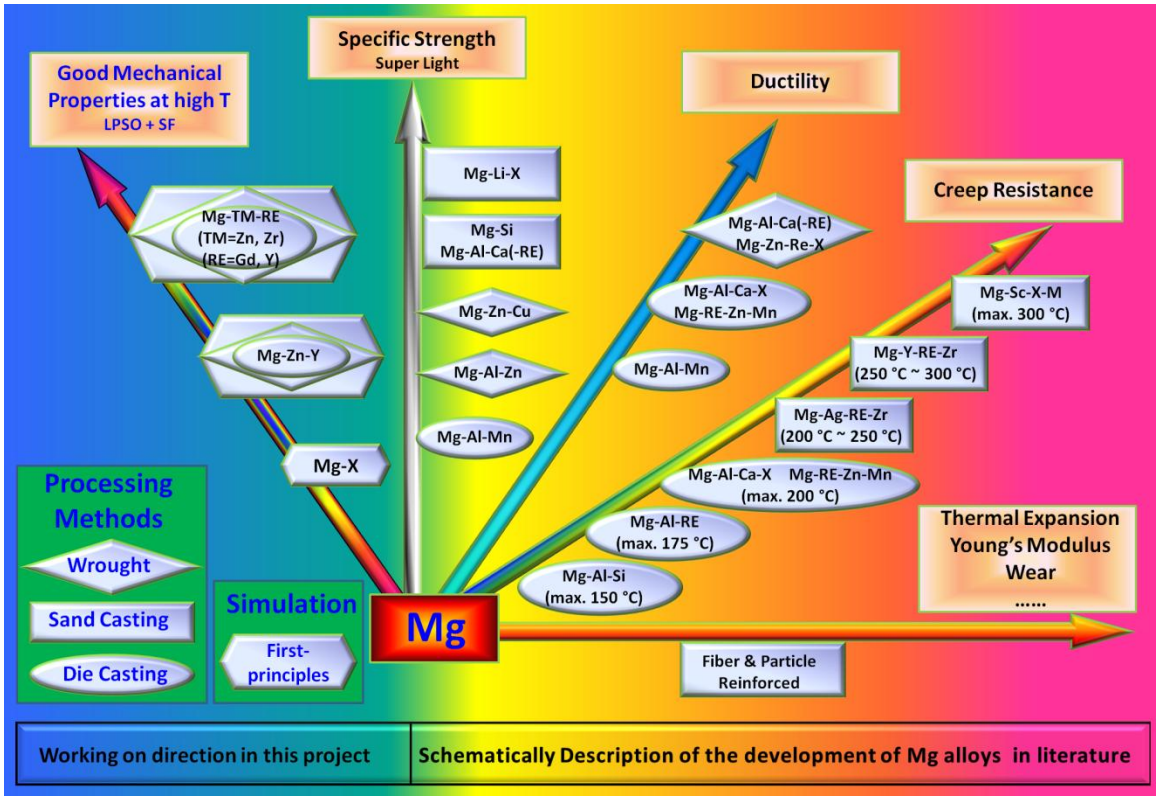

Figure 1.1. Schematically description of the present work together with the description of the development of Mg alloys reported in literature.

Chapter 2 Computational Methodology

2.1. Introduction

In this chapter, theory background and computational methodology in studying the energy, electronic structures, elastic and phonon properties of stacking faults and long period stacking order structures of Mg alloys are presented. First, a brief overview of first-principles calculations based on density functional theory is introduced, followed by a discussion of equations of state fitting to obtain the volume dependence of total energy. Second, the bond structure characterized by deformation electron density and the bond strength identified by electron localization function are presented, both of which are along with first-principles calculations. Third, the Voigt's method is applied to calculate elastic properties describing the deformation of a solid under applied stress. Next, the phonon approach is used to describe the lattice vibration states affected by faults layers in stacking faults and LPSOs. Afterwards, models arranging alloying element in the solid solute of Mg alloys are selected, which provides the essential information to generate crystal structure of a given Mg alloy before doing first-principles calculations.

2.2. First-principles Calculations Based on Density Functional Theory

2.2.1 Density functional theory

In principle, the time-independent stationary Schrödinger Equation describes the quantum mechanical behavior of particles by defining their relative wave functions, from which the total energy can be determined, shown as

Equation 2.1 $$\hat{H}\Psi = E\Psi$$

where $\hat{H}$ is the Hamiltonian operator, Ψ the wavefunction and E the total energy of the system. However, it is impossible to get the exact solution of Equation 2.1 in the N-body system until applying some approximations. Otherwise variables (electron coordinates) are too many and cannot be separated in the N-body electron wavefunction Ψ.

Based on the so-called Born-Oppenheimer approximation [55] (or adiabatic approximation), the motion of electron and nuclei can be considered separately because of the large mass difference between electron and nuclear. Therefore, it is possible to solve the problem of electron motion for fixed positions of nuclei since the Hamiltonian operator in Equation 2.1 can be rewrote as electronic Hamiltonian ($\hat{H}_{ele}$, in atomic unites). Following the Hohenberg-Kohn-Sham theorem [56, 57], (i) the external potential is an unique functional of the electron density and (ii) the exact ground state density of electron dominates the minimize of the total energy, the total energy can be described as a function of electron density ($\rho(\vec{r})$) as

Equation 2.2 $$E = E[p(\vec{r})] = T[p(\vec{r})] + E_{ext}[p(\vec{r})] + E_{Hatree}[p(\vec{r})] + E_{xc}[p(\vec{r})]$$

where $T[p(\vec{r})]$ is the kinetic energy of the electrons without interactions, $E_{ext}[p(\vec{r})]$ the external potential energy of the ions applying on the electron and $E_{Hatree}[p(\vec{r})]$ the interaction energy of electrons. $E_{xc}[p(\vec{r})]$ is the exchange and correlation energy, which can be solved by using the Local Density Approximation (LDA) or Generalized Gradient Approximation (GGA). Thus, the total energy of N-body system can be obtained through applying proper pseudopotential, which describing all electrostatic and quantum-mechanical interactions of valence electrons with the cores and producing true potential and valence orbitals outside a particular core region but remaining weaker and smoother inside.

2.2.2 Equations of state (EOS) fitting

Four-parameter Birch-Murnaghan (BM4) equation [58-60] is used to describe the relation between volume and energy, shown as following,

$$E(V) = a + \frac{B_0 V}{B_0^{'}}\left(1 + \frac{(V_0/V)^{B_0^{'}}}{B_0^{'}-1}\right)$$

Equation 2.3

where the fitting parameter $a = E_0 - \frac{B_0 V}{B_0^{'}-1}$. The parameters V_0, E_0, B_0 and $B_0^{'}$ represent the equilibrium volume, energy, bulk modulus and its first derivative with respect to pressure, respectively.

2.3. Bond Structure Characterization

2.3.1. Deformation electron density (Δρ) and simulated HRTEM image

Deformation electron density (Δρ) [61, 62], defined as the difference between the total electron density and the electron density associated with unbounded atoms, is used to characterize the electronic structures of stacking faults and LPSOs in the form of chemical bonds. Since the electron density is a scalar field, the change in electron distribution field results in directional bonds [63] and correlates to the formation energy of stacking fault [64]. Therefore, the isosurface structures with different values of Δρ generated using VESTA [65, 66] reveal the core structures of stacking faults and LPSOs.

The important application of deformation electron density is to produce an experimental comparable outcome with high resolution transmission microscopy (HRTEM) by displaying the contrast of the electron density profile. It is well know that X-ray and electron structure factors are essential for numerous crystallographic calculations, especially for structure refinements and electron-microscopy image simulations. X-ray diffraction measures the total electron density in crystal and can be calculated from the charge density of the atom assuming radial symmetry through [67]

Equation 2.4
$$f_X(s) = 4\pi \int_0^\infty r^2 \rho(\vec{r}) \frac{\sin(4\pi s\vec{r})}{4\pi s\vec{r}} d\vec{r}$$

where $s = \sin\theta / \lambda$ is the normalized scattering angel, λ the wavelength. The electron scattering factor can be obtained through Mott-Bethe formula, [67, 68]

Equation 2.5 $$f_{el}(s) = \frac{me^2}{8\pi h^2 \varepsilon_0} \frac{Z - f_X(s)}{s^2}$$

where e is the electron charge, m the electron mass, Z the atomic number, ε_0 the dielectric constant and h the Planck's constant. Through Fourier transformation, the electrostatic potential can be obtained from X-ray scattering factor, which is shown as

Equation 2.6 $$\rho(\vec{r}) = \int f_X(\vec{k}) e^{-i\vec{k}\vec{r}} d\vec{k}$$

Therefore, the projected potential can be expressed as

Equation 2.7 $$V(\vec{k}) = \frac{2me}{4\pi^2 \varepsilon_0 h^2} \int \frac{\rho(\vec{r})}{\vec{k}^2} e^{2\pi\vec{k}\cdot\vec{r}} d\vec{r}$$

2.3.1.1 Simulation of HRTEM based on charge density calculation

The simulated high resolution transmission electron microscopy (HRTEM) could be generated directly via projecting the electron density associated to each atom or the intensity by converting the electron density into electron scattering factor [67, 69-71]. In the literature, there are two different methods applied into simulate HRTEM through fist-principles calculations.

First, the calculation of the projected potential used for HRTEM image simulations is connected with the charge density via the twofold integration of the

Poisson equation in reciprocal space. The implementation of the charge density difference is performed as a correction term for the project potential ($V(\vec{k})$). This relation is described as [67, 71, 72]

Equation 2.8 $$V\left(\vec{k}\right)=\frac{2me}{4\pi^2\varepsilon_0 h^2}\left\{\sum_j\left[\frac{\int\rho_{n,j}(\vec{r}-\vec{r_j})e^{2\pi\vec{k}\cdot\vec{r}}d\vec{r}}{k^2}-\frac{\int\Delta\rho(\vec{r})e^{2\pi\vec{k}\cdot\vec{r}}d\vec{r}}{k^2}\right]\right\}$$

which demonstrates the possibility to split the charge density ρ into separated parts for the calculation of the projected potential $V\left(\vec{k}\right)$. Here, $\rho_{n,j}$ denotes the charge density of one nucleus j including the electron shell for the neutral atom on site n and $\Delta\rho(\vec{r})$ stands for the charge redistribution per unit cell due to the bonding. The charge density difference $\Delta\rho(\vec{r})$ is integrated over the CASTEP or DACAPO grid of the supercell, which is implemented as correction term in the source code of the EMS software package simulating HRTEM images [71, 73]. To ensure consistency, the neutral atom charge density is always calculated by CASTEP or DACAPO through perform the calculation with only one atom in the supercell [67].

Second, HRTEM images are conventionally analyzed on the basis of the so-called independent atom model (IAM), which also called the procrystal model. In this model, the potential of a solid is calculated as a superposition of atomic potentials that have once been calculated for an isolated atom of every element. This is reasonable as a first approximation because the adjustments to the potentials due to bonding electrons are small. Moreover, the IAM result is useful for comparison, because the effects of

chemical bonds can be easily recognized from the difference between the ‘real’ situation and the IAM approximation [69].

In this work, the simulated HRTEM images are obtained by projecting the deformation electron density, method of which is based on the second one mentioned above. Since it is challenging to accurately predict the lightweight atoms in HRTEM image through IAM model, the enhanced contrast image could be predicted through removing a line profile with periodic components [69]. For instance, a quantitative comparation between the simulation and experiment based on IAM and DFT potentials is shown in Figure 2.1(a). It can be seen that an excellent confirmation of the DFT-based simulations is obtained, providing the direct experimental verification of the DFT-based electron densities and without requiring any filters [69]. Moreover, a microscopy could be yielded with enhanced contrast through removing the periodic components in the electron density profile. For example, the intensity dip at nitrogen defect is 7 times stronger than the standard deviation, shown as Figure 2.1(b).

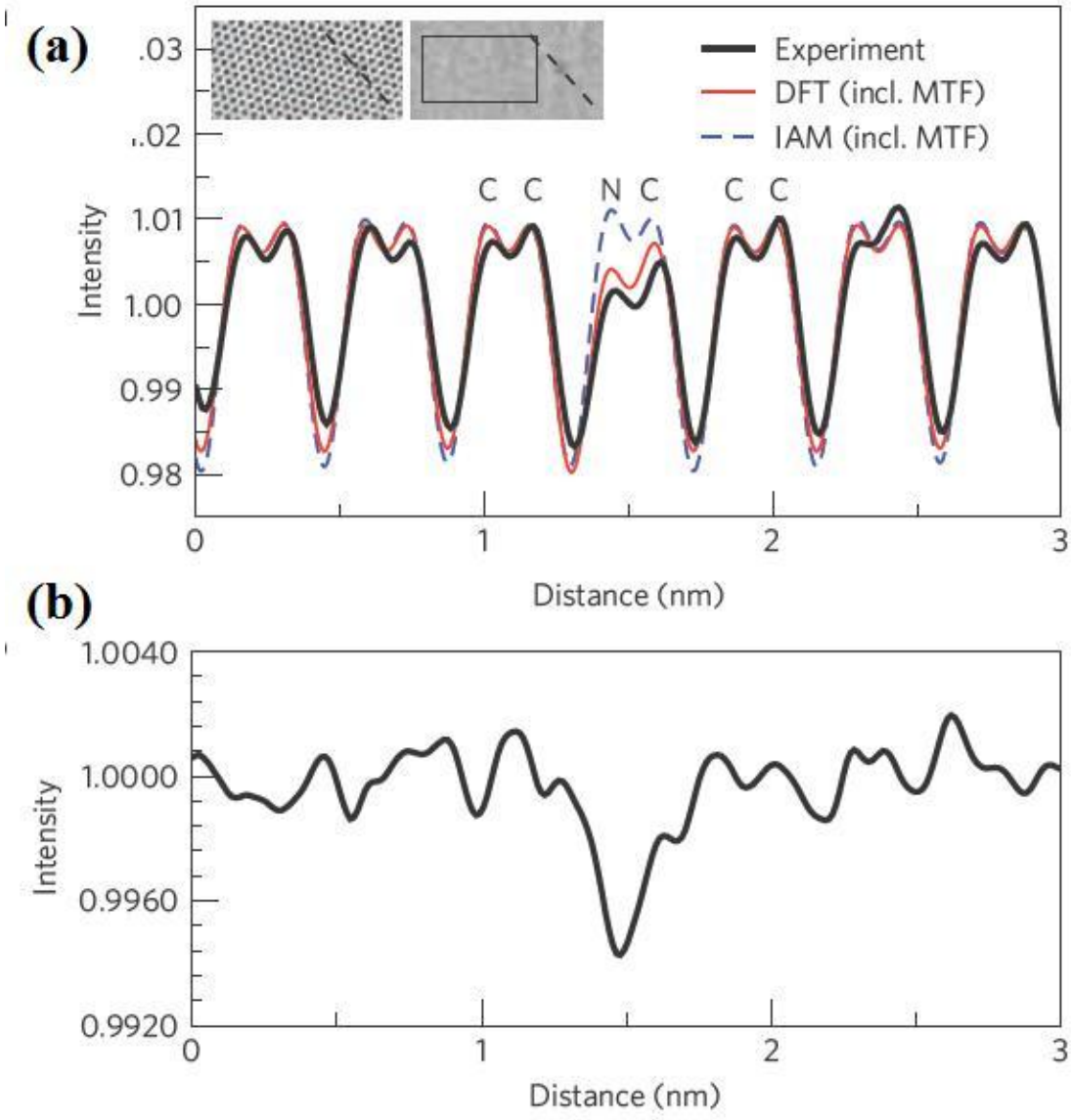

Figure 2.1. Analysis of the nitrogen substitution defect [69]. (a) comparison between experiment and simulations based on IAM and DFT potentials for a specific defocus value. MTF: modulation transfer function. Inset: the image and profile, and the Fourier-filtered image (graphene lattice removed). (b) Line profile with the periodic components removed.

2.3.2. Electron localization function (ELF)

Electron localization function (ELF) is obtained from the excess of local kinetic energy density due to the Pauli exclusion principle, D(ρ), and the Thomas-Fermi kinetic energy density, $D_h(\rho)$, as follows [74, 75]

Equation 2.9 $$ELF = \left[1 + \left(\frac{D(\rho)}{D_h(\rho)}\right)^2\right]^{-1}$$

For a single determinantal wave function, these quantities are evaluated from the Hatree-Fock or Kohn-Sham orbitals, φ_i, and the charge density $\rho = \sum_i |\varphi_i|^2$

Equation 2.10 $$\mathrm{D}(\rho) = \frac{1}{2}\sum_i |\nabla\varphi_i|^2 - \frac{1}{8}\frac{|\nabla\varphi_i|^2}{\rho}$$

Equation 2.11 $$D_h(\rho) = \frac{3}{10}\left(3\pi^2\rho\right)^{5/3}$$

As can be seen from Equation 2.9, the value of ELF is between 0 and 1, with ELF=1 corresponding to a perfect localization, i.e. $D(\rho) = 0$, and ELF=0.5 to a homogeneous electron gas, i.e. $D(\rho) = D_h(\rho)$ For a covalent bonding, ELF exhibits a maximum on the line connecting the atoms with a typical range between 0.6 and 1 depending on how strong the bonding is [76].

2.4. Elastic Constants

Elastic constants calculated by first-principles calculations are obtained by using the efficient strain-stress method [77, 78]. Based on the Hooke's law, the elastic stiffness constants C_{ij} (i, j=1, 2, 3, 4, 5, and 6) can be expressed as

Equation 2.12

$$C_{ij} = \varepsilon^{-1}\sigma = \begin{pmatrix} C_{11} & C_{12} & C_{13} & 0 & 0 & 0 \\ C_{21} & C_{22} & C_{23} & 0 & 0 & 0 \\ C_{31} & C_{32} & C_{33} & 0 & 0 & 0 \\ 0 & 0 & 0 & C_{44} & 0 & 0 \\ 0 & 0 & 0 & 0 & C_{55} & 0 \\ 0 & 0 & 0 & 0 & 0 & C_{66} \end{pmatrix}$$

where ε^{-1} represents the inverse of the sets of strains, $\varepsilon = (\varepsilon_1, \varepsilon_2, \varepsilon_3, \varepsilon_4, \varepsilon_5, \varepsilon_6)$ and $\sigma = (\sigma_1, \sigma_2, \sigma_3, \sigma_4, \sigma_5, \sigma_6)$. The bulk, Young's (E) and shear moduli (G) of the orthorhombic structure can be derived from the calculated first-principles elastic constants through Voigt's method [79, 80], shown as following

Equation 2.13

$$B = (\overline{C}_{11} + \overline{C}_{12})/3$$

Equation 2.14

$$G = (\overline{C}_{11} + \overline{C}_{12} + 3\overline{C}_{44})/5$$

Equation 2.15

$$E = (9GB)/(G + 3B)$$

where $\overline{C}_{11} = (C_{11} + C_{22} + C_{33})/3$, $\overline{C}_{12} = (C_{12} + C_{13} + C_{23})/3$ and $\overline{C}_{44} = (C_{44} + C_{55} + C_{66})/3$.

2.5. Lattice Vibrational States via Phonon Supercell Approach

In order to discussing the stability of stacking faults and LPSOs at finite temperature, it is essential to investigate the lattice vibration contributions of the fault layers in stacking faults and LPSOs to the Helmholtz free energy. Under quasiharmonic approximation [4, 81-83], the Helmholtz free energy at temperature T and volume V combines the static energy at 0 K, the thermal electronic contributions and the lattice vibrational contribution.

From phonon density of states, the lattice vibrational contribution to Helmholtz free energy can be calculated through [4, 81-84]

Equation 2.16
$$F_{vib}(V,T) = \kappa_B T \int \ln\left\{2\sinh\left[\frac{\hbar\omega}{2\kappa_B T}\right]\right\} g(\omega) d\omega$$

where κ_B is the Boltzmann constant; T the temperature, $g(\omega)$ the phonon density of states as a function of phonon frequency ω at volume V. Alternatively, $F_{vib}(V,T)$ can also be described by the Debye Temperature (Θ_D) as

Equation 2.17
$$\kappa_B \Theta_D(n) = h\omega_D(n)$$
$$\omega_D(n) = \left[\frac{n+3}{3}\int_0^{\omega_{\max}} \omega^n g(\omega) d\omega\right]^{1/n} \quad \text{with n} \neq 0, \text{n} > -3$$

where $\omega_D(n)$ is the Debye cutoff frequency. The nth moment Debye temperature is obtained by

Equation 2.18
$$\Theta_D = \frac{\hbar}{\kappa_B}\omega_D(n)$$

With different value of n, the obtained Debye temperature related to different physical meaning [85], for instance, $\Theta_D(2)$ usually links to the Debye temperature gained from the heat capacity data [83, 84].

Based on the predicted local phonon density of states, it is easy to express the vibrational entropy and the specific heat at constant volume as [86]

Equation 2.19 $$S_{vib} = \kappa_B \int_0^{\infty} \left[\frac{\hbar\omega}{2\kappa_B T} \coth\left(\frac{\hbar\omega}{2\kappa_B T} \right) - \ln\left(2\sinh\left(\frac{\hbar\omega}{2\kappa_B T} \right) \right) \right] g(\omega) d\omega$$

Equation 2.20 $$C_v = \kappa_B \int_0^{\infty} \left\{ \left(\frac{\hbar\omega}{2\kappa_B T} \right)^2 \left[\coth^2\left(\frac{\hbar\omega}{2\kappa_B T} \right) - 1 \right] \right\} g(\omega) d\omega$$

Hence, entropy stabilized structure could be discussed according to the obtained thermodynamic properties.

Since the Debye model could efficiently predict the lattice vibrational energy, it is expected to capture the lattice vibrational contribution to the free energy of the stacking faults and LPSOs. In this model, the vibrational contribution to Helmholtz free energy can be expressed as [84]

Equation 2.21 $$F_{vib}(V,T) = \frac{9}{8}\kappa_B \Theta_D + \kappa_B T \left\{ 3\ln\left[1 - \exp\left(-\frac{\Theta_D}{T} \right) \right] - D\left(\frac{\Theta_D}{T} \right) \right\}$$

where $D(\Theta_D / T)$ is the Debye function given by

Equation 2.22 $$D(x) = \frac{3}{x^3} \int_0^x \frac{t^3}{\exp(t) - 1} dt$$

The vibrational entropy can be wrote as

Equation 2.23 $$S_{vib} = 3\kappa_B \left\{ \frac{4}{3} D\left(\frac{\Theta_D}{T} \right) - \ln\left[1 - \exp\left(-\frac{\Theta_D}{T} \right) - \right] \right\}$$

In the present work, the supercell approach via the Yphon package [87-89] together with Vienna *ab initio* simulation package [90, 91] is used to predict the phonon frequencies of stacking faults and LPSOs in Mg. The capability of Yphon package yielding accurate phonon frequencies has shown in the application of polar materials [87] and random alloys [89] since all of the interaction force constants between the atom within the supercell are included, as demonstrated by Parlinski et al [92]. As we know, the phonon frequencies can be calculated by soling the eigenvalue problems of the reciprocal dynamic matrix ($D_{\alpha\beta}^{ij}$), shown as following

Equation 2.24 $$\widetilde{D}_{\alpha\beta}^{ij}(\boldsymbol{q})\boldsymbol{e}(\mathbf{q}, l) = \omega^2(\mathbf{q}, l)\boldsymbol{e}(\mathbf{q}, l)$$

where α and β are the Cartesian axes of either x, y or z; $\boldsymbol{q}$ the wave vector; l the phonon mode; $\boldsymbol{e}(\mathbf{q}, l)$ the corresponding normalized atomic displacement weighted by the square root of the atomic mass. Within the supercell approach, the dynamic matrix ($D_{\alpha\beta}^{ij}(\mathbf{q})$) is defined from the primitive unit cell of the ideal lattice, through the following Fourier transformation [87, 89, 92]

Equation 2.25 $$\widetilde{D}_{\alpha\beta}^{jk}(\boldsymbol{q}) = \frac{1}{\sqrt{u_j u_k}} \frac{1}{N} \sum_P \phi_{\alpha\beta}^{ij}(M, P) exp\{i\boldsymbol{q}[\boldsymbol{R}(M, j) - \boldsymbol{R}(P, k)]\}$$

where u_j is atomic mass of the j^{th} atom in the primitive cell of the ideal lattice, P the index of the primitive unit cell of the ideal lattice in the supercell, $\phi_{\alpha\beta}^{ij}$ is the cumulative force constant between the atom positioned at **R**(P,j) and the atom positioned at **R**(P, k). **R**(P) the position of the P^{th} primitive unit cell in the phonon supercell. N is the supercell size in terms of the number of primitive unit cell of the ideal lattice. The procedure to calculate the phonon properties of Mg with stacking faults and LPSOs is as same as that used in the calculating of random alloy [89].

2.6. Models for Arrangement of Alloying Elements in Stacking Faults and LPSOs

The calculation of total energy of an alloy is one of the most important outputs in understanding its fundamental properties based on density functional theory. Generating the crystal structure of the alloy is the key to produce the behavior of total energy affected by alloy elements, which cause the lattice distortions. In the following, models for arrangement of alloying elements in stacking faults and LPSOs of Mg will be discussed, which could be applied in the multicomponent system with a high concentration of alloying elements. Through choosing the specific model, segregation behavior of the alloying elements and their contributions on the formability and the electronic structures of stacking fault and LPSOs can be investigated efficiently in binary and multicomponents systems via first-principles calculations.

2.6.1. Reported models in the literature

2.6.1.1. Axial next-nearest-neighbor Ising (ANNNI) model

Within the axial next-nearest-neighbor Ising (ANNNI) model, which is also called axial interaction model, the stacking fault energy of close packed structures, i.e., FCC and HCP, can be calculated by taking into account interactions between layers up to several (typical value is 2-3) nearest neighbors [93-96]. Through combining with density functional theory, quantitative prediction of stacking faults energy affect by alloy elements via this approach has been successfully applied in austenitic stainless steels [95], Fe-Mn alloys [97], Fe-C alloys [98] and Mg-Y alloys [96]. The main challenge is to setup a simple but accurate model to be able to gain the total energy of alloys.

It is worth to mention that under coherent potential approximation (CPA) [93, 99, 100] (local lattice relaxation is not considered), random alloys can be investigated through the exact muffin-tin orbitals [101] since the total energy will be calculated based on the excellent smoothed average electron density of each alloy component within the spherical cell approximation [99]. Unfortunately, the coherent potential approximation cannot describe a structure with short range order and thus cannot be applied to study the effects of short range order on the electronic states of an alloy because of its single-site approximation [100].

In the effective tetrahedron model [102], the total energy of an alloy may be expressed as a sum of smallest tetrahedron clusters, in which the local lattice relaxation caused by alloying element and structural defect in a specific configuration will be

considered. The lattice distortions determined by the atomic size could occur and the energy of lattice relaxations can be quite large [102]. For instance, in binary $A_{1-c}B_c$ alloy, the total energy via a tetrahedron model (E_{rel}) can be written in the form [102]

Equation 2.26 $$E_{rel} = \frac{1}{4}\sum_{i,j,k,l} V_{rel}(c_i, c_j, c_k, c_l)$$

where V_{rel} is the relaxation interaction which is a function of the occupation number $\{c_i\} = c_i, c_j, c_k$ and c_l ($c_i = 1$ if site i is occupied by a B atom; otherwise it is 0) for the corresponding tetrahedron vertices i, j, k, and l. By using first-principles calculations, the volume interaction as a function of the volume relaxation energy of some special α structures can be calculated through

Equation 2.27 $$V_{rel}\{c_i\} = E^{\alpha}[\Omega_{rel}(\{c_i\})] - E^{\alpha}(\Omega_0)$$

where E^{α} is the total energy per atom of an ordered α structures associated with a given tetrahedron configuration $\{c_i\}$ and Ω_0 the volume of the unrelaxed tetrahedron. The volume of the fully relaxed tetrahedron with configuration $\{c_i\}$ embedded in the effective medium, $\Omega_{rel}(\{c_i\})$, may be obtained from the corresponding bond lengths which from the tetrahedron sites and can be determined in a simple harmonic spring model. Considering the chain M-A-B-M, where M are the effective medium and their positions are assumed to be fixed, the position of A and B atoms are allowed to relax according to the initial equilibrium bond length (d^0_{XY}) and spring constants (K_{XY}) for the individual pair of X and Y atoms (schematic image is shown in Figure 2.2). In order to solve the

spring model for each pair of atoms, the equilibrium bond length and spring constants of the following bonds: A-A, A-B, B-B, M-M, M-A and M-B, should be estimated. Through the calculations of ground state of pure A, B and M, parameters for A-A, B-B and M-M bonds of binary $A_{1-c}B_c$ alloy are obtained. For the A-B bond, the simplest order structure AB is suggested to get d_{XY}^0 and K_{XY}, while Zen's law (or Vegar's law) is used to calculate d_{XY}^0 and K_{XY} of M-A and M-B bonds [102]. It is clearly shown that investigation of the interactions among different atoms is the key to calculate the total energy of a solid solution with short range order.

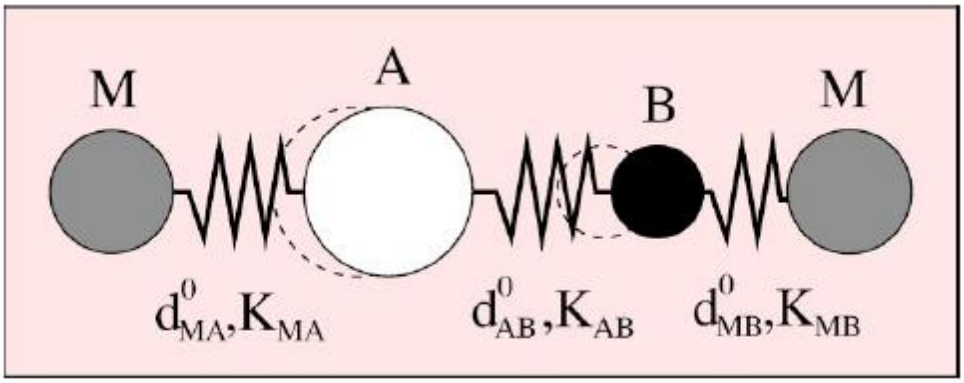

Figure 2.2 Schematic picture of the harmonic spring model [102]: M are the effective medium and their positions are assumed to be fixed, while the position of A and B atoms are allowed to relax according to the initial equilibrium bond length and spring constants.

2.6.1.2. Special quasirandom structures (SQS)

Special quasirandom structures (SQS) of disordered solution phases have been successfully applied into fcc [103], bcc [104]and hcp [105]systems. The essence of the SQS method is to use an ordered structure to mimic the properties of the corresponding disordered structure, which is as same as the cluster expansion method (CEM) [106]. Through SQS approach, a given structure can be characterized by a set of correlation function [103, 107]. Therefore, it is suitable for first-principles calculations since limited numbers of ordered structures are applied instead of the disordered one. Unfortunately, the application of SQS in the study of solute atoms segregated in short range order of stacking faults and LPSOs has not been tested. The fundamental idea of the SQS approach, proposing a local structure model, will be used in the current work.

2.6.1.3. Suzuki segregation

Since Suzuki [108] pointed out the importance of the chemical interaction between solute atoms and an extended dislocation in FCC alloys, the segregation of solute atoms to fault planes is known as Suzuki Segregation, which has been reported in various alloy systems, for example, Co-Ni-based alloys [109], Cu-based alloys [110, 111], Al-Ag alloys, Fe-Ni-Cr stainless steels [112], Mg-Zn-Y alloys [113, 114]. While the segregation of solute atoms to the fault planes could reduce the elastic strain (lattice distortion), it would tend to decrease the repulsion between two Shockley partial dislocations and hence, for a given stacking fault energy, would decrease the equilibrium width of the fault [113]. In Mg alloy, it has been observed that the creep strength of Mg-

Y solid solution alloy has been improved by the addition of Zn, which results in forming the basal plane stacking fault and decreasing of stacking fault energy [115]. Moreover, the study of dislocation dissociation and Suzuki segregation in $Mg_{97}Zn_1Y_2$ alloy has confirmed that higher Zn/Y segregation in two and five fault planes associated to the <a> and <a+c> dislocation, separately [114]. Unfortunately, Suzuki segregations in the Mg alloys haven't been systematically studies due to the essential models describing the arrangement of solute atoms is not available. Therefore, segregation behavior of the alloying elements in Mg alloys should be studied.

2.6.1.4. Local $L1_2$-type short range order (TM_3RE_4) in LPSO of Mg alloys

Recently, in the study of short range order of alloying elements in LPSOs of Mg alloys, a $L1_2$-type (TM_3RE_4) cluster has been proposed. For example, it is assumed that the Zn_6RE_8 cluster embedded in fcc stacking layers of 18R LPSO in $Mg_{85}Y_6Zn_9$ (at%) [116] and $Mg_{89}Y_4Zn_7$ (at%) [117], shown in Figure 2.3. Through applying this model into the study of Mg-Zn-Y alloys, it is predicted that the transformation between 18R and 14H LPSO ($Mg_{29}Y_4Zn_3\,(18R\,\mathrm{Gradual}) + 6Mg \rightarrow Mg_{35}Y_4Zn_3\,(14H\,\mathrm{Gradual})$) is energetic favorable, in agreement with experimental observations [118]. It is clearly shown that the lattice distortion existing in the Zn6Y8 cluster of 18R LPSO of Mg alloy, shown as Figure 2.4 [119]. Although the local occupation behavior of alloying elements in 14H and 18R LPSOs could be effectively discussed by the $L1_2$-type (TM_3RE_4) cluster model, the essential condition for the application of this model is to assume the stoichiometric LPSO structures incorporate few extra TM_3RE_4 clusters, which results in the concentration of alloying elements in LPSOs is higher than that of in HCP stacking

layers [29], shown in Figure 2.5. Moreover, the concentrations of Zn and Y in 14H and 18R LPSO are fixed in the ratio of 3/4. In fact, various compositions of Zn and Y in LPSO structures in Mg-Zn-Y alloys have been experimentally observed and cannot be considered to be ideal stoichiometric one in a fixed ratio, i.e. $Mg_{100-x}Zn_{2\pm1}Y_{4\pm2}$ [33], $Mg_{87}Zn_3Y_{10}$ [120] for 6H, $Mg_{87}Zn_7Y_6$ [32], $Mg_{94}Zn_2Y_4$ [29], $Mg_{86}Zn_7Y_7$ [121] for 14H, $Mg_{91}Zn_3Y_6$ [32], $Mg_{85}Zn_6Y_9$ [29], $Mg_{84}Zn_8Y_8$ [121] and $Mg_{100-x}Zn_{13.7\pm1}Y_{7.5\pm1}$ [122] for 18R. Accordingly, more non-stoichimetric Zn_mY_n(Mg) clusters derived from Zn_6Y_8 have been proposed in the study of 14H and 18R LPSO structures [119]. Therefore, more works are required to reveal the segregation behavior of alloying elements in LPSOs and the stabilities of the microstructures generated by those models. Particularly, segregation behavior of the alloying elements and their contributions on the formability and the electronic structures of 6H LPSOs have not been reported in Mg alloys.

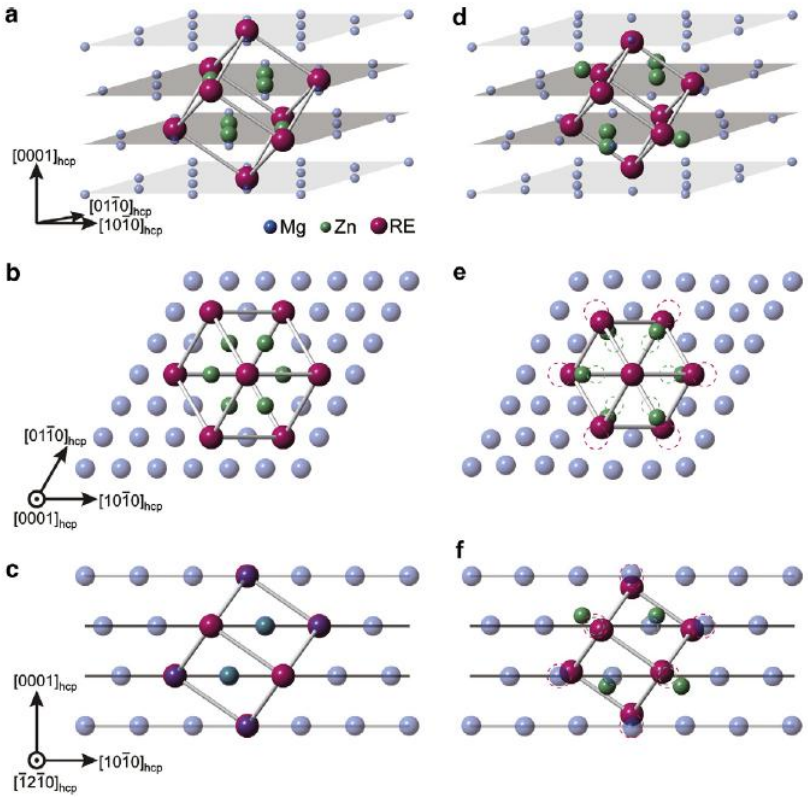

Figure 2.3 Local structure around the Zn_6RE_8 cluster embedded in fcc stacking layers in the LPSO phases [29]; (a-c) initial configuration and (d-e) energetically optimized configuration. Structures are shown: (a, d) schematic view; (b, e) $[0001]_{hcp}$ projection; (c, f) $[\bar{1}2\bar{1}0]_{hcp}$ projection.

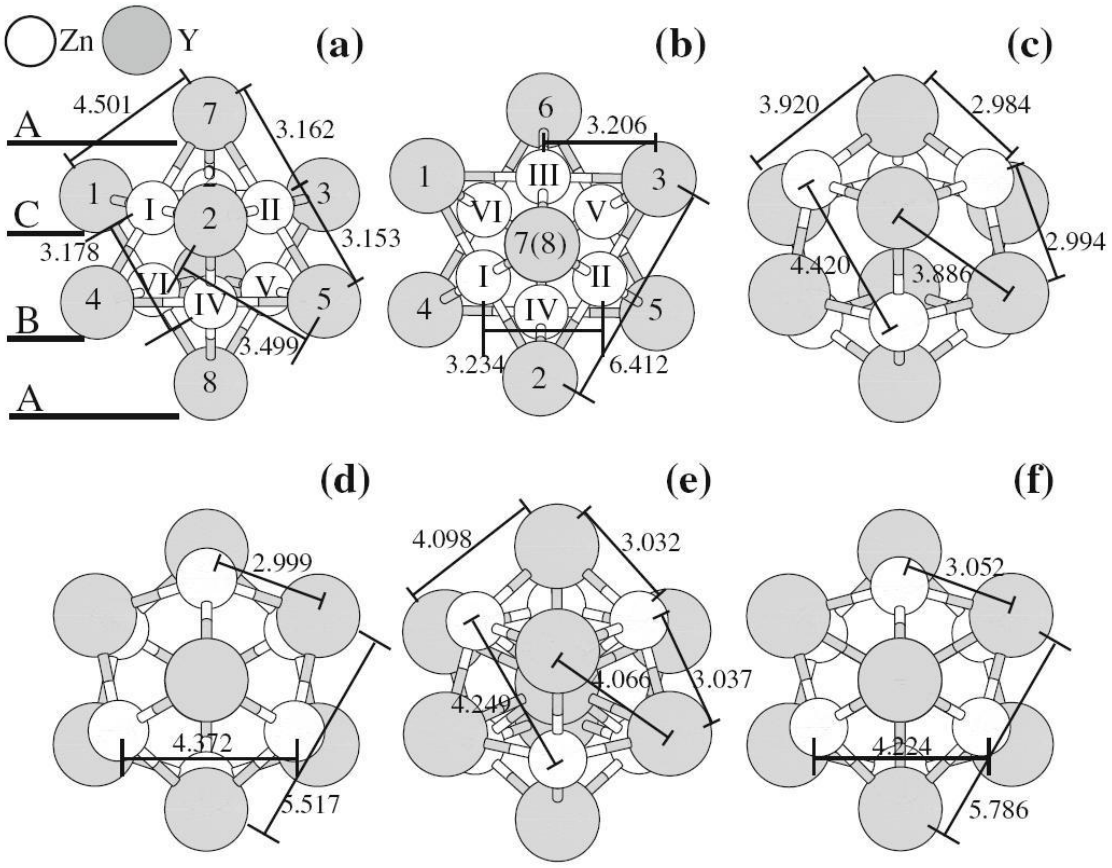

Figure 2.4 Schematic sides (a, c, e) and top views (b, d, f) of unrelaxed Zn_6Y_8 (a, b), relaxed Zn_6Y_8 (c, d) and relaxed Zn_6Y_9 (a, b) clusters [119]. The unit of atomic distance is Å.

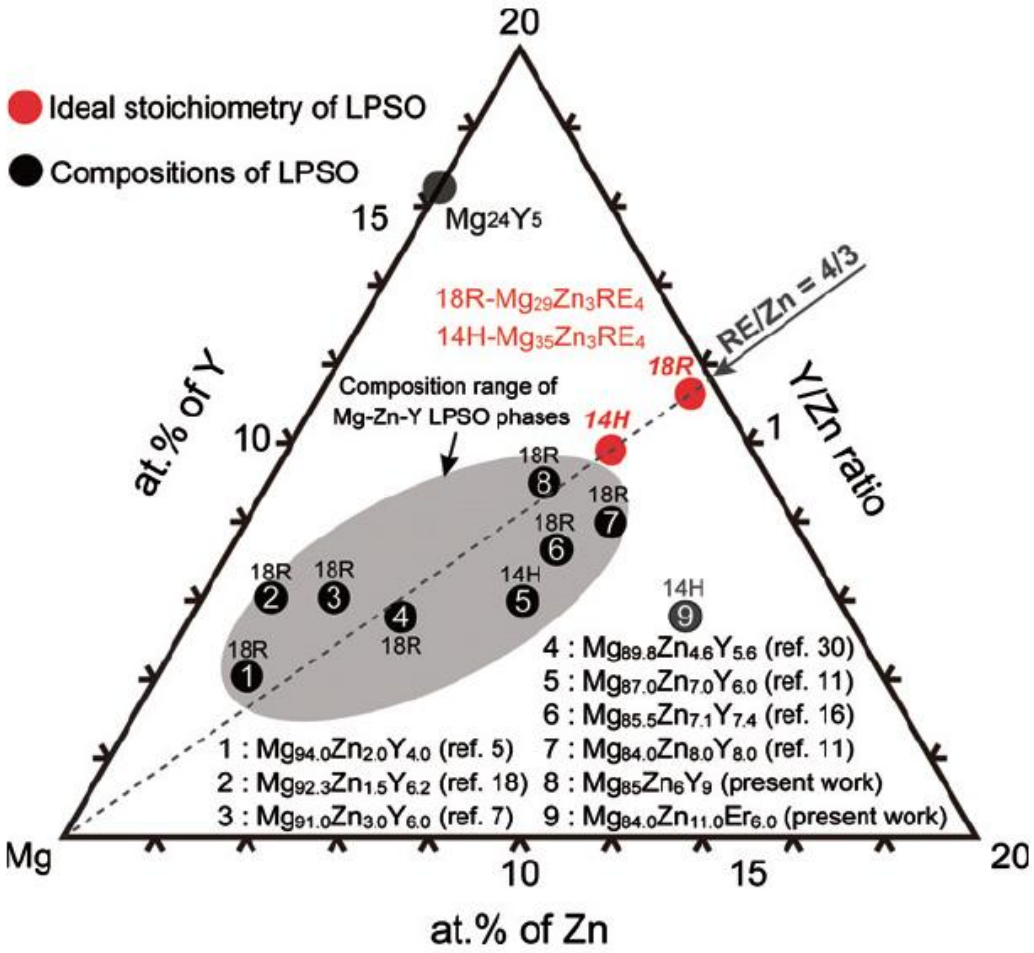

Figure 2.5. Schematic quasi-isothermal section of Mg-Zn-Y ternary phase diagram [29]. Experimentally determined compositions of Mg-Zn-Y LPSO phases annealed at temperatures of 573-793K are plotted together with the ideal stoichiometry compositions of the present LPSO models (red). 14H in $Mg_{83}Zn_{11}Er_6$ is also plotted as no.9 for comparation.

2.6.1.5. Alloying elements arrangements in two layers around fault plane in Mg alloy

In Mg alloys, works on the microstructures of Mg-Zn and Mg-Zn-Gd alloys with deformation twins [38]and Mg-8Y-2Zn-0.6Zr (wt. %) with LPSOs [121, 123, 124] have shown that the ordered arrangement of Zn and RE atoms are around fault layers; For example, Zhu et al. [124] observed the enrichment of Zn and Y atoms at two stacking fault layers of 14H LPSO through HAADF-STEM. Correspondingly, they proposed that Zn and Y atoms are enriched at two stacking fault layers in ordered arrangements as $Mg_{12}YZn$ in 14H LPSO. Similarly, the sharp change in the concentration of Zn and Y in 6H LPSO of $Mg_{97}Zn_1Y_2$ alloy has suggested that the enrichment occurs in one or two atomic layers [120], the measurement of which is by using 3D atomic probe analysis together with HRTEM image and agrees with previous observations by using energy-dispersive spectroscopy [33]. However, the ordered arrangement of Zn and RE alloys in the fault layers isn't well defined till now.

Recently, an unusual phenomenon in Mg alloys was reported, which is the equilibrium segregation of solute atoms into patterns within fully coherent terraces of deformation twin boundaries [38]. This ordered segregation provides a pinning effect for twin boundaries. Microstructural examination of $\{10\bar{1}2\}$ twin boundaries in $Mg_{98.1}Zn_{1.9}$ and $Mg_{98.4}Gd_{1.0}Zn_{0.4}Zr_{0.2}$ alloys present a periodic segregation of solute atoms in the twin boundaries, shown in Figure 2.6. Theoretically investigations by first-principles calculations have shown that strain energy minimization induced periodic segregation of solute atoms in twin boundaries. Two different types of Zn segregation in the Mg-Gd-Zn

alloy along the column direction in the $\{10\bar{1}2\}$ twin boundary have been proposed, shown in Figure 2.7. Accordingly, with various Gd and Zn segregations in the boundary, the variation tendency of the system total energy can be efficiency estimated, revealing the contributions of solute atoms to the total energy and lattice strain energy. Therefore, based on the TEM observation and first-principles calculations, the segregation behavior of solute atoms are expected to be understood through applying a model estimating their initial interactions. Hence, this procedure will provide new insights into the relationship between structure and composition of the alloy.

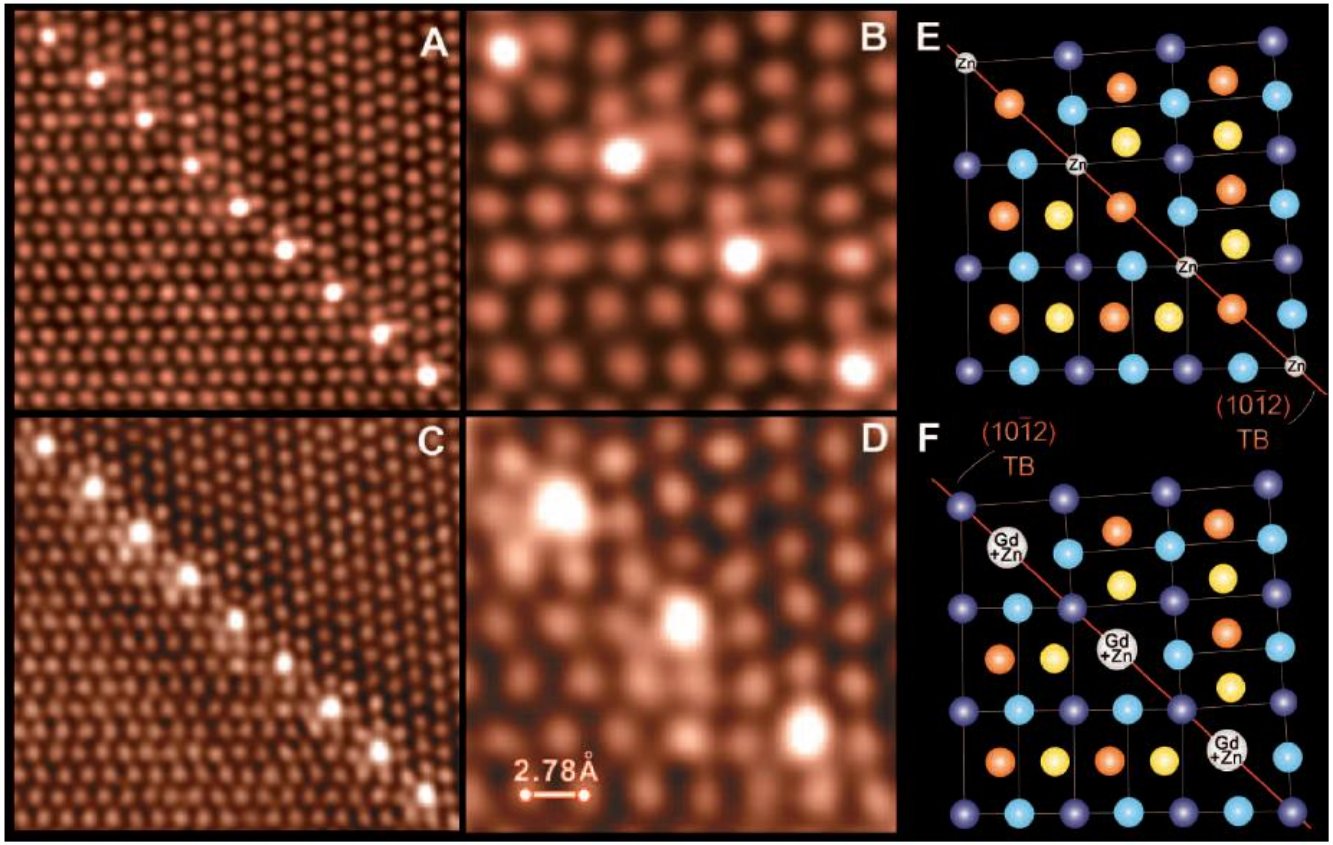

Figure 2.6 Periodic segregation of solutes in twin boundary [38]. HAADF-STEM image showing {10$\bar{1}$2} twin boundaries in (A and B) $Mg_{98.1}Zn_{1.9}$ and $Mg_{98.4}Gd_{1.0}Zn_{0.4}Zr_{0.2}$ alloys. (E) and (F) are schematic illustrations of (B) and (D).

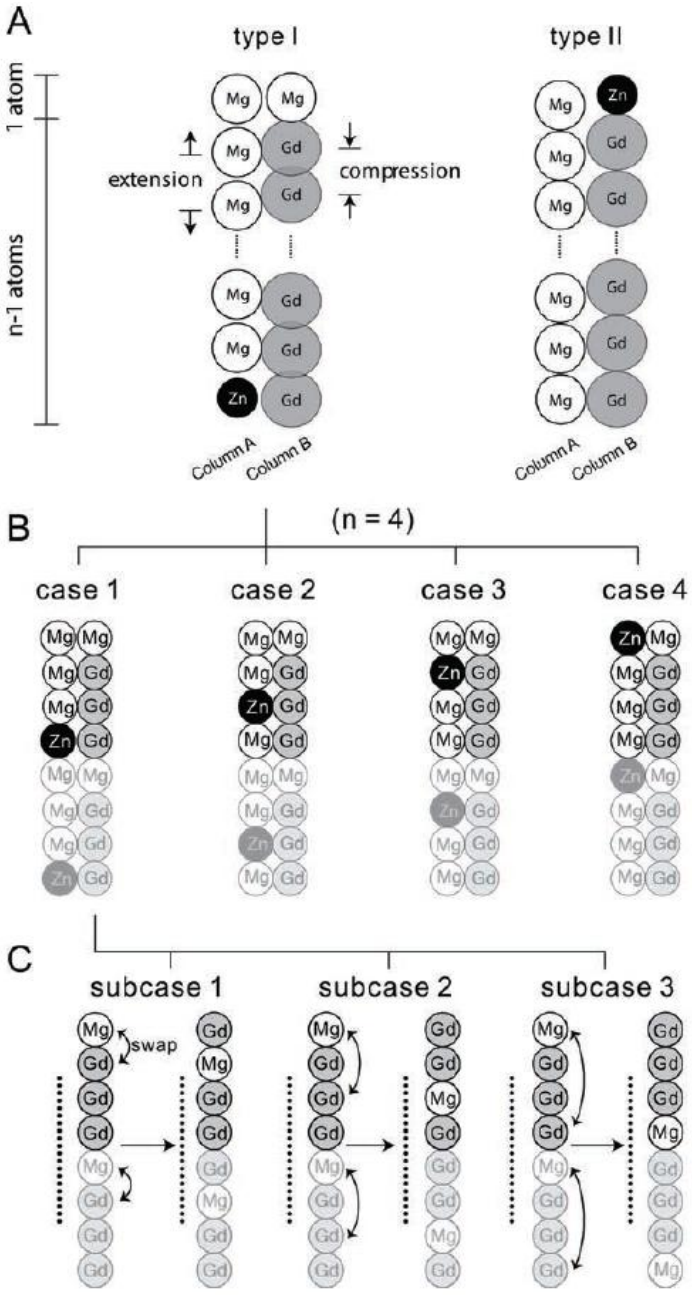

Figure 2.7 Schematic diagram showing two different types of Zn segregation in the Mg-Gd-Zn alloy along the column direction in a $\{10\bar{1}2\}$ twin boundary. Note n (number of atoms in a single column) cannot reach infinity. (B) and (C) all possible atomic structures for type I with n=4 [38].

2.6.2. Atomic array and atomic cluster models in this work

The common type of disordered solid is the substitutional alloy or solid solution, the structure of which can be captured by imaging a periodic array of points or lattice site. Previously, the assumed $Mg_2Si_2Al_7$ with Si_2 pillars have been successfully applied in the study of nanoprecipitates hardening AlMgSi alloys, in which pillarlike silicon double columns are observed by atomic-resolution electron microscopy [125], shown in Figure 2.8.

In the present work, to deduce the ordered/disordered structure of alloying elements in LPSOs of Mg alloys, the atomic array and the atomic cluster models are generated by estimating whether the chemical bond between alloying elements form among alloying elements. Our proposed two models are considering (i) Zn and Y atoms preferring to locate at two specific layer in LPSOs of $Mg_{97}Y_2Zn_1$alloys has been observed by HRTEM and HAADF-STEM [23, 33, 121]; (ii) it has been assumed that a simple chemical ordering structure of Zn and Y forms by occupying every $A\dot{B}$ layers in the 6H LPSO of $Mg_{97}Y_2Zn_1$ alloy, in which the Zn and Y have a random distribution in one fault (A layer) and one non-fault layer ($\dot{B}$ layer) [33, 126]; (iii) previous works on the microstructures of Mg-Zn and Mg-Zn-Gd alloys with deformation twins [38] and Mg-8Y-2Zn-0.6Zr (wt. %) with LPSOs [121, 123] have shown that ordered arrangement of Zn and RE atoms around fault layers; (iv) it is conceivable that the elastic strain caused by the fault layers and alloying elements (Zn and Y) in our models will be reduced since the lattice parameter of Mg is larger than Zn but smaller than Y, resulting in the regions

adjacent to fault layers are expected to be rich in Zn and Y; and (v) the required number of configurations in our models is significantly reduced under the condition that there is no interaction between alloying elements if their distance is larger than 12 Å (the typical reported value in the literature [127-130]).

Thus, it is expected to be able to derive an efficient model calculating the total energy of a solid solution with short range order through investigating the interactions among different atoms, approach of which has been used in the tetrahedron model [102], solute atoms interacting in columns [38] shown in Figure 2.7 and atomic pillar model [125]. Finally, several essential physical parameters, which can be conveniently determined by experiments, would be provided; (i) lattice parameter of the given structure; (ii) global and local concentration of the alloying elements; (iii) crystal structure morphology based on HRTEM.

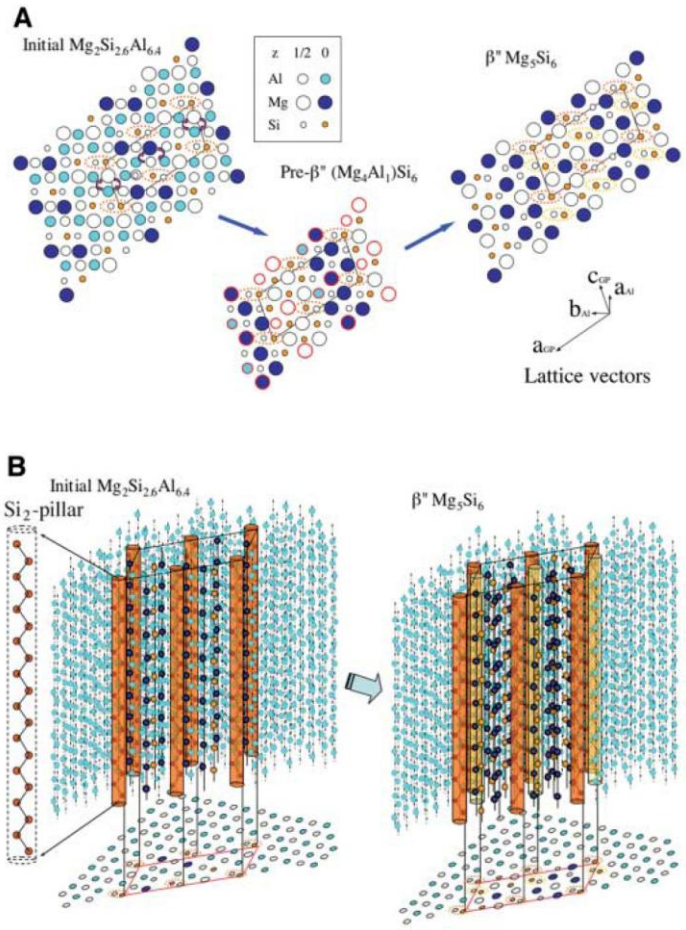

Figure 2.8 The structures of different hardening precipitates [125]. (A) The structures projected along $c_{Al}(=b_{GP})$. (a_{Al}, b_{Al}, c_{Al}) and (a_{GP}, b_{GP}, c_{GP}) denote Al and precipitate lattice vectors, respectively. The Al atoms in $(Mg_4Al_1)Si_6$ are outlined with red circles. The Mg atoms outlined with red circles indicate the special position at which the Mg atoms have to be shift $b_{GP}/2$ to become Mg_5Si_6. (B) The 3D view of $Mg_2Si_{2.6}al_{6.4}$ and Mg_5Si_6 particles surrounded by Al, showing that the Si double columns are the common structural component of these precipitates and may serve as the stable pillar in the structure evolution. More Si2 component (yellow ones) can be found in Mg_5Si_6 but they no longer act as pillars for Mg_5Si_6 to evolve.

Chapter 3

Formation Energy, Electronic and Phonon Properties of Stacking Faults in Mg

3.1. Introduction

Formation of stacking faults is an important deformation mechanism in materials with hcp structure such as Co, Hf, Mg, Ti, Zr and their alloys. They affect core structures and mobility of dislocations [6, 7], twinnability and ductility[11, 12], and creep rate [14]. There are three typical basal-plane stacking faults in hcp alloys, i.e. growth fault (I1, $ABA\dot{B}CBCB$), deformation fault (I2, $ABA\dot{B}\dot{C}ACA$), both intrinsic, and extrinsic fault (EF, $ABA\dot{B}\dot{C}\dot{A}BAB$). Previous calculations for a range of hcp elements of Be, Co, Hf, Mg, Re, Ru, Sc, Ti, Y and Zr showed that the I1 stacking fault energy is considerably lower than the I2 stacking fault energy, with the latter lower than that of extrinsic fault [20-22, 131]. The fundamentals of this interesting observation have not been articulated and understood in the literature. Due to their importance in deformation of hcp alloys, in this part of work, we determine the energies of the three basal-plane stacking faults of hcp Mg via first-principles calculations based on density functional theory (DFT) [57]. Furthermore, we examine the details of charge transfer in the fault and non-fault atomic planes through electron localization morphology and quantitatively correlate the stacking

fault energy with respect to the number of atomic layers deformed due to the charge density redistribution. The physical significance of this correlation is investigated in terms of the difference of the deformation charge density and electron localization function of the fault and non-fault atomic planes.

3.2. Crystal Structures and Computational Details

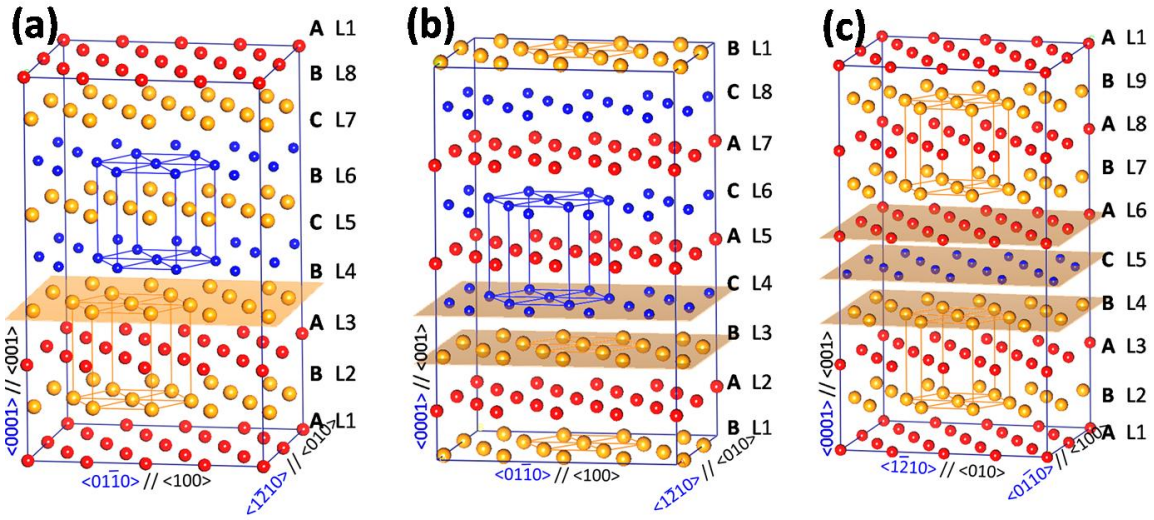

Figure 3.1. Crystallography structure of (a) growth fault – I1; (b) deformation fault – I2 and (c) extrinsic fault – EF. The corresponding closed packed sequence of each stacking fault is given a layer number (L#). Lattice vectors of the primitive hcp Mg parallel to these of the orthorhombic supercell are labeled. Fault layers are identified by the {001}//{0001} miller plane.

In the present first-principles calculations, the orthorhombic supercell sizes of I1, I2, and extrinsic faults are $4a \times 2\sqrt{3}a \times 4c$, $4a \times 2\sqrt{3}a \times 4c$ and $4a \times 2\sqrt{3}a \times 4.5c$ with 128, 128, and 144 atoms, respectively, where *a* and *c* are the theoretical lattice parameters of primitive hcp Mg [132]. The lattice vectors of the orthorhombic supercell are related to those of the hcp Mg as $\langle 01\bar{1}0 \rangle \| \langle 100 \rangle$, $\langle 1\bar{2}10 \rangle \| \langle 010 \rangle$, and $\langle 0001 \rangle \| \langle 001 \rangle$, shown as Figure 3.1.

Calculations of electronic structures and stacking fault energy at 0 K are conducted by employing the Vienna *ab initio* simulation package [90, 91] with the generalized gradient approximation [133] for the exchange correlation functional and the projector augmented wave [134] for the electron-ion interaction. The wave functions are sampled on Γ-centered mesh of $5 \times 5 \times 3$. The plane wave cutoff energy is set as 300 eV, i.e. 1.4 times the default energy cutoff for high accuracy calculations, and the energy convergence criterion of electronic self-consistency is 10^{-6} eV/atom. While the structures are fully relaxed by the Methfessel-Paxton technique [135], the final total energy calculations are performed by the tetrahedron method incorporating Blöchl correction [136]. The isosurface and the contour plots of the charge density are generated using VESTA. [65, 66]

The stacking fault energy, γ, is defined as,

Equation 3.1
$$\gamma = \frac{1}{A}(E_{sf} - E_{Bulk})$$

where E_{sf} and E_{Bulk} are the total energies of supercells with and without stacking fault, respectively, and *A* is the total stacking fault area. It should be pointed out that there are two fault planes in the I1 and I2 supercells, while only one in the supercell containing the extrinsic fault.

3.3. Results and Discussions

3.3.1. Stacking fault energy

The calculated stacking fault energies are summarized in Table 3.1 together with the available experimental measurements and theoretical predictions in the literature. Even though both experimental and calculated data are rather scattered, it is clearly shown that the values of stacking fault energies are in the order of $\gamma_{I1} < \gamma_{I2} < \gamma_{EF}$.

Table 3.1. Stacking fault energy of growth, deformation and extrinsic faults at 0 K

Stacking fault energy mJ/m^2	**This work**	**Other theoretical works**	**Experiment**
Growth fault (I1)	14.4	8.1~17.8[a], 11[b], 18[c e], 16[h], 27[d], 22[d], 15[d]	78 [8] 50 [137]
Deformation fault (I2)	48.2	38.3[a], 33.8[c], 23[b], 33[e], 34[h], 54[d], 44[d], 30[d] ,36[i]	
Extrinsic fault (EF)	99.3	80.6[g], 52.6[c], 36[b], 140[f], 59[h]	

[a] Wang et al., first-principles calculation with GGA [20]
[b] Chetty et al., first-principles calculation with LDA [6]
[c] Fan et al., first-principles calculation with GGA [138]
[d] Han et al., molecular dynamic (MD) calculation with EMA and MEAM [139]
[e] Han et al., first-principles calculation [139]
[f] Wang et al., first-principles calculation with GGA [140]
[g] Datta et al., first-principles calculation with LDA [2]
[h] Wen et al., first-principles calculation with GGA [18]

3.3.2. Electronic structure characterization by Δρ and ELF

Figure 3.2 shows the comparation of deformation electron density between non-fault planes in an extrinsic fault and these in a perfect Mg together with the result of previous theoretical work by Blaha et al. [141]. It can be seen that the electronic structure of the non-fault planes in an extrinsic fault match well with a perfect Mg, which is a rod-shaped directional bond along [0001] direction.

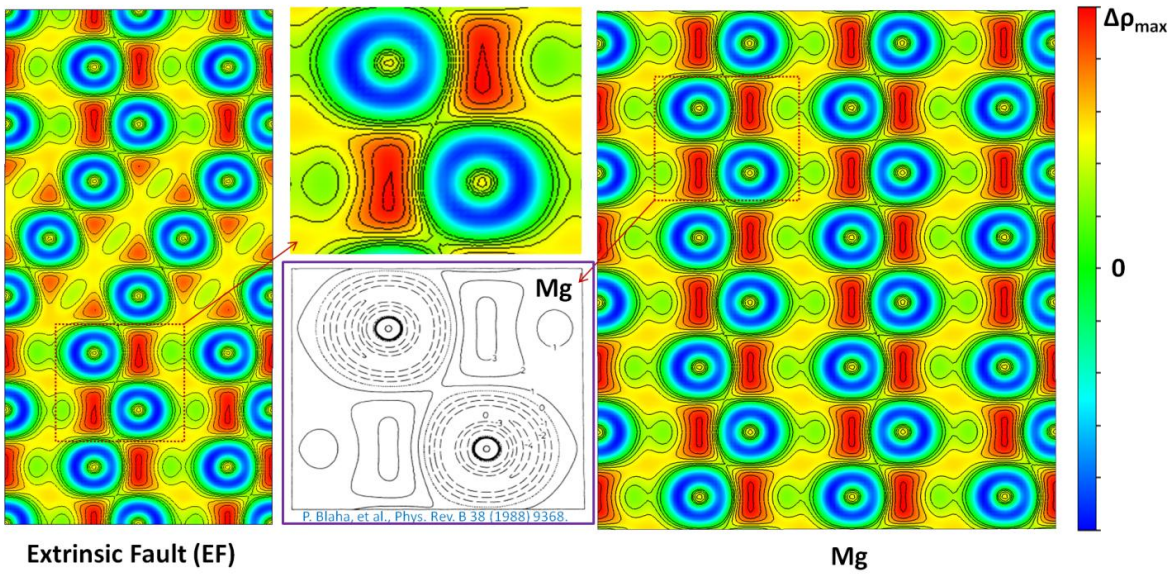

Figure 3.2. The comparation of deformation electron density between non-fault planes in an extrinsic fault and these in a perfect Mg together with the previous theoretical work by Blaha et al. [141].

Figure 3.3 shows the contours of Δρ in (010). The triangle-shaped directional bonds are observed within fault planes (L4 for I1, L3 and L4 for I2, and L4, L5, and L6

for extrinsic fault) in contrast to the rod-shaped directional bonds within non-fault planes. The electron re-distribution ranges in Figure 3.3 increase from I1, I2, to extrinsic fault. It can be expected that the relative shear deformation range and stacking fault energy would increase in the same order [63]. Moreover, it is necessary to point out that the rod-shaped directional bonds within non-fault planes of each stacking fault transfer into tetrahedron type directional bonds in fault planes.

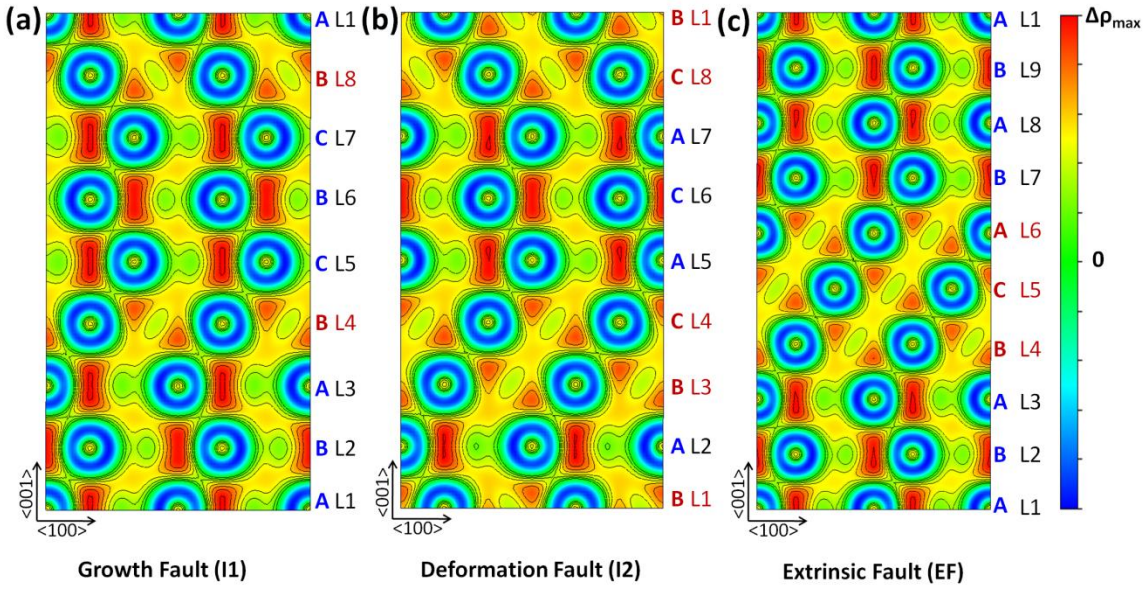

Figure 3.3. $(010)_{s.c.}$ plane contour plots of Δρ of Mg (a) I1; (b) I2 and (c) EF with 0.0005 $e^-/Å^3$ intervals, generated using VESTA [65, 66] with red for Δρ>0 and blue for Δρ<0.

The contours of Δρ in (001) are plotted in Figure 3.4 along with ELF. In non-fault planes, the charge distributions in the Mg atomic basin and between Mg atoms are triangle-shaped, while in fault planes they are spherical and hexagonal, respectively. The

significant lower Δρ in fault planes depicts considerable re-distribution of electrons in the planes, increasing the energy of the system. In Figure 3.4, ELF is plotted with the same color scheme with red for ELF_{max}≈0.60~0.70 and blue for ELF_{min}~0, showing similar morphology variation as Δρ with lower values in fault planes with respect to non-fault planes.

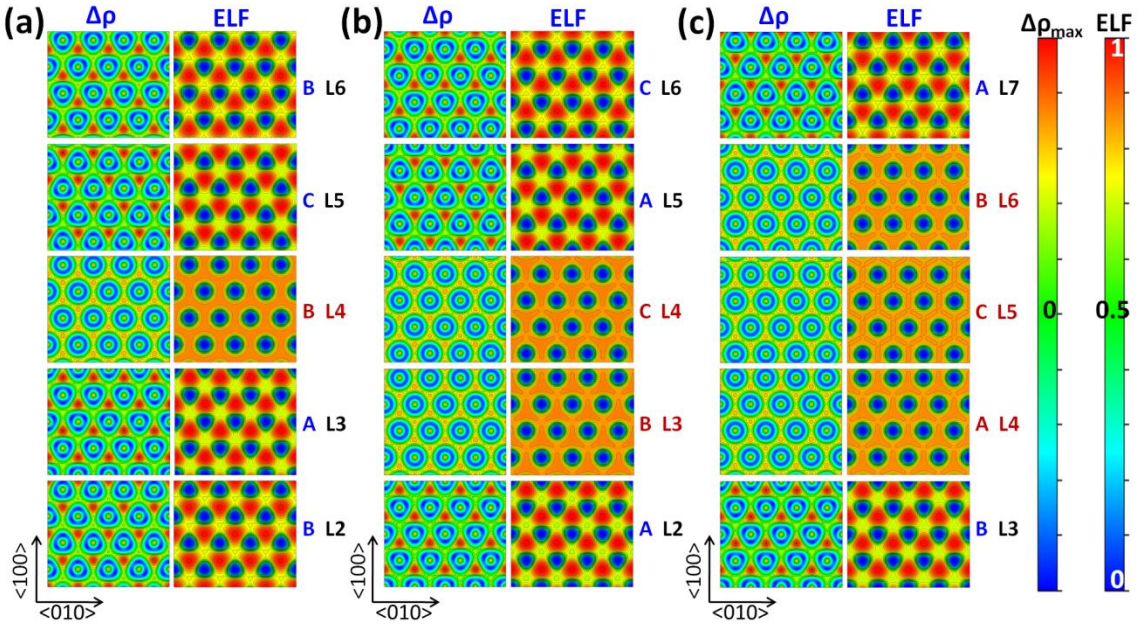

Figure 3.4. $(001)_{s.c.}$ plane contour plots of Δρ and ELF of Mg (a) I1; (b) I2 and (c) EF generated using VESTA [65, 66]. The same setting used in Figure 3.3 is also applied here when plotting Δρ. ELF is plotted with 0.05 intervals and red for 0.60<ELF <0.70 and blue for ELF~ 0.

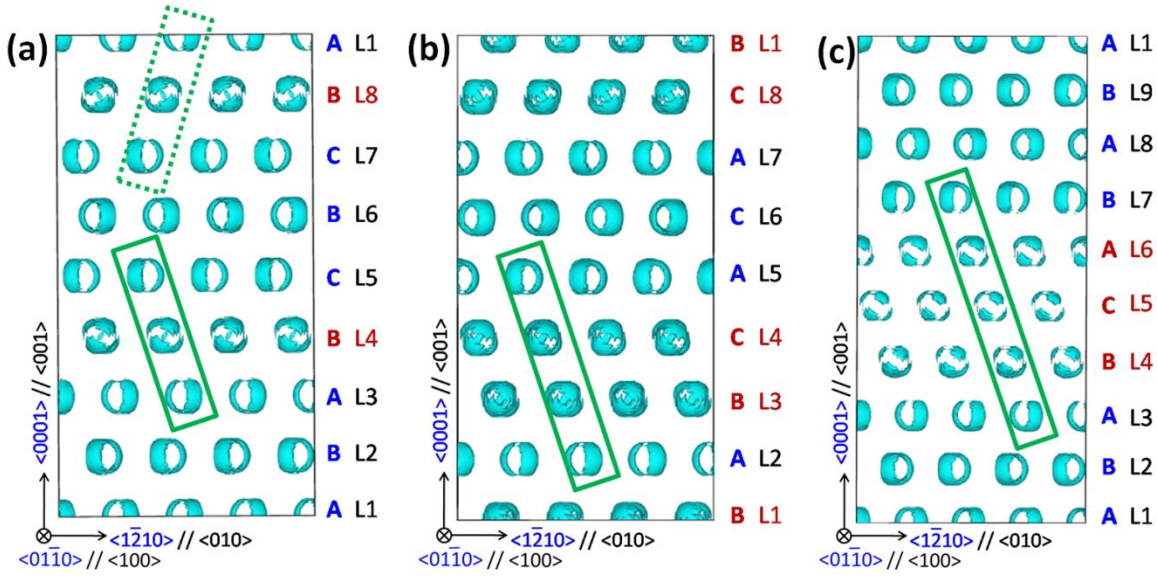

Figure 3.5. Isosurface of maximum deformation charge density, $\Delta\rho_{max}$, in (100) plane view, (a) I1 with $\Delta\rho_{max}$=0.0037 $e^-/Å^3$; (b) I2 with $\Delta\rho_{max}$=0.0036 $e^-/Å^3$ and (c) EF with $\Delta\rho_{max}$=0.0036 $e^-/Å^3$. The lattice vectors of the primitive hcp Mg parallel to these of the orthorhombic supercell are labeled. Plots are generated using VESTA in the Positive and Negative mode [65, 66]. The fault planes are layer L4 for I1, layers L3 and L4 for I2, and layers L4, L5, L6 for extrinsic faults. Stacking features across fault layers and non-fault layers are highlighted by rectangle

Figure 3.5 plots the isosurface of the maximum value of deformation electron density, $\Delta\rho_{max}$, for the three types of stacking faults in (100) plane view. Using the Positive and Negative mode in VESTA [65, 66], $\Delta\rho_{max}$ is found to be 0.0037, 0.0036 and 0.0036 $e^-/Å^3$ for I1, I2, and extrinsic faults, respectively. It is self evident that the shape of the $\Delta\rho_{max}$ isosurface in the fault planes is different from that in the non-fault planes. Furthermore, it can be seen that the number of atomic layers with altered charge density

is dependent on the stacking fault type, which is one layer (L4) for I1, two layers (L3, L4) for I2, and three layers (L4, L5, L6) for the extrinsic fault, evident from the shapes of $\Delta\rho_{max}$ isosurface. This indicates that the extent of electron re-distribution is the largest for the extrinsic fault and the smallest for the I1 fault with the I2 in between. Since the charge density is a scalar field, the change in electron distribution field results in directional bonds [63] and correlates to the stacking faults' formation energy. [64] It is further observed that the electron re-distribution occurs in the layers with their two neighboring layers being different, i.e. the L3 and L5 layers are different, resulting in the electron re-distribution in the L4 layer in Figure 3.5(a), while in Figure 3.5(b) the L2 and L4 layers are also different resulting in the electron re-distribution in both L3 and L4 layers. For the extrinsic fault in Figure 3.5(c), the different layers of L3/L5, L4/L6, and L5/L7 re-distribute the electrons in L4, L5, and L6 layers, respectively.

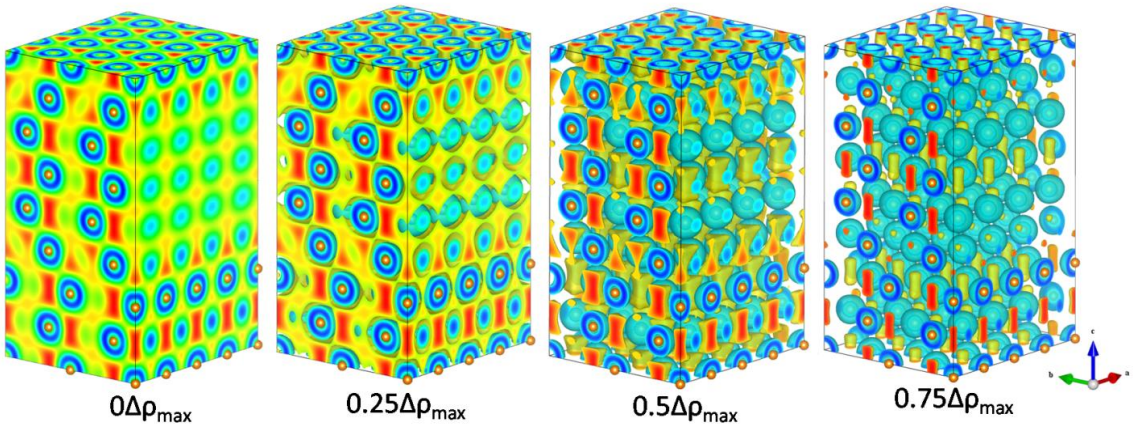

Figure 3.6. The electron density isosurface of I1 in different levels. B-G-R (Blue-Golden-Red) section plots are also used. The points in red are the charge distribution region with $\Delta\rho>0$, while the points in blue are the charge distribution region with $\Delta\rho<0$.

Through the electron tomography, the electronic structure of a specific structure could be present clearly. For instance, Figure 3.6 plots the electron density isosurface of I1 in different levels. By setting $\Delta\rho=0$, section plots are present, which are as same as those shown in Figure 3.3 and Figure 3.4. By setting $\Delta\rho>0$ together with the color scale of B-G-R (Blue-Golden-Red), the points in red are the electron distribution region, while the points in blue are the charge distribution region with $\Delta\rho<0$.

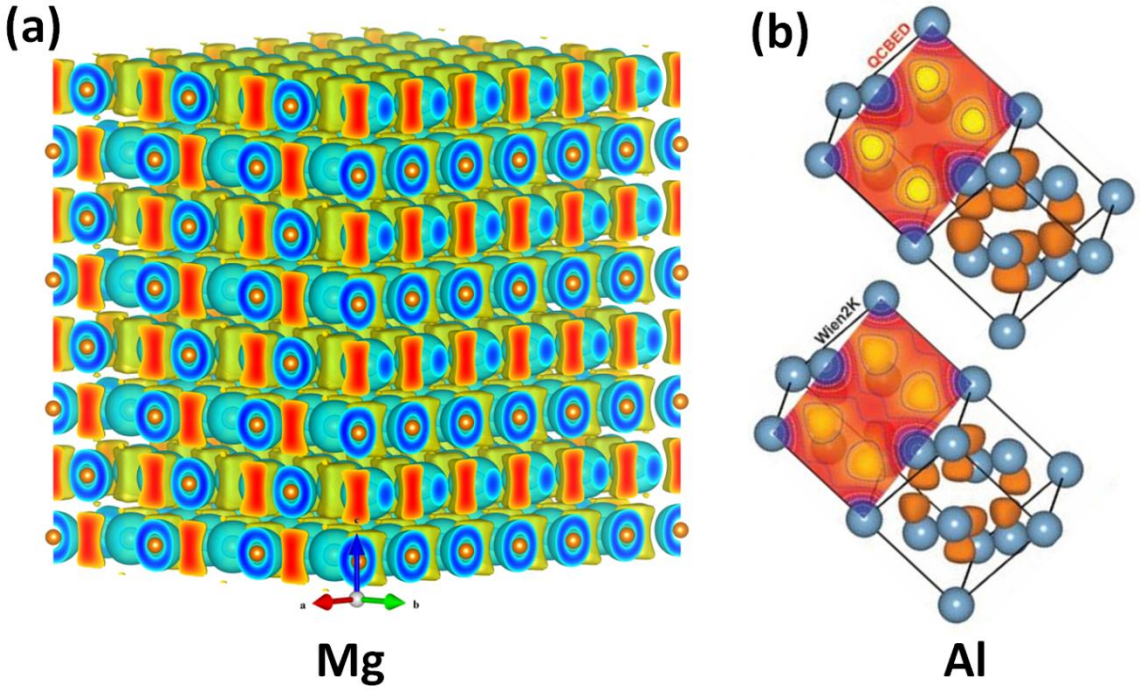

Figure 3.7. Electron structure of HCP- Mg and FCC-Al, (a) $0.5\Delta\rho_{max}$ isosurface of HCP-Mg investigated by first-principles calculations and (b) the (110) plane contour plots of $\Delta\rho$ and the 0.5 $\Delta\rho$max isosurface of FCC-Al investigated by quantitative convergent-beam electron diffraction (QCBED) and first-principles calculation via Wien2K [61].

Figure 3.8 presents the $0.5\Delta\rho_{max}$ charge density isosurface of the investigated stacking faults. At this level, variation of the chemical bond structure from non-fault layer to fault layer is revealed clearly. It is observed that the bond structures of fault layers in I1, I2 and EF are identical, which are the rod-shaped in non-fault layers transferred into tetrahedron-shaped in fault layers. It can be seen that the tetrahedron-shaped directional bonds are characteristics of the fcc structure such as Al [61], shown as Figure 3.7(b). Based on the information presented in Figure 3.7 and Figure 3.8, it should be emphasized that the electron localization morphology in this work clearly reveals that the FCC building block across the fault layers, i.e. $A\dot{B}CB$, $A\dot{B}\dot{C}A$ and $A\dot{B}\dot{C}\dot{A}$, are made up of I1, I2 and EF. It is interesting to note that the stacking fault energies are proportional to the number of fault layers.

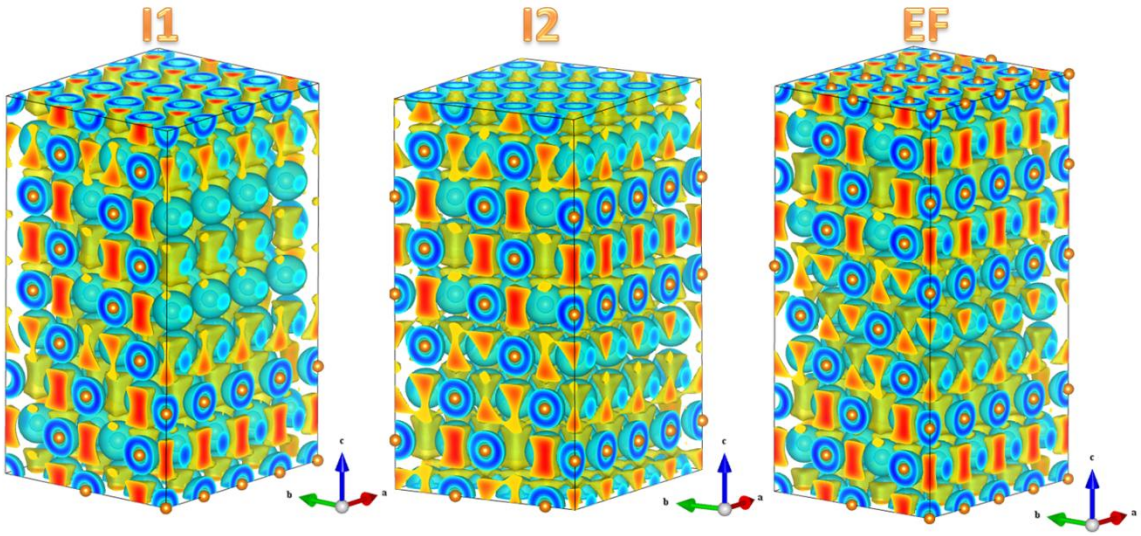

Figure 3.8. The $0.5\Delta\rho_{max}$ charge density isosurface of the investigated stacking faults. The rod like directional bonds in regular planes transform into tetrahedrons due to the formation of fault planes.

3.3.3. Simulated HRTEM images of stacking faults

As mentioned in the methodology part, HRTEM images are analyzed on the independent atom model (IAM) [61, 69] or the procrystal model [142] or the electron density from DFT with a correction in term of charge density difference [71]. Moreover, the intensity difference between electron densities from DFT and IAM is sensitive to the structure defect and the impurity (even lightweight element) [69]. The simulated HRTEM images in this work are obtained through the projection of the calculated deformation charge density ($\Delta\rho$) using the procedure described in Ref. [69]. The comparation of electron density profiles along different lines in I1, I2 and EF are shown as Figure 3.9, Figure 3.10 and Figure 3.11, separately. It has confirmed that the difference of electron density between DFT and IAM is sensitive to the structure defects and could be improved, which is similar to that in nitrogen substituted graphene, shown as Figure 2.1(b) [69]. For example, through the comparation of electron density profiles in I1, the electron redistribution range caused by the fault layers can be identified since the significant change occurs in the line profile of $\Delta\rho$, shown as the line 1 in Figure 3.9. Moreover, the pattern of the $\Delta\rho$ of two fault layers (L6 and L7; L11 and L12) in I2 can be recognized directly through investigating the line profile of $\Delta\rho$, shown as Figure 3.10. Since there are 3 fault layers (L4, L5 and L6) in EF, a line capturing the total effect zone due to the existence of those layers should be selected. As shown in the profile of line 2 in Figure 3.11, the pattern of only two fault layers (L4 and L5) can be observed. On the contrary, the specific patterns of fault layers in EF are displayed clearly in the profile of line 1 in Figure 3.11.

Figure 3.12 shows the simulated (100) HRTEM images of the stacking faults in I1 (a), I2 (b) and EF (c). Fault and non-fault layers are labeled in red and blue letters, respectively. Stacking features across fault and non-fault layers are highlighted by rectangle. The stacking sequences of I1, I2 and EF can be wrote as $A\dot{B}C$, $A\dot{B}\dot{C}A$ and $A\dot{B}\dot{C}\dot{A}$ across the fault layers, forming basic unites of rectangles with 3, 4 and 5 atomic layers, respectively, as the same as those shown in Figure 3.4. According to the electronic structures and HRTEM patterns of those stacking faults, the physical nature of the long periodic stacking order structure could be revealed thoroughly in the next chapter.

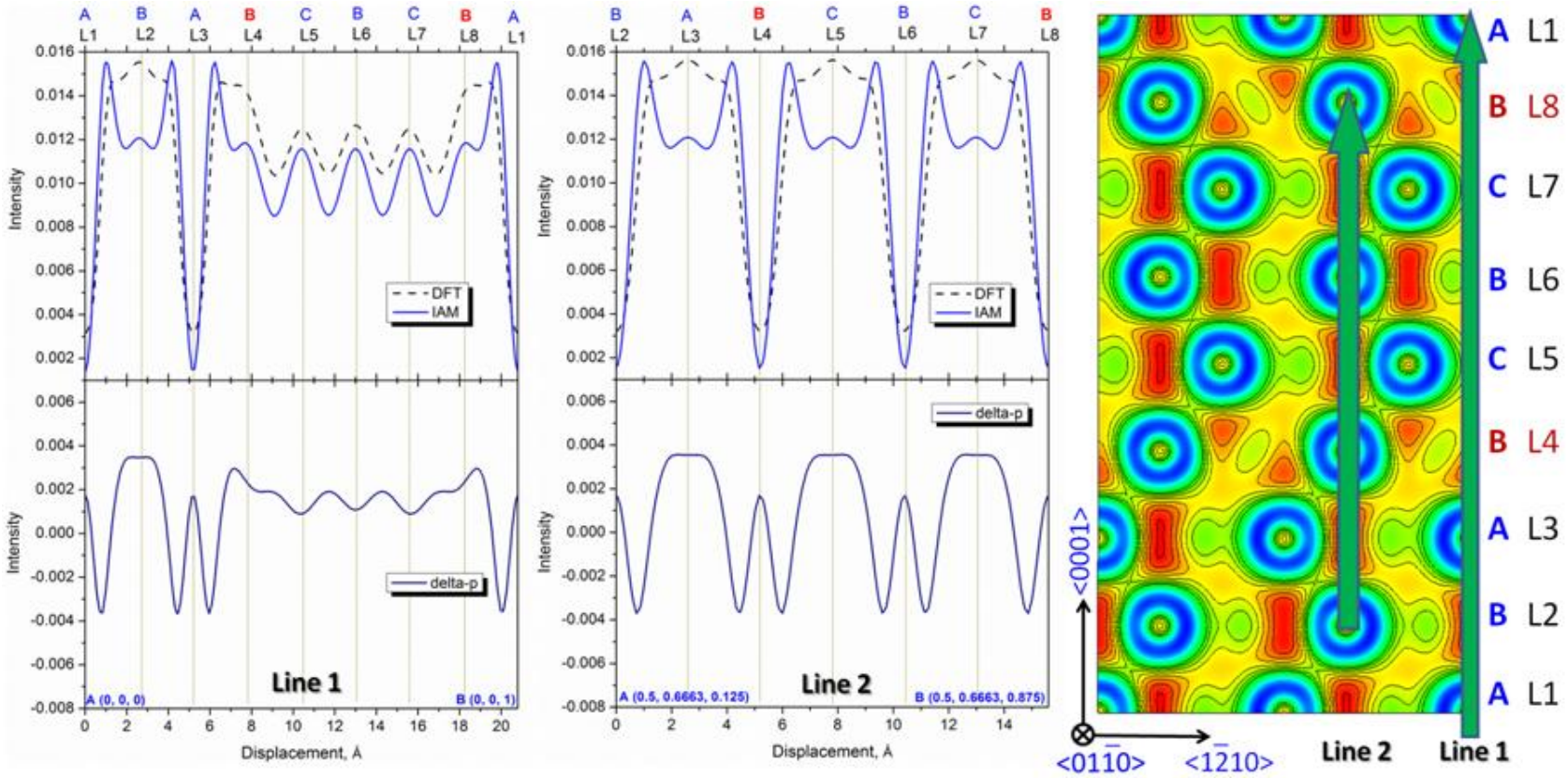

Figure 3.9. Comparation of electron density profiles along different lines in I1. Fault layers are labeled with letters in red.

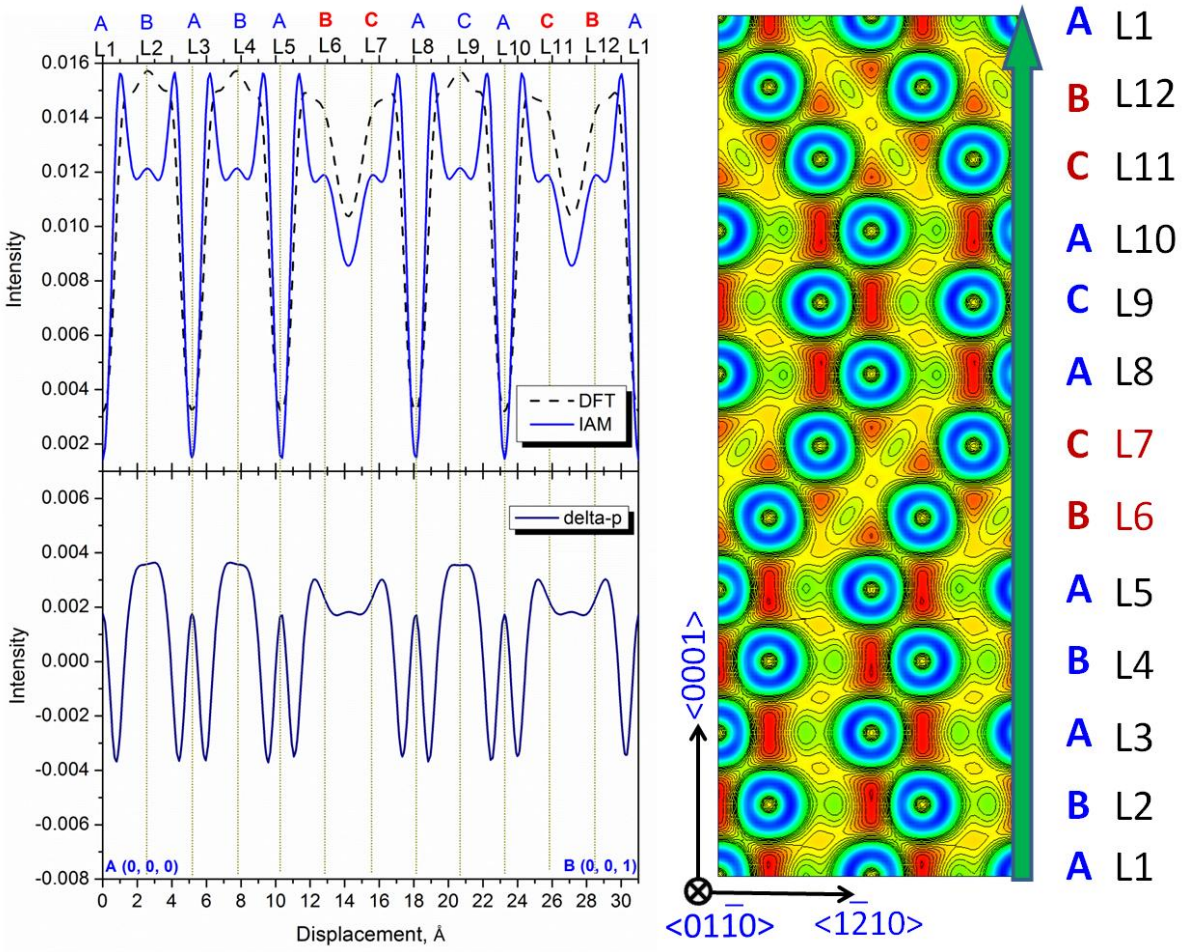

Figure 3.10. Comparation of electron density profiles between IAM and DFT in I2. Fault layers are labeled with letters in red.

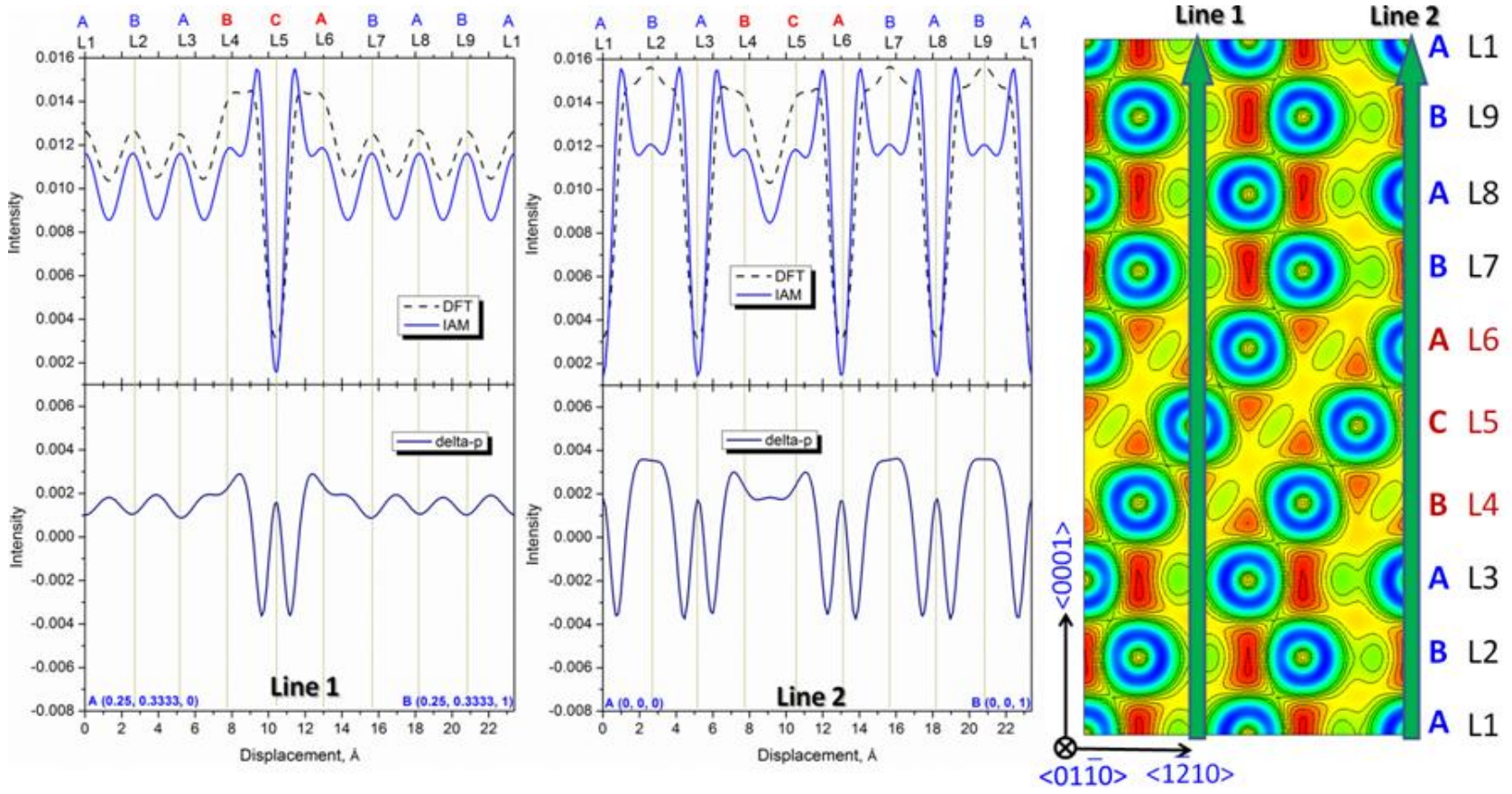

Figure 3.11 Comparation of electron density profiles along different lines in EF. Fault layers are labeled with letters in red.

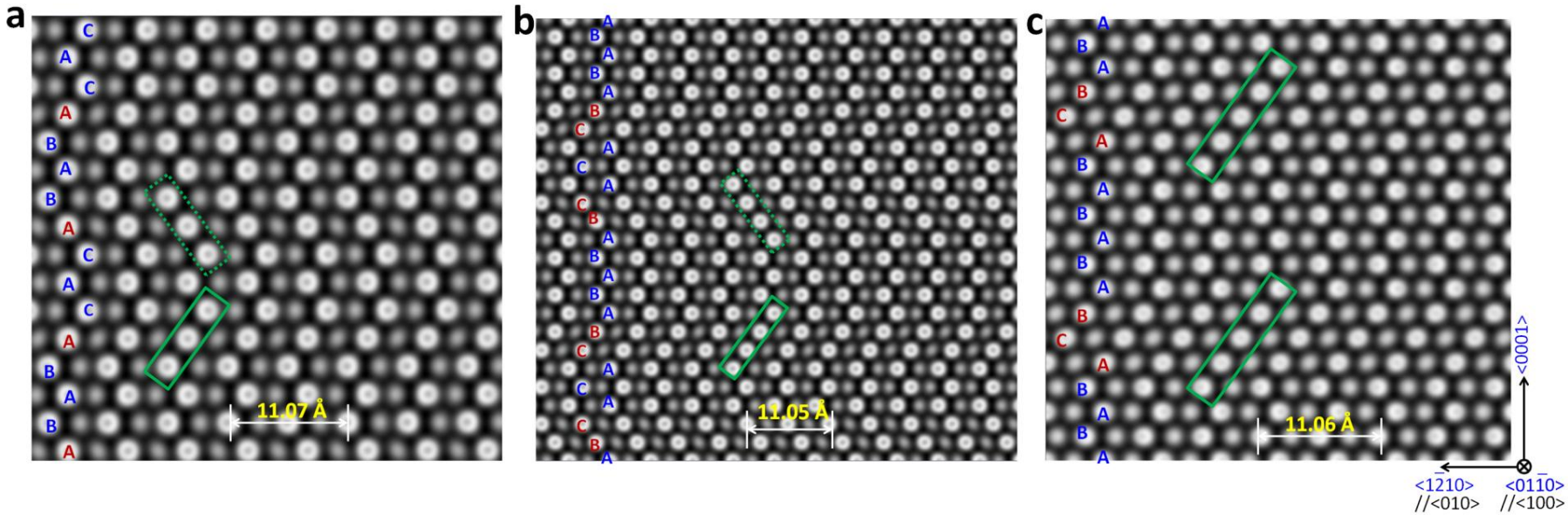

Figure 3.12. Simulated (100) HRTEM images of the stacking faults in I1 (a), I2 (b) and EF (c). Fault and non-fault layer are labeled with letters in red and blue, respectively. Stacking features across fault and non-fault layers are highlighted by the rectangle.

3.3.4. Correlation between stacking fault energy and deformation electron density

To quantify the electron re-distribution, the differences in $\Delta\rho_{max}$ and ELF_{max} between the fault and non-fault planes, $d(\Delta\rho_{max})$ and $d(ELF_{max})$, are investigated. As noted above, there are one, two, and three fault planes for I1, I2, and extrinsic faults, respectively. $d(\Delta\rho_{max})$ thus represents the total amount of electrons redistributed due to the stacking fault formation, while $d(ELF_{max})$ indicates the disparity of their electron kinetic energies. It can then be postulated that the larger the $d(\Delta\rho_{max})$, the more electrons are displaced by the stacking fault, resulting in higher stacking fault energy. By the same token, the larger the $d(ELF_{max})$ the higher the stacking fault energy. Based on the current results plotted in Figure 3.13, one can see that stacking fault energy of Mg is proportional to $[d(\Delta\rho_{max})]^2$ and $|d(ELF_{max})|$, respectively, i.e. $\gamma = A[d(\Delta\rho_{max})]^2$ and $\gamma = B|d(ELF_{max})|$. The different proportionality is likely related to the approximate dependence of ELF on ρ^2 implicated in Figure 3.13(b).

Through quantitative comparison of bonding properties (ELF and $\Delta\rho$) between different stacking faults in Mg, the physical nature of the stacking fault energy can be considered as the total work done to the system adiabatically, which induces the redistribution of charge and results of the transformation of bond morphology from rods to tetrahedrons (as shown in Figure 3.7 and Figure 3.8). According to energy conservation, the required work for transporting the charge from the initial state of perfect crystal to the final state of the stacking fault can be expressed as the integration of the Coulomb force on the each electron and its displacement. Since the Coulomb force (

$F_{Coulomb}$) is proportional to the charge distribution of the atoms (q_1) and the bonding charge distribution (q_2), the value of Young's modulus (E) has been manifested as equivalent to the charges as $E \propto F_{Coulomb} \propto q_1 q_2$ [61]. Correspondingly, elastic energy of the lattice strain can be expressed as a function of ρ^2, which is the integration of the lattice stress-strain curve during the elastic deformation. Therefore, the aforementioned correlation between stacking fault energy and ρ^2 shown as Figure 3.13**(a)** can be understood in terms of the total work.

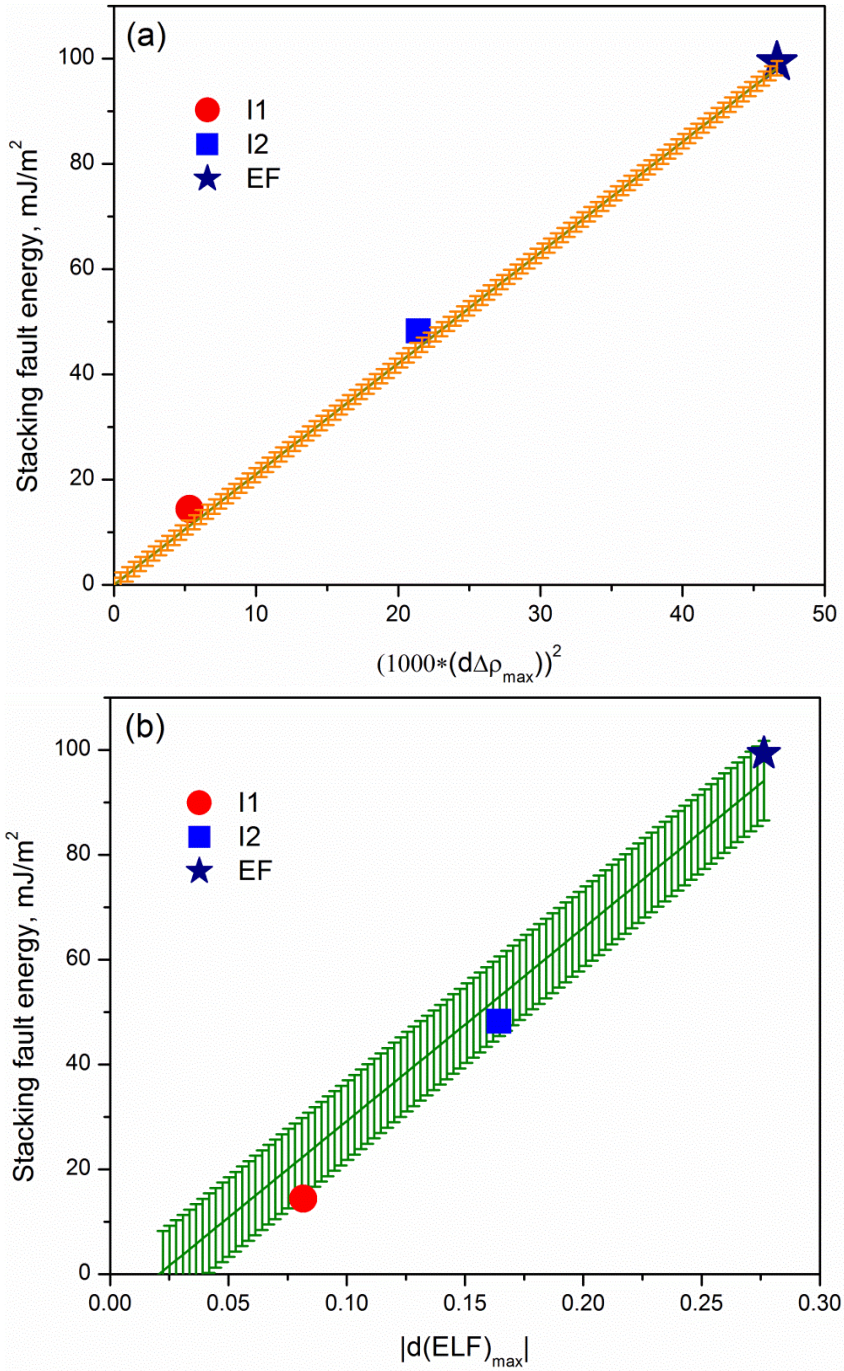

Figure 3.13. Correlation of stacking fault energy with deformation charge density and electron localization function, displaying that the stacking fault energy is proportional to the square of the difference of deformation charge density.

3.3.5. Phonon properties and vibrational entropy of stacking faults

Phonon dispersion curve of Mg at the equilibrium volume comparing with the available experimental data [143, 144] is shown as Figure 3.14. A good agreement between the current theoretical calculation and the inelastic-neutron-scattering measurement indicates the accurate calculations of the force constants and the reliability of the current approach. Thus, same parameters in the first-principles calculations are applied in the study of local phonon density of states (LPDOS) of the atoms occupying positions in fault layers.

Respecting to the contribution of thermal electron, phonon play the dominate role to contribute the thermodynamic properties at finite temperature [80, 145]. Since the entropy is proportional to the logarithmic moment of phonon DOS (Equation 2.19), the Helmholtz energy could be reduced with the contributions of atomic layers with higher entropy. Previous studies have shown that high entropy stabilization the ordered structure in Zn_4Sb_3 [146] and Ni_3Pt [145]. In particular, the higher value of phonon DOS in the low frequency region dominates the reduction of Helmholtz energy of Ni_3Pt, which also results in the higher entropy [145]. More interestingly, based on the analysis of LPDOS of Σ5(310) grain boundaries in Al, it has suggested that the atomic vibrations of the atoms around the boundaries are different from those far away in the bulk, which could generally strengthen the resonant mode at low frequency and weaken the mode at high frequency [147]. Similarly, with the formation of Σ5(310) grain boundary in Cu, the most striking feature is the increase of the LPDOS at low frequency and its decrease at high frequency. This displacement towards to the low frequency is due to the large free

volume [86]. It is worth to mention that the strange peaks are also observed at high frequency region in the LPDOS curve of Σ5 grain boundaries in both Al and Cu [86, 147]. Therefore, it is essential to study the contributions of fault layers on the phonon density of states and vibrational energies of Mg at finite temperature.

Comparing with the total phonon DOS of Mg, it can be seen that the frequency of the phonon peaks (ω > 7 THz) of stacking faults has shift to the right part with a high frequency mode, shown in Figure 3.15. In fact, the displacement toward to the high frequency region has been captured when investigating the LPDOS of Σ5(310) grain boundaries in Al (ω_{max} increases from 10 THz of the bulk to 11 THz of the boundary), crystal structure of which doesn't contain the coincident site lattice at the interface [147]. This displacement toward to the high frequency region may be caused by the tensile strain around the fault layers for existing more free volume. Besides deformation fault (I2), there is no change in the peak position of low frequency mode (ω< 4 THz) for growth fault (I1) and extrinsic fault (EF), comparing to that of perfect Mg. Moreover, no significant change in width is observed.

According to Equation 2.24 and Equation 2.25, it can be seen that the force constant is the key to obtain the phonon frequency. In order to understand the contribution of fault layers to the shift of phonon mode and the vibrational entropy, it is essential to show the force constant variation associated with the faults. Variations in force constants as a function of bond length between atoms up to 8 Å of growth fault; deformation fault and extrinsic fault are shown in Figure 3.16. The stretching and bending force constants are calculated through the Spring model [89, 92, 102]. Here, the

stretching force constant is derived by the projection of a force constant tensor into the direction joining the two atoms in focus. The bending force constant is derived by an average over the two projected force constant whose directions are perpendicular to the stretching direction. With the formation of fault layers in the HCP lattice, the bond length and the stretching force constant corresponding to the first nearest neighbor display a significant change, shown in Figure 3.16. Therefore, it can be concluded that the displacement of the phonon DOS towards high frequency mode of stacking faults is caused by the reduced bond length while the change of low frequency mode is due to the elongated bond length. Moreover, the interactions between fault-fault, fault-non-fault, non-fault-non-fault layers have been revealed distinctly in the format of bond length splitting of the first nearest neighbor, shown in Figure 3.16. More interestingly, the reduction of stretching force constant at higher bond length of the first nearest neighbor indicates the increase of vibrational entropy. Because introducing configurational disorder in an ordering system should increase the vibration entropy since the process reduces the number of stiff bonds and increase the number of soft bonds [148]. In the following, vibrational entropy of each atomic layer in stacking faults is discussed based on its local phonon density of states.

Figure 3.17 shows the LPDOS of the atoms in each layer of I1 together with their bond structure characterized by the $0.5\Delta\rho_{max}$ charge density isosurface. It can be seen that the atoms occupying the first nearest neighbor layer of a fault layer, such as L1, L3, L5 and L7, play the important role yielding the excess frequency mode at ω = 7.25 THz. For example, values of LPDOS of atoms in L5 and L7 are higher than the others, lines of

which are labeled with solid lines in blue and pink in Figure 3.17(a). The value of phonon DOS of fault layers (L4 and L8) in the low frequency and middle frequency regions are higher than that of non-fault layer. Moreover, LPDOS of the first nearest neighbor layers of the fault layers (L3 and L7) shows a shift towards the low frequency region. Based on Equation 2.16, Equation 2.19 and Equation 2.20, vibrational contributions to Helmholtz energy, entropy and specific heat at constant volume of each atomic layer in growth fault are gained, shown in Figure 3.18. It can be seen that the fault layers (L8) together with its near neighbor could stabilized the growth fault at high temperature since their entropy and specific heat are higher while the Helmholtz energy are lower, consisting with the displacement of LPDOS towards the low frequency region.

Similarly, LPDOS of the atoms in each layer of I2 and EF together with their bond structure characterized by the $0.5\Delta\rho_{max}$ charge density isosurface are presented in Figure 3.19 and Figure 3.21, separately. It can be seen that the low frequency mode of atoms in fault layers (L6, L7, L11 and L12 in I2; L4, L5 and L6 in EF) are dominate. For example, the LPDOS peak of L6 in I2 and L4 in EF at ω = 3.75 THz are larger than those in the non-fault layers, shown in Figure 3.19(a) and Figure 3.21(a). On the contrary, their peak at ω = 7.5 THz are smaller than those in the non-fault layers. It is necessary to point out that the LPDOS of L5 in EF is different with those of L4 and L6 at ω = 4.5 THz. This is caused by the difference of their interactions with first nearest neighbor, matching well with their bond structures shown in Figure 3.21(b). Correspondingly, fault layers (L6, L7 and L11) could stabilized the deformation fault at high temperature since their entropy and specific heat are higher while the Helmholtz

energy are lower, shown in Figure 3.20. However, non-fault layers far away from the fault layer (L1 and L9) in extrinsic fault seem to play the significant role to make the structure stable at high temperature since their LPDOS value at high frequency are dominate and larger than fault layers, which is caused by the shorter bond length or compressive strain in these atomic layers.

Since the Debye model could efficiently predict the lattice vibrational energy, it is expected to capture the lattice vibrational contribution to the free energy of the stacking faults and LPSOs. Hence, Debye temperature (Θ_D) is proposed to be a validate parameter quantitatively identifying the contributions of fault layers to the vibrational energies. Table 3.2 summarizes the predicted Debye temperature of the atom in each layer of stacking faults of Mg. It can be seen that Θ_D is sensitive to the density of the structure defects. Moreover, Θ_D of fault layers and its nearest neighbors layers are usually smaller than that of non-fault layer. Similarly, each individual atom in the Σ5(310) grain boundary of Al vibrates with a very different spectrum resulting in the difference of Θ_D [147]. Unfortunately, it is difficult to use Θ_D together with Debye model (shown as Equation 2.21 and Equation 2.23) to qualitatively characterize contributions of fault layer to the vibrational energies in the local structure/property analysis.

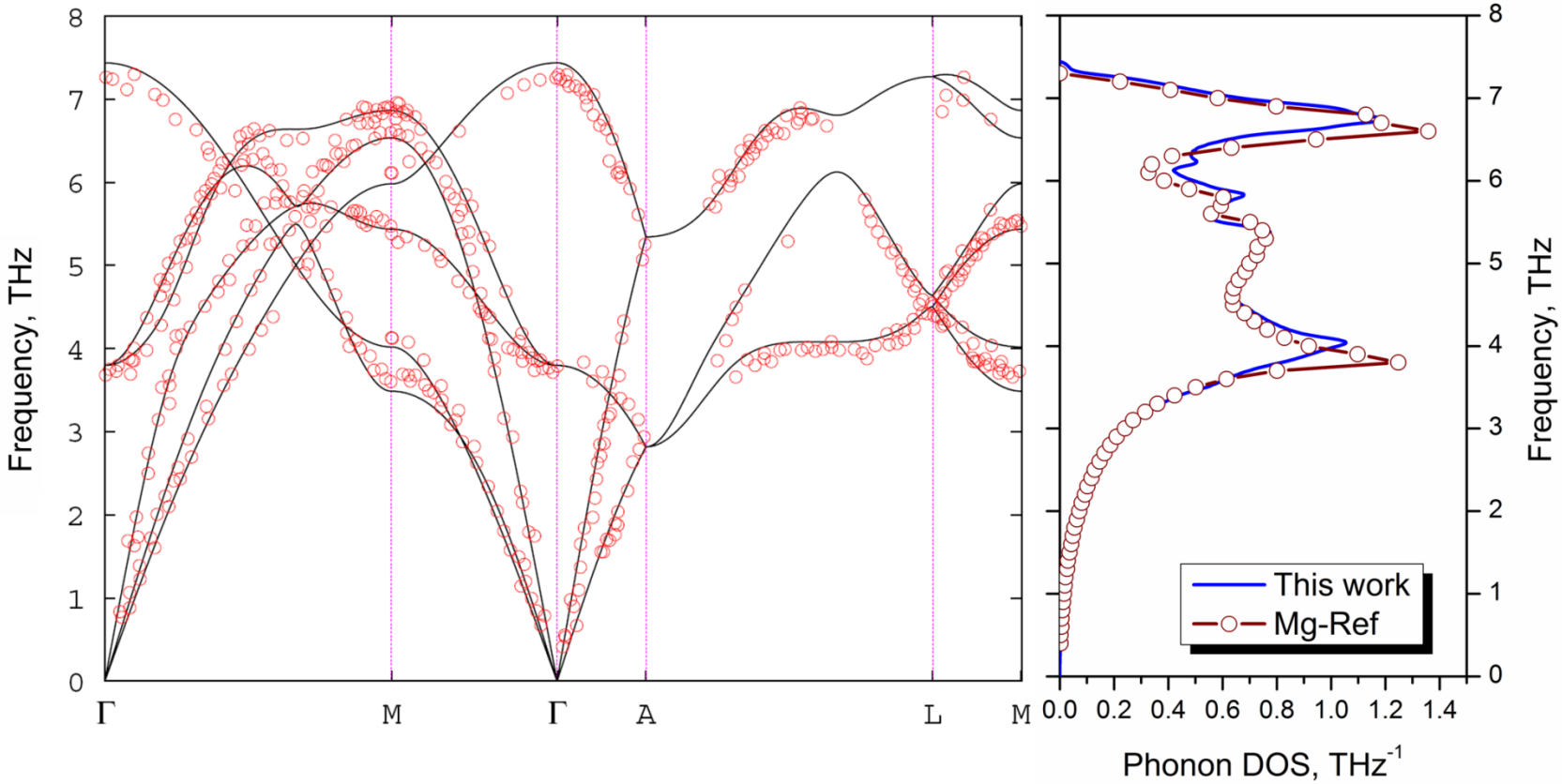

Figure 3.14. Phonon dispersion curve of Mg at the equilibrium volume comparing with the inelastic-neutron-scattering measurement at 290 K [143, 144].

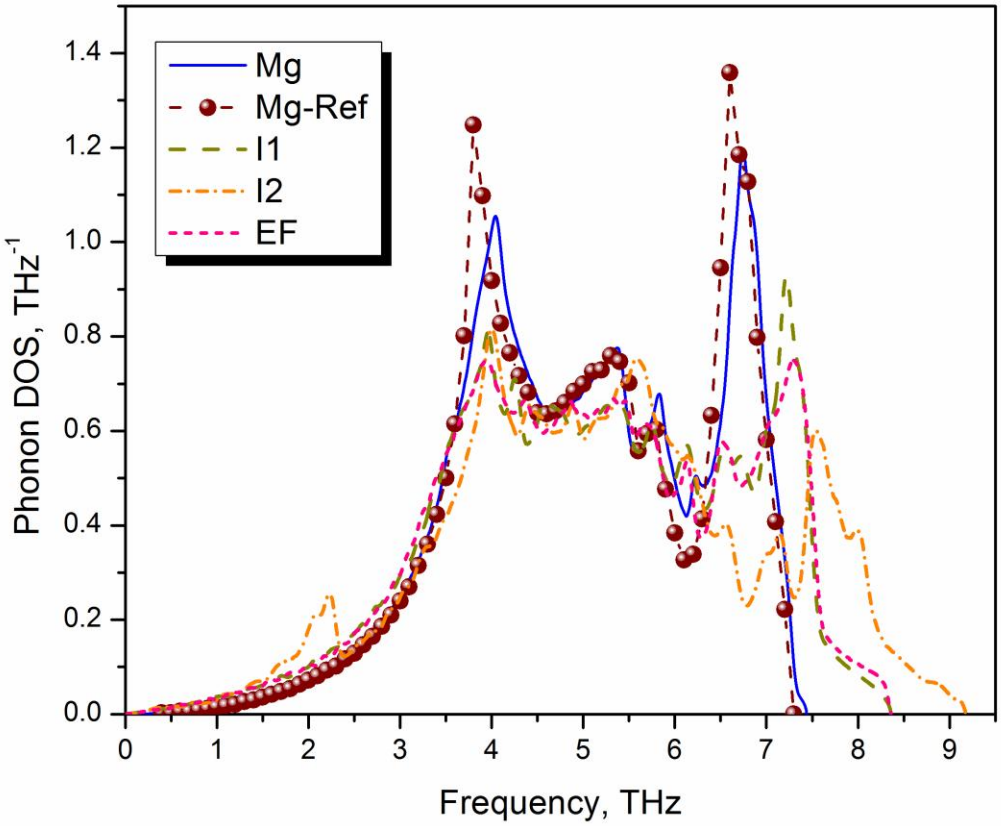

Figure 3.15. Effect of fault layers on the phonon density of states of Mg in comparison with the available experimental data (labeled with dash line and a sphere symbol) [143, 144].

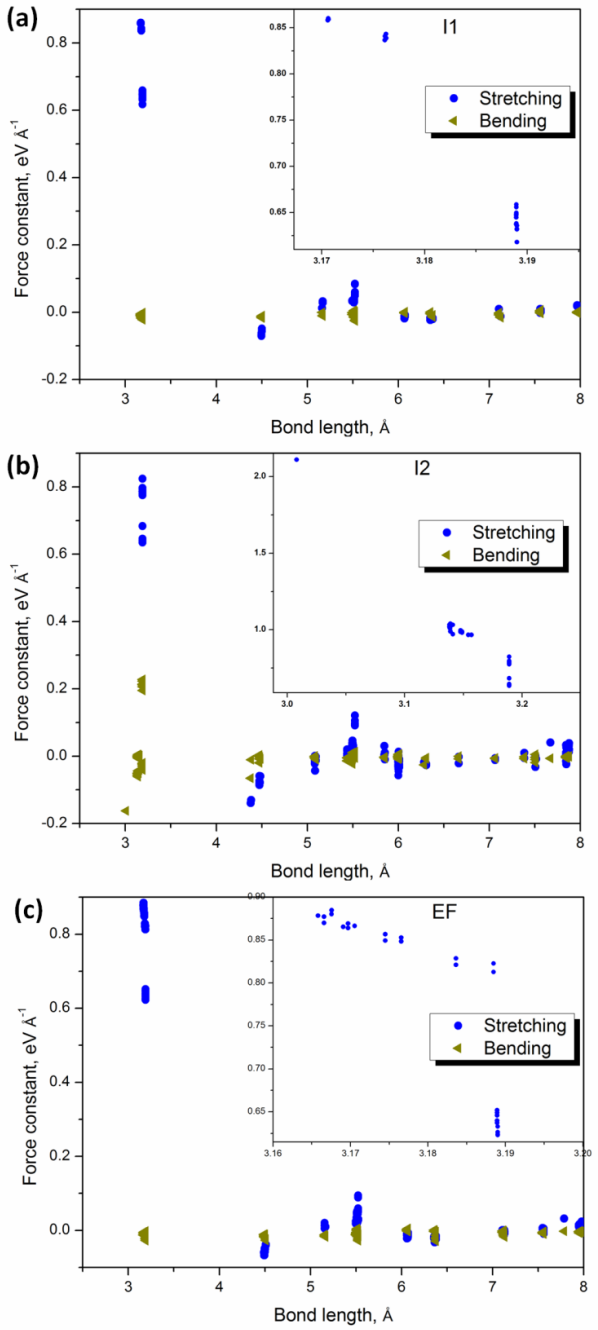

Figure 3.16. Variation in force constants as a function of bond length between atoms up to 8 Å, (a) growth fault; (b) deformation fault and (c) extrinsic fault. Bond length splitting of the first nearest neighbor shown in the insert image presents the interactions between fault-fault, fault-non-fault and non-fault-non-fault layers.

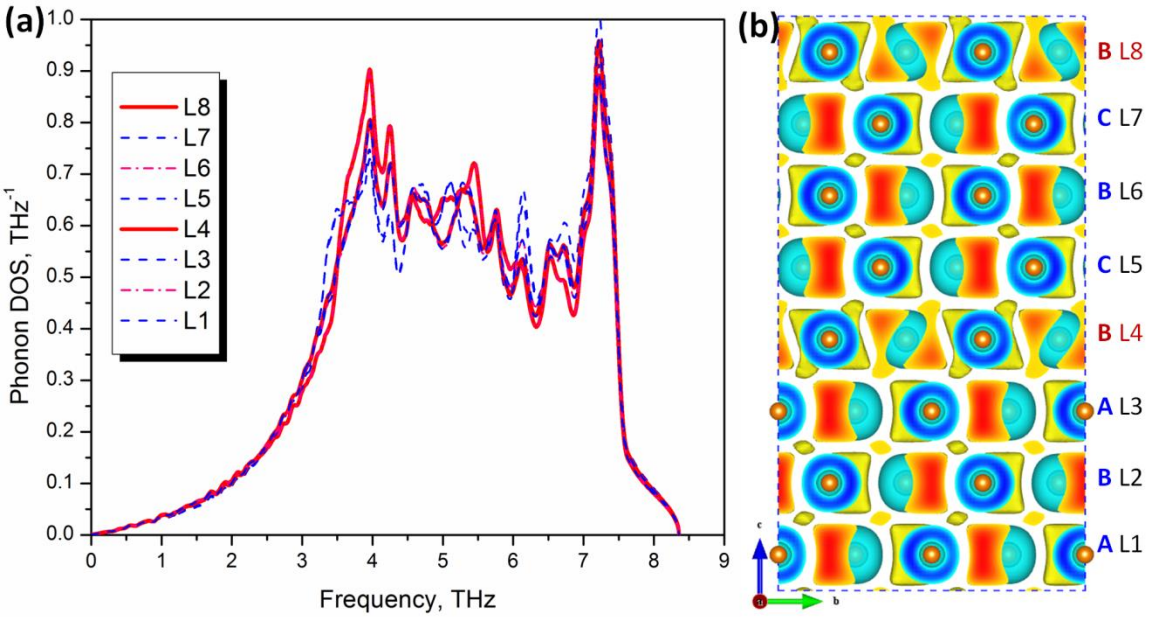

Figure 3.17. Local phonon density of states (LPDOS) of atoms in each layer of I1 together with their bond structure, (a) LPDOS curve and (b) the $0.5\Delta\rho_{max}$ charge density isosurface plotted in prismatic plane.

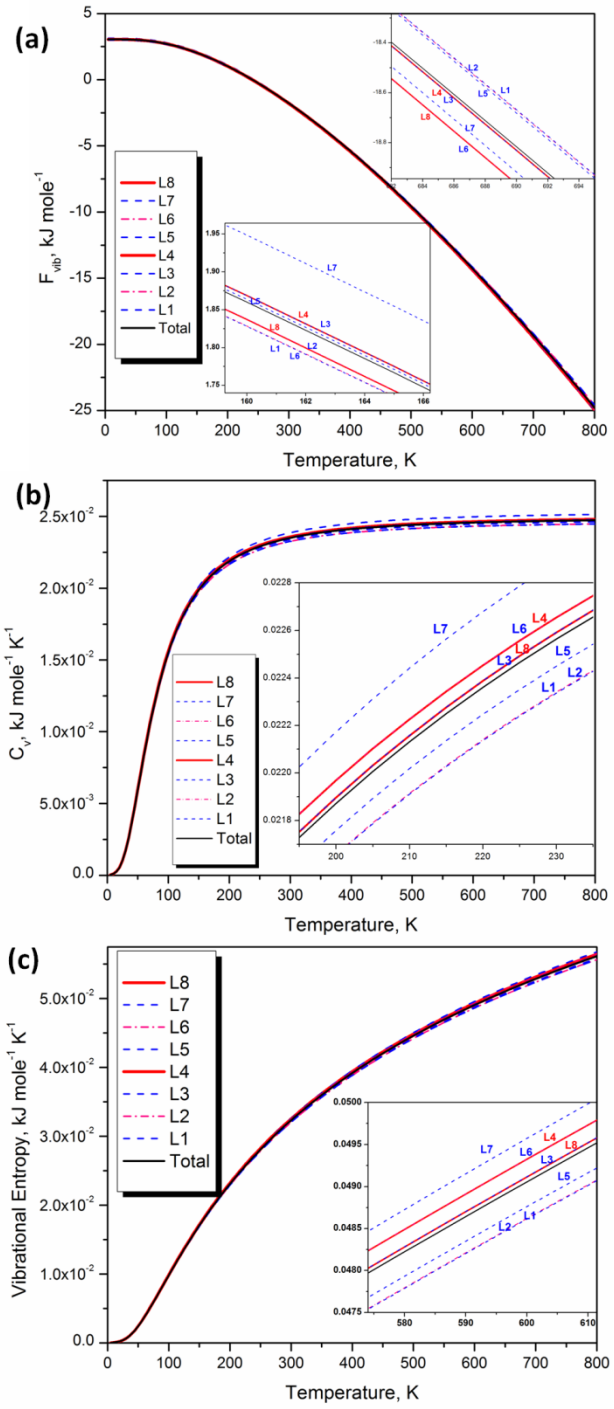

Figure 3.18. Vibrational contributions to Helmholtz energy (a), specific heat at constant volume (b) and entropy (b) of each atomic layer in growth fault.

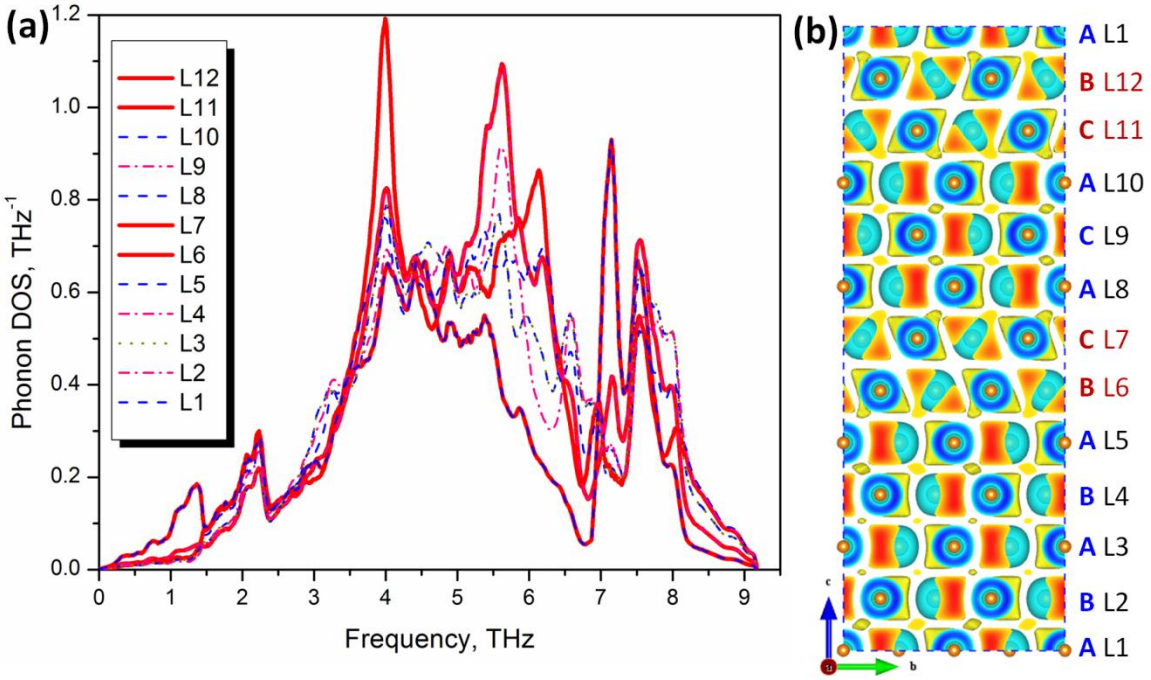

Figure 3.19. Local phonon density of states (LPDOS) of atoms in each layer of I2 together with their bond structure, (a) LPDOS curve and (b) the $0.5\Delta\rho_{max}$ charge density isosurface plotted in prismatic plane.

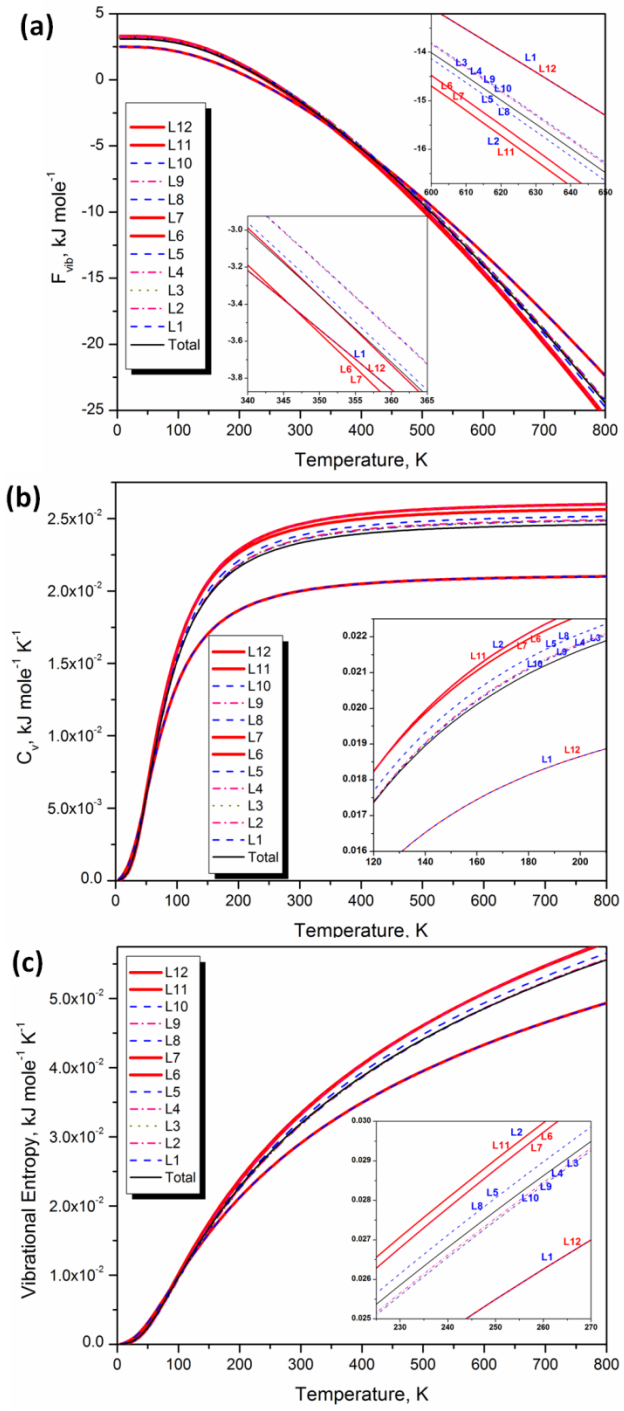

Figure 3.20. Vibrational contributions to Helmholtz energy (a), specific heat at constant volume (b) and entropy (b) of each atomic layer in deformation fault.

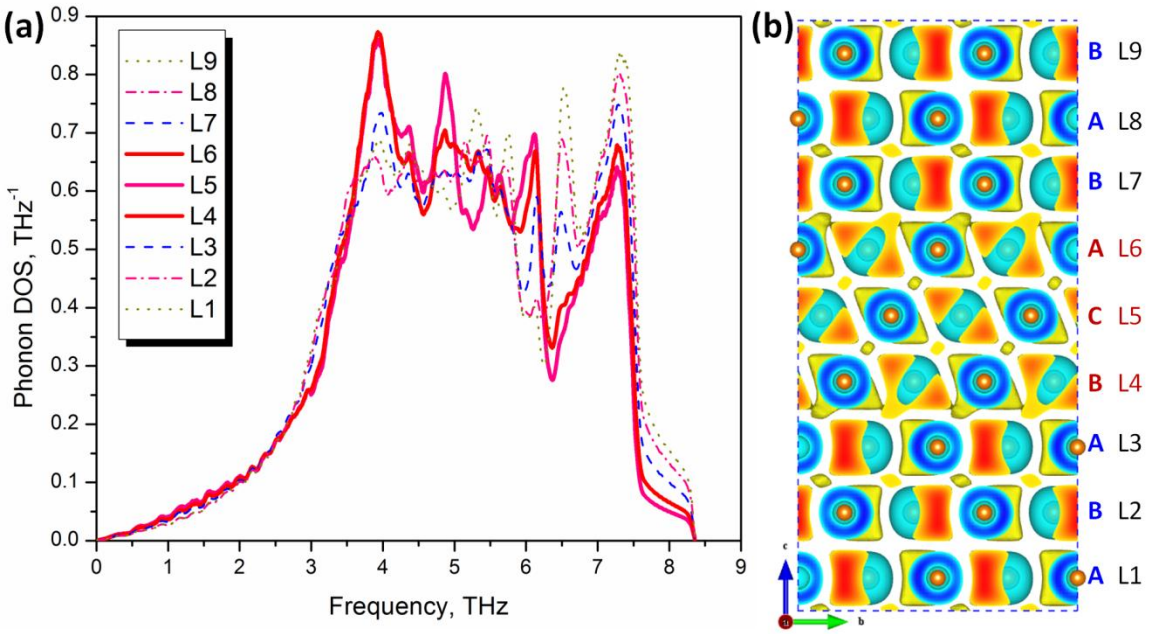

Figure 3.21. Local phonon density of states (LPDOS) of atoms in each layer of EF together with their bond structure, (a) LPDOS curve and (b) the $0.5\Delta\rho_{max}$ charge density isosurface plotted in prismatic plane.

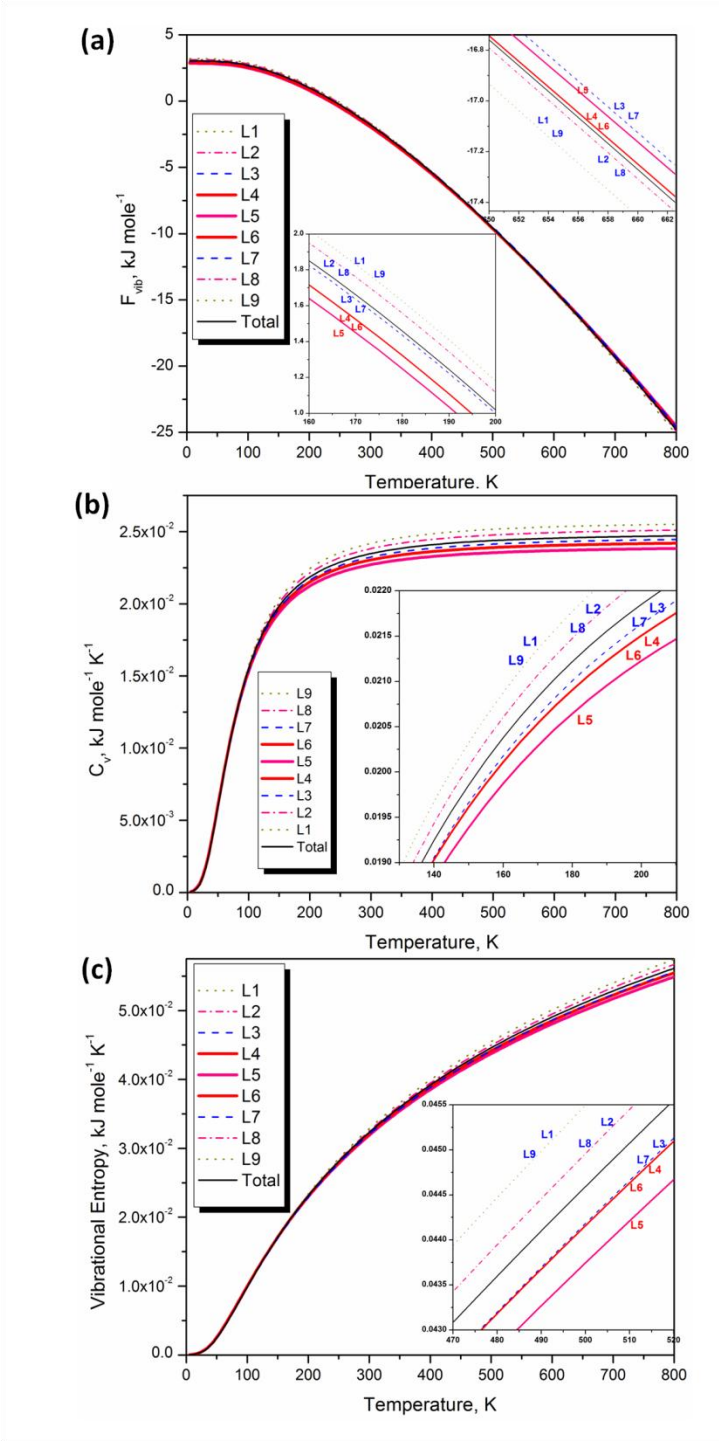

Figure 3.22. Vibrational contributions to Helmholtz energy (a), specific heat at constant volume (b) and entropy (b) of each atomic layer in extrinsic fault.

Table 3.2. Debye temperature (Θ_D) of the atom in each layer of stacking faults of Mg. The second moment of phonon DOS is used to derive the Θ_D in this work.

Atomic Layer		I1		I2		EF	
		Θ_D (K)	Note	Θ_D (K)	Note	Θ_D (K)	Note
SFs	L1	327.9		326.6		337.2	S_{High}
	L2	333.8		341.1	S_{High}	334.6	S_{High}
	L3	328.0		344.3		330.1	
	L4	330.9	S_{High}	344.9		323.4	
	L5	330.9		341.6		320.4	
	L6	330.9	S_{High}	335.1	S_{High}	323.4	
	L7	329.6	S_{High}	335.1	S_{High}	330.1	
	L8	329.6		341.6		334.6	S_{High}
	L9			344.9		334.6	S_{High}
	L10			344.3			
	L11			341.1	S_{High}		
	L12			326.6			
	Total	330.2		339.3		330.3	
Bulk		321.5 323[a], 325[b], 320[c]					

Note: S_{High}: the atomic layers with high vibrational entropy at high temperature
[a.] Zhang, et al., derived from the second moment of phonon DOS. [83]
[b.] Seitz F. and Trunbull D. Solid. State. Physics. New York: Academic Press;1964 (Exp.)
[c.] Dederch ,et al., Metals: Phonon states, electron states and Fermi surfaces. Berlin: Springer-Verlag: 1981 (Exp.)

3.4. Conclusion

In this chapter, three typical basal-plane stacking faults of pure Mg, i.e. growth fault (I1), deformation fault (I2) and extrinsic fault (EF), are investigated, showing that the stacking fault energy of I1 is considerably lower than the I2 stacking fault energy, with the latter even smaller than that of external fault. Moreover, through the electron localization morphology, electronic structures of these three stacking faults are revealed in terms of deformation electron density ($\Delta\rho$) and electron localization function (ELF). These results yield a quantitative description of charge transfer between atoms in and out of the stacking faults. We also obtain a brief physical correlation between stacking fault energy and the difference of $\Delta\rho$ and ELF between fault and the regular planes. Furthermore, through detailed investigations of deformation electron density, we show that the variation of the chemical bond structure from non-fault layer to fault layer is revealed clearly. It is observed that the bond structures of fault layers in I1, I2 and EF are identical, which are the rod-shaped in non-fault layers transferred into tetrahedron-shaped in fault layers. The simulated images of high resolution transmission electron microscopy compare well with experimental observed ones.

In the end, effects of fault layers on the local phonon density of states, vibrational free energies and Debye temperatures are discussed together with their specific electronic structures. It can be seen that the frequency of the phonon peaks ($\upsilon > 7$ THz) of stacking faults has shift to the right part with a high frequency mode. Besides deformation fault (I2), there is no change in the low frequency mode ($\upsilon < 4$ THz) for growth fault (I1) and extrinsic fault (EF), comparing to that of perfect Mg. With the formation of fault layers

in the HCP lattice, the bond length and the stretching force constant corresponding to the first nearest neighbor display a significant change, shown. Therefore, it can be concluded that the displacement of the phonon DOS towards high frequency mode of stacking faults is caused by the reduced bond length while the change of low frequency mode is due to the elongated bond length. More interestingly, the reduction of stretching force constant at higher bond length of the first nearest neighbor indicates the increase of vibrational entropy. Moreover, Debye temperature (Θ_D) is proposed to be a validate parameter quantitatively identifying the contributions of fault layers to the vibrational energies. It can be seen that Θ_D is sensitive to the density of the structure defects. Furthermore, Θ_D of fault layers and its nearest neighbors layers are usually smaller than that of non-fault layer. Unfortunately, it is difficult to use Θ_D together with Debye model to qualitatively characterize contributions of fault layer to the vibrational energies in the local structure/property analysis.

Chapter 4

Effect of Alloying Element (X) on the Formation Energy and Electronic Structures of Stacking Faults in Binary Mg-X Alloys

5.1. Introduction

According to the abbreviations in the standard of American Society for Testing and Materials (ASTM), shown in Figure 4.1(a), alloying elements labeled with the background in blue are commonly applied in the development of Mg alloys. Figure 4.1(b) shows the selected alloying elements in the present work. Contributions of alloying elements on the formation energy, electronic and elastic properties of stacking faults (SFs) and LPSOs in Mg alloys will be discussed in this chapter. It is worth to mention that based on the physical properties of alloying elements, i.e. lattice parameter, solubility, valence, and so on, their functions in solid solution of Mg will be different [106, 149], briefly summarized as following

Al, Mn, Zn and Zr

The most widely used alloys in Mg are AZ (Mg-Al-Zn) and AM (Mg-Al-Mn) series. Figure 4.2 displays the mechanical properties of classical Mg alloys at room

temperature and 300K. It can be seen that elements of Al (A), Mn (M), Zn (Z)and Zr (K) are necessary alloying elements in high strength Mg alloys. For example, Al could improve the castability of Mg alloys and decrease the corrosion resistance until ~8 wt %. If Al content excesses 6 wt %, Mg alloys could be heat treated. However, if the Al content is over 8 at %, the corrosion resistance will suffer a reversal behavior. Similarly, Zn will also improve the fluidity of Mg, making it castable. Together with Al, they will increase the strength without reducing the ductility of Mg alloys. Moreover, incorporating to Mg alloy with Ni and Fe impurities, the corrosion resistance could be enhanced. The addition of Mn improves the saltwater corrosion resistance of Mg-Al and Mg-Al-Zn alloys. Since the solubility of Mn (M) in Mg is low, it is usually incorporated with other alloys elements like Al. On the contrary, Zr can be used together with Al and Mn because of the stable compounds with these elements could form. If Zr incorporated into Mg alloys containing Zn, Th or RE, Zr can function as an excellent grain refiner.

Rare earth metals (RE)

RE are added to increase the high temperature strength, creep resistance and corrosion resistance of Mg. They can modify the microstructure feature and improve the oxidation resistance too. Their presence also assists in reducing the freezing range of Mg alloys, resulting in less casting porosity and weld crack. Since it is costive when alloying with RE, these alloys (i.e., EK, WE, ZE series) will be mainly used for aerospace applications.

Li, Na, K, Ca, Sr

In the development of superlight Mg alloys, these alloying elements including Li, Na, K, Ca and Sr are attracting attentions. Li with a relatively high solid solubility in Mg and smaller density than Mg, its addition will leads to decrease the density and strength but increases the ductility. Ca can serve as grain refiner, improving the creep resistance, corrosion resistance, thermal and mechanical properties of Mg alloys. Its presence also results in better rollability of Mg sheet. However, the sheet will be prone to cracks during welding if its content excesses 0.3 wt %. Sr is normally added to Mg together with other major alloying elements to enhance the creep resistance of Mg alloys but no significant impact on yield and ultimate tensile strength has been observed yet. Na and K are rare alloying into Mg alloys and not recommended for use in commercial alloys since the storage as a raw material poses some safety problems. In order to investigating their effect on the bond strength of Mg as unfavorable element, it is also considered in the present work.

Fe, Ni, Cu

Fe, Ni and Cu are unfavorable alloying elements in Mg. For example, the corrosion resistance of Mg alloys will be decreased only with 0.005 wt % Fe. Since the solid solubility of Cu and Ni are limited in Mg, both of them could form Mg_2X intermetallics, resulting in improving the strength at room temperature but decreasing the ductility.

Si, Sn

Si could improve the fluidity of molten alloys thus to enhance the castability. Sn together with Al in Mg improves the ductility and assists in reducing the cracking tendency during forging.

Theoretical investigations of stacking fault energies of some binary Mg-X alloys have recently been reported in the literature [150-153] along with contour plots of electron density in 2D and electron density isosurface figures in 3D [2, 138, 139, 154, 155]. However, the detailed chemical bond structures of the fault and non-fault layers and the contributions of alloying elements on the electronic structure of Mg with stacking faults have not been reported in the literature. In the present work, the effects of major alloying elements on the energies and bond structures of I1, I2, and EF of Mg-X alloys are systematically investigated through first-principles calculations. Moreover, based on their usage in advanced Mg alloys, the following alloying elements are included in the present study, i.e. Al, Ca, Cu, Fe, K, La, Li, Mn, Na, Nd, Pr, Si, Sn, Sr, Y, Zn and Zr.

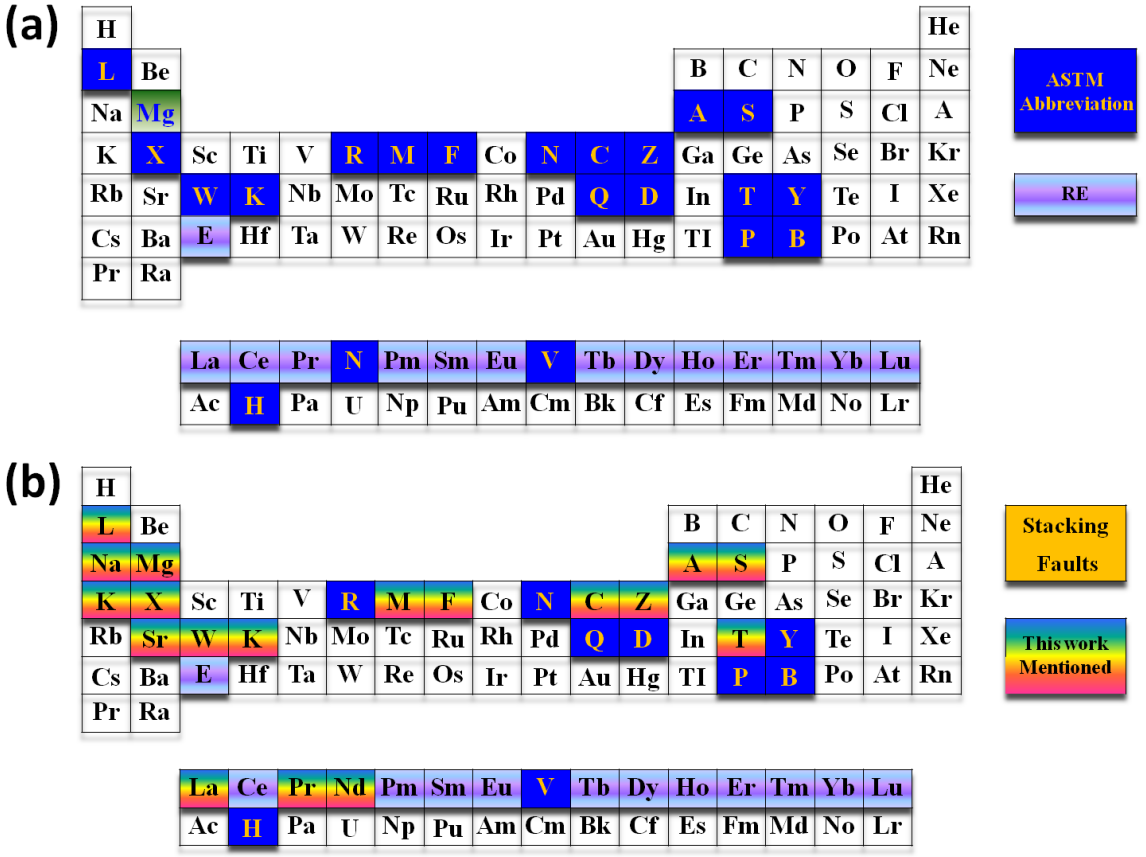

Figure 4.1. Periodic table of the element, (a) classical alloying elements applied in Mg alloys with an ASTM abbreviation and (b) the mentioned element in the current work on stacking faults.

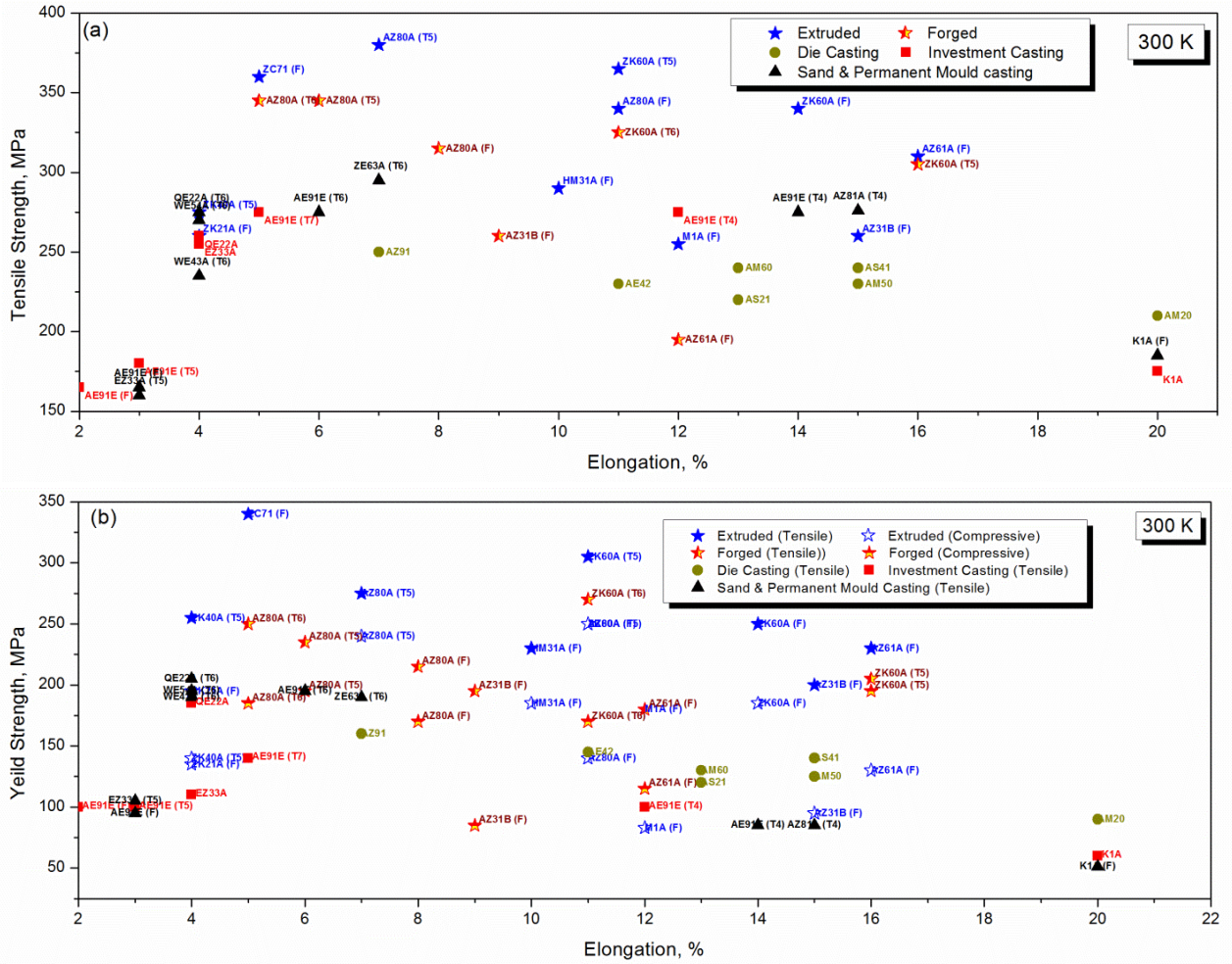

Figure 4.2. Mechanical properties of classical Mg alloys at room temperature and 300K, (a) the tensile strength and (b) the yield strength.

5.2. Crystal Structures and Computational Details

In the present first-principles calculations, the orthorhombic supercell of I1, I2 and extrinsic faults are $4\alpha' \times 2\sqrt{3}\alpha' \times 4c'$, $4\alpha' \times 2\sqrt{3}\alpha' \times 4c'$ and $4\alpha' \times 2\sqrt{3}\alpha' \times 4.5c'$ with 128, 128, and 144 atoms, respectively, where *a'* and *c'* are the lattice parameters of primitive hcp Mg [132]. In Figure 4.3, the lattice vectors **a**, **b** and **c** are parallel to the directions of $\langle 01\bar{1}0\rangle$, $\langle 1\bar{2}10\rangle$, and $\langle 0001\rangle$ of hcp Mg, respectively..

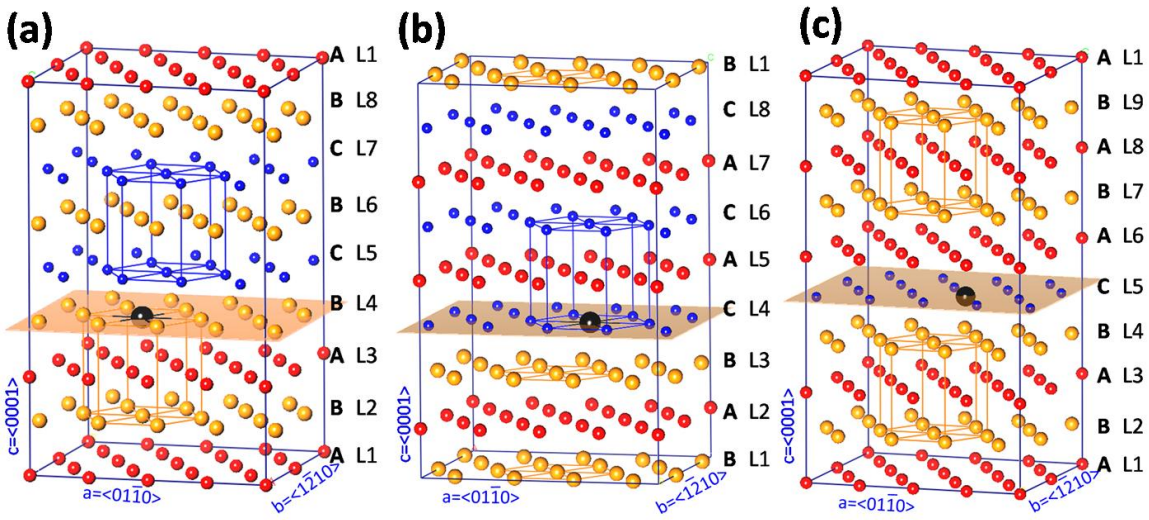

Figure 4.3. Schematic structure of the Mg-X alloys with different stacking faults (shown as (0001) miller plane), (a) growth fault - I1; (b) deformation fault – I2 and (c) extrinsic fault - EF. The atoms in different stacking layers are in various color and size, especially for the alloying elements. The concentrations of the alloying element in fault planes are 6.25 at%.

Calculations of stacking fault energy at 0 K are conducted by employing the Vienna *ab initio* simulation package (VASP) [90, 91] with the generalized gradient approximation (GGA) [133] for the exchange-correction functional and the projector

augmented wave (PAW) [134] for the electron-ion interaction. The wave functions are sampled on the Γ-centered mesh structures generated automatically with same scaling length l=60 for stacking faults and l=40 for LPSOs, respectively. The plane wave cutoff energy is set as 1.4 times of the default energy cutoff (ENCUT=300 eV) and the energy convergence criterion of electronic self-consistency is 10^{-6} eV/atom. The structures are fully relaxed by the Methfessel-Paxton technique [135], while the final total energy calculations are performed by the tetrahedron method incorporating Blöchl correction [156]. The total energies of I1, I2, and EF structures as a function of volume are fitted by a four parameters Birch-Murnaghan equation of state [60]. From previously examined results looking at the effects of supercell size (on the [0001] direction) [157], it was seen that the difference between three and seven atomic layers separating the stacking faults (I1, I2 and EF) is less than 3%. The deformation electron density [61], Δρ, is calculated using the Harris-Foulkes functional [158, 159], also known as the reference state in the independent atom model. The isosurface and the contour plots of the charge density are generated using VESTA [66].

5.3. Results and Discussions

5.3.1. Stacking faults energy

The stacking fault energy (γ_{sf}) is defined as,

Equation 4.1 $$\gamma_{sf} = \frac{1}{A}(E_{sf} - E_{Bulk})$$

where E_{sf} and E_{Bulk} are the total energies of supercells with and without stacking fault, respectively, and A is the total area of the stacking fault planes. Due to the periodic

boundary conditions used in our calculation, there are two identical interfaces in the I1 and I2 supercells, while one in the extrinsic fault. Taking the stacking fault energy of pure Mg (γ_{sf}) as the reference, the segregation energy per area of alloying elements ($E_{seg}(X)$) is expressed as [38, 160]

Equation 4.2 $$E_{seg}(X) = \frac{\left[\left(E_{sf}(Mg_{n-m}X_m) - E_{sf}(Mg_n)\right) - \left(E_{Bulk}(Mg_{n-m}X_m) - E_{Bulk}(Mg_n)\right)\right]/m}{A} = \gamma_{sf}(X) - \gamma_{sf}$$

where $\gamma_{sf}(X)$ is the energy per area with alloying element in stacking fault; m and n are the number of solute atoms and the total number of atoms in the supercell.

Through the four parameters Birch-Murnaghan equation of state [60], the total energies of I1, I2, and EF structures at equilibrium volume are obtained and summarized in Table 4.1 along with various computational data in the literature with the majority of data for I1 from Zhang et al., [150] and those of I2 from Zhang et al.,[152] and Muzyk et al. [151]. Correspondingly, the segregation behavior of the alloying element in stacking faults are obtained and shown in Figure 4.4. According to the crystal structures of each individual solute atom at room temperature, it can be seen that some alloying elements with HCP and FCC structures reduce the stacking fault energies the most. If a reduction of stacking fault energies results in a high density of stacking fault, the strength can be improved without significant losses in ductility [34, 161]. Thus, by decreasing the width of Shockley partial dislocations in Mg [8, 113], the following allying elements (La, Y, Zn. Al, Sr, Ca, Nd, and Pr) that are used in advanced Mg alloys are likely to be beneficial.

It should be pointed out that the concentrations of alloying elements in a fault plane in the works by Muzyk et al. [151] and Zhang et al. [150, 152] are 25 at% with all Mg atoms involved in Mg-X bonds and 11 at.% with only one Mg-Mg bond, respectively, yielding strong interactions between alloying elements through X-Mg-X bonds in the fault plane. In the present work, the concentration of the alloying elements in the fault plane is 6.25 at% without the X-Mg-X bonds in the fault plane. The distance between two alloying element is larger than 11 Å, avoiding the interaction between them [127, 157]. The present setting is also in line with the experimentally determined concentrations of alloying element in the fault layers of Mg alloys, typically lower than 10at% such as 2±1at%Zn-4±2at%Y [33], 7at%Zn-6at%Y [32], 6at%Zn-9at%Y [29] and 3at%Zn-6at%Y [32] in the alloys of Mg-1at%Zn-2at%Y. This is probably the reason that our results are different from those by Muzyk et al. [151] and Zhang et al. [150, 152].

Since the local chemical environments for alloying elements in I1 (ABC), I2 (ACB) and EF (ACB) are similar to that of FCC, the calculated stacking fault energies and the Mg-X supercell volumes are plotted in Figure 4.5 with respect to the volume of each individual alloying element X in the FCC structure [60, 132]. It can be seen that the equilibrium volumes of Mg-X supercells increases almost linearly with the volume of alloying element X in the FCC structure. Consequently, it is plausible to select two alloying elements, both decreasing the stacking fault energy but changing the equilibrium volume in opposite way so that their co-segregation will be more energetic favorable due to the minimization of elastic lattice strain [38].

Table 4.1. First-principles calculated stacking fault energy (γ_{sf}, mJ/m^2), and segregation energy per unit area of the dopants ($E_{seg}(X)$, mJ/m^2) of Mg-X alloys with different structures at 0 K

System	Growth fault (I1) Mg-0.78at%X		Deformation fault (I2) Mg-0.78at%X		Extrinsic fault (EF) Mg-0.69at%X	
	γ_{sf}	$E_{seg}(X)$	γ_{sf}	$E_{seg}(X)$	γ_{sf}	$E_{seg}(X)$
Mg	14.4 8.1~17.8[a], 11[b], 18[c e], 16[h], 27[d], 22[d], 15[d], 17[g, i], 21[k]	-	48.2 38.3[a], 33.8[c], 23[b], 33[e], 34[h], 54[d], 44[d], 30[d], 36[j], 34[g, i]	-	99.3 80.6[g], 52.6[c], 36[b], 140[f], 59[h], 40[i]	-
Mg - Al	12.5 13[e], 19[k]	-1.8 -5[e], -3[k]	33.6 23[e], 21[j]	-14.6 -10[e], 16[j]	55.7 130[f],	-43.6 -10[f]
Mg - Ca	13.8 12[k]	-0.6 -9[k]	33.5	-14.7	49.6	-49.7
Mg - Cu	16.6 23[k]	2.3 2[k]	41.0 53[j]	-7.2 17[j]	66.4	-32.9
Mg - Fe	3.3 (17.48 FM) 37[k]	-11.1 (3.1) 16[k]	40.3 (14.8 FM) 52[j]	-7.9 (-33.4) 16[j]	79.8 (119.0 FM)	-19.6 (19.7)
Mg - K	13.5 7[k]	-0.9 -14[k]	32.5	-15.7	47.5	-51.8
Mg - La	12.1 -3[k]	-2.3 -18[k]	24.7	-23.5	29.9	-69.5
Mg - Li	16.7 28[e], 23[k]	2.3 10[e], 2[k]	48.2 46[e], 47[j]	-0.0 13[e, j]	63.2	-36.1
Mg - Mn	13.5 33[k]	-0.9 12[k]	40.3 38[j]	-7.9 2[j]	81.4	-18.0
Mg - Na	15.7 18[k]	1.3 -3[k]	46.8	-1.4	66.7	-32.7
Mg - Nd	10.8 0[k], -2[i]	-3.6 -21[k], -19[i]	32.3 4[i]	-15.9 -29[i]	51.9 29[i]	-47.4 -10[i]
Mg - Pr	15.0 -1[k], -4[i]	0.6 -22[k], -21[i]	31.9 0.5[i],	-16.3 -34[i]	50.7 21[i]	-48.6 -19[i]
Mg - Si	13.8	-0.6	33.9	-14.3	50.5	-48.8
Mg - Sn	13.8 16[k]	-0.6 -5[k]	37.2 2[j]	-11.0 -32[j]	50.1 126[f],	-49.2 -14[f]
Mg - Sr	15.6 4[k]	1.3 -17[k]	33.2	-15.0	46.3	-53.0
Mg - Y	1.8 4[g], 5[k]	-12.5 -13[g],-16[k]	32.9 25[j], 16[g]	-15.3 -11[j], -12[g]	47.1	-52.3
Mg - Zn	8.5 18[g], 21[k]	-5.9 1[g], 0[k]	30.8 37[j], 35[g],	-17.5 1[j], 1[g]	58.8 18.9[l]	-40.5 -61.7[l]
Mg - Zr	9.8 13[k]	-4.5 -8[k]	35.3 26[j]	-12.9 -10[j]	67.5	-31.9

Note: Experimental method determined the stacking fault energies along the basal plane (0001) are 78 mJ/m^2 [8] and ~50 mJ/m^2 [162]. The ferromagnetic (FM) moment of Fe atom is considered and listed in the bracket.

[a] Wang et al., first-principles calculation with GGA [20]
[b] Chetty et al., first-principles calculation with LDA [6]
[c] Fan et al., first-principles calculation with GGA [138]
[d] Han et al., MD with different potentials [139]
[e] Han et al., first-principles calculation of Mg-1.67at%X alloys [139]
[f] Wang et al., first-principles calculation of Mg-0.69at%X alloys with GGA and the stacking sequence is supposed to be ABACAB based on their cited literature by Datta et al. [140]
[g] Zhnag et al., first-principles calculation of Mg-1at%X alloys with GGA and the concentration of alloying elements is ~11.1at% in the slip plane [153]
[h] Wen et al., first-principles calculation with GGA [18]
[k] Muzyk et al., first-principles calculation of Mg-2at%X alloys with GGA-PBE and the concentration of alloying elements is 25at% in the slip plane [151]
[l] Datta et al., first-principles calculation of Mg and Mg-2.08at%X alloys with LDA [2]
[m] Zhang et al., first-principles calculation of γ_{I1} with GGA-PBE and the concentration of alloying elements is 11at% in the fault plane [150]

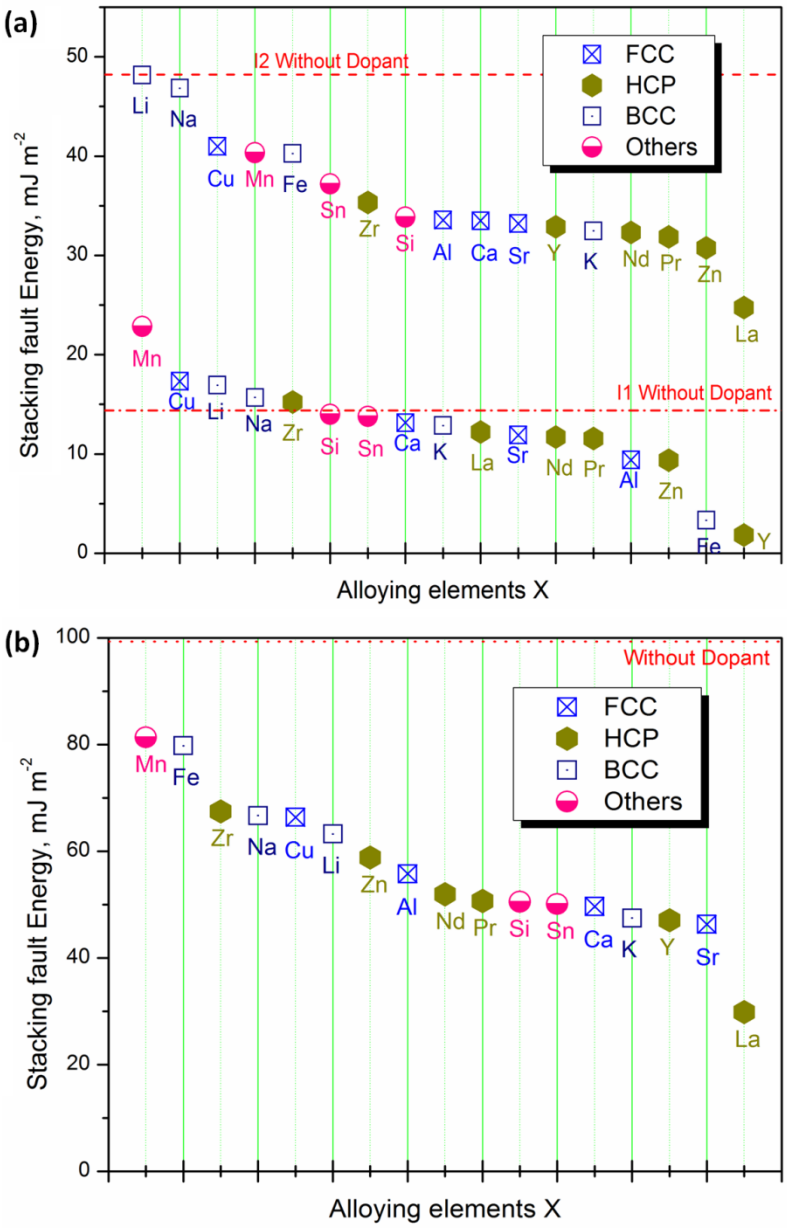

Figure 4.4. Contribution of alloying element on the formation energy of the basal plane stacking faults of binary Mg-X alloys, (a) Mg-0.78at%X alloys with growth (I1) and deformation (I2) faults; (b) Mg-0.69at%X alloys with extrinsic faults. Various symbols are used to identify the crystal structures of each individual solute atom at room temperature, such as FCC, BCC, HCP and others.

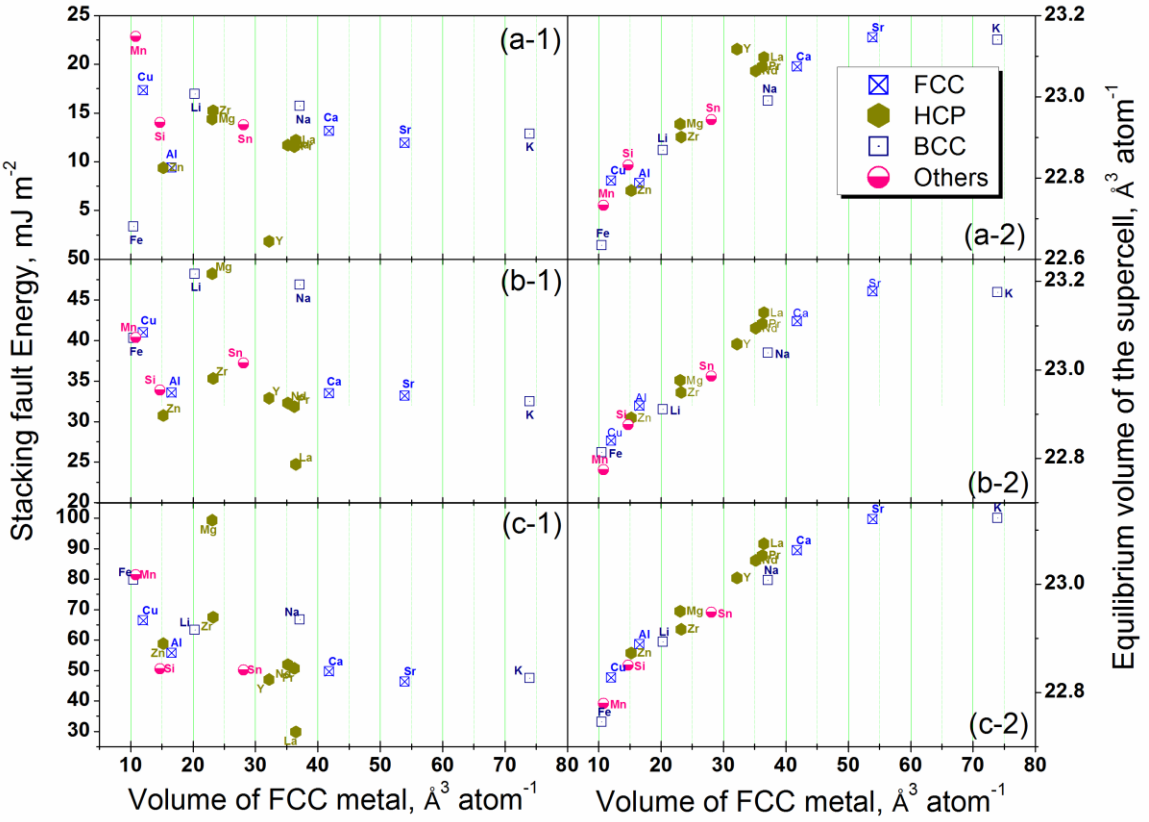

Figure 4.5. The calculated stacking fault energy and equilibrium volume of Mg-X alloys, referring to the alloying element X in FCC structure [60], (a) growth fault; (b) deformation fault and (c) extrinsic fault. The number 1 and 2 are applied to characterize stacking fault energy and equilibrium volume in y axis.

5.3.2. Effect of alloying elements on the electronic structure of stacking faults

In our previous study, isosurfaces of the deformation electron density (corresponding to $\Delta\rho_{max}$) of I1, I2 and EF in pure Mg were used to study the effects of stacking faults and alloying elements on the bond structure [163]. It was observed that the shape of the $\Delta\rho_{max}$ isosurface in fault planes is different from that in non-fault planes, and the number of atomic layers with altered electron density depends on the structure of stacking faults, i.e., 1, 2 and 3 for I1, I2, and EF, respectively. This indicates that the change of electron distribution is the largest for the EF and the smallest for I1 with that of I2 in between, in the same order as their stacking fault energies.

Figure 4.6 shows various contour plots of $\Delta\rho$ in I1, I2 and EF of the Mg-Al binary system. In $(1\bar{2}10)$ plane view, the rod-shaped directional bonds within the non-fault planes match well with the previous investigation by Blaha et al. [141], while the triangle-shaped directional bonds are observed in the fault planes (L4 for I1, L3 and L4 for I2, and L4, L5, and L6 for extrinsic fault). It can be seen that $\Delta\rho$ around the Al atomic basin has been increased compared to that without Al, i.e. Al and Mg atom in L5 of EF. In (0001) plane view, $\Delta\rho$ around the Al atomic hexagonal basin is enhanced with respect to the case without Al, indicating the bond strength of basal plane is strengthened by Al. This is also consistent with the views of $(1\bar{2}10)$ and $(01\bar{1}0)$ planes. Furthermore, the number of atomic layers with altered electron density around Al atom is one non-fault planes for I1, one fault plane and one non-fault for I2, and two fault planes for EF as shown in Figure 4.6.

Figure 4.7 shows the $0.75\Delta\rho_{max}$ (75% of the maximum value of $\Delta\rho$) isosurface of I1, I2 and EF with Al, Zn and Na as alloying elements, respectively. It can be seen that the rod-like directional bonds have transformed into the tetrahedral shape with the addition of alloying elements in the fault plane. For alloying elements with the same crystallography structure, the similar electron localization morphology can be seen by plotting $\Delta\rho_{max}$ isosurface. For example, the $0.75\Delta\rho_{max}$ isosurface of I1, I2 and EF affected by FCC-Cu is similar to these of FCC-Al, shown as the second column of Figure 4.7. Moreover, the tetrahedral-shaped charge distributions in the fault planes are enhanced when alloyed with FCC-Al and HCP-Zn, see the second and third columns of Figure 4.7, indicating the stronger pinning effect and improved thermal stability of stacking faults [38]. On the contrary, the BCC elements show different behaviors, shown by the reduced size of the tetrahedral-shaped charge distribution when alloyed with BCC-Na, agreeing with previous observations that Na reduces the bond strength in interfaces [164, 165].

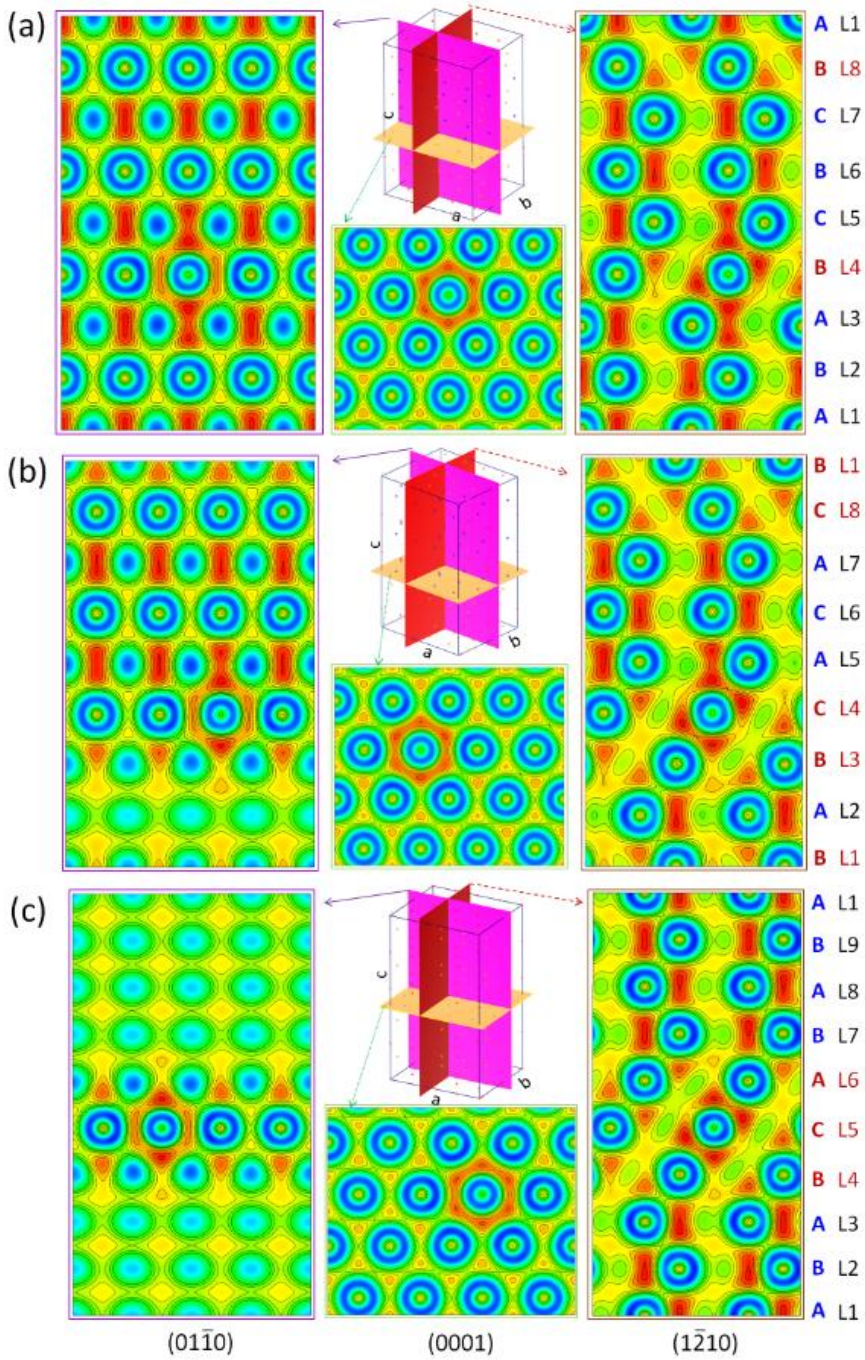

Figure 4.6. Contour plots of Δρ of Mg-Al in different views, (a) I1; (b) I2 and (c) EF with 0.0005 $e^-/Å^3$ intervals. Plots are generated using VESTA [66] with red for Δρ>0 and blue for Δρ<0. The coordinates of each plane is identified by the corresponding miller plane in the supercell.

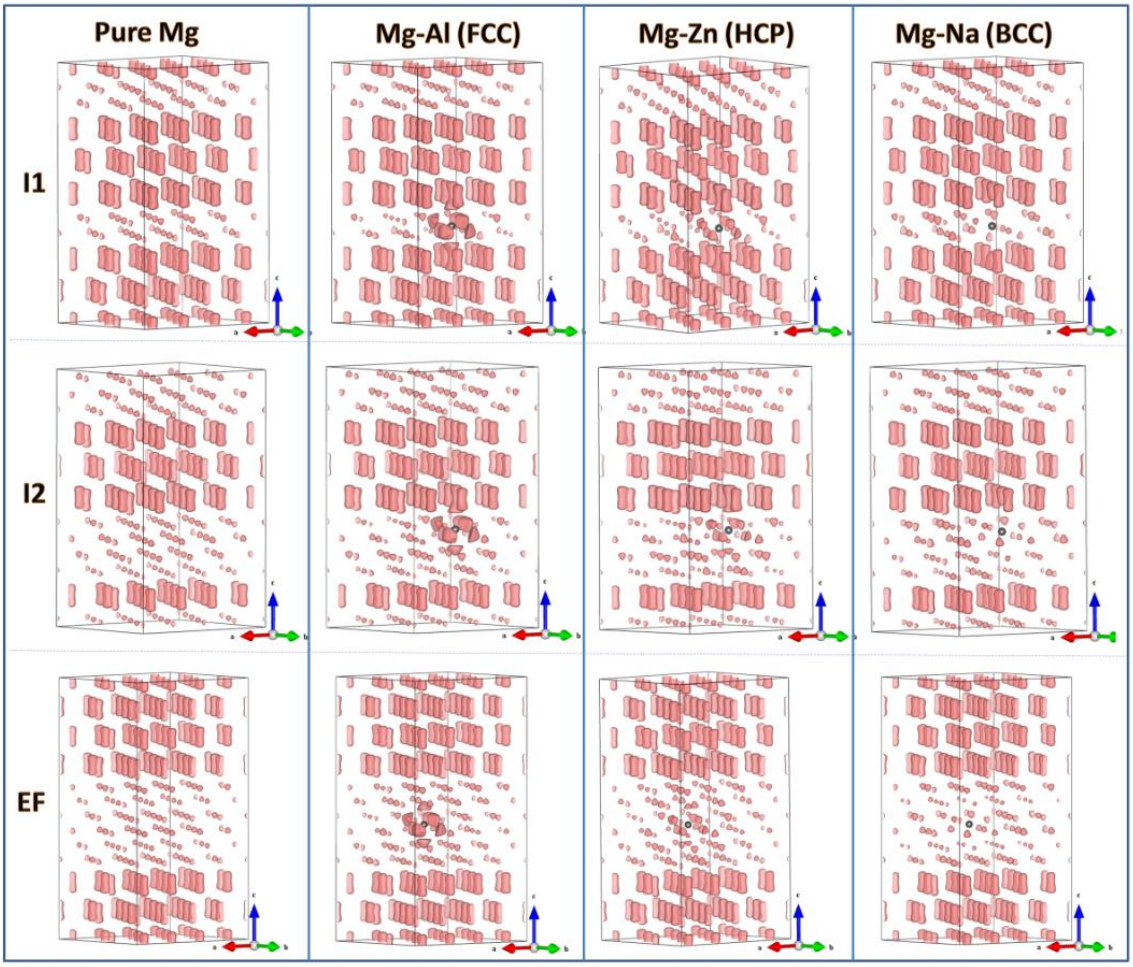

Figure 4.7. Deformation electron density isosurface ($0.75\Delta\rho_{max}$) of Mg, Mg-Al, Mg-Zn and Mg-Na with I1, I2 and EF (from top to bottom). Only alloying elements in the supercells are displayed in black.

5.3. Conclusion

The effect of 17 alloying elements on stacking fault energies of growth, deformation and extrinsic faults in Mg is investigated through first-principles calculations. It is observed that all of them reduce the stacking fault energies of the deformation and extrinsic faults with La showing the least reduction for both. For the growth fault, five elements, i.e. Mn, Cu, Li, Na and Zr, increase the stacking fault energy with the rest of them decreasing the fault energy. As all stacking faults can be recognized as the local HCP-FCC transformation, the calculated results show that the bond strength is enhanced by alloying elements of FCC and HCP structures such as FCC-Al and HCP-Zn.

Chapter 5

Formation Energy, Electronic and Phonon Properties of Long Periodic Stacking Order Structures (LPSOs) in Mg

4.1. Introduction

According to the stacking sequence of close packed atomic planes (basal planes), several types of LPSOs in Mg alloys have be experimentally determined, which are 6H [23, 33, 120, 166], 10H [167-169], 14H [25, 26, 29, 124, 169], 18R [25, 26, 29, 124, 168, 170, 171] and 24R [123, 169]. The significant features of the atomic arrangement in those LPSOs are (i) FCC-type stacking sequence ($A\dot{B}\dot{C}A$) indicates two fault layers (letters with dots above) within four atomic layers in 10H, 14H, 18R and 24R; (ii) a mirror plane with the stacking sequence of three atomic layers ($A\dot{B}C$) exists in 6H ($BC\dot{B}A\dot{B}C$); and (iii) alloying elements of Zn and Y prefers to segregated around these fault layers (letters with dots). It has been estimated that the formation energy of 6H twice that of the growth fault (I1), while the formation energies of other LPSO structures depend on the number of the deformation fault (I2) they contain [138]. The ABCA-type stacking sequence in I2, 14H and 18R are similar, but with distinct spatial arrangements

[123, 172]. This similarity has in some cases results in the transformations between variant structure, such as 18R to 14H observed at high temperature by transmission electron microscopy (TEM) in a Mg-2Zn-8Y-0.6Zr (wt%) alloy [123]. Such intricate connections among stacking faults and all LPSO structure have not been fully explored and understood, particularly the electronic structures of various LPSO structures and their dependences on alloying elements. Experimentally, the technique of electron tomography provides not only the atomic structure, but also the electronic structures together with simulations based on density functional theory (DFT) [173], such as the nature of chemical bond and the charge redistribution [69, 142, 174-177]. It is noted that the electron density predicted from DFT-based first-principles calculations can be directly compared with the charge transfer obtained from electron tomography measurements and used to simulate the HRTEM images by projecting the electron density or converting the electron density into electron scattering factor [67, 69-71].

According the results shown in Chapter 3, it was shown that the stacking fault energy ascends in the order of I1, I2, and extrinsic faults and is proportional to the square of the difference of maximum deformation charge density, the difference of maximum electron localization function, and the number of faulted layers In this chapter, the electron localization morphologies of LPSO structures in hcp Mg are investigated in details to unearth the intrinsic correlations among various LPSO structures. Such knowledge paves the path to understand the effects of alloying elements on properties of LPSO structures and design Mg alloys for better performance.

4.2. Crystal Structures and Computational Details

In the present first-principles calculations, the orthorhombic supercell sizes of 6H, 10H, 14H, 18R and 24R LPSO structures are $2a \times 4\sqrt{3}a \times 3c$, $a \times \sqrt{3}a \times 5c$, $a \times \sqrt{3}a \times 7c$, $a \times \sqrt{3}a \times 9c$ and $a \times \sqrt{3}a \times 12c$ with 96, 20, 28, 36 and 48, respectively, where *a* and *c* are the theoretical lattice parameters of primitive hcp Mg and an orientation relationship of $\langle 01\bar{1}0\rangle_{\mathrm{hcp}} \parallel \langle 100\rangle_{\mathrm{s.c.}}$, $\langle 1\bar{2}10\rangle_{\mathrm{hcp}} \parallel \langle 010\rangle_{\mathrm{s.c.}}$, and $\langle 0001\rangle_{\mathrm{hcp}} \parallel \langle 001\rangle_{\mathrm{s.c.}}$. Setting parameters for I1 and I2 can be found in our previous work [163].

Calculations of electronic structures and formation energies at 0 K are carried out by means of the Vienna ab initio simulation package [90, 91] with the generalized gradient approximation [133] for the exchange-correction functional and the projector augmented wave [134] for the electron-ion interaction. The wave functions are sampled on Γ-centered Monkhorst-Pack grids of $9 \times 3 \times 4$, $19 \times 11 \times 2$, $19 \times 11 \times 2$, $19 \times 11 \times 1$, $19 \times 11 \times 1$ for 6H, 10H, 14H, 18R and 24R structures generated automatically with same scaling length (l=60), respectively. The plane wave cutoff energy is set as 300 eV, i.e. 1.4 times the default cutoff energy for high accuracy calculation, and the energy convergence criterion of electronic self-consistency is 10^{-6} eV/atom. While the structures are fully relaxed by the Methfessel-Paxton technique [135], the final total energy calculations are performed by the tetrahedron method incorporating Blöchl correction [156].

Four-parameter Birch-Murnaghan equation of states [58-60] is used to describe the relation between energy and volume. The formation energy of LPSO structures, γ, can be obtained through

Equation 5.1 $$\gamma = \frac{1}{A}(E_{LPSO} - E_{Bulk})$$

where E_{LPSO} and E_{Bulk} are the total energies of supercells with and without LPSO structures, respectively, and A is the area of basal plane of supercells.

Procedures obtaining deformation electron density (Δρ) and the HRTEM images in this work are as same as that described in the methodology part in Chapter 3

4.3. Results and Discussion

4.3.1. Formation energy and electronic structures of LPSOs

Table 5.1 summarizes the predicted stacking sequence, lattice parameter (a and c), bulk modulus (B_0), formation energy (γ) of I1, I2, and LPSO structures, and the ratio of formation energy with respect to that of I2 (γ/γ_{I2}). The total energies of I1, I2, and LPSO structures as a function of volume are fitted by a four parameters Birch-Murnaghan equation of state, shown in Figure 5.1. It can be seen in Table 5.1 that our predicted lattice parameters of I1, I2 and LPSO structures are consistent with experimental data, whose bulk modules are lower than that of Mg indicating the increase of atomic volume cased by fault layers and matching well with our previous prediction (the B_0 of FCC Mg decreases from 35.7 of HCP to 34.7 GPa with the volume increases from 22.887 of HCP to 23.068 $Å^3$/atom) [60]. The ratios of formation energy indicate that the formation energies of LPSO structures in Mg can be scaled to the formation

energy of I2, approximately one for 6H, two for 10H and 14H, and three for 18R and 24R, respectively.

To understand this scaling correlation, Figure 5.3 plots the isosurface of the maximum deformation electron density ($-\Delta\rho_{\max}$) for I1, I2 and LPSO structures in the prismatic plane of $\{11\bar{2}0\}_{\text{hcp}} \parallel \{100\}_{\text{s.c.}}$, using the positive and negative mode in VESTA [65, 66]. Since the charge density is a scalar field, the change in electron distribution results in directional bonds [63] and can be correlated to the formation energy of stacking faults [64] and LPSO structures. Furthermore, the examination of deformation electron density can directly reveal the fault layers and its number in those structures through isosurface structure of each layer[163]. It can be seen in Figure 5.3 that two fault layers in 6H LPSO with altered charge density are separated by a non-fault plane, different from both I1 with single fault layers separated by three non-fault layers and I2 with double-fault layers separated by three and five non-fault layers, respectively. That is the reason why the predicted γ_{6H} is larger than $2\gamma_{I1}$ and close to γ_{I2}, indicating strong interactions of two fault layers in accordance with previous theoretical work [157]. It is further observed in Figure 5.3 that all the 10H, 14H, 18R and 24R structures have double-fault layers like I2, and the numbers of non-fault layers between double-fault layers are three, five, four, and six, respectively, equal or larger than that in I2. The total numbers of double-fault layers are two for 10H and 14H structures and three for 18R and 24R structures, respectively, coinciding with the ratios of their formation energies to that of I2 as discussed above. The stacking sequences across the fault layers are highlighted by rectangles with 3 or 4 atomic layers of $A\dot{B}C$ or $A\dot{B}\dot{C}A$ and solid and dotted lines for

different directions, further demonstrating the correlations between I1 and 6H, and I2 and other LPSO structures.

Figure 5.4 presents the $0.5\Delta\rho_{max}$ isosurface in stacking faults and LPSO structures in the prismatic plane. At this level, variation of the chemical bond structure from non-fault layer to fault layer is revealed clearly. It is observed that all LPSO structures have similar bond morphologies as I1 and I2 stacking faults [141, 163], i.e. rod-shaped in non-fault layers and tetrahedron-shaped in fault layers, respectively. It should be noted that the tetrahedron-shaped directional bonds are characteristics of the fcc structure such as Al [61], in line with the fact that stacking faults and LPSO structures represent the local fcc atomic environment in a hcp matrix. Based on the information presented in Figure 5.2 and Figure 5.3, it seems logical to correlate the formation energy of LPSO structures with the number of fault or double-fault layers, shown in Figure 5.4 with a near linear relation depicted. This indicates the weak interaction between double-fault layers in the LPSO structures.

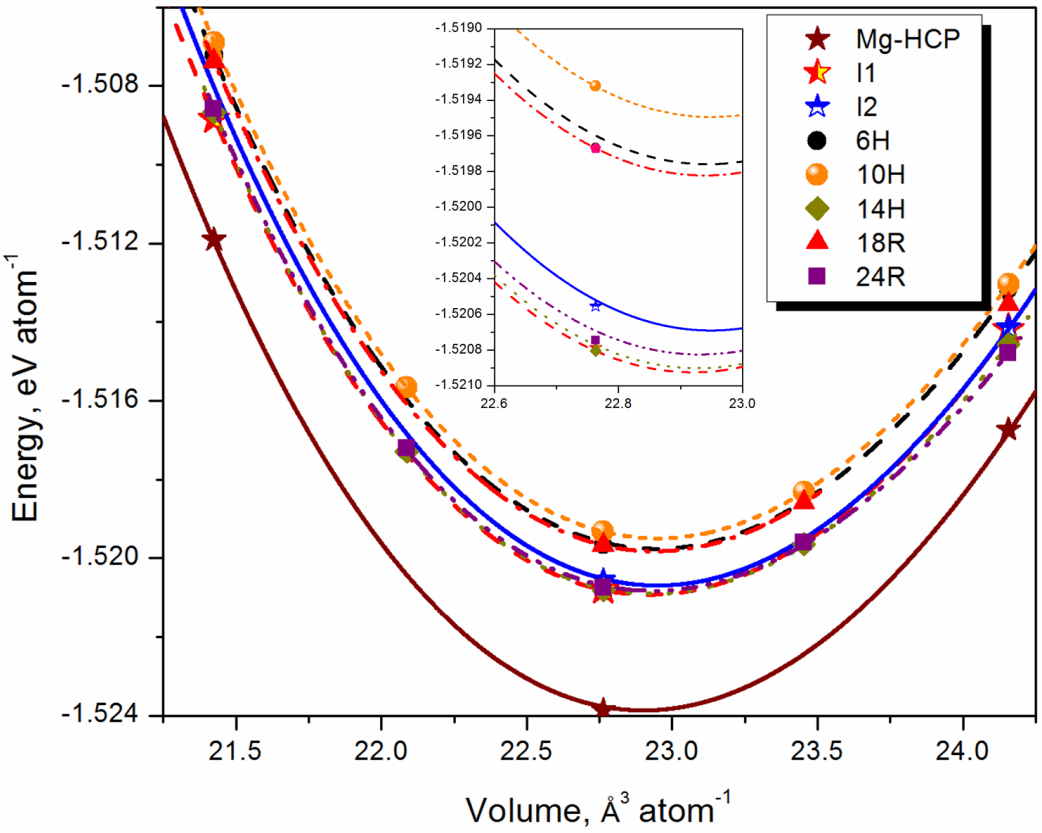

Figure 5.1. Total energies as a function of volume fitted by four parameters Birch-Murnaghan equation of state. The insert plot shows the region closing to equilibrium volume of stacking faults and LPSOs.

Table 5.1. Stacking character, lattice parameter (a), bulk modulus (B_0) and formation energy of stacking faults and long period stacking orders (γ_{LPSO}) in Mg. B_0, a (with c/a=1.621) and γ_{LPSO} are obtained through four parameters Birch-Murnaghan (BM4) equation.

	Stacking Order	Lattice Parameter		B_0 GPa	J/m²	$\frac{\gamma_{LPSO}}{\gamma_{I2}}$
		a Å	C-LPSO Å			
Mg	$\cdots ABAB \cdots$ or $\cdots BCBC \cdots$ or $\cdots ACAC \cdots$	3.195 3.189 [a] 3.215 [b] 3.199 [j]	-	35.9 35.6 [c] 36.9 [d]	-	-
I1	$\cdots CBCBC\,\dot{B}\,ABABAB \cdots$	3.196	-	35.6	14.4 18.0 [h]	0.3
I2	$\cdots ABABA\,\dot{B}\,\dot{C}\,ACACAC \cdots$	3.198	-	35.2	48.2 33.8 [h] 45.0 [i]	1
6H	$\dot{A}\,BAB\,\dot{A}C$ or $\dot{B}\,CBC\,\dot{B}A$	3.197 3.22 [e] 3.202 [g] 3.200 [j]	15.549 15.6 [e] 15.482 [g]	35.6 - 36.28 [g]	44.6 44.1 [h]	0.9I2 2I1 [h]
10H	$\dot{C}\,BCB\,\dot{C}\,\dot{A}\,BAB\,\dot{A}$	3.198 3.25 [f] 3.202 [j]	25.917 26.03 [f]	35.5	98.2 65.0 [h]	2.0 2 [h]
14H	$\dot{A}\,BABAB\,\dot{A}\,\dot{C}\,BCBCB\,\dot{C}$	3.197 3.25 [f] 3.199 [j]	36.273 36.94 [f]	34.5	93.2 63.3 [h]	1.9 2 [h]
18R	$\dot{A}\,CBCBC\,\dot{B}\,\dot{A}\,CACAC\,\dot{B}\,ABA\,\dot{B}$	3.197 3.20 [f] 3.202 [j]	46.644 46.78 [f]	35.6	163.4 94.0 [h]	3.4 3 [h]
24R	$\dot{A}\,BABABA\,\dot{B}\,\dot{C}\,ACACAC\,\dot{A}\,\dot{B}\,CBCBCB\,\dot{C}$	3.197 3.22 [f]	62.185 61.81 [f]	33.6	164.1 101.6 [h]	3.4 3 [h]

Note: The letter with a dot above is applied to identify the fault layer.

[a] Wang, et. al., first-principles calculations with PAW-GGA [132]

[b] Karen, et. al. powder neutron diffraction measurement (c/a=1.623) [178]

[c] Wazzan, et. al., experimental measurements of single crystal Mg [179]

[d] Slutsky, et. al., experimental measurements of single crystal Mg [180]

[e] Inoue, et. al., high temperature extrusion prepared $Mg_{97}Zn_1Y_2$ (at%) observed by HRTEM [23]

[f] Matsuda, et. al., rapidly solidified $Mg_{97}Zn_1Y_2$ (at%) alloys observed by HRTEM [169]

[g] Tang, et. al., first-principles calculations of with PAW-GGA (c/a=1.612) [155]

[h] Fan, et. al., first-principles calculations with PAW-GGA [138]

[i] Pan, et. al., first-principles calculations with PAW-GGA [172]

[j] Iikubo, et. al., first-principles calculations with PAW-GGA(c/a=1.624) [181]

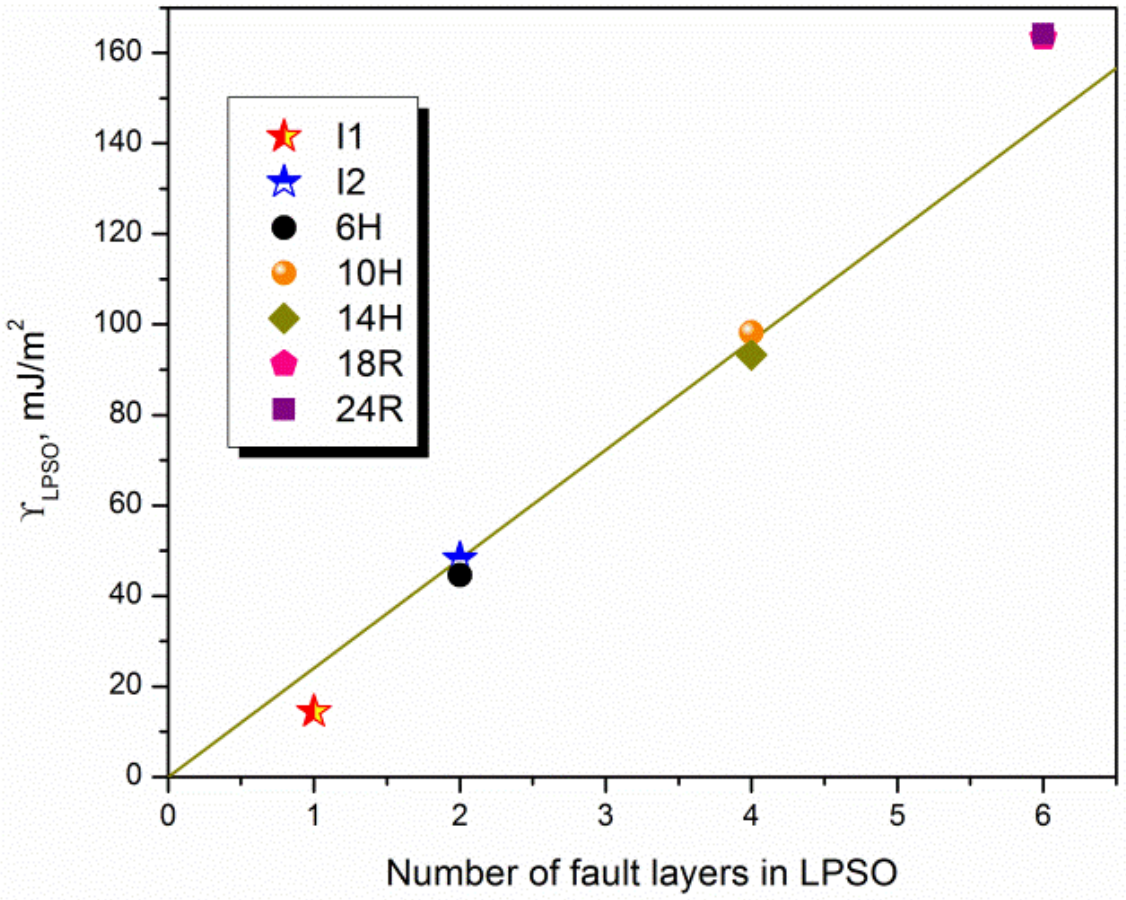

Figure 5.2. Correlation between the formation energy of LPSOs and the number of fault layers. The line stands for the ideal case that the formation energy of LPSO is depends on the number of I2.

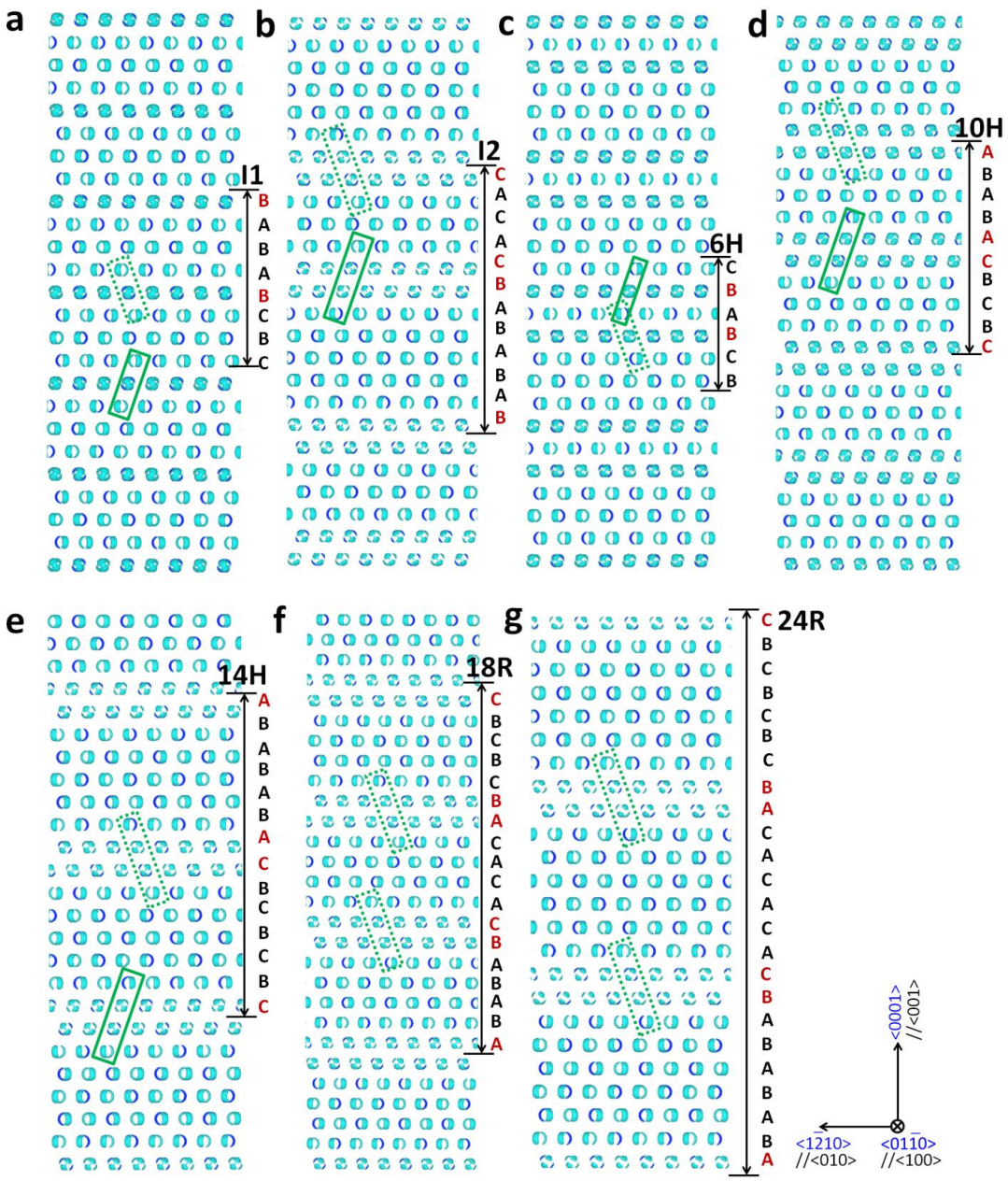

Figure 5.3. (100) plane view of orthorhombic supercells characterizing by the isosurface of deformation charge density, $\Delta\rho = -\Delta\rho_{max}$. a-g,I1, I2, 6H, 10H, 14H, 18R and 24R. The lattice vectors of the primitive hcp Mg parallel to those of the orthorhombic supercell are labeled. Plots are generated using VESTA [65, 66]. The fault layers are identified by letters in red.

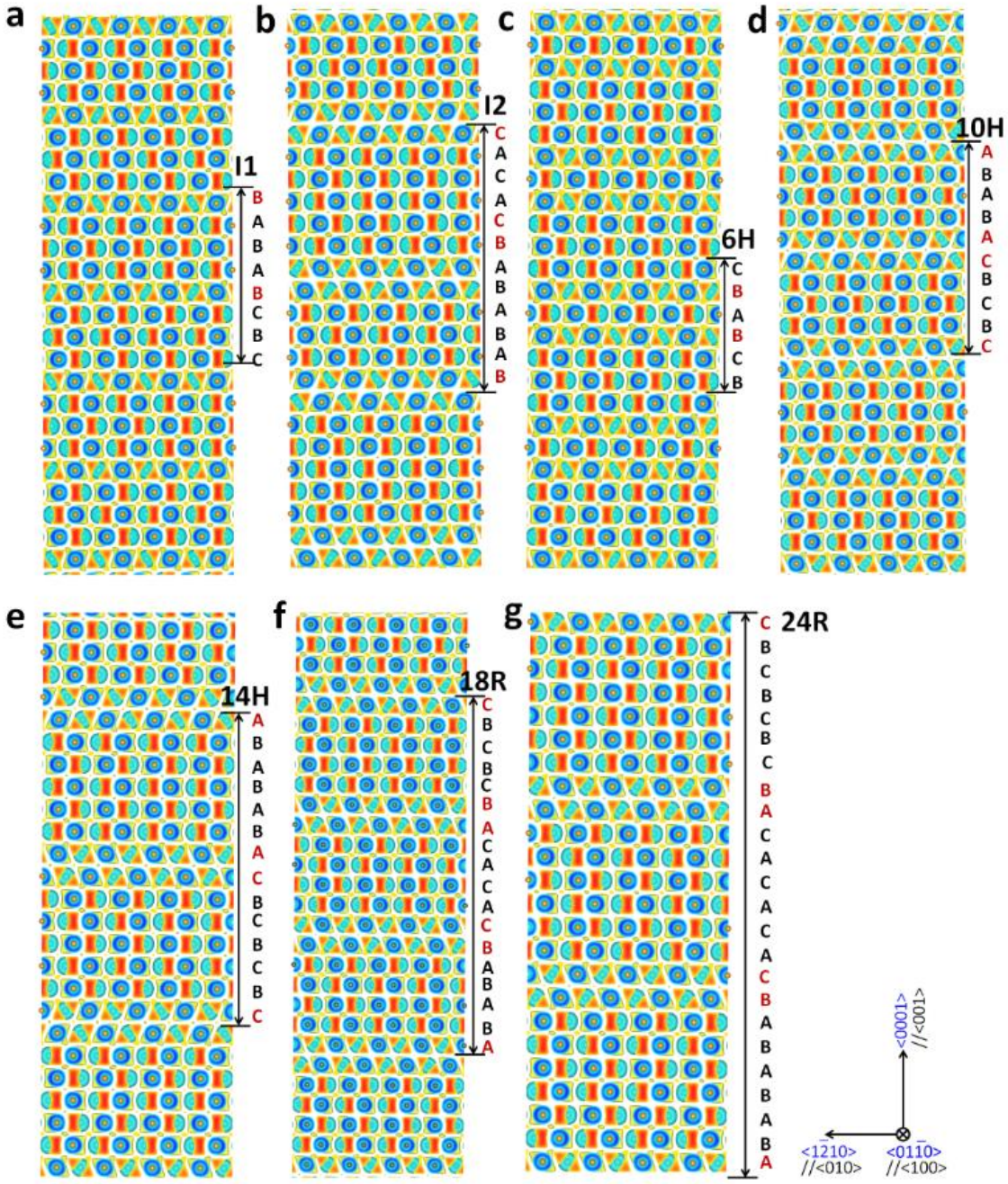

Figure 5.4. 0.5Δρmax isosurface of (100) plane view, a-g: I1, I2, 6H, 10H, 14H, 18R and 24R, generated using VESTA [65, 66], with letters in red denoting fault layers.

4.3.3. Simulated HRTEM images and electron diffraction patterns of LPSOs

Figure 5.5 shows the simulated (pure Mg) and experimental ($Mg_{97}Zn_1Y_2$) (100) TEM images of 6H and 10H structures. It can be seen in Figure 5.5a that the non-fault layer between the two-fault layers in 6H is a mirror plane with the stacking sequence of three atomic layers of $A\dot{B}C$ to both sides of the mirror plane, similar to that in I1. While in 10H shown in Figure 5.5b, the non-fault layer between two non-fault layers is a mirror plane with the stacking sequence of four atomic layers of $A\dot{B}\dot{C}A$ to both sides of the mirror plane, similar to that in I2. On the contrary, there are no mirror planes in 14H, 18R and 24H though the stacking sequence of four atomic layers of $A\dot{B}\dot{C}A$, similar to that in I2, seems sheared in opposite directions in 14H and in the same direction in 18R and 24H, as shown in Figure 5.6. The observation in 14H is consistent with interpretation of the two twin-related building blocks with ABCA-type stacking sequence derived from TEM results [121]. It should be emphasized that the electron localization morphology in this work clearly reveals that each twin-related building block is made up of two fault layers, i.e. $A\dot{B}\dot{C}A$ shown in Figure 5.6a.

The detailed electronic structures of LPSO structures discussed above provide insights on transformations between them. It is shown that the densities of fault layers are in the descending order from 10H, 18R, 14H, to 24R as 2/5, 1/3, 2/7, and 1/4. The transformation from LPSO structures with a higher density of fault layers to those with lower density is thus energetically favorable such as the 18R to 14H transformation observed experimentally at high temperatures [123]. Since the formation of fault layers

is related to the dissociation of dislocations to Shockley partials, the above transformation thus reduces the dislocation density during heat treatment. It should be pointed out that the higher density of fault layers does not mean higher formation energy of LPSO structures shown in Figure 5.3 and Figure 5.4, which are correlated with the total number of fault layers in each LPSO structure.

Related to the simulated HRTEM images of LPSO structures, the simulated $<100>_{S.C.}\|<10\bar{1}0>_{LPSO}$ electron diffraction pattern of Mg matches well with experimental observations [121, 122, 169], shown in Figure 5.7. Comparing to the experimental data of Mg-Zn-Y alloys [121, 122, 169], the intensity difference some of predicted pots is caused by the composition difference. With the addition of Zn and Y into Mg, the lattice parameters will be changed resulting in the disappearance of streaks and intensity maxima in the selected area electron diffraction pattern [121]. Hence, based on the simulated HRTEM images and related electron diffraction patterns, it would convenient to estimate the contributions of fault layers in LPSOs to the crystal morphology, supporting valuable supplementary information for experiments.

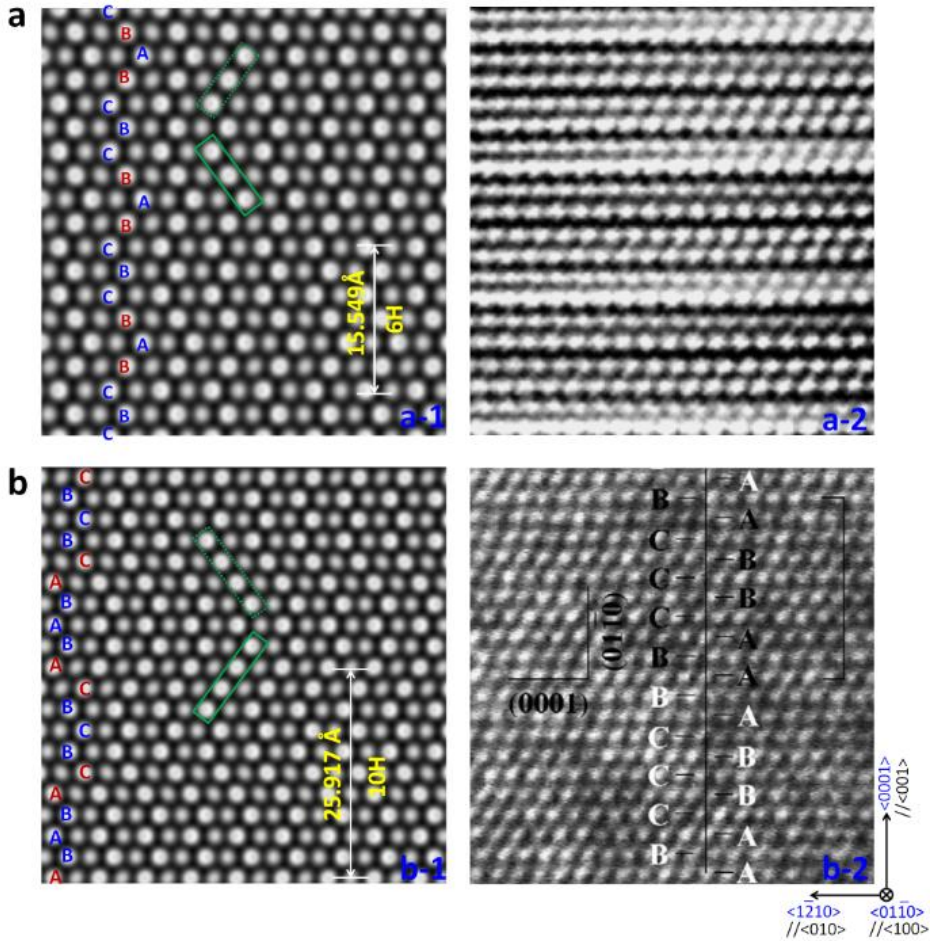

Figure 5.5. Simulated (100) HRTEM images in 6H (a) and 10H (b) with the stacking sequence of four atomic layers highlighted by the rectangles and fault layers in red. The HRTEM images of 6H and 10H of $Mg_{97}Zn_1Y_2$ in a-2 and b-2 are reproduced from [23] and [169] with permissions of The Japan Institute of Metals and by Elsevier, respectively.

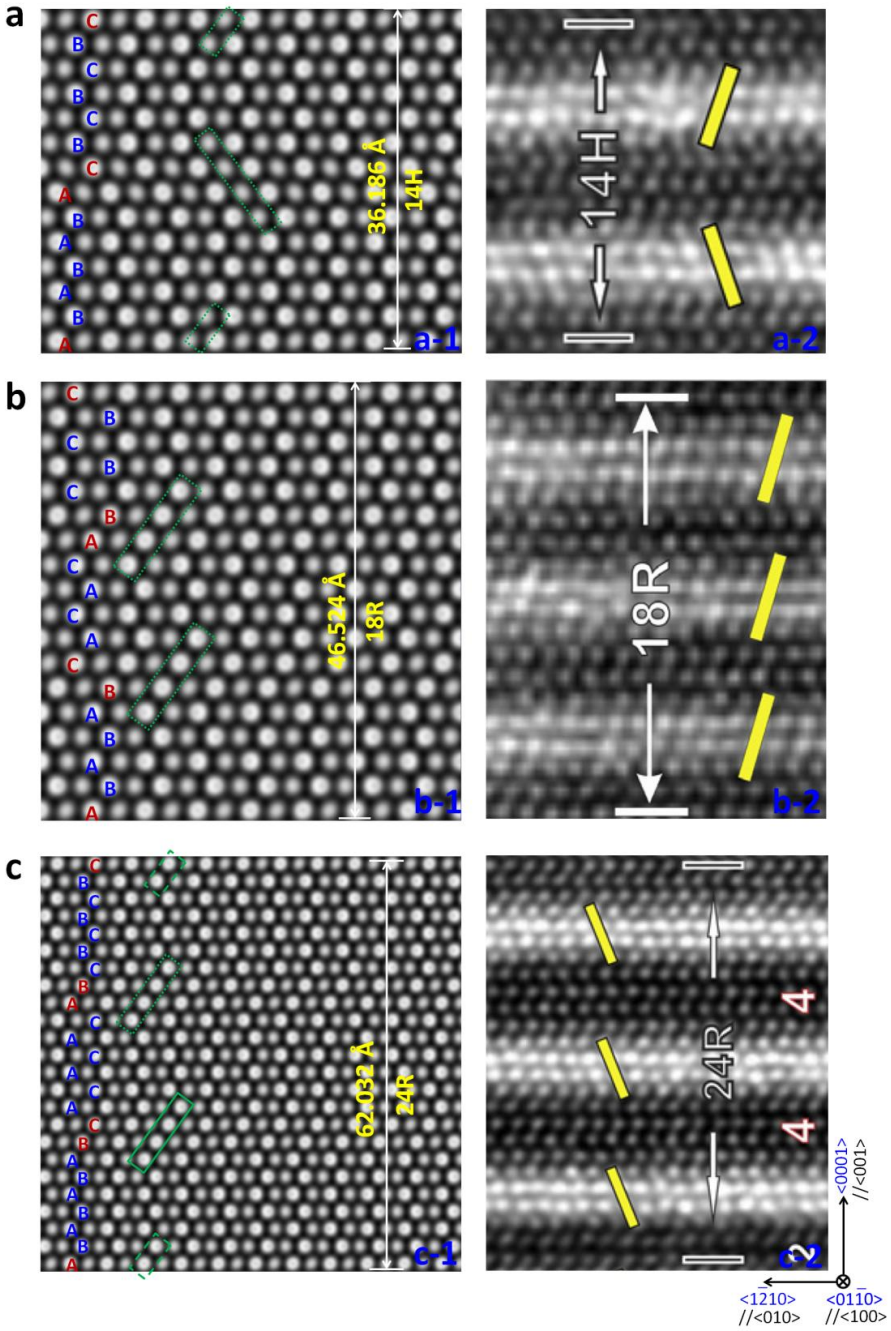

Figure 5.6. Simulated (100) HRTEM images with stacking sequence of four atomic layers in 14H (a), 18R (b) and 24H (c) structures and fault layers in red. The HRTEM images of 14H, 18R and 24R of Mg-Zn-Y alloys in a-2, b-2 and c-2 are reproduced from [123].

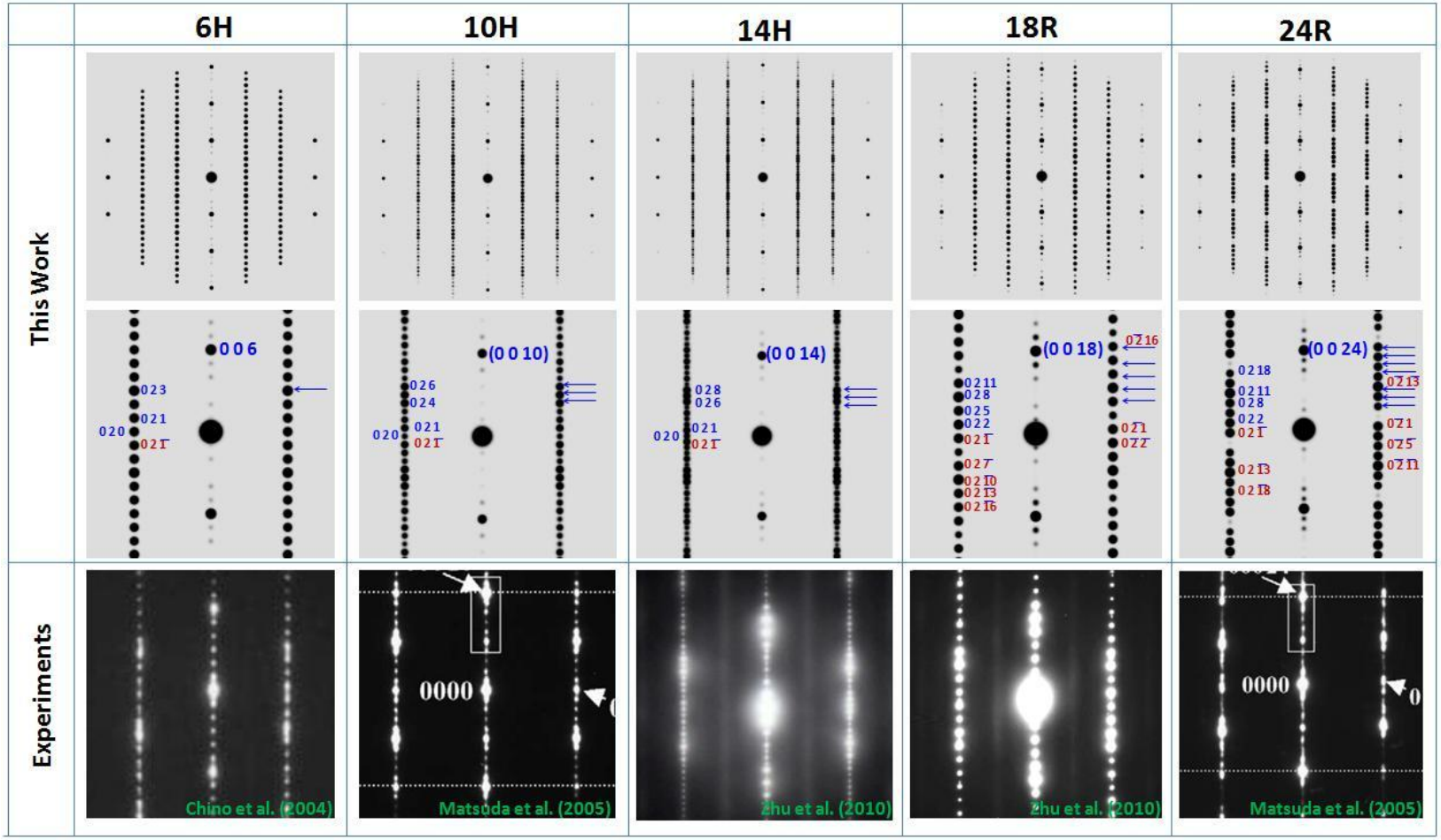

Figure 5.7 Comparation of the simulated and the experimental determined electron diffraction pattern [121, 122, 169] of long periodic stacking order structures in Mg. The simulated electron bean direction is parallel to $<100>_{S.C.} \| <10\bar{1}0>_{LPSO}$. The planner index is based on the orthorhombic supercell.

4.3.4. Phonon properties and vibrational entropy of LPSOs

In Figure 5.8, effect of fault layers on the phonon density of states of Mg with various LPSOs in comparison with the available experimental data [143, 144] is presented. It can be seen that the frequency of the phonon peaks (ω > 6.5 THz) of LPSOs have shift to the right part with a high frequency mode. There is no change in the low frequency mode (ω < 3.5 THz) for LPSOs, comparing to that of perfect Mg. However, the significant change of the first peak of LPDOS (ω = 4 THz) of Mg with LPSOs is observed, whose height and width shrink in the order of 10H > 18R > 14H > 6H > 24H. Additionally, there is no peak at ω = 4 THz in 24H. As for the high frequency mode (ω > 6.5 THz), no obviously change of the height and width occurs in 10H LPSO, comparing with that of perfect Mg. However, the height of the second peak of LPDOS of Mg with LPSOs shrink in the order of 6H > 14H > 18R > 24R and the position of the second peak moves to the higher frequency mode in the same order.

Based on the Spring model [89, 92, 102], stretching and bending force constants of 6H, 10H, 14H, 18R and 24R are calculated. Variations in force constants as a function of bond length between atoms up to 8 Å are shown in Figure 5.9. It can be seen that the bond length and the stretching force constant corresponding to the first nearest neighbor display a significant change with the formation of fault layers in the HCP lattice, which is similar to the variation tendency caused by fault layers in stacking faults. Therefore, it can be concluded that the displacement of the phonon DOS towards high frequency mode of stacking faults is caused by the reduced bond length while the change of low frequency mode is due to the elongated bond length. The interactions between fault-

fault, fault-non-fault, non-fault-non-fault layers have been revealed distinctly in the format of bond length splitting of the first nearest neighbor, shown in Figure 5.9. More interestingly, the reduction of stretching force constant of the first nearest neighbor indicates the increase of vibrational entropy. Because introducing configurational disorder in an ordering system should increase the vibration entropy since the process reduces the number of stiff bonds and increase the number of soft bonds [148]. In the following, vibrational entropy of each atomic layer in LPSOs is discussed based on its local phonon density of states.

Figure 5.10 shows the LPDOS of Mg with 6H together with their bond structure characterized by the $0.5\Delta\rho_{max}$ charge density isosurface. It can be seen that atoms occupying the fault layers, such as L2 and L4, play the important role yielding the excess frequency mode (ω > 7.25 THz), which are highlighted in Figure 5.10(a) in navy and blue, separately. Moreover, there is difference between the non-fault layer (L3) within two fault layers and the other non-fault layers (L1, L5 and L6). This is cause by interactions between two fault layers, which can be characterized as emerging electron particles in the basal plane into tetrahedron-shaped directional bonds, shown in Figure 5.10 (b). Thus, there are three typical LPDOS curves in 6H LPSOs, matching well with the bond structure characterization by charge density isosurface. Based on Equation 2.16, Equation 2.19 and Equation 2.20, vibrational contributions to Helmholtz energy, entropy and specific heat at constant volume of each atomic layer in growth fault are gained, shown in Figure 3.18. It can be seen that the fault layers (L8) together with its near neighbor could stabilized the growth fault at high temperature since their entropy and

specific heat are higher while the Helmholtz energy are lower, consisting with the displacement of LPDOS towards the low frequency region.

Figure 5.12 shows the LPDOS of Mg with 10H together with their bond structure characterized by the $0.5\Delta\rho_{max}$ charge density isosurface. It can be seen that there are three typical LPDOS curves in 10H LPSOs, matching well with the bond structure characterization by charge density isosurface. Atoms occupying the 2^{nd} nearest neighbor layer, such as L3 and L8, play the important role strengthening the high frequency mode (ω = 6.75 THz) while atoms in fault layers mainly contribute the first peak of low frequency mode (ω = 3.75 THz). Moreover, the displacement of LPDOS of the first nearest neighbor of the fault layer (L2, L4, L7 and L9) towards low frequency mode is presented, accompanying with the splitting of LPDOS peaks at both low and high frequency mode. Thus, those changes in the LPDOS are expected to result in high entropy to stabilize the structure at high temperature. As can be seen in Figure 5.13, the reduction of Helmholtz energy of 10H LPSO by the fault layers (L1 and L5) and their first nearest neighbors (L2 and L4) at the temperature below 650 K has been presents. At the low temperature range, the vibrational entropies of the fault layers (L1 and L5) and their first nearest neighbors (L2 and L4) are the highest, shown in Figure 5.13(c).

The LPDOS of 14H together with their bond structure characterized by the $0.5\Delta\rho_{max}$ charge density isosurface are presents in Figure 5.14. Four typical LPDOS curves match well with the bond structure characterization, which identify the local vibration behavior of fault layers and their 1^{st}, 2^{nd} and 3^{rd} neighbor layers. It clearly shows that peaks of LPDOS curve of fault layers at low and high frequency modes have

been strengthened while the displacement of LPDOS curve of their 1st neighbor layers towards the low frequency mode occur. Through investigating the vibrational contributions to Helmholtz energy, specific heat at constant volume and entropy of each atomic layer in 14H, shown in Figure 5.15, fault layers (L1, L7, L8 and L14) stabilizing the 14H at high temperature has been displayed in terms of the decrease of Helmholtz energy and the increase of vibrational entropy.

Similarly, the LPDOS of 18R and 24R LPSOs together with their bond structure characterized by the $0.5\Delta\rho_{max}$ charge density isosurface are presents in Figure 5.16 and Figure 5.18. In general, number of typical LPDOS curves in 18R and 24R LPSOs dominated by the bond length respecting to the atom in fault layer. Comparing with 14H, there is no 3rd nearest neighbor layer between two fault layers in 18R while there are two in 24R. Therefore, local vibration behavior of the fault layers and their 1st neighbor layers in 18R and 24R is different with that of 14H. For example, the middle non-fault layers (2nd nearest neighbor layer of 18R and 3rd nearest neighbor layer of 18R) show a significant contribution to the LPDOS at high frequency mode while fault layers play an important role at low frequency mode. Correspondingly, the reduction of Helmholtz energy by the middle non-fault layers of 18R and 24R at high temperature range (T> 400) have been observed while by the fault layers at low temperature range (T< 400), shown in Figure 5.17 and Figure 5.19.

Since Debye temperature (Θ_D) is sensitive to the density of the structure defects, it could be a validate parameter quantitatively identifying the contributions of fault layers to the vibrational energies of LPSOs. Table 5.2 summarizes the Debye temperature (Θ_D)

of the atom in each layer of LPSOs in Mg. It can be seen that the larger of Θ_D the higher of highest vibrational entropy at high temperature. For example, non-fault layer (L4) between two fault layers (L3 and L5) in 6H has the largest Θ_D and the highest vibrational entropy at high temperature. Fault layers (L1, L7, L8 and L14) in 14H have the largest Θ_D and the highest vibrational entropy at high temperature. On the contrary, the middle non-fault layers (L5, L13 and L21) between fault layers in 24R have the largest Θ_D and the highest vibrational entropy at high temperature.

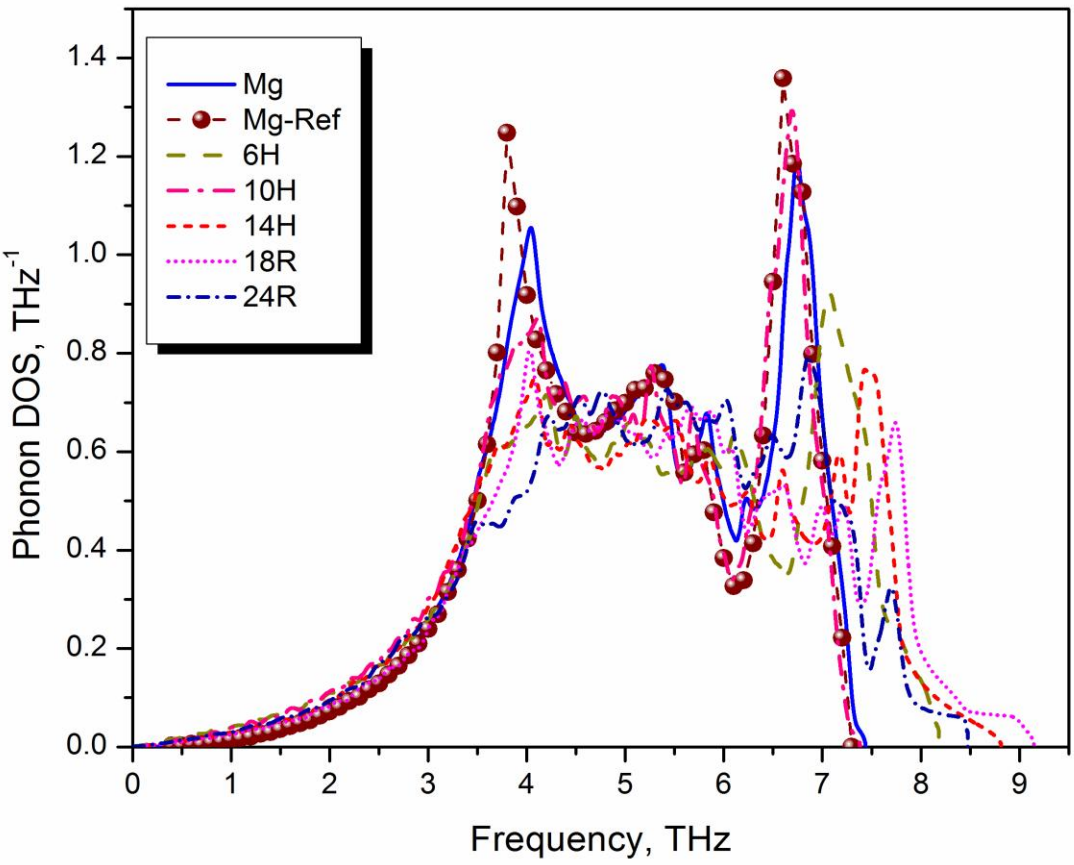

Figure 5.8. Effect of fault layers on the phonon density of states of Mg with various LPSOs, comparing with the available experimental data (labeled with dash line and a sphere symbol) [143, 144].

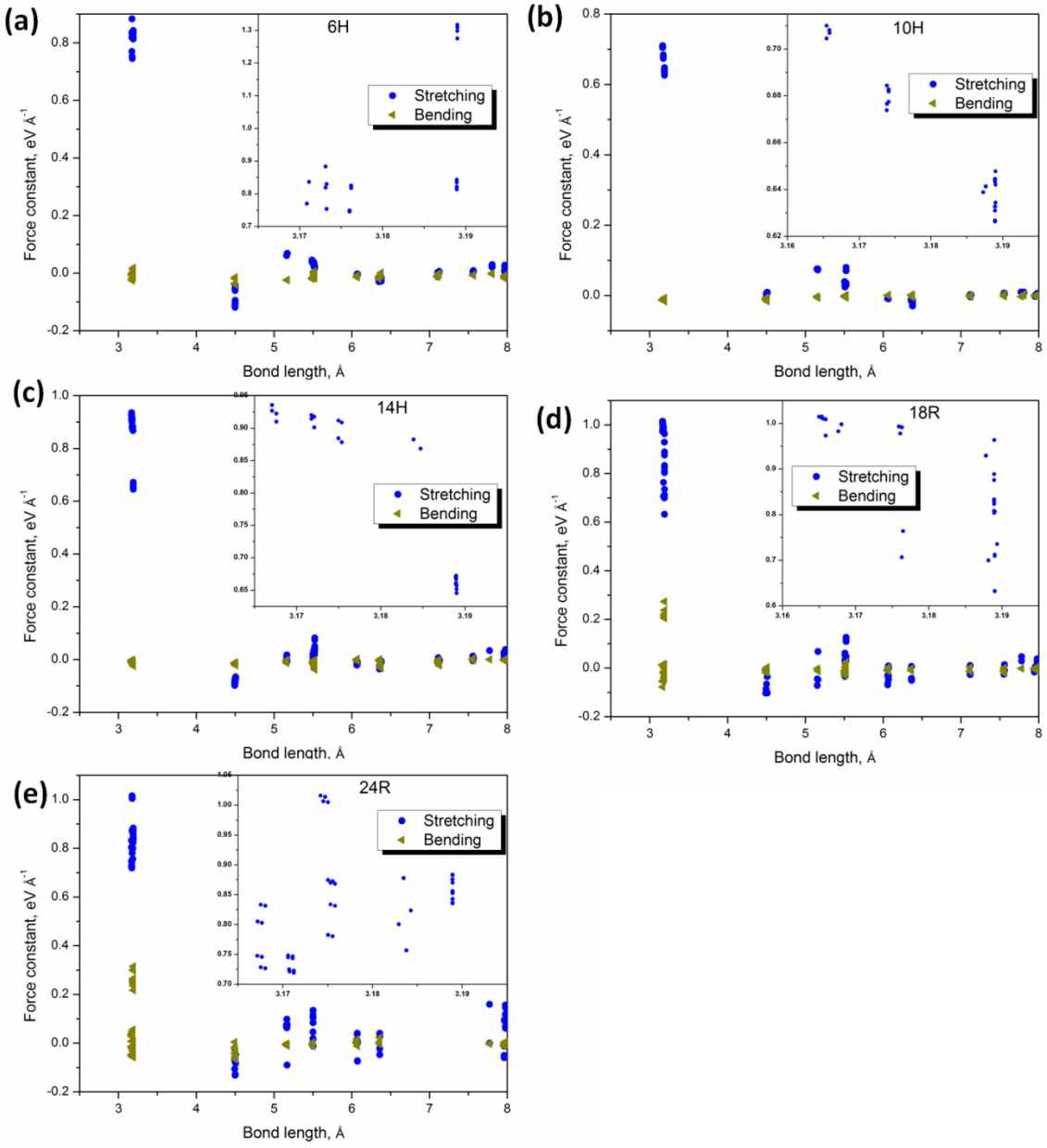

Figure 5.9 Variation in bond length and force constants versus atom pair type, (a) 6H; (b) 10H; (c) 14H; (d) 18R and (e) 24R. Bond length splitting of the first nearest neighbor shown in the insert image presents the interactions between fault-fault, fault-non-fault and non-fault-non-fault layers.

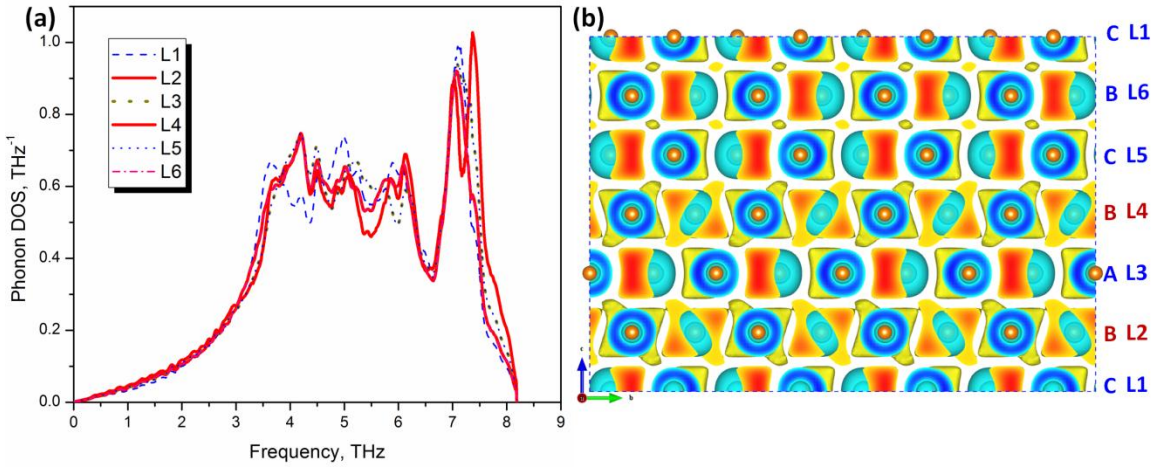

Figure 5.10. Local phonon density of states (LPDOS) of Mg with 6H together with their bond structure, (a) LPDOS curve and (b) the 0.5Δρmax charge density isosurface plotted in prismatic plane. The fault layers are identified with solid lines in red while non-fault layers use dash line or dash dot line.

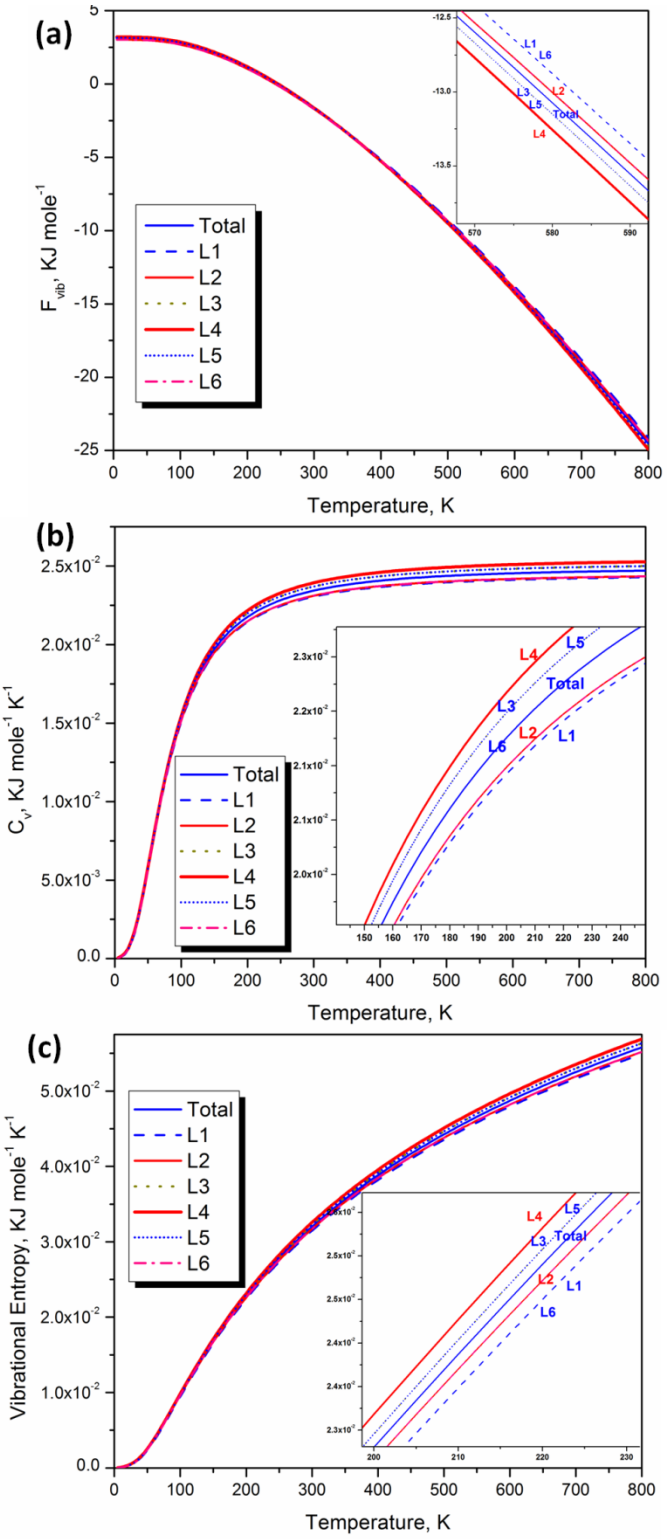

Figure 5.11. Vibrational contributions to Helmholtz energy (a), specific heat at constant volume (b) and entropy (c) of each atomic layer in 6H LPSO.

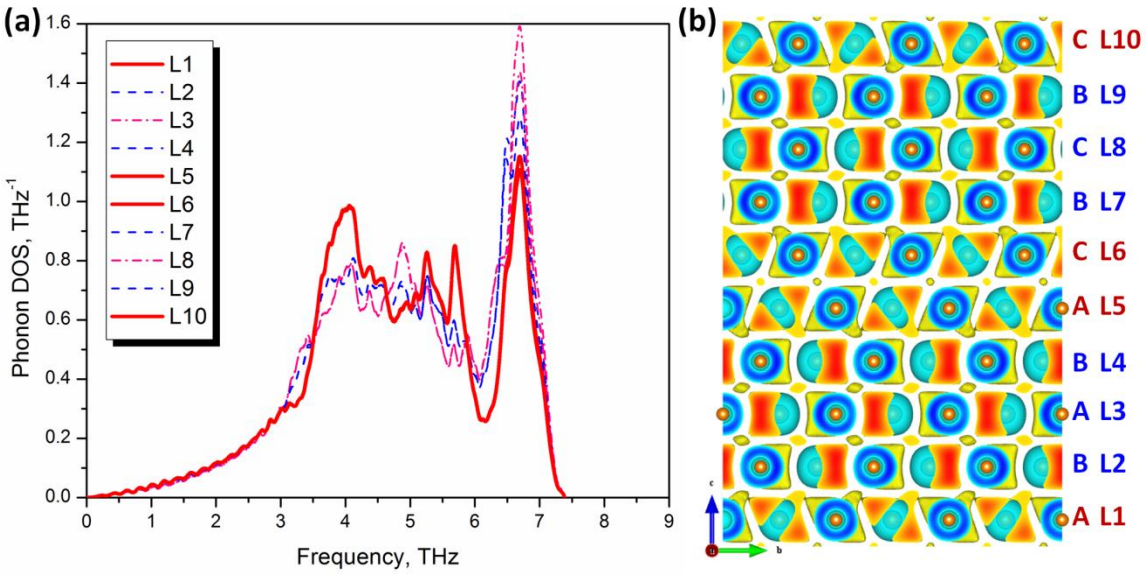

Figure 5.12. Local phonon density of states (LPDOS) of Mg with 10H together with their bond structure, (a) LPDOS curve and (b) the $0.5\Delta\rho_{max}$ charge density isosurface plotted in prismatic plane. The fault layers are identified with solid lines in red while non-fault layers with same distance to fault layer use same dash line or dash dot line.

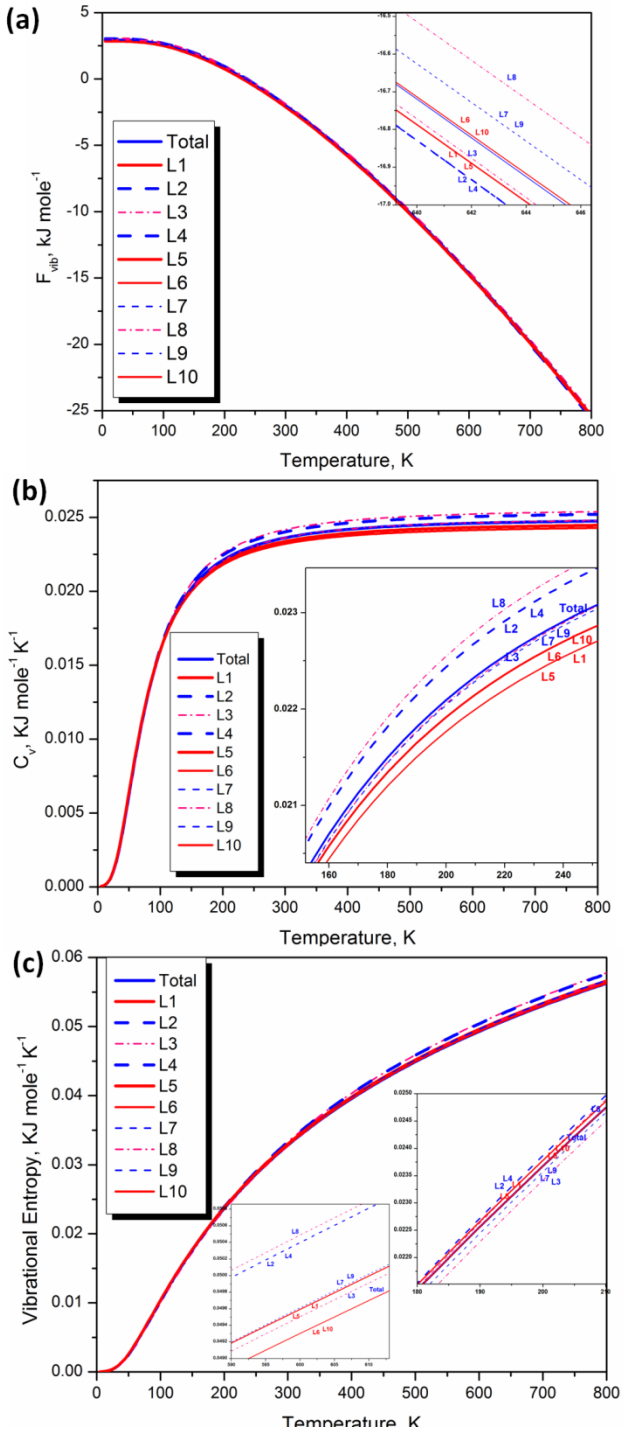

Figure 5.13. Vibrational contributions to Helmholtz energy (a), specific heat at constant volume (b) and entropy (c) of each atomic layer in 10H LPSO.

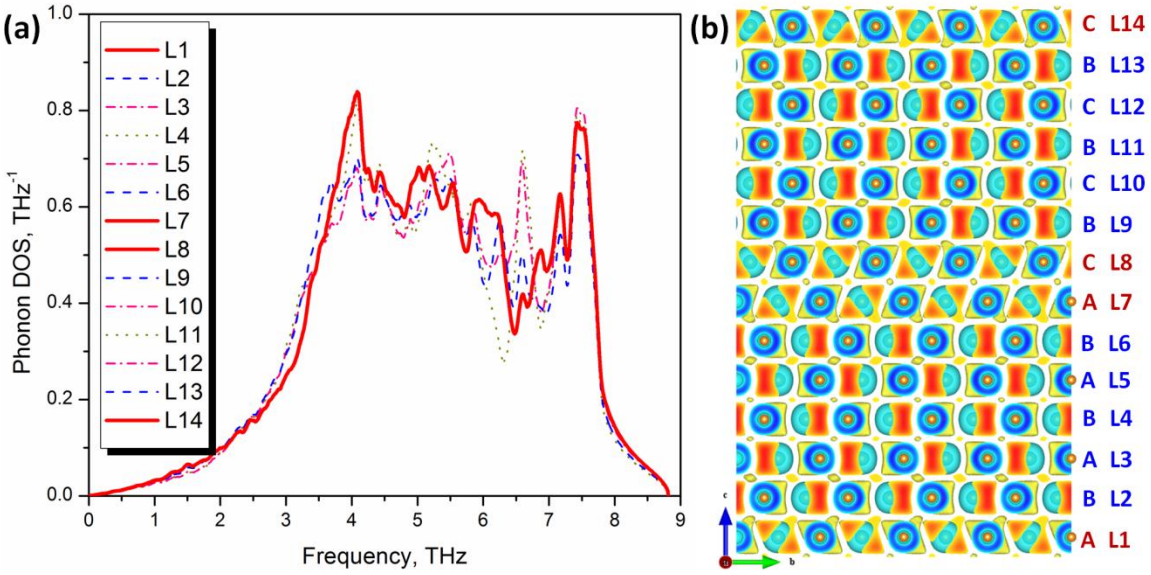

Figure 5.14. Local phonon density of states (LPDOS) of Mg with 14H together with their bond structure, (a) LPDOS curve and (b) the $0.5\Delta\rho_{max}$ charge density isosurface plotted in prismatic plane. The fault layers are identified with solid lines in red. According to the distance to the fault layer, various types of line are applied for non-fault layers. Dash line in blue and dash dot line in pink are used to identify the 1st and 2nd neighbor layer.

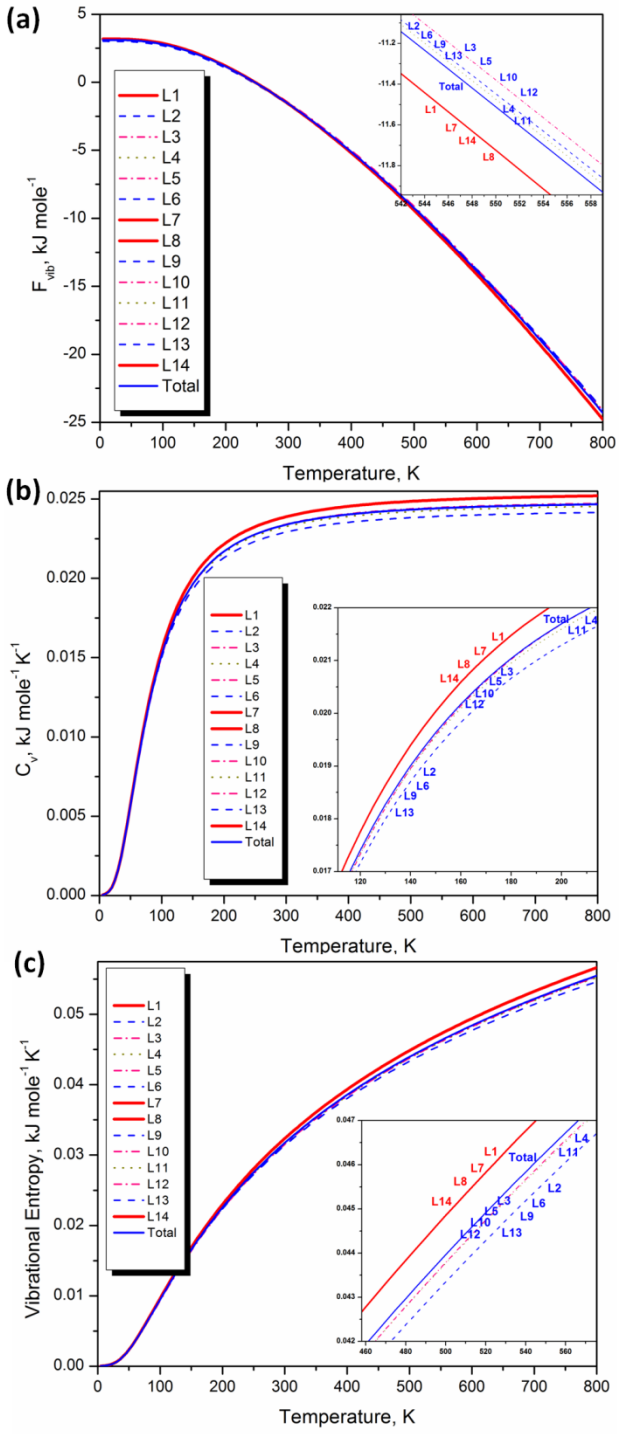

Figure 5.15. Vibrational contributions to Helmholtz energy (a), specific heat at constant volume (b) and entropy (c) of each atomic layer in 14H LPSO.

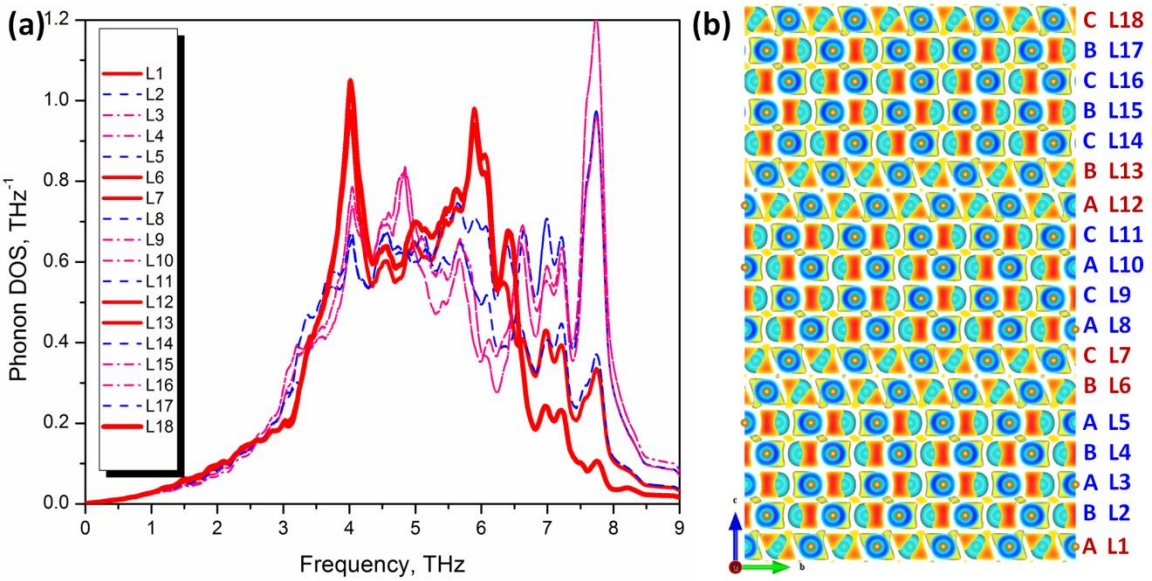

Figure 5.16. Local phonon density of states (LPDOS) of Mg with 18R together with their bond structure, (a) LPDOS curve and (b) the $0.5\Delta\rho_{max}$ charge density isosurface plotted in prismatic plane. The fault layers are identified with solid lines in red. According to the distance to the fault layer, various types of line are applied for non-fault layers. Dash line in blue, dash dot line in pink and short dot line in green are used to identify the 1st, 2nd and 3rd neighbor layers.

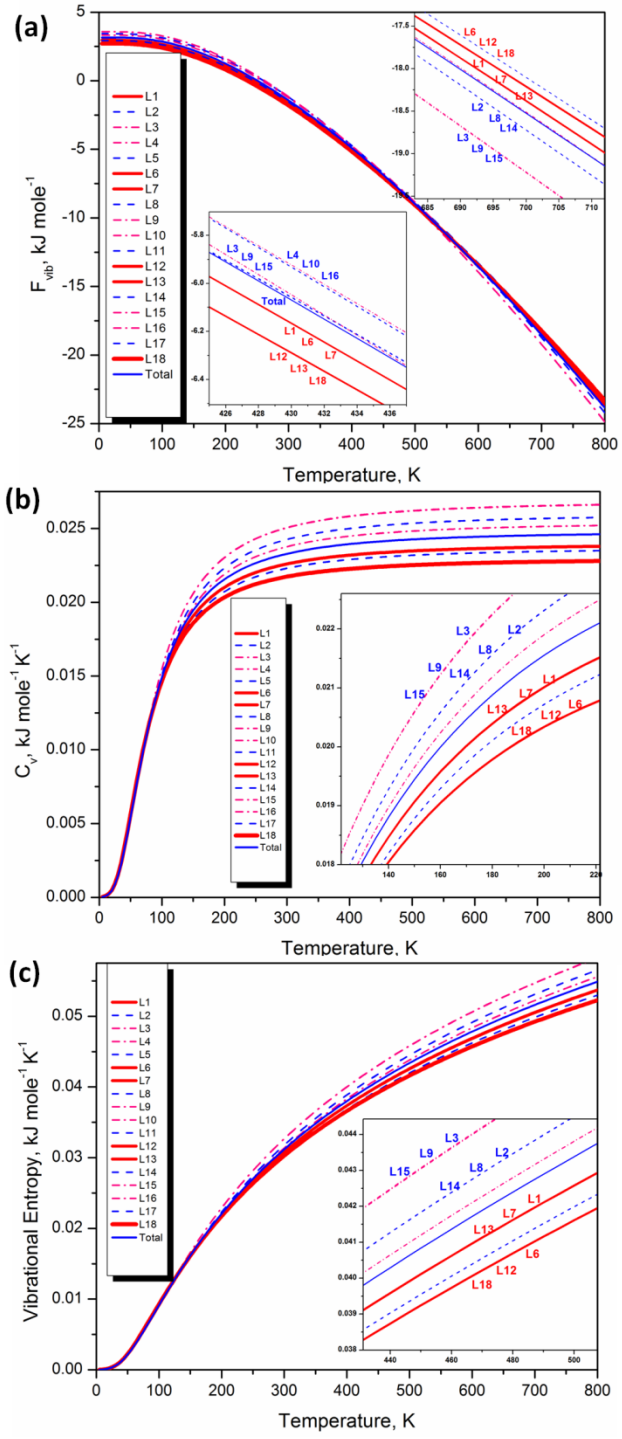

Figure 5.17. Vibrational contributions to Helmholtz energy (a), specific heat at constant volume (b) and entropy (c) of each atomic layer in 18R LPSO.

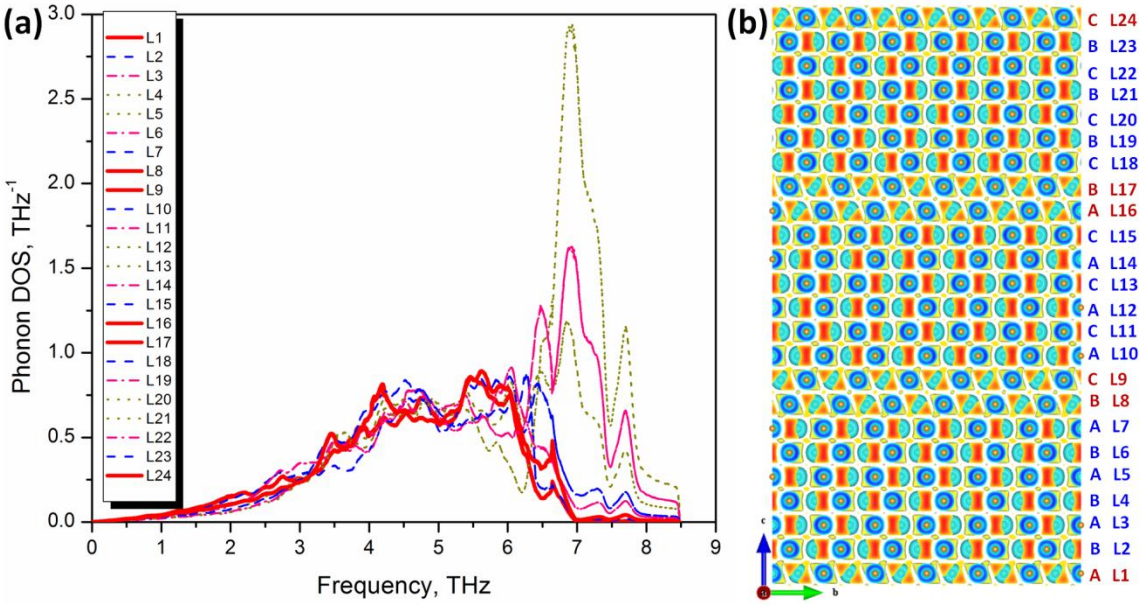

Figure 5.18. Local phonon density of states (LPDOS) of Mg with 24R together with their bond structure, (a) LPDOS curve and (b) the $0.5\Delta\rho_{max}$ charge density isosurface plotted in prismatic plane. The fault layers are identified with solid lines in red. According to the distance to the fault layer, various types of line are applied for non-fault layers. Dash line in blue and dash dot line in pink are used to identify the 1st and 2nd neighbor layer.

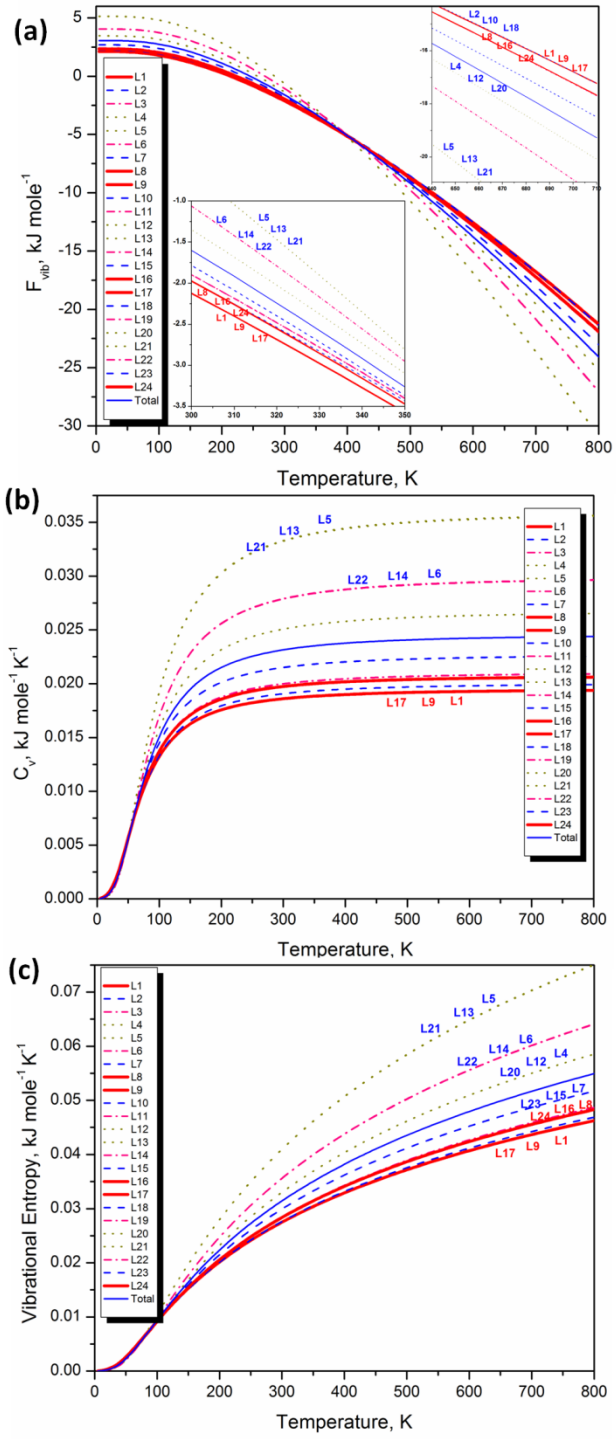

Figure 5.19 Vibrational contributions to Helmholtz energy (a), specific heat at constant volume (b) and entropy (b) of each atomic layer in 24R LPSO.

Table 5.2. Debye temperature (Θ_D) of the atom in each layer of LPSOs in Mg. The second moment of phonon DOS is used to derive the Θ_D in this work.

Atomic Layer		6H		10H		14H		18R		24R	
		Θ_D (K)	Note	Θ_D (K)	Note	Θ_D (K)	Note	Θ_D (K)	Note	Θ_D (K)	Note
LPSO	L1	333.5		311.1		338.9	S_{High}	332.1		292.7	
	L2	332.9		320.3	S_{High}	334.7		354.3		301.7	
	L3	337.7		323.1		341.3		357.6	S_{High}	309.1	
	L4	341.3	S_{High}	320.3	S_{High}	336.9		354.3		346.7	
	L5	337.7		311.1		341.3		334.1		379.8	S_{High}
	L6	332.9		310.1		334.7		317.4		360.9	
	L7			318.0		338.9	S_{High}	332.1		317.7	
	L8			320.5	S_{High}	338.9	S_{High}	357.5		302.7	
	L9			318.0		334.7		359.8	S_{High}	292.7	
	L10			310.1		341.3		354.3		301.7	
	L11					336.9		334.3		308.8	
	L12					341.3		317.5		346.7	
	L13					334.7		332.2		380.0	S_{High}
	L14					338.9	S_{High}	357.4		361.0	
	L15							359.8	S_{High}	317.7	
	L16							354.3		302.7	
	L17							334.2		292.6	
	L18							317.4		301.7	
	L19									308.9	
	L20									346.6	
	L21									380.0	S_{High}
	L22									361.1	
	L23									317.6	
	L24									302.6	
	Total	336.0		316.4		338.1		343.8		334.5	
Bulk		321.5 323[a], 325[b], 320[c]									

Note: S_{High}: the atomic layers with high vibrational entropy at high temperature

a. Zhang, et al., derived from the second moment of phonon DOS. [83]
b. Seitz F. and Trunbull D. Solid. State. Physics. New York: Academic Press;1964 (Exp.)
c. Dederch ,et al., Metals: Phonon states, electron states and Fermi surfaces. Berlin: Springer-Verlag: 1981 (Exp.)

4.4. Conclusions

In summary, the electronic structures of 6H, 10H, 14H, 18R and 24R LPSO structures are investigate by first-principles calculations, which are similar to that of deformation stacking fault. Except 6H, all of them can be considered as stacking of double-fault layers with variable non-fault layers between. The electron localization morphology further confirms the fcc characteristics of the fault layers based on the tetrahedron-shaped directional bonds. The simulated HRTEM images reveal a mirror plane with the stacking sequence of three atomic layers in 6H and four atomic layers in 10 H, and a sheared displacement of the stacking sequence of four atomic layers in 14H, 18R and 24R. It is articulated that transformation between LPSO structures is related to the reduction of dislocation density during heat treatment.

Contributions of fault layers to the phonon density of states of Mg with various LPSOs in comparison with the available experimental data are discussed. It can be seen that the frequency of the phonon peaks ($\upsilon > 6.5$ THz) of LPSOs have shift to the right part with a high frequency mode. Comparing to the LPDOS of perfect Mg, there is no change in the low frequency mode ($\upsilon < 3.5$ THz) for all the LPSOs. However, the significant change of the first peak of LPDOS ($\upsilon = 4$ THz) of Mg with LPSOs is observed, whose height and width shrink in the order of 10H > 18R > 14H > 6H > 24H. Additionally, there is no peak at $\upsilon = 4$ THz in 24H. As for the high frequency mode ($\upsilon >$ 6.5 THz), no obviously change of the height and width occurs in 10H LPSO, comparing with that of perfect Mg. However, the height of the second peak of LPDOS of Mg with

LPSOs shrink in the order of 6H > 14H > 18R > 24R and the position of the second peak moves to the higher frequency mode in the same order.

Based on variations in stretching and bending force constants of 6H, 10H, 14H, 18R and 24R, it can be seen that the bond length and the stretching force constant corresponding to the first nearest neighbor display a significant change with the formation of fault layers in the HCP lattice. The displacement of the phonon DOS towards high frequency mode of stacking faults is caused by the reduced bond length while the change of low frequency mode is due to the elongated bond length. The interactions between fault-fault, fault-non-fault and non-fault-non-fault layers have been revealed distinctly in the format of bond length splitting of the first nearest neighbor. More interestingly, the reduction of stretching force constant of the first nearest neighbor indicates the increase of vibrational entropy. Contributions of each individual atomic layer to the thermal dynamic properties of LPSOs have been qualitatively and quantitatively described by Helmholtz energy, vibrational entropy and Debye temperature.

Chapter 6

Effect of Alloying Element (X) on the Formation Energy and Electronic Property of 6H and 10H LPSOs in Binary Mg-X Alloys

6.1. Introduction

In recent years, Mg-RE alloys with excellent mechanical properties have been obtained for combining fine grain size, precipitates, and long period stacking order (LPSO) structures. For instance, the tensile yield strength and the elongation of $Mg_{97}Y_2Zn_1$ (at %) alloy with the 6H LPSO structure produced by rapid solidification can reach 610 MPa and 5%, respectively, with grain sizes in range of 100 nm to 150 nm [23]. When the grain size of Mg matrix is about 330 nm, the tensile yield strength and the elongation become 400 MPa and 2%, respectively [24]. It is commonly accepted that fine precipitates or local clustering of solute atoms together with different types of LPSO structures, including 6H, 10H, 14H, 18R and 24R, contribute to strengthening of Mg alloys [25-34].

Works focusing on the precipitating behavior of alloying elements are important to optimize the microstructure and to improve the mechanical properties of Mg alloys [30, 33, 35-40]. In the development of advanced Mg alloys with good performance,

effect of LPSOs and its enrichment of alloying elements on electronic structure and elastic properties of Mg remain ambiguous.

In this chapter, contributions of alloying element to the energy and electronic structures of 6H and 10H LPSOs in binary Mg-X alloys are discussed, providing the energetic favorable configurations to study the following ternary system. The validation of the proposed atomic array and atomic cluster model are estimated in various Mg-X alloys. Typical alloying elements in Mg alloys are selected, which are Gd, Y, Al, Ca, Mn, Zn and Zr.

It is worth to mention that Mg-10Gd (wt%) and Mg-10Y with 6H and 10H LPSOs are studied in order to investigate the segregation behavior of rare earth elements in LPSOs and their effect on the formability of LPSOs. This is because (i) both Y and Gd are essential alloying elements forming LPSOs in Mg alloys, shown in Table 1.1 and Figure 6.1; (ii) Mg-Zn-Gd alloys show the best mechanical properties at both room temperature and 473K among all the Lanthanides; (iii) in the heavy Lanthanides forming LPSO in Mg-Zn-RE alloys, the tensile strength and the elongation of Mg-Zn-Gd is the highest; (iv) in view of the atomic radius of alloying elements, the lattice strain will be different when alloying Gd and Y since the difference of atomic radius between them is the biggest, shown in Figure 6.2; (v) the Mg-Y and Mg-Gd alloys always show excellent mechanical properties, shown as Table 6.1. It has been recently reported that the ultimate tensile strength of Mg-8.5Gd-2.3Y-1.8Ag-0.4Zr is 600 MPa with the elongation of 5.2 % [34].

According to the contributions of alloying element (X) to the stacking fault energy discussed in Chapter 4, these elements significantly reducing stacking fault energies, Al, Ca, Y and Zn are chosen. Since Mn and Zr are essential transition metals in improving the strength, the corrosion resistance and refining the grain size, both of them are also contained in the present work.

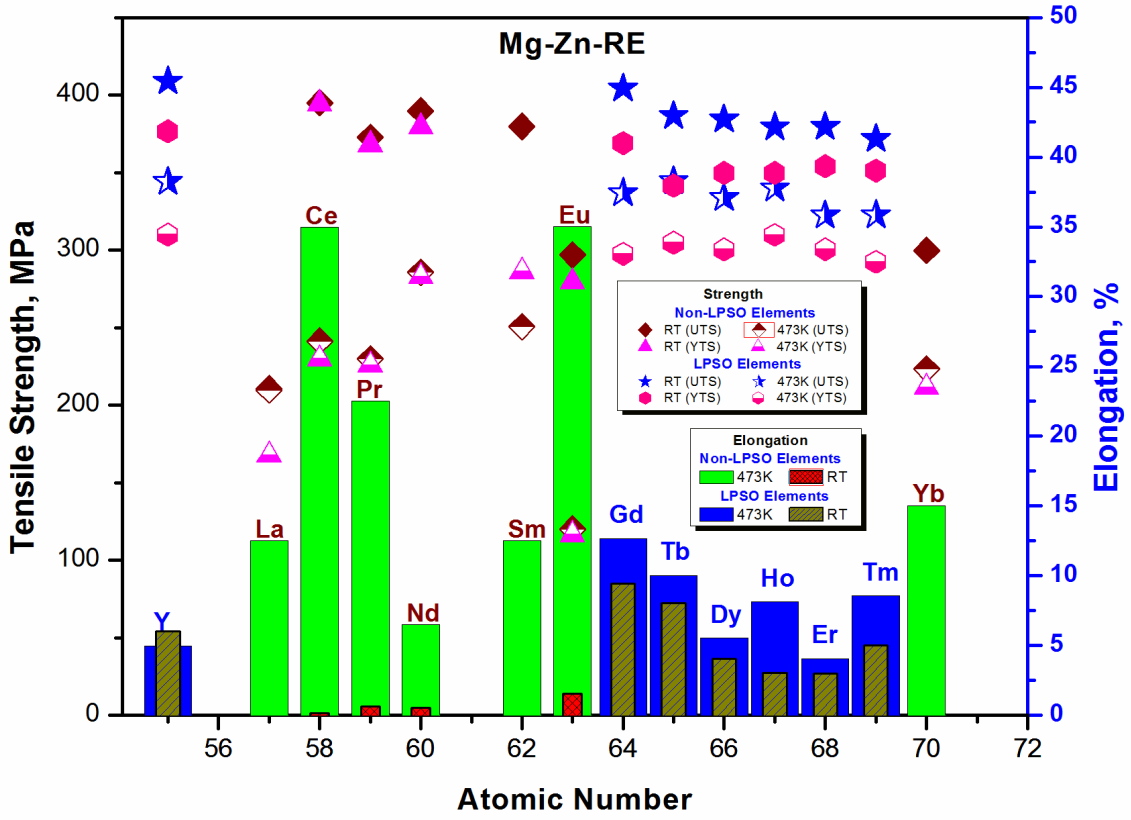

Figure 6.1. Effect of rear earth elements (RE) on the tensile strength and the elongation of Mg-Zn-RE at room temperature and 473K. These lanthanides are classified into two categories, one called LPSO elements could form long periodic structures in Mg-Zn-RE alloys and the other called non-LPSO elements cannot. Solid symbols are used to identify the tensile strength of Mg-Zn-RE at room temperature while open symbols are used at 473K. Bars are applied to show the elongation of Mg-Zn-RE.

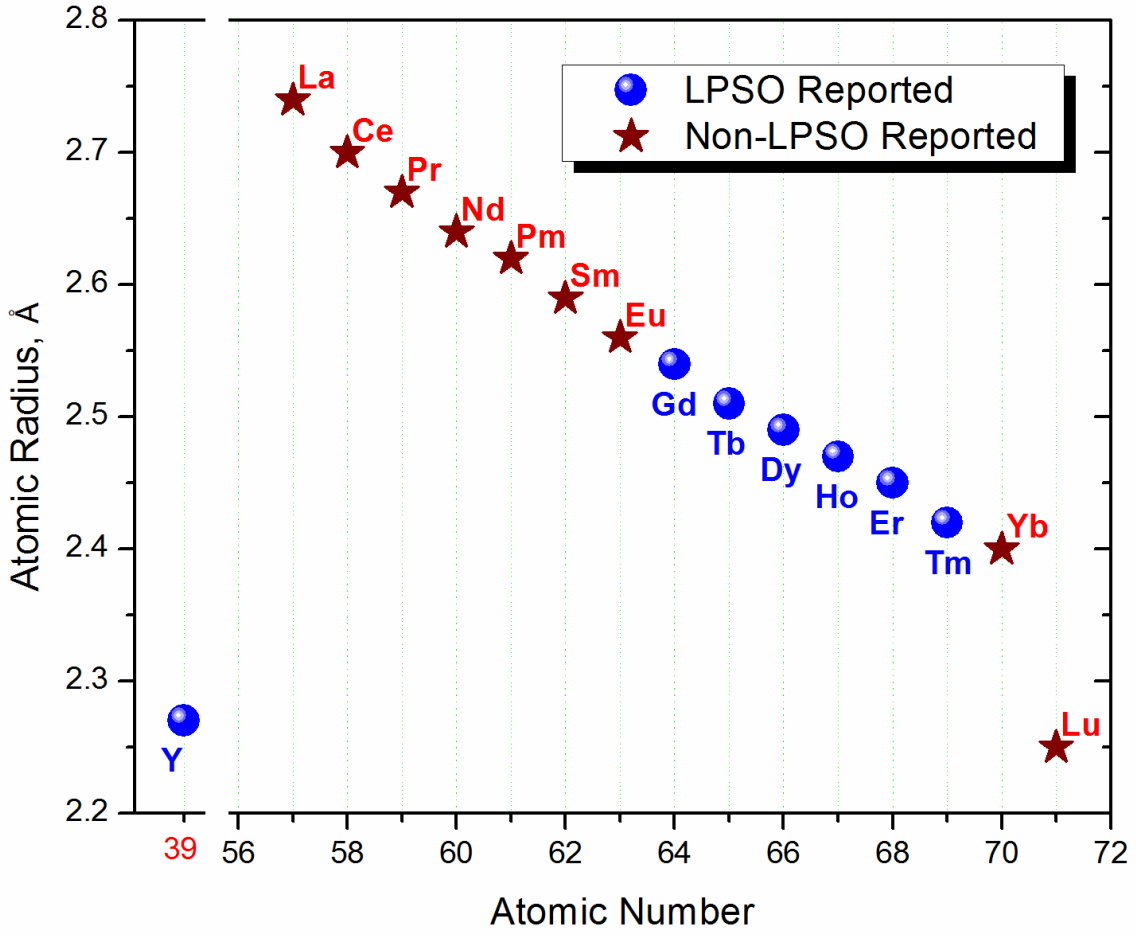

Figure 6.2. Classification of rare earth elements according to whether forming LPSOs in Mg-Zn-RE alloys.

Table 6.1. Tensile properties of Mg-Gd and Mg-Y alloys

Alloy Composition Mass%		Room Temperature			High Temperature			Ref
		TS MPa	TYS MPa	E %	TS MPa	TYS MPa	E %	
Mg-10Gd-0.6Mn (HE)		340	280	10	170	140	26	a
Mg-10Gd-6Y-0.6Mn (HE)		440	390	5	230	200	15	a
Mg-8.5Gd-2.3Y-1.8Ag-0.4Zr		600		5.2				f
Mg-9.1Y (HE)	Not Aged	266	207	13.0	166	140	19	b
	Aged	323	204	6.4	177	147	32	b
Mg-8.3Y-0.6Nd (HE)	Not Aged	291	205	13.8	183	140	22.6	b
	Aged	319	258	7.4	183	183	41	b
Mg-7Y (PM/RS)		345	300	9.9				c
Mg-7Y (IN)		290	235	8.0				c
Mg-11.5Y (PM/RS)		381	367	9.1				c
Mg-11.5Y (IN)		330	275	3.0				c
Mg-6.14Y (HE)	Not Aged	272	212	8.4	187	125	20.3	e
	Aged	229	176	9.8	151	80	27.5	e
Mg-12.12Y (HE)	Not Aged	356	290	9.0	284	229	15.4	e
	Aged	293	229	15.4	284	227	13.6	e
Mg-10.5Y-4.2Sc-0.79Mn (HE)	Not Aged	370	280	8.5	235	190	41	d
	Aged	385	325	5.0	265	225	29.0	d
Mg-10.5Y-4.2Sc-0.79Mn (CD)	Not Aged	395	375	4.5	265	225	26.9	d
	Aged	420	385	4.5	275	235	27.0	d

Note: **300 ℃** **250 ℃**

* The table are summarizing reported data in the literature, which can be found in Ref. [149].

a. The hot extruded (**HE**) Mg alloys with an aging time of 200 ℃/24h after extrusion, high-T is at **300 ℃**;
b. Aged regimes were 200 ℃/100h, high-T is at **300 ℃ ;**
c. Mg alloy rods prepared by using the powder metallurgy/ rapid solidification (PM/RS) and ingot (IN) technologies, high-T is at **250 ℃**;
d. The hot extruded (**HE**) and cold deformed 5% (**CD**) Mg alloys with an aging regimes of 200 ℃/100h after deformation, high-T is at **300 ℃**;
e. The hot extruded (**HE**) Mg alloys with a solute treatment + aging regimes of 200 ℃/100h after deformation, high-T is at **250 ℃;**
f. Hot rolling sample with T4 heat treatment [34].

6.2. Crystal Structures and Computation Details

Two different models, atomic cluster and atomic array of alloying elements, are applied into the interactions between alloying elements and faults layers in Mg-10Gd and Mg-10Y with 6H and 10H. In atomic array model, the chemical bond could form between alloying elements and extend in the long range following the periodic boundary condition, shown in Figure 6.4 (b). In atomic cluster model, there is no chemical bond form between alloying elements or the chemical bond can't be extended in the long range, shown in Figure 6.4(b). Thus, it will estimate the segregation tendency of the alloying elements in the fault/non-fault layer corresponding to whether their interactions are favorable in the 6H LPSO of Mg-X alloys. Here, these alloying elements include Al, Ca, Gd, Mn, Y, Zn and Zr.

Based on the orientation relationship between the orthorhombic of 6H and 10H LPSOs and the primitive cell of hcp Mg, listed in Table 6.2 and Table 6.3, crystal structures of Mg-10Gd and Mg-10Y with 6H and 10H are presented in Figure 6.4, Figure 6.5, Figure 6.6 and Figure 6.7. The lattice vectors of the orthorhombic supercell are related to those of the hcp Mg as $\langle 01\bar{1}0\rangle_{HCP} \| \langle 100\rangle_{S.C.}$, $\langle 1\bar{2}10\rangle_{HCP} \| \langle 010\rangle_{S.C.}$, and $\langle 0001\rangle_{HCP} \| \langle 001\rangle_{S.C.}$. In Mg-10Gd and Mg-10Y alloys with 6H LPSO, 9 configurations are required to identify whether the alloying element (Gd or Y) forms clusters or atomic array, in which positions labeled with P8 and P9 show the atomic array locating in the non-fault layer between two fault layers (P8) and in the fault layer (P9), shown in Figure

6.4 and Figure 6.5. On the contrary, 12 configurations are used to identify whether the alloying element (Gd or Y) forms clusters or atomic array.

Details of first-principles calculations and procedures obtaining deformation electron density (Δρ) and the HRTEM images in this work are as same as that described in the methodology part in Chapter 5.

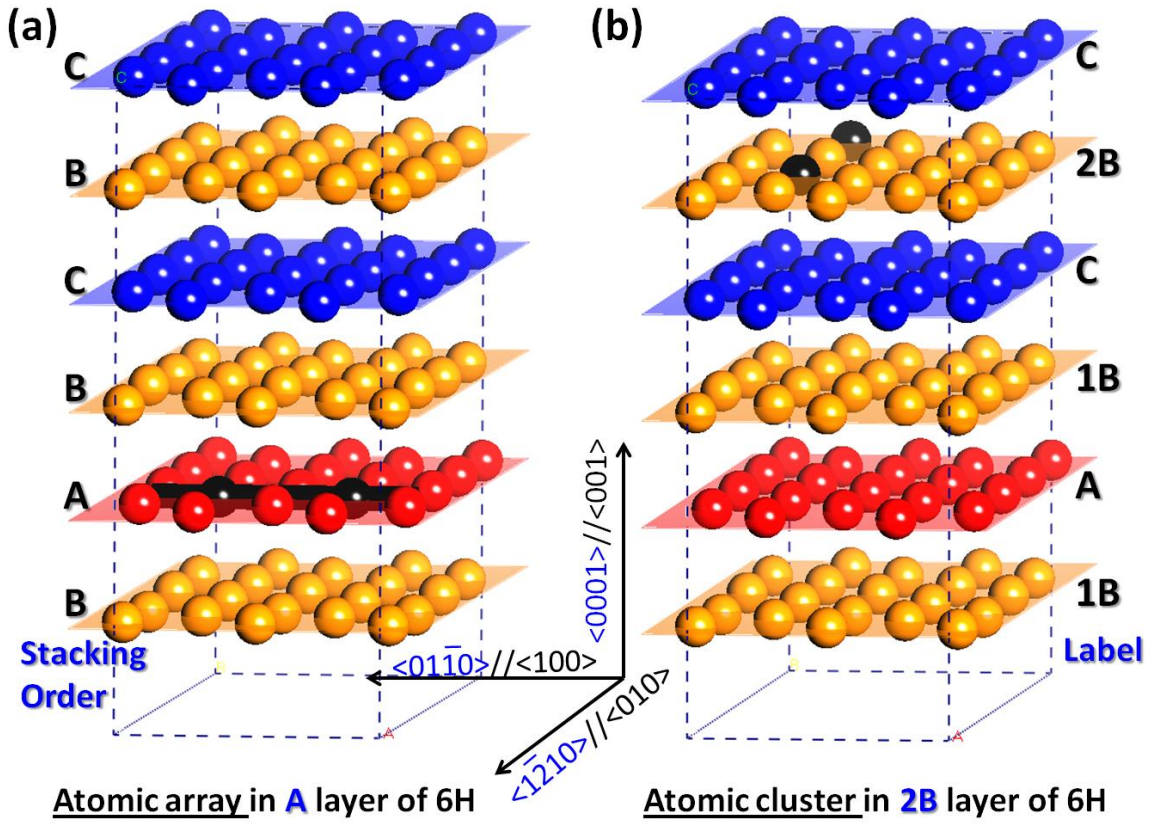

Figure 6.3. Position of alloying elements in 6H LPSO with a stacking order and a label, (a) atomic array shown in A layer, where there is a chemical bond between alloying elements and (b) atomic cluster in 2B layer, where no chemical bond forming between alloying elements. Lattice vectors of the primitive hcp Mg parallel to these of the orthorhombic supercell are labeled.

Table 6.2. The setting parameters for the first-principles calculations of Mg-10Gd and Mg-10Y with 6H LPSO

Alloys with 6H LPSO		**Theory work**			**Note Supercell Setting**
		# of atoms	at%	wt %	
Mg-10Gd	Mg	118	98.33	90.12	$5\,a' \times \sqrt{3}\ a' \times C_{LPSO}$
	Gd	2	1.67	9.98	
Mg-10Y	Mg	76	97.44	91.22	$2\,a' \times \sqrt{3}\ a' \times C_{LPSO}$
	Y	2	2.56	8.78	

Table 6.3. The setting parameters for the first-principles calculations of Mg-10Gd and Mg-10Y with 10H LPSO

Alloys with 10H LPSO		**Theory work**			**Note Supercell Setting**
		# of atoms	at%	wt %	
Mg-10Gd	Mg	118	98.33	90.12	$3\,a' \times \sqrt{3}\ a' \times C_{LPSO}$
	Gd	2	1.67	9.98	
Mg-10Y	Mg	78	97.50	91.42	$2\,a' \times \sqrt{3}\ a' \times C_{LPSO}$
	Y	2	2.50	8.58	

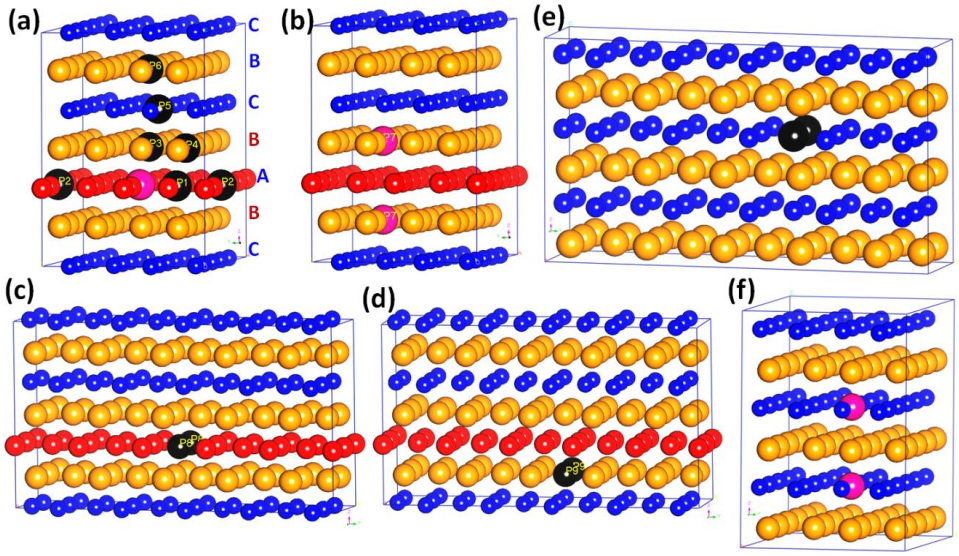

Figure 6.4. Crystal structure of Mg-10Gd with 6H LPSO, (a)-(d), 9 configurations tested to identify whether Gd forms clusters or atomic array (P8 and P9 cases); (e), reference state of P7; (f), reference state of P8 and P9.

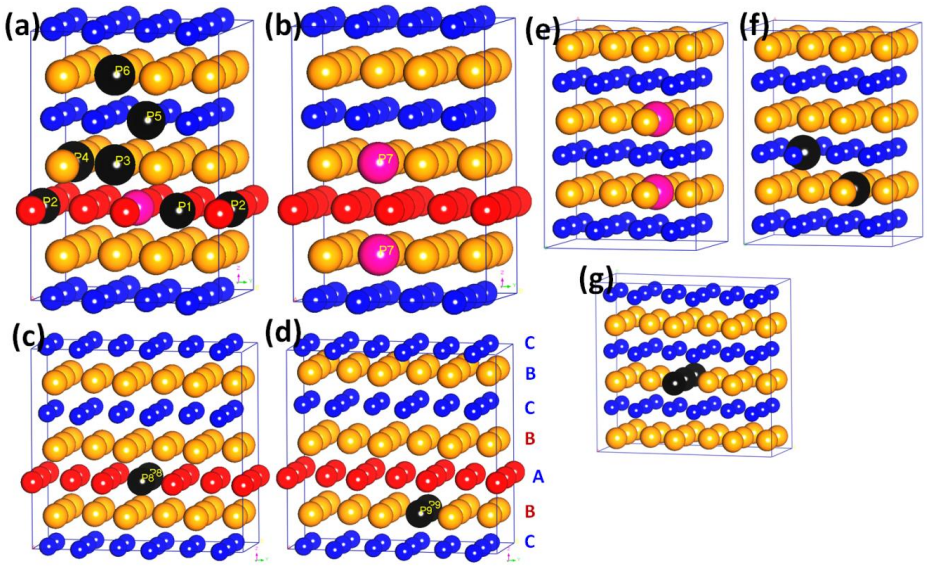

Figure 6.5. Crystal structure of Mg-10Y with 6H LPSO, (a)-(d), 9 configurations tested to identify whether Y forms clusters or atomic array (P8 and P9 cases); (e), reference state of P7; (f), reference state of P4; (g), reference state of P8 and P9.

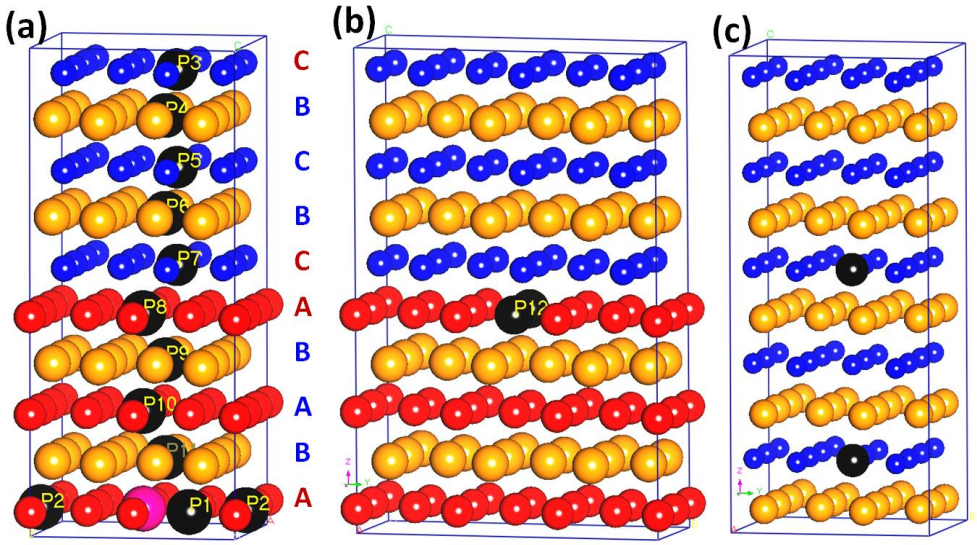

Figure 6.6. Crystal structure of Mg-10Gd with 10H LPSO, (a)-(b), 12 configurations tested to identify whether Gd forms clusters or atomic array (P12 cases); (c), reference state of P8.

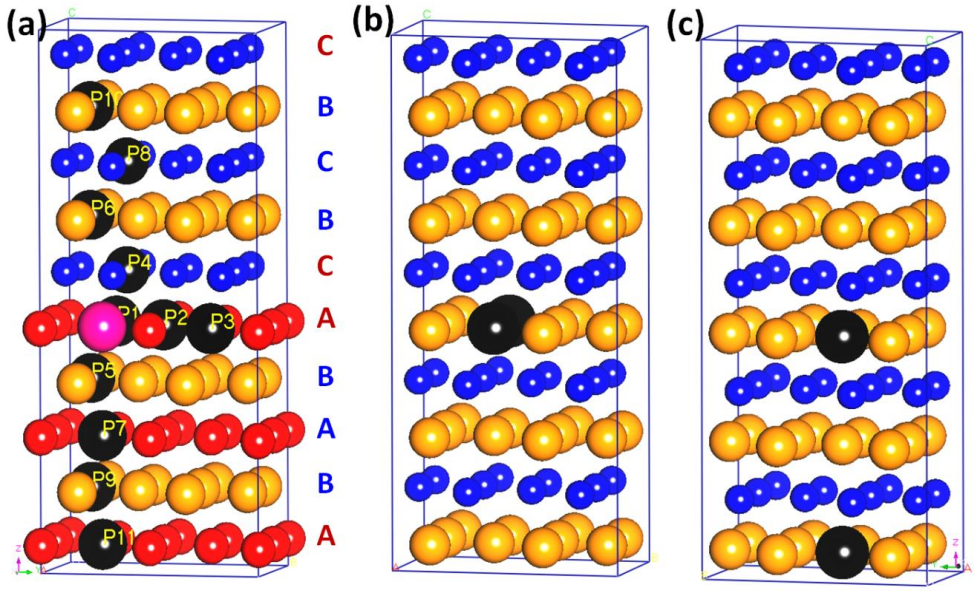

Figure 6.7. Crystal structure of Mg-10Y with 10H LPSO, (a) 12 configurations tested to identify whether Y forms clusters or atomic array (P1); (b) reference state of P1; (c) reference state of P11.

6.3. Results and Discussion

6.3.1. Application of atomic array and atomic cluster models in 6H LPSO of $Mg_{98}X_2$ (at%)

Table 6.4 and Table 6.5 summarize the lattice parameter, bulk modulus and Excess energy of atomic array in the solid solution of $Mg_{98}X_2$ (at%, X= Al, Ca, Gd, Mn, Y, Zn and Zr) without and with 6H long period stacking order, separately. According to the variation tendency of the excess energy caused by the alloying element, the energetic favorable configurations of the alloying elements in 6H LPSO together with their reference state can be captured, shown in Figure 6.8. Here, the labeled names of *HCP-Array*, *6H-A*, *6H-1B*, *6H-2B* and *6H-C* stand for the atomic array of alloying elements locating in the HCP Mg matrix, A layer of 6H, 1B layer of 6H, 2B layer of 6H and C layer of 6H. *6H-2B-cluster* means the atomic cluster of alloying element occupying the 2B layer of 6H. It can be seen that atomic arrays of Al and Y prefer to locate at the non-fault layer (A) between two fault layers in 6H while atomic arrays of Mn, Zr and Gd occupy the fault layers (1B). On the contrary, Ca and Zn atoms forming atomic clusters favor to segregate at the non-fault layer (2B) far away from the fault layer.

It is necessary to mention that the normalized excess energy by the equilibrium volume should be used to identify the energetic favorable configurations since the change of volume /lattice parameters introduces the local lattice strain, listed in Table 6.5. The reduction of local lattice strain could reduce the total energy, stabilizing the structure. For example, the segregations of Gd and Zn, or both, into the twin boundary of Mg alloy decrease the elastic strain energy and minimize the total energy, making the structure

thermodynamically stable [38]. Figure 6.9 shows the effect of atomic position in various configurations on equilibrium volume of Mg and Mg-X (X=Al, Ca, Gd, Mn, Y, Zn and Zr). It can be seen that the equilibrium volume of Mg will be increased by the formation of fault layers in 6H LPSO. With the addition of alloying element, the change of equilibrium volume of $Mg_{98}X_2$ depends on the volume of alloying element. More interestingly, the energetic favorable configuration of $Mg_{98}X_2$ always has the smallest volume difference with that of 6H of Mg, producing the minimized local lattice strain. In fact, the local lattice strain caused by the fault layers and alloying elements can be captured in the simulated selected area electron diffraction patterns. According to the Bragg's law ($2d_{hkl}\sin\theta = n\lambda$), the intensity of diffraction spots/streaks will be strengthened or weakened by lattice strain, which results in the fluctuation of distance (d_{hkl}) between two adjacent and parallel planes with a give miller indices (*h*,*k*,*l*). For example, comparing to the electron diffraction patterns of 6H LPSO in pure Mg, more diffraction pots appear in $Mg_{98}Gd_2$, which are introduced by atomic array and atomic cluster of Gd, shown in Figure 6.10. It can be seen that more diffraction spots disappear when the atomic array of Gd locates in the 2B layer of 6H, shown as the configuration of Mg98Gd2-6H-2B in Figure 6.10.

Through deformation electron density [61, 141, 163, 182], effect of alloying elements on the bond structure of LPSOs can be investigated conveniently, providing fundamental information on how alloying elements can either strengthen or weaken a Mg alloys [182]. Currently, the attributes of the bond structure and bond strength of $Mg_{98}X_2$ alloys affected by 6H LPSO and alloying element are obtained. Since the Coulomb force

is proportional to the charge distribution of the atoms and the bonding charge distribution ($\Delta\rho$), the higher of $\Delta\rho$ the stronger of the bond. Figure 6.11 shows $(100)_{s.c.}$ views of deformation electron density isosurface of 6H LPSO in $Mg_{98}X_2$ (X=Al, Y, Ca, Zn, Zr and Gd). It can be seen that the rod-like directional bonds of Mg matrix have changed into tetrahedrons in the fault layer. Alloying elements of Al, Zr, Y and Gd display the better capability in enhancing the deformation electron density in basal plane than Zn and Ca. Moreover, with the segregation of these atoms, electron distributions in the basal plane are enhanced significantly. However, around the atomic array or atomic cluster of alloying elements, the deformation electron densities are decreased in prismatic and pyramidal planes. In other words, the bond strength is increased in the basal plane but decreased in prismatic and pyramidal planes by alloying element, indicating a possible improvement of the ductility of Mg alloys through non-basal slip during deformation.

Table 6.4 Lattice parameter (a), Bulk modulus (B_0) and Excess energy of atomic array in the solid solution of $Mg_{98}X_2$ (at%). Four parameters Birch-Murnaghan (BM4) equation is applied to calculate these properties at equilibrium volume.

HCP	**Lattice Parameter**		**B_0** GPa	**Excess Energy** meV/atom	**Excess Energy** meV/ Å^3
	a Å	C-LPSO			
Mg	3.197 3.220 [a] 3.202 [b] 3.200 [c]	15.549 15.600 a 15.482b	35.6 - 36.3 [b] -	4.107	0.183
Al	3.187	15.499	36.4	-44.230	-1.987
Ca	3.219	15.629	35.1	-5.978	-0.263
Gd	3.205	15.631	35.8	-64.828	-2.859
Mn	3.164	15.483	36.6	-117.758	-5.359
Y	3.206	15.593	36.0	-102.541	-4.524
Zn	3.186	15.491	36.3	6.819	0.307
Zr	3.193	15.530	36.9	-140.769	-6.286

Note: The area of basal plane is used to estimate formation energy of atomic array.

[a] Inoue, et. al., high temperature extrusion prepared Mg-1Zn-2Y (at%) observed by HRTEM [23]
[b] Tang, et. al., first-principles calculations of with PAW-GGA (c/a=1.612) [155]
[c] Iikubo, et. al., first-principles calculations with PAW-GGA (c/a=1.624) [181]
[d] Fan, et. al., first-principles calculations with PAW-GGA [138]

Table 6.5 Lattice parameter (a), Bulk modulus (B_0) and Excess energy of atomic array in 6H long period stacking order of $Mg_{98}X_2$ (at%). Four parameters Birch-Murnaghan (BM4) equation is applied to calculate these properties at equilibrium volume.

6H LPSO	Al	Ca	Gd	Mn	Y	Zn	Zr	Note
Lattice Parameter Å (a is above C-LPSO)	3.189 15.510	3.218 15.666	3.202 15.665	3.177 15.491	3.208 15.602	3.188 15.501	3.195 15.538	**A**
	3.190 15.514	3.224 15.645	3.224 15.607	3.183 15.429	3.209 15.604	3.188 15.502	3.196 15.540	**1B**
	3.189 15.508	3.220 15.658	3.217 15.696	3.162 15.518	3.209 15.607	3.188 15.503	3.195 15.539	**2B**
	3.189 15.508	3.220 15.659	3.210 15.678	3.178 15.488	3.208 15.600	3.188 15.502	3.195 15.539	**C**
	3.189 15.510	3.220 15.669	3.205 15.665	3.165 15.511	3.209 15.607	3.187 15.500	3.196 15.540	**2B-Cluster**
Bulk modulus GPa	36.06	34.76	33.15	35.96	35.58	35.93	36.68	**A**
	35.97	34.67	35.48	36.31	35.61	35.94	36.61	**1B**
	36.04	34.77	35.55	36.31	35.56	35.92	36.57	**2B**
	36.04	34.79	35.55	35.93	35.78	36.08	36.62	**C**
	35.92	34.63	35.45	36.23	35.58	35.92	36.56	**2B-Cluster**
Excess Energy meV/atom	**-40.322**	-2.612	-58.294	-111.933	**-99.216**	10.914	-134.702	**A**
	-39.872	-1.741	**-61.483**	**-113.850**	-99.043	10.871	**-137.515**	**1B**
	-40.149	**-2.849**	-60.720	-112.396	-98.384	10.883	-134.968	**2B**
	-40.285	-2.544	-61.281	-112.769	-99.114	10.883	-135.251	**C**
	-39.689	-1.311	-60.713	-113.758	**-99.216**	**10.858**	-135.829	**2B-Cluster**
Excess Energy meV/ $Å^3$	**-1.808**	-0.115	-2.556	-5.084	**-4.365**	0.490	-6.005	**A**
	-1.788	-0.076	**-2.707**	**-5.170**	-4.362	**0.488**	**-6.131**	**1B**
	-1.799	**-0.125**	-2.670	-5.116	-4.331	0.489	-6.016	**2B**
	-1.807	-0.112	-2.698	-5.121	**-4.367**	0.489	-6.029	**C**
	-1.779	-0.057	-2.672	-5.168	-4.365	**0.488**	-6.054	**2B-Cluster**

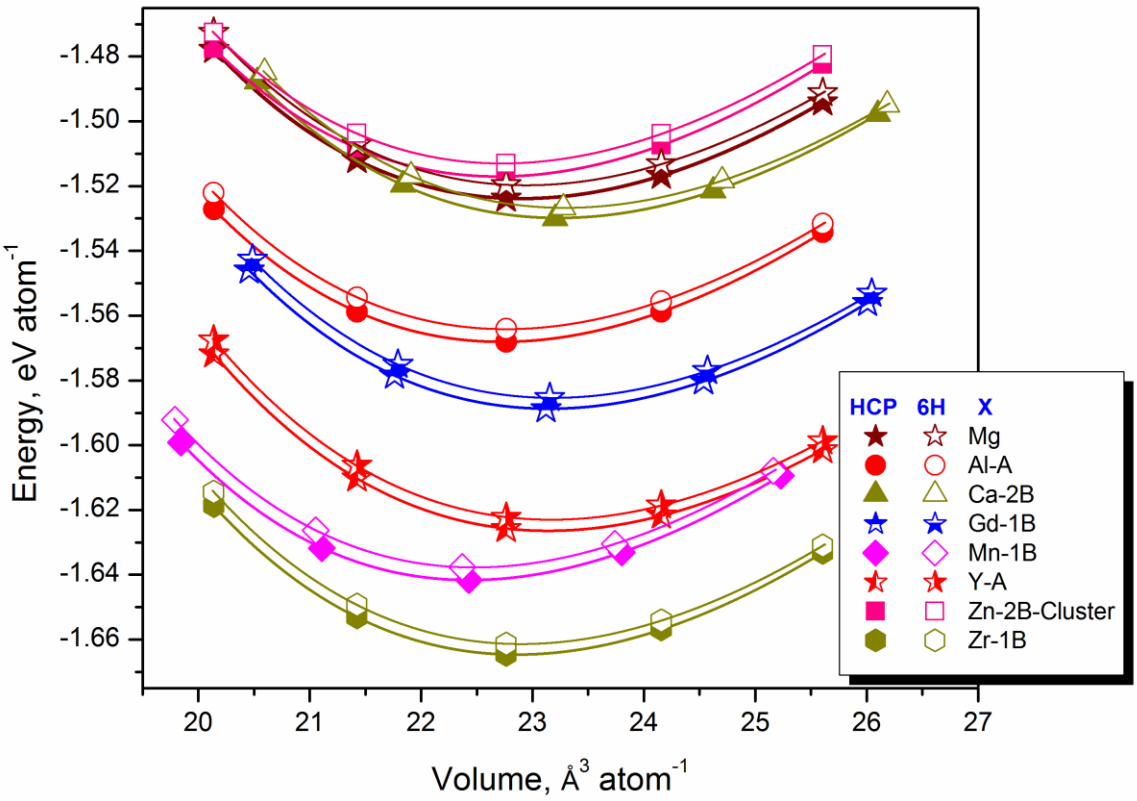

Figure 6.8 Energy-volume curve of the energetic favorable configurations of $Mg_{98}X_2$ (X=Al, Ca, Gd, Mn, Y, Zn and Zr) fitted by four-parameter Birch-Murnaghan equation.

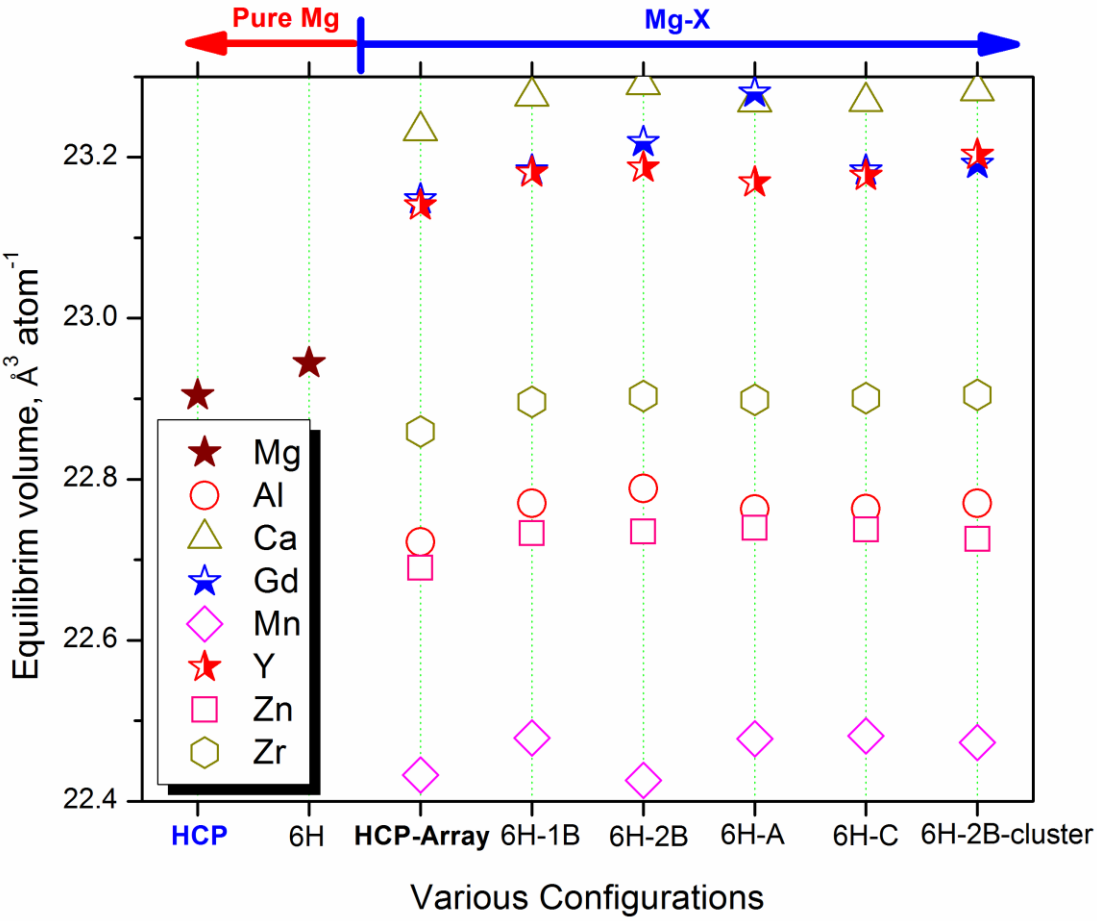

Figure 6.9 The equilibrium volume of Mg and $Mg_{98}X_2$ (X=Al, Ca, Gd, Mn, Y, Zn and Zr) with various configurations. HCP-Array, 6H-A, 6H-1B, 6H-2B and 6H-C stand for the atomic array of alloying elements locating in the HCP Mg matrix, A layer of 6H, 1B layer of 6H, 2B layer of 6H and C layer of 6H, individually. The 6H-2B-cluster means the atomic cluster of alloying element occupying the 2B layer of 6H.

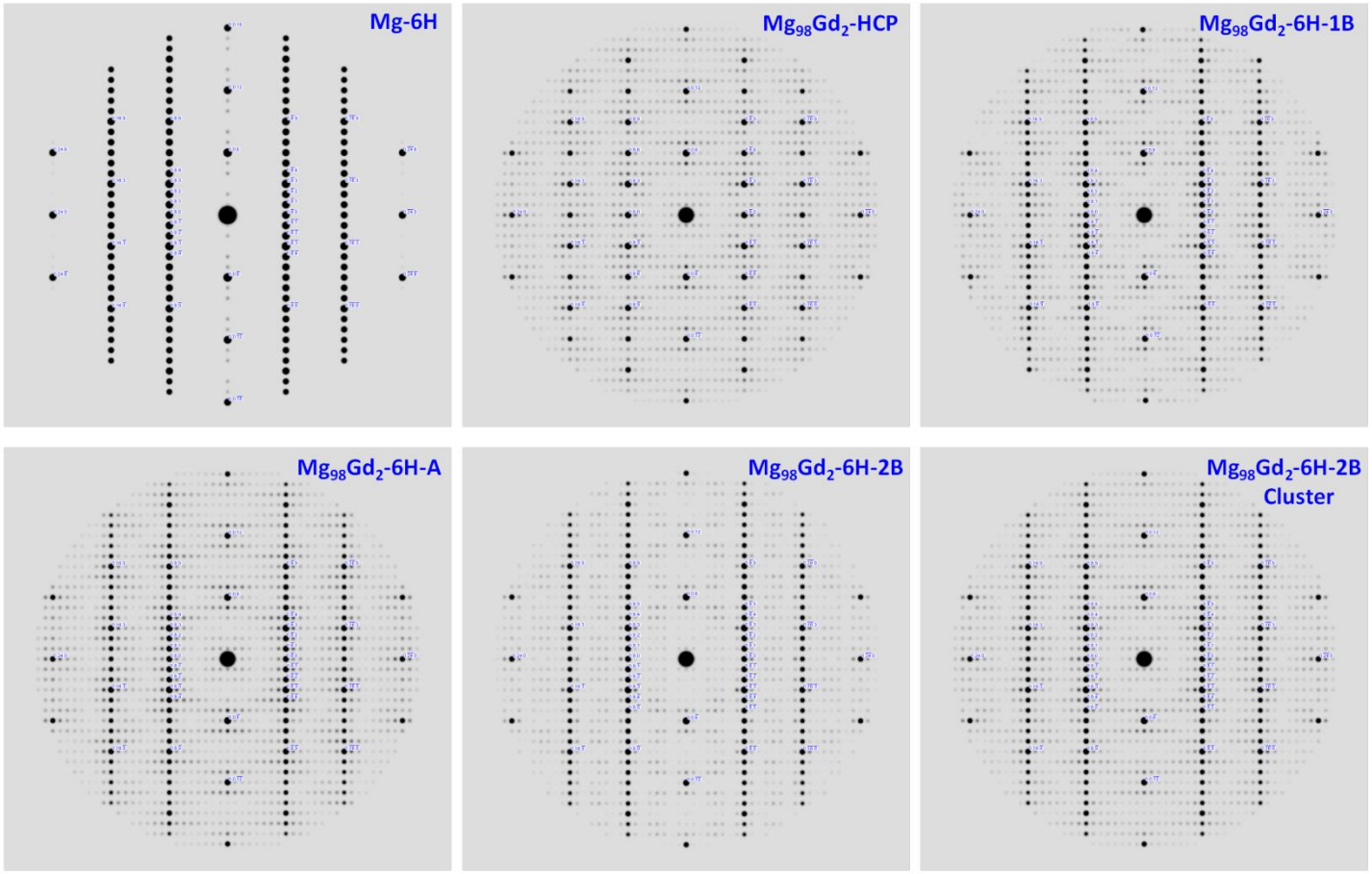

Figure 6.10. Simulated selected area electron diffraction patterns of Mg and atomic array and atomic clusters in $Mg_{98}Gd_2$ with and without 6H. The electron bean direction is parallel to $<100>_{S.C.} \| <10\bar{1}0>_{LPSO}$. The planner index is based on the orthorhombic supercell.

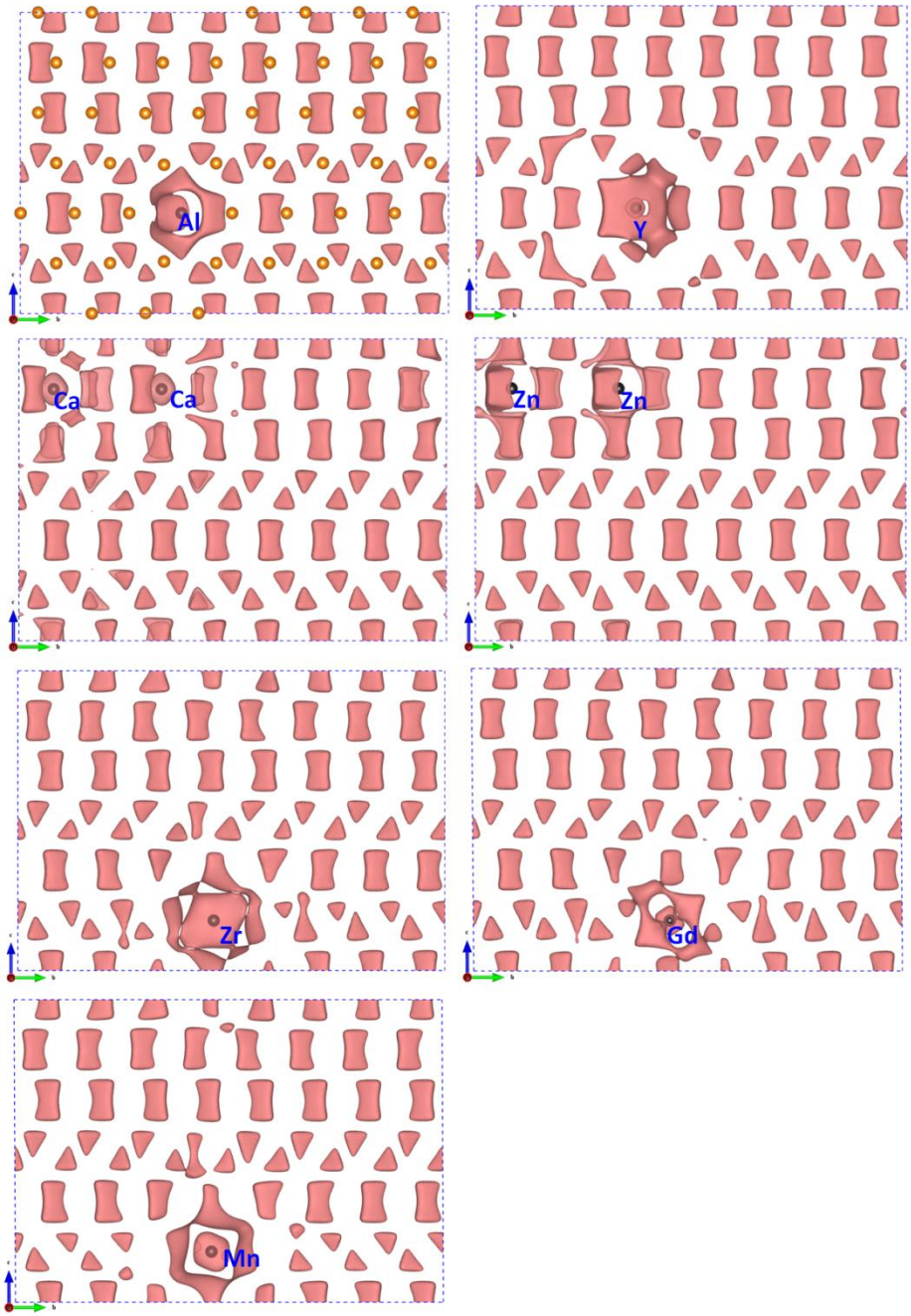

Figure 6.11. $(100)_{s.c.}$ views of deformation electron density isosurface ($\Delta\rho$=0.0021 $e^-/Å^3$) of the energetic favorable configurations in 6H LPSO of $Mg_{98}X_2$ (X=Al, Y, Ca, Zn, Zr and Gd). Positions of Mg atoms in the supercell are labeled in $Mg_{98}Al_2$ alloy while only alloying elements are displayed in black in the other alloys.

6.3.2. Bond structure of energetic favorable configurations in 6H and 10H LPSOs of Mg-10Gd (wt%)

Based on the four-parameter Birch-Murnaghan (BM4) equation (Equation 2.3), total energies of these tested 9 configurations in 6H LPSO of Mg-10Gd are obtained, shown in Figure 6.12. At the equilibrium volume, configurations numbered P7, P8 and P9 with the lower total energies than the others, being the energetic favorable configurations in 6H LPSO of Mg-10Gd. Their energy-volume curves together with their related reference state are presented in Figure 6.12(b). Hence, it can be determined that Gd atoms prefer to group together forming atomic array in 6H LPSO through Gd-Gd bonds, segregating at the non-fault layer (A) between two fault layers, shown as configuration P8 in Figure 6.4. When the Gd-Gd bonds cannot form, they will segregate at the fault layers, shown as configuration P7 in Figure 6.4. Therefore, the fault layers and its first nearest neighbor layer in 6H LPSO have the tendency to be enriched of Gd alloys in Mg-10Gd alloys. Similarly, it has been observed that Gd atoms segregate at the coherent $\{10\bar{1}1\}$ deformation twin of $Mg_{99.8}Gd_{0.2}$ (at%) and $\{10\bar{1}2\}$ twin of $Mg_{98.4}Gd_1Zn_{0.4}Zr_{0.2}$ (at%), where has the extension stress [38]. In this case, the local elastic strain energy could be reduced due to the large lattice parameter of Gd than the Mg matrix.

Figure 6.13 shows total energies of the tested 11 configurations in 10H LPSO of Mg-10Gd. Clearly, configurations numbered P7 and P8 with the lower total energies than the others, being the energetic favorable configurations. It means that Gd atoms prefer to segregate at the fault layers of 10H without forming Gd-Gd bonds. Thus, the atomic cluster model should be used in the study of 10H LPSO in Mg-Gd alloys. The

different segregation behaviors of Gd in 6H and 10H are caused by their chemical environment difference, which is the two fault layers are separated by one non-fault layer in 6H while two fault layers grouping together in 10H (shown in Figure 5.4).

The $(010)_{s.c.}$ and $(100)_{s.c.}$ views of deformation electron density isosurfaces of 6H and 10H LPSOs in Mg-10Gd are shown in Figure 6.14 and Figure 6.15, separately. It can be seen that the rod-like directional bonds of Mg matrix have changed into tetrahedrons in the fault layer. Moreover, with the segregation of Gd atoms, the deformation electron densities are decreased in prismatic and pyramidal planes around the effect zone of the Gd atoms while increased in the basal plane. Therefore, the weakened bond strength of Mg matrix in the prismatic plane by the fault layers and alloying element indicates a possible non-basal slip system could occur during deformation, which could improve the ductility of Mg alloys.

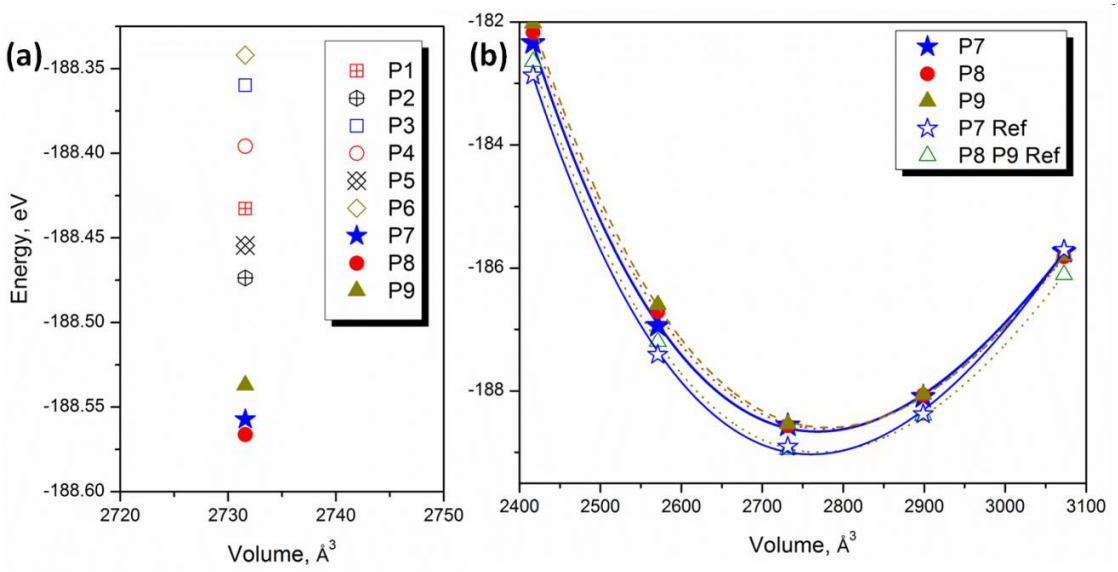

Figure 6.12. Total energies of 6H LPSO in Mg-10Gd, (a) the energy at equilibrium volume and (b) energy-volume curve of the energetic favorable configurations fitted by four-parameter Birch-Murnaghan (BM4) equation.

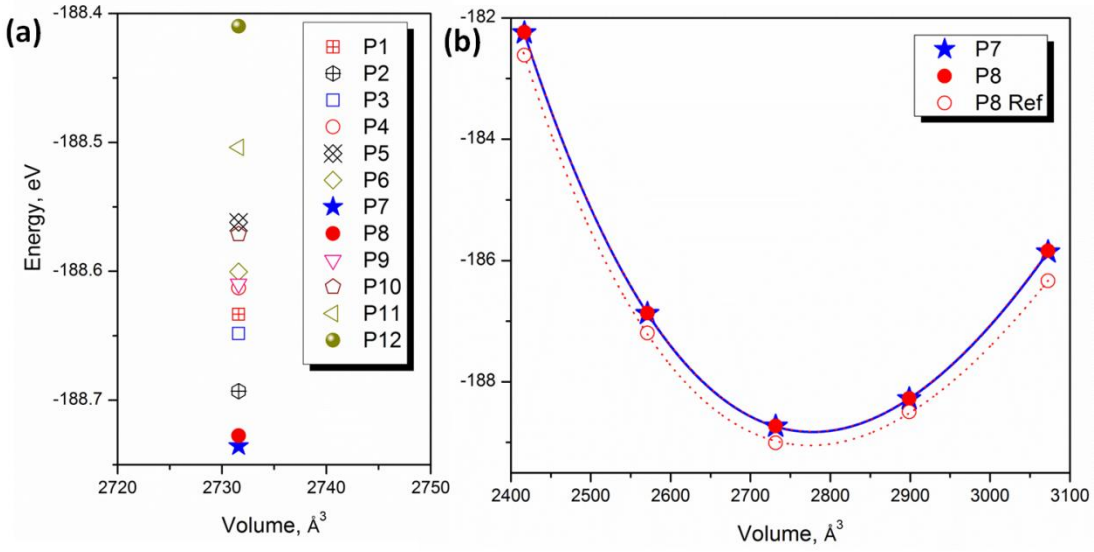

Figure 6.13. Total energies of 10H LPSO in Mg-10Gd, (a) the energy at equilibrium volume and (b) energy-volume curve of the energetic favorable configurations fitted by four-parameter Birch-Murnaghan (BM4) equation.

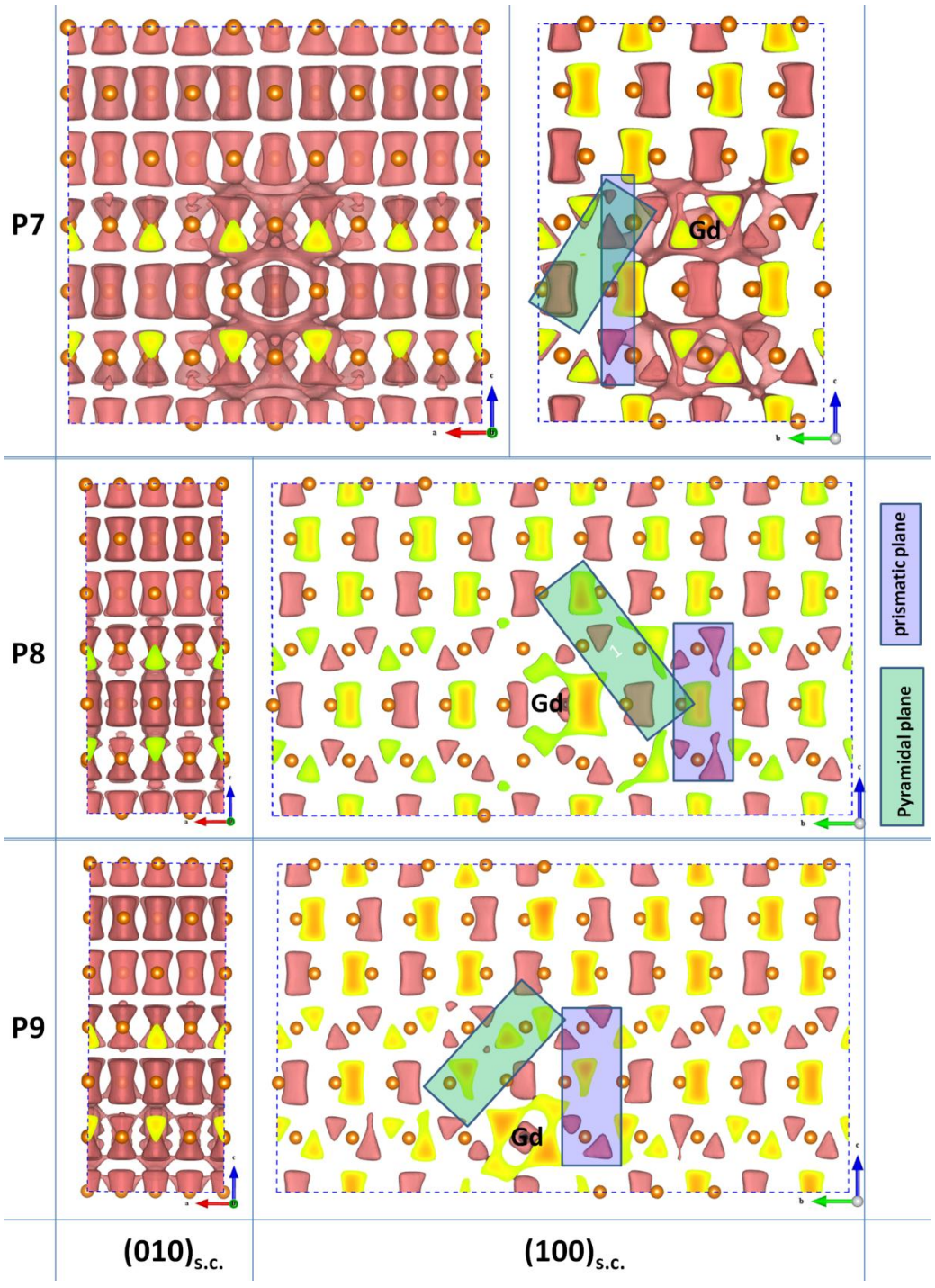

Figure 6.14. $(010)_{s.c.}$ and $(100)_{s.c.}$ views of deformation electron density isosurface ($\Delta\rho$=0.0021 $e^-/Å^3$) Mg-10Gd with 6H LPSO. The atoms of alloying element Gd are highlighted.

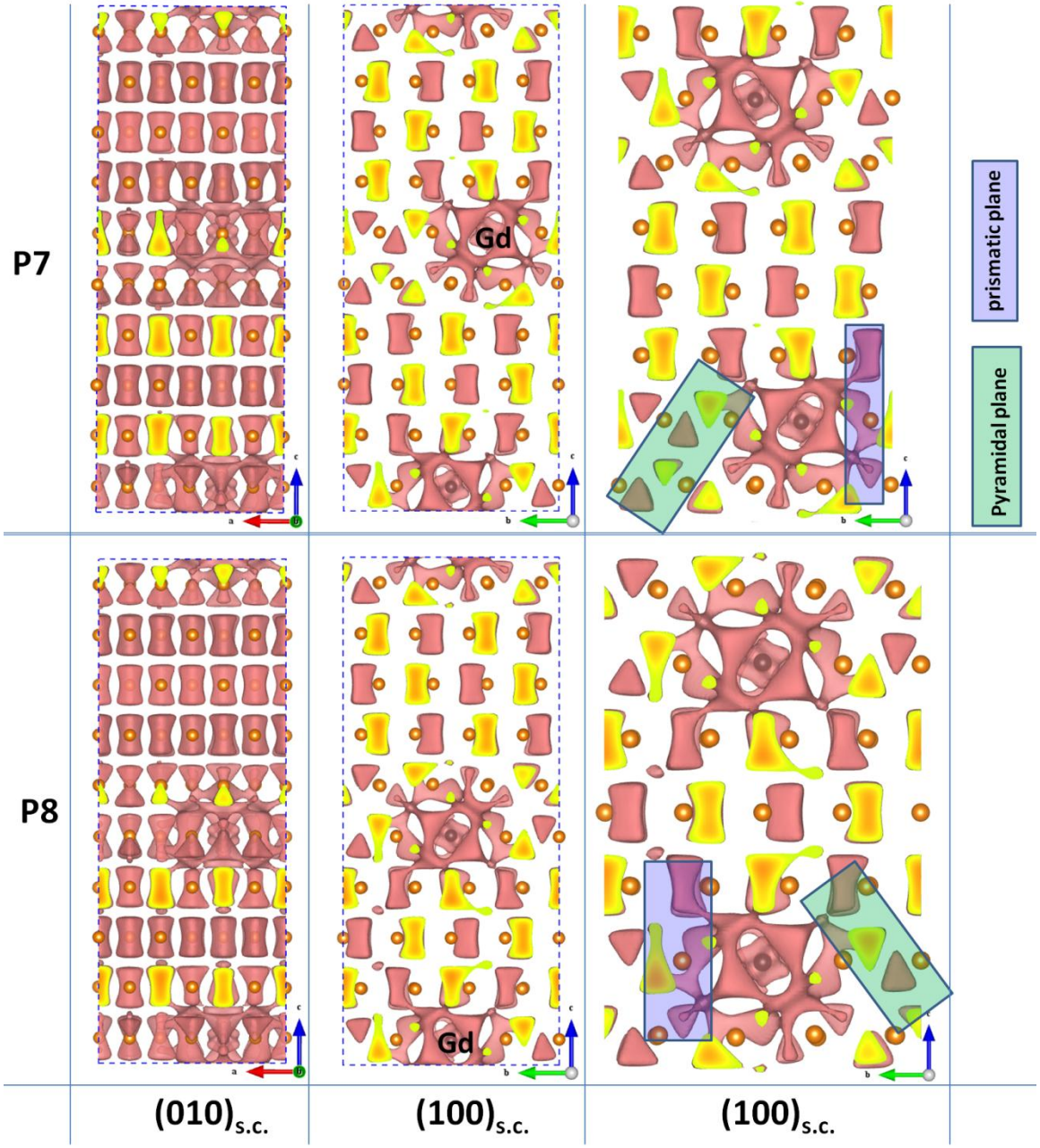

Figure 6.15. $(010)_{s.c.}$ and $(100)_{s.c.}$ views of deformation electron density isosurface ($\Delta\rho$=0.0021 $e^-/Å^3$) Mg-10Gd with 10H LPSO. The atoms of alloying element Gd are highlighted in black. The third column is the rearrangement of the third according to the periodic boundary conditions.

6.3.2. Bond structure of energetic favorable configurations in 6H and 10H LPSOs of Mg-10Y (wt %)

Figure 6.16 shows total energies of these tested 9 configurations in 6H LPSO of Mg-10Y. At the equilibrium volume, the configurations numbered P4 and P7 with the lower total energies than the others, being the energetic favorable configurations in 6H LPSO of Mg-10Y. Similarly, the energetic favorable configurations in 10H LPSO of Mg-10Y are P6 and P11, shown in Figure 6.17. It is worth to mention that the total energy of configuration with atomic array of Y is always in the middle range in both 6H and 10 LPSOs. Thus, it can be estimated that Y atoms prefer to segregate at the fault layer and its first neighbor non-fault layer and have the tendency to form cluster in 6H and 10H LPSOs.

The $(010)_{s.c.}$ and $(100)_{s.c.}$ views of deformation electron density isosurface of 6H and 10H LPSOs in Mg-10Gd are shown in Figure 6.18 and Figure 6.19, separately. It can be seen that the bond strength of Mg matrix in the prismatic and pyramidal planes are weakened by the segregation of Y atoms while strengthened in the basal plane. Y could be the good alloying element improving ductility of Mg alloys by introducing the possible non-basal slip during deformation.

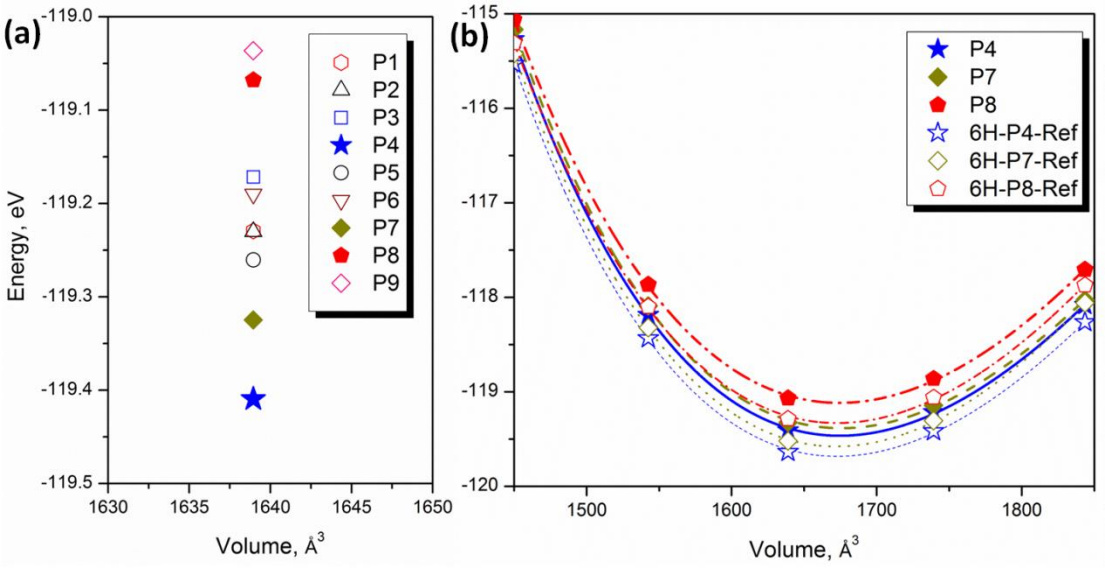

Figure 6.16. Total energies of 6H LPSO in Mg-10Y, (a) the energy at equilibrium volume and (b) energy-volume curve of the energetic favorable configurations fitted by four-parameter Birch-Murnaghan (BM4) equation.

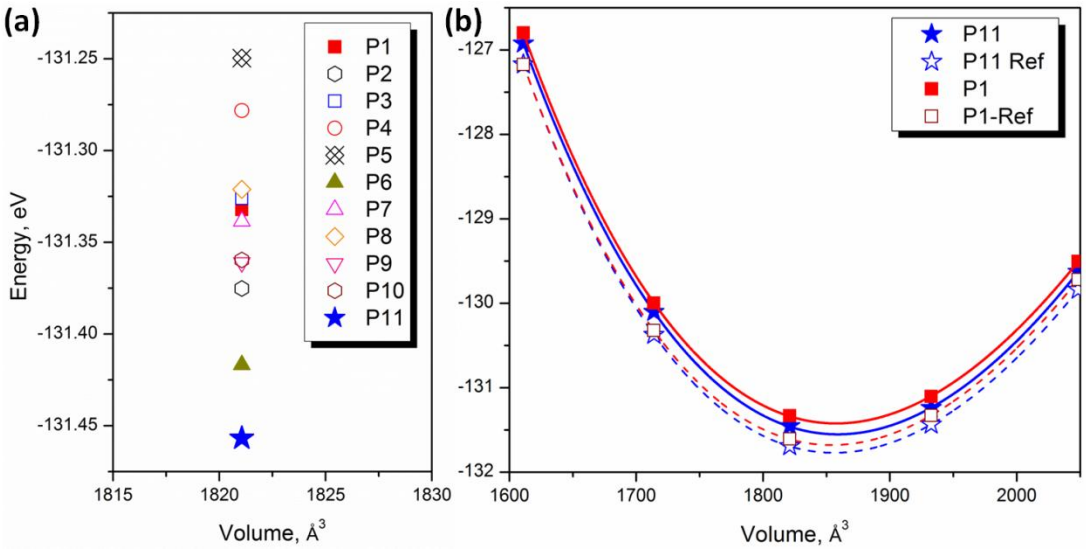

Figure 6.17. Total energies of 10H LPSO in Mg-10Y, (a) the energy at equilibrium volume and (b) energy-volume curve of the energetic favorable configurations fitted by four-parameter Birch-Murnaghan (BM4) equation.

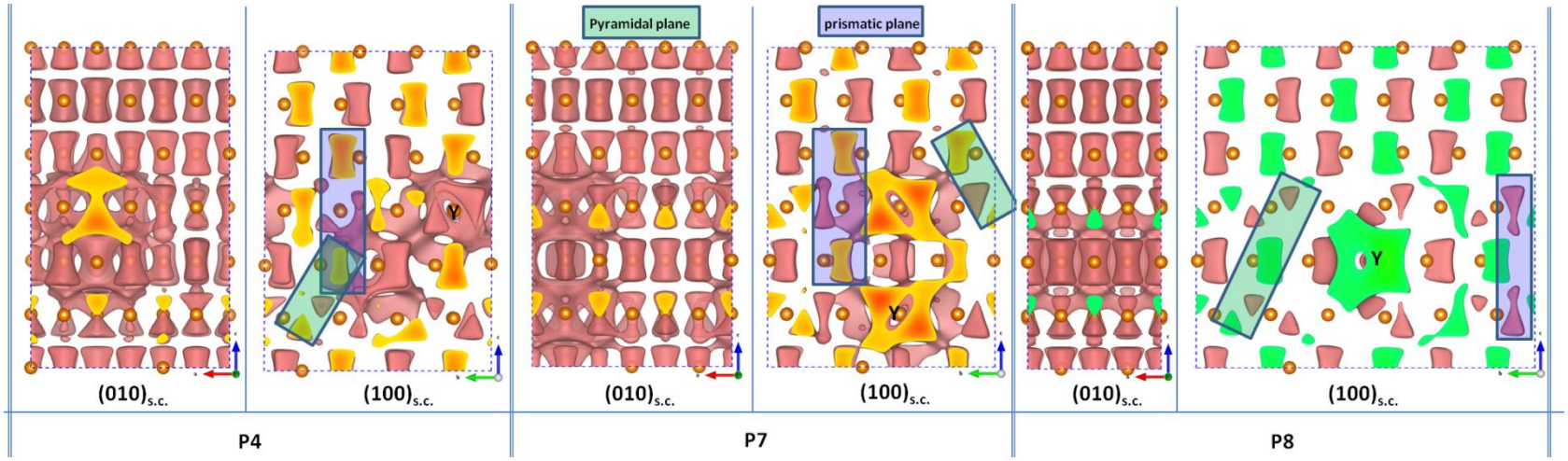

Figure 6.18. $(010)_{s.c.}$ and $(100)_{s.c.}$ views of deformation electron density isosurface ($\Delta\rho$=0.0021 $e^-/Å^3$) Mg-10Y with 6H LPSO. The atoms of alloying element Y are highlighted.

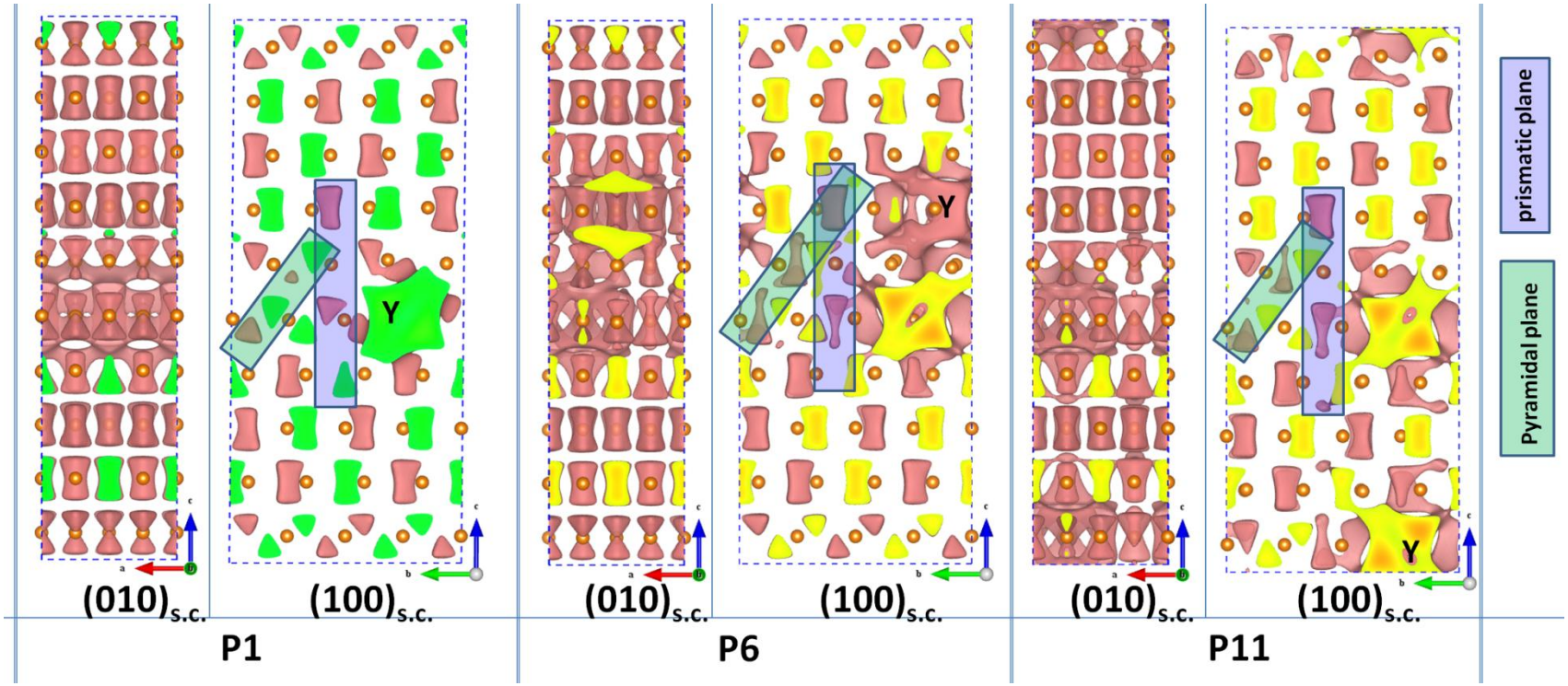

Figure 6.19. $(010)_{s.c.}$ and $(100)_{s.c.}$ views of deformation electron density isosurface ($\Delta\rho$=0.0021 $e^-/Å^3$) Mg-10Y with 10H LPSO. The atoms of alloying element Y are highlighted out.

6.4. Conclusion

In summary, the segregation behavior of the alloying elements (X=Al, Ca, Gd, Mn, Y, Zn and Zr) in 6H LPSOs of $Mg_{98}X_2$ (at%) has been estimated through the proposed atomic array and atomic cluster models. In the view of excess energy caused by the contributions of alloying elements and fault layers, it can be seen that atomic arrays of Al and Y prefer to locate at the non-fault layer (A) between two fault layers in 6H while atomic arrays of Mn, Zr and Gd occupy the fault layers (1B). On the contrary, Ca and Zn atoms forming atomic clusters favor to segregate at the non-fault layer (2B) far away from the fault layer. In view of deformation electron density, the attributes of the bond structure and bond strength of $Mg_{98}X_2$ alloys affected by the 6H LPSO and the alloying element are captured. Alloying elements of Al, Zr, Y and Gd display the better capability in enhancing the deformation electron density in basal plane of 6H LPSO than Zn and Ca. Moreover, with the segregation of these atoms, electron distributions in the basal plane are enhanced significantly. However, around the atomic array or atomic cluster of alloying elements, the deformation electron densities are decreased in prismatic and pyramidal planes. In other words, the bond strength is increased in the basal plane but decreased in prismatic and pyramidal planes by alloying element, indicating a possible improvement of the ductility of Mg alloys through non-basal slip during deformation.

The validation of atomic array and atomic cluster models are further estimated in 6H and 10H LPSOs of Mg-10Gd (wt%) and Mg-10Y, discussing the segregation behavior of rare earth elements in LPSOs and their effect on the formability of LPSOs. It

has determined that Gd atoms prefer to group together forming atomic array in 6H LPSO through Gd-Gd bonds, segregating at the non-fault layer (A) between two fault layers. When the Gd-Gd bonds cannot form, they will segregate at the fault layers, indicating the fault layers and its first nearest neighbor layer in 6H LPSO have the tendency to be enriched of Gd alloys in Mg-10Gd alloys. In 10H LPSO, Gd atoms prefer to segregate at the fault layers without forming Gd-Gd bonds. This difference segregation behavior of Gd in 6H and 10H is caused by their chemical environment difference, which is the two fault layers are separated by one non-fault layer in 6H while two fault layers grouping together in 10H. Similarly, the Y atoms prefer to segregate at the fault layer and its first neighbor non-fault layer and have the tendency to form cluster in 6H and 10H LPSOs of Mg-10Y. Furthermore, bond strength of Mg matrix in the prismatic and pyramidal planes are weakened by the segregation of Gd and Y atoms while strengthened in the basal plane. The Gd and Y atoms could be the good alloying element improving ductility of Mg alloys by introducing the possible non-basal slip during deformation.

Chapter 7

Atomic Array/Cluster Nanoprecipitates of Alloying Elements in 6H and 10H LPSOs of Ternary Mg Alloys

7.1. Introduction

As mentioned before, works focusing on the segregation behavior of solute atoms are important to optimize the microstructure and to improve the mechanical properties of Mg alloys [30, 33, 35-40]. In the development of advanced Mg-Zn-Y alloys, effect of LPSOs and its enrichment of solute atoms on electronic structure and elastic properties of Mg remain ambiguous. According to the stacking sequence of close packed atomic planes (basal planes), several types of LPSOs in Mg-Zn-Y alloys have be experimentally determined, which are 6H [23, 33, 120, 166], 10H [167-169], 14H [25, 26, 29, 124, 169], 18R [25, 26, 29, 124, 168, 170, 171] and 24R [123, 169]. The significant features of the atomic arrangement in those LPSOs are (i) FCC-type stacking sequence ($A\dot{B}\dot{C}A$) indicates two fault layers (letters with dots above) within four atomic layers in 10H, 14H, 18R and 24R; (ii) a mirror plane with the stacking sequence of three atomic layers ($A\dot{B}C$) exists in 6H ($BC\dot{B}A\dot{B}C$); and (iii) solute atoms of Zn and Y prefers to segregated around these fault layers (letters with dots). For example, through the high angle annular dark field TEM imaging, it is demonstrated that a simple chemical ordering structure of Zn and Y forms by occupying every $A\dot{B}$ layers in the 6H LPSO of

$Mg_{97}Y_2Zn_1$ (at%) alloy [33, 120]. The ordered arrangement of Zn and Y in two fault layers of the FCC-type building blocks of 14H and 18R in Mg-8Y-2Zn-0.6Zr (wt. %) has been estimated and supported by the appearance of some unique reflections or intensity maxima in electron diffraction pattern [124]. On the contrary, a $L1_2$-type (TM_3RE_4) cluster precipitated in short range of 18R LPSOs has been proposed in $Mg_{85}Y_6Zn_9$ (at%) [116] and $Mg_{89}Y_4Zn_7$ (at%) [117]. Although the local occupation behavior of solute atoms in 14H and 18R LPSOs could be effectively discussed by the $L1_2$-type (TM_3RE_4) cluster model, the essential condition for the application of this model is to assume the stoichiometric LPSO structures incorporate few extra TM_3RE_4 clusters, which results in the concentration of solute atoms in LPSOs is higher than that of in HCP stacking layers [29]. In other words, the concentrations of Zn and Y in 14H and 18R LPSO are fixed in the ratio of 3/4. Accordingly, more non-stoichimetric Zn_mY_n(Mg) clusters derived from Zn_6Y_9 have been proposed in the study of 14H and 18R LPSO structures [119].

In fact, various compositions of Zn and Y in LPSO structures of Mg-Zn-Y alloys have been experimentally observed and cannot be considered to be ideal stoichiometric one in a fixed ratio of Zn/Y, i.e. $Mg_{100-x}Zn_{2\pm1}Y_{4\pm2}$ [33], $Mg_{87}Zn_3Y_{10}$ [120] for 6H, $Mg_{87}Zn_7Y_6$ [32], $Mg_{94}Zn_2Y_4$ [29], $Mg_{86}Zn_7Y_7$ [121] for 14H, $Mg_{91}Zn_3Y_6$ [32], $Mg_{85}Zn_6Y_9$ [29], $Mg_{84}Zn_8Y_8$ [121] and $Mg_{100-x}Zn_{13.7\pm1}Y_{7.5\pm1}$ [122]. Therefore, more works are required to reveal the segregation behavior of solute atoms in LPSOs and the stabilities of the microstructures generated by those models are still under investigation. Particularly, segregation behavior of the solute atoms and their contributions on the formability and the electronic structures of 6H LPSOs have not been reported in Mg alloys. Base on the previous results shown in Chapter 6, the arrangement of alloying

element in the ternary Mg alloys will be estimated via atomic array and atomic cluster models, deducing the order/disorder structure of alloying elements in LPSOs of Mg alloys.

Moreover, Mg-Gd based high strength casting alloys containing Zn and Zr present excellent mechanical properties. For instance, the hardness at 498K, elongation, yield strength and ultimate tensile strength at 473K of $Mg_{96.1}Gd_{3.2}Zn_{0.5}Zr_{0.2}$ alloy (0.5GZ) [44] are 138 HV, 7.5%, 280 MPa and 390 MPa. It is worth to mention that the high tensile strength of about 400 MPa of 0.5GZ alloy could be kept up to 473K. The $Mg_{95.85}Gd_{2.0}Y_{1.2}Zr_{0.75}Zr_{0.2}$ alloy [183] with 14H LPSO shows high toughness and excellent ultimate tensile strength, which could reach more than 400 MPa. Recently, Mg-8.5Gd-2.3Y-1.8Ag-0.4Zr (wt%) alloy with nano-spaced stacking faults produced a yield strength of ~575 MPa, an ultimate strength of ~600 MPa, and a uniform elongation of ~5.2 %. [34] The strengthen mechanism to make Mg ultrastrong is the reduction of stacking fault energy enable the introduction of high density of stacking fault, which impeded dislocation slip and promoted dislocation accumulation [34]. Therefore, it is essential to study the segregation behavior of the selected alloying element (such as Zn and Zr) in the LPSOs in order to design the advance Mg alloys with high strength and good ductility.

In this chapter, contributions of alloying elements and fault layers to the energy, electronic structure and elastic properties of 6H and 10H LPSOs in the ternary $Mg_{97}Zn_1Y_2$ and Mg-Gd-TM (TM=Zn and Zr) alloys are discussed through our introduced atomic array/cluster model discussed in Chapter 6. These two models simplify the investigation of interactions among various elements and fault layers in LPSOs, yielding

the energetic favorable configurations and explaining the segregations behaviors of alloying elements in Mg alloys.

7.2. Computational Details

In the present first-principles calculations, the orthorhombic supercell sizes of 6H LPSO structure of $Mg_{97}Y_2Zn_1$ (at %) alloy is $2a \times 4\sqrt{3}a \times 3c$ with 96 atoms, where a and c are the theoretical lattice parameters of primitive hcp Mg and an orientation relationship of $\langle 01\bar{1}0\rangle_{\text{hcp}} \parallel \langle 100\rangle_{\text{s.c.}}$, $\langle 1\bar{2}10\rangle_{\text{hcp}} \parallel \langle 010\rangle_{\text{s.c.}}$, and $\langle 0001\rangle_{\text{hcp}} \parallel \langle 001\rangle_{\text{s.c.}}$. Through estimating whether a bond between alloying elements form, the atomic array and the atomic cluster models are generated.

Calculations of electronic structures and energies at 0 K are carried out by means of the Vienna ab initio simulation package [90, 91] with the generalized gradient approximation [133] for the exchange-correction functional and the projector augmented wave [134] for the electron-ion interaction. The wave functions are sampled on Γ-centered Monkhorst-Pack grids of 9×3×4, generated automatically with a scaling length l=60. The plane wave cutoff energy is set as 300 eV, i.e. 1.4 times the default cutoff energy for accurate calculations, and the energy convergence criterion of electronic self-consistency is 10^{-6} eV/atom. While the structures are fully relaxed by the Methfessel-Paxton technique [135], the final total energy calculations are performed by the tetrahedron method incorporating Blöchl correction [156]. Procedures obtaining

deformation electron density (Δρ) and the HRTEM images in this work are as same as that described in the methodology part in Chapter 3.

Four-parameter Birch-Murnaghan equation of states [58-60] is used to describe the relation between energy and volume. Elastic constants calculated by first-principles calculations are obtained by using the efficient strain-stress method [77, 78]. The bulk, Young's (E) and shear moduli (G) of the orthorhombic structure can be derived from the calculated first-principles elastic constants through Voigt's method [79, 80]

The formation energy of 6H LPSO structure, γ_{6H} , can be obtained through

Equation 7.1 $$\gamma_{6H} = \frac{1}{A}(E_{6H} - E_{Bulk})$$

where E_{6H} and E_{Bulk} are the total energies of supercells with and without LPSO structures, respectively, and A is the area of basal plane of supercells. Taking the energy of pure Mg as the reference, the excess energy of atomic array (or atomic cluster) structure of alloying elements in 6H LPSO and bulk structure ($\Delta E_{6H}(X)$ and $\Delta E_{Bulk}(X)$) are expressed as

Equation 7.2 $$\Delta E_{6H}(X) = E_{6H}(Mg_{n-m}X_m) - E_{6H}(Mg_n)$$

Equation 7.3 $$\Delta E_{Bulk}(X) = E_{Bulk}(Mg_{n-m}X_m) - E_{Bulk}(Mg_n)$$

where $E_{6H}(Mg_{n-m}X_m)$ and $E_{Bulk}(Mg_{n-m}X_m)$ are the total energy of atomic array (or atomic cluster) in $Mg_{n-m}X_m$ alloy; *m* and *n* are the number of solute atoms and the total number of atoms in the supercell.

7.3. Results and Discussions on $Mg_{97}Zn_1Y_2$

7.3.1. Excess energy of atomic array of Zn and Y in 6H LPSO

Through four parameters Birch-Murnaghan equation of state, total energy of Mg, $Mg_{98}Y_2$, $Mg_{98}Zn_2$ and $Mg_{97}Zn_2Y_1$ (at%) with various configurations as a function of volume can be obtained, shown in Figure 7.1. Total energy of energetic favorable configurations of $Mg_{98}Y_2$ and $Mg_{97}Zn_2Y_1$ (at%) with 6H LPSOs as a function of volume are presented in Figure 7.1(f). The present predicted formation energy of 6H LPSO in Mg is 44.6 mJ/m^2, matching well with previous reported data (44.1 mJ/m^2) [155]. In $Mg_{98}Y_2$ alloy, through comparing the total energies of these configurations generated by atomic array and atomic cluster models shown in Figure 7.1(b), it can be seen that atoms array of Y prefer to segregations in the A layer. In the view of excess energy listed in Table 7.1, it is energetic favorable to form atomic array of Y in $Mg_{98}Y_2$ since the excess energy $\Delta E_{6H}(Y)$ is smaller than $\Delta E_{Bulk}(Y)$, indicating the strong interaction existing among Y atoms in $Mg_{98}Y_2$ alloy. It is necessary to point out that the configuration of atomic array of Y in A layer (named 6H-A) should be applied in the work of $Mg_{97}Zn_1Y_2$ alloy instead of the 6H-C although its excess energy is smaller than that of 6H-A. The reasons are (i) the excess energy of 6H-A is smaller than 6H-C although equilibrium volume normalized excess energies is larger than that of 6H-C; and (ii) the atomic

morphology of 6H-A is more close to the experimental observations that is alloying elements prefers occupying every A$\dot{B}$ layers in the 6H LPSO of $Mg_{97}Y_2Zn_1$ (at%) alloy [33].

In $Mg_{98}Zn_2$ alloy, the total energies of atomic array in 1B layer (6H-1B (Array)) and atomic cluster in 2B layer (6H-2B (Cluster)) from first-principles calculations are almost identical, shown in Figure 7.1(d). According to the four-parameter Birch-Murnaghan equation of states fitting, the excess energy of 6H-2B (Cluster) is the smallest than the others, listed in Table 7.1. Comparing with excess energy of HCP-Array, the excess energy will be increased by forming atomic array and atomic cluster of Zn in 6H LPSO, which means the pre-existing structure of Zn in the bulk Mg dominated the final segregation behavior of Zn in 6H LPSO. As mentioned in previous experimental results, it has pointed that certain amount of Y and Zn – particularly Zn - is essential to form the 6H LPSO and the precipitation has occurred for the pre-existing (Zn, Y)-rich Mg solid solution [33]. The present results provide the direct evidence in view of excess energy caused by alloying Zn.

To deduce the ordered/disordered structure of Zn and Y in the laminar structure (A$\dot{B}$ layers) of 6H LPSO, nine configurations (shown in Figure 7.3(d)) displaying positions of Zn are required since atoms array of Y prefer to segregations in the A layer. As shown in Figure 7.1(e), the total energy is significantly decreased when Zn locating at the first nearest neighbor of atomic array of Y (labeled as P5) comparing with the other configurations. Thus, the most energetic favorable configuration with arranging ordered

alloying elements of Zn and Y has been estimated in $Mg_{97}Zn_1Y_2$ alloy, which is the atomic array of Y with Zn occupying its 1st nearest neighbor (6H-A-P5), shown in Figure 7.2. The present predicted morphology of enrichment of Zn and Y in 6H LPSO matches well with previous 3D atom probe characterization of the local chemistry of $Mg_{97}Zn_1Y_2$ alloy, which is the Y and Zn occurs in one or two atomic layers in the unit cell of 6H LPSO [120]. Furthermore, as listed in Table 7.1, the present predicted lattice parameters of $Mg_{97}Zn_1Y_2$ alloy via atomic array model agree with previous reported data [155]. With the formation of atomic array of Y in A layer of 6H LPSO, the lattice parameters, $\boldsymbol{a}$ and $\boldsymbol{C_{LPSO}}$, are increased from 3.197 Å and 15.549 Å to 3.208 Å and 15.604 Å, separately, which is due to the atomic radius of Y is larger than that of Mg. On the contrary, lattice parameters, $\boldsymbol{a}$ and $\boldsymbol{C_{LPSO}}$, are decreased with the addition of Zn into Mg matrix with 6H LPSO. Thus, the lattice mismatch of $Mg_{97}Zn_1Y_2$ alloy with atomic array of Y and Zn (6H-A-P5) to Mg with 6H LPSO is limited, resulting in almost no lattice strain since the lattice parameters change very small. In particular, $\boldsymbol{a}$ and $\boldsymbol{C_{LPSO}}$ are enhanced from 3.197 Å and 15.549 Å of Mg to 3.201 Å and 15.567 Å of $Mg_{97}Zn_1Y_2$ (6H-A-P5).

Table 7.1. Lattice parameter (a), formation energy (γ_{6H}) of 6H LPSO of Mg and excess energy (γ'_{Array}) of atomic array of alloying element in Mg alloys (at%). Four parameters Birch-Murnaghan (BM4) equation is used to obtain a and γ_{LPSO}.

	Structure	**Lattice Parameter**		**Excess Energy** (meV/atom)	**Excess Energy** (meV/Å^3)
		a (Å)	C_{LPSO} (Å)		
Mg	6H	3.197 3.202 [a] 3.200 [b]	15.549 15.482[a] 15.601[b]	4.107	0.183
$Mg_{98}Y_2$	HCP-Array	3.206	15.593	-102.541	-4.524
	6H-A	3.208	15.602	-99.216	-4.365
	6H-1B	3.209	15.604	-99.043	-4.362
	6H-2B	3.209	15.607	-98.384	-4.331
	6H-C	3.208	15.600	-99.114	-4.367
	6H-2B-Cluster	3.209	15.607	-99.216	-4.365
$Mg_{98}Zn_2$	HCP-Array	3.186	15.491	6.819	0.307
	6H-A	3.188	15.501	10.914	0.490
	6H-1B	3.188	15.502	10.871	0.488
	6H-2B	3.188	15.503	10.883	0.489
	6H-C	3.188	15.502	10.883	0.489
	6H-2B-Cluster	3.187	15.500	10.858	0.488
$Mg_{97}Zn_1Y_2$	HCP-Array	3.201	15.567	-100.195	-4.442
	6H-A-P5	3.202 3.220 [c] 3.20 [d]	15.574 15.600 [c] 15.60 [d]	-96.741	-4.285

Note: The area of basal plane is used to estimate formation energy of atomic array.
[a] Tang, et. al., first-principles calculations of with PAW-GGA (c/a=1.612) [155]
[b] Iikubo, et. al., first-principles calculations with PAW-GGA (c/a=1.624) [181]
[c] Inoue, et. al., high temperature extrusion prepared Mg-1Zn-2Y (at%) observed by HRTEM [23]
d Abe, et al., experimental estimated concentration of 6H LPSO is to be $Mg_{95}(Zn, Y)_5$ in $Mg_{97}Zn_1Y_2$ [33]

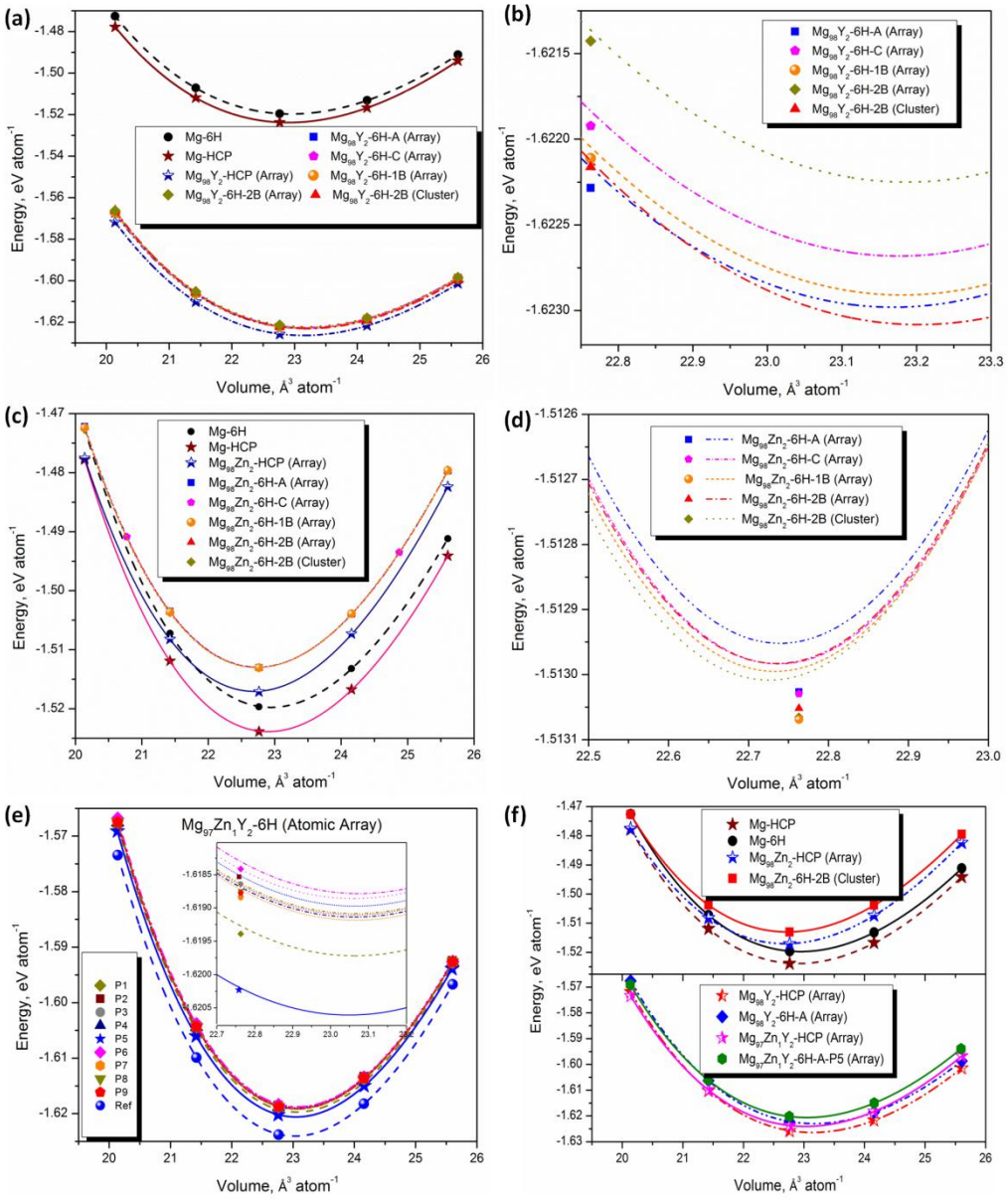

Figure 7.1 Total energy as a function of volume fitted by four parameters Birch-Murnaghan (BM4) equation of energetic favorable configurations of $Mg_{98}Zn_2$, $Mg_{98}Y_2$ and $Mg_{97}Zn_2Y_1$ (at%) with 6H LPSOs, (a) and (c) total energy of bulk Mg and $Mg_{98}Y_2$ with 6H LPSO; (b) and (d) total energy of $Mg_{98}Y_2$ and $Mg_{98}Zn_2$ at equilibrium volume; (e) total energy of various configurations of $Mg_{97}Zn_2Y_1$; and (f) comparation of energies for energetic favorable configurations of $Mg_{98}Zn_2$, $Mg_{98}Y_2$ and $Mg_{97}Zn_2Y_1$..

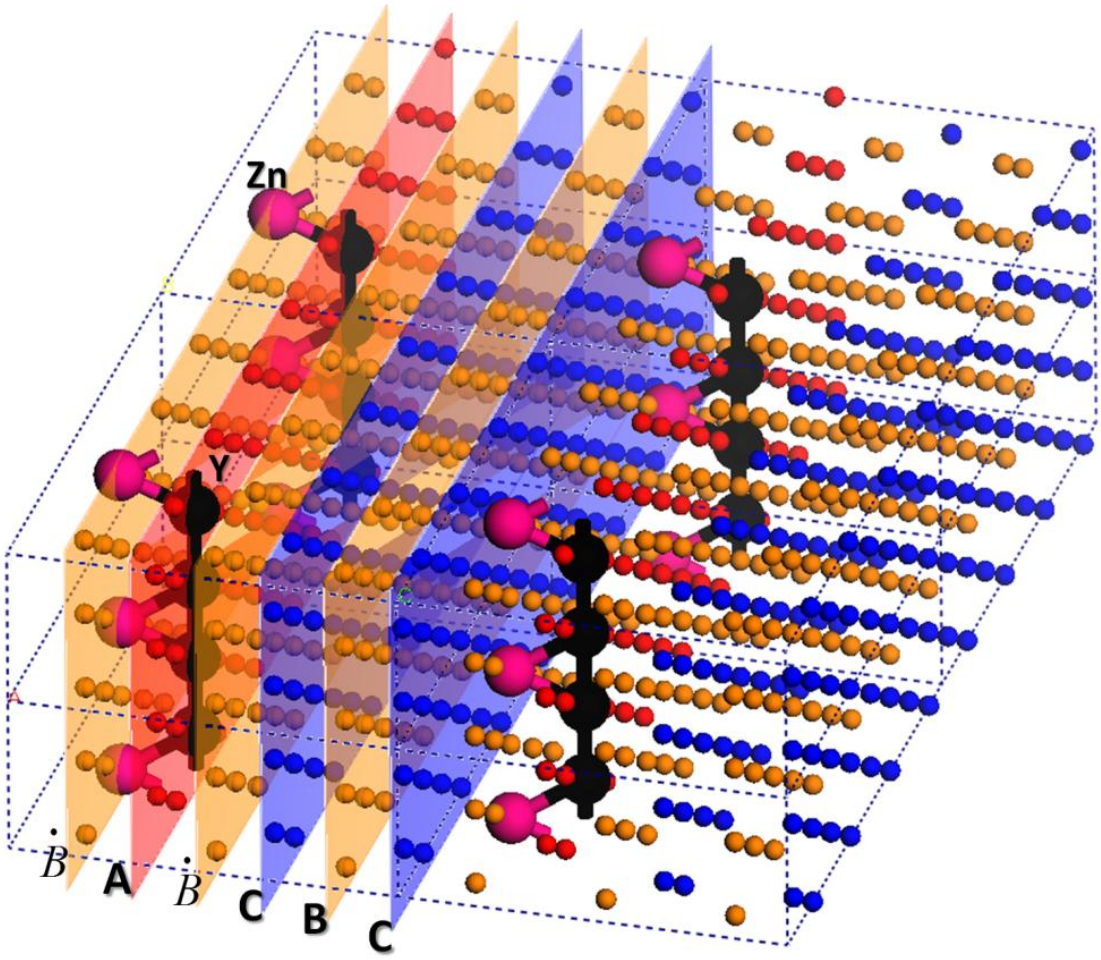

Figure 7.2. 3D view of the energetic favorable positions for alloying elements Zn and Y in $Mg_{98}Zn_2Y_1$ (at%) with 6H LPSOs. It displays that Y prefers to occupy the non-fault A layer while Zn to occupy the first nearest neighbor of Y in the fault layer labeled as $\dot{B}$.

7.3.2 Bond structure and strength affected by solute atoms and fault layers

Through deformation electron density [61, 141, 163, 182], effect of alloying elements on the bond structure of stacking faults can be investigated conveniently, providing fundamental information on how alloying elements can either strengthen or weaken a Mg alloys [182]. Currently, bond structure and strength of $Mg_{97}Zn_1Y_2$ alloy affected by 6H LPSO and alloying elements (Zn and Y) are obtained through investigating the deformation electron density and electron localization function (ELF). Isosurfaces of the deformation electron density (corresponding to $\Delta\rho_{max}$) of Mg, $Mg_{98}Zn_2$, $Mg_{98}Y_2$, and $Mg_{97}Zn_1Y_2$ in the prismatic plane view are presented as Figure 7.4. Electronic structures of fault layers (labeled 1B) and non-fault layers (A, C and 2B) of 6H LPSO in Mg have been displayed in Figure 7.4(a). It can be seen that the non-fault layer A is between two fault layers named 1B, which is one of the two layers ($A\dot{B}$ layers) enriched with alloying elements as mentioned before. Contributions of Zn and Y to the electronic structures of their energetic favorable configurations in $Mg_{98}Zn_2$ and $Mg_{98}Y_2$with 6H LPSO are presented in Figure 7.4(b) and Figure 7.4(c). The efficiency of our proposed atomic array model can be seen since nine configurations are required in the calculation of $Mg_{97}Zn_1Y_2$ with 6H LPSO, shown in Figure 7.3(d).

The bond strength of Mg affected by the fault layer in 6H LPSO and alloying elements Zn and Y is discussed in views of deformation electron density ($\Delta\rho$) and electron localization function (ELF) in the following. Since the Coulomb force ($F_{Coulomb}$) is proportional to the charge distribution of the atoms and the bonding charge distribution

($\Delta\rho$), the higher of $\Delta\rho$ the stronger of the bond. The bond strength of Mg with 6H LPSO is characterized by the isosurface and contour plots of $\Delta\rho$, shown in Figure 7.4. It can be observed that two fault layers in 6H LPSO with altered charge density are separated by a non-fault plane and bond strength of Mg in the basal plane can be strengthened by the formation of fault layers. For instance, if assuming electron locating within the thickness of 0.56 Å (thickness of 4 layers of the grid region along $[0001]$, shown in Figure 7.8) contribute the bond strength of the basal plane. The number of grid region with the highest $\Delta\rho$ in basal plane increases from 11 to 23 by the formation of fault layer.

The $(001)_{s.c.}$ plane view of $-\Delta\rho_{max}$ and $0.5\Delta\rho_{max}$ isosurface plots of Mg, $Mg_{98}Zn_2$ with Zn cluster in 2B layer, $Mg_{98}Y_2$ with Y array in A layer and $Mg_{97}Zn_1Y_2$ with possible positions of Zn (P1-P9) for a fixed position of Y are shown in Figure 7.5 and Figure 7.6. Since more valence electrons existing in Y than Zn, it can be seen that the electron redistribution range affect by Y is significantly larger than that of Zn. With the interaction with Zn occupying the first and second nearest neighbor of Y array, the electron redistribution range of Zn will be verified, shown as 6H-A-P1, 6H-A-P5 and 6H-A-P6 in Figure 7.6. The $(100)_{s.c.}$ plane view of $0.4\Delta\rho_{max}$ isosurface plots of $Mg_{97}Zn_1Y_2$ with possible positions of Zn (P1-P9) for a fixed position of Y are shown in Figure 7.4, which clearly displays the bond morphology change of Mg affected by the fault layers and alloying elements. It can be see that the deformation electron density around Y is significant higher than the other zone. Particularly, the dispersion of more electrons along the basal plane caused by Y atomic array indicates the basal plane is strengthened. Incorporated with Zn occupying its first nearest neighbor along $[0001]$, the bond strength

of the more basal plane is enhanced with alloying elements affecting zone, shown as 6H-A-P5 in Figure 7.7.

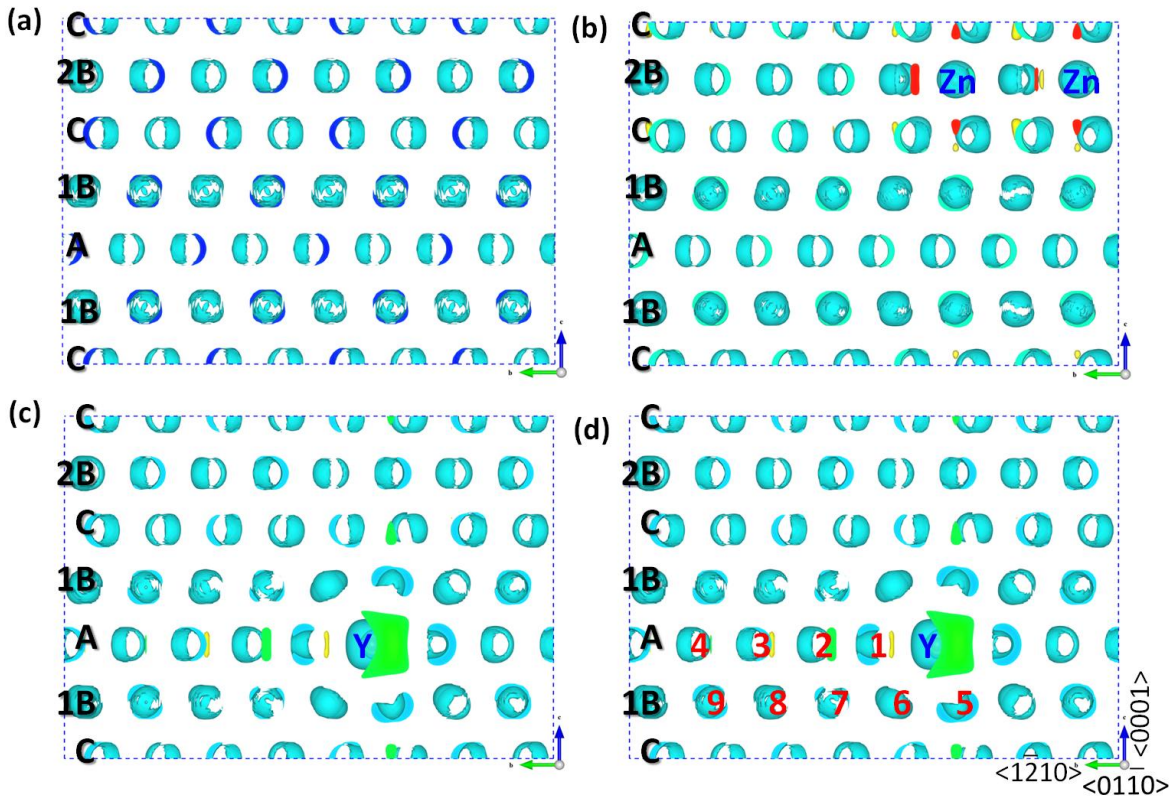

Figure 7.3. (100) plane view of $\Delta\rho$=0.00367 $e^{-}/Å^{3}$ isosurface plots of (a) pure Mg; (b) $Mg_{98}Zn_2$ with Zn cluster in 2B layer; (c) $Mg_{98}Y_2$ with Y array in A layer and (d) $Mg_{97}Zn_1Y_2$ with most favorable positions of Zn (P1-P9) for a fixed position of Y.

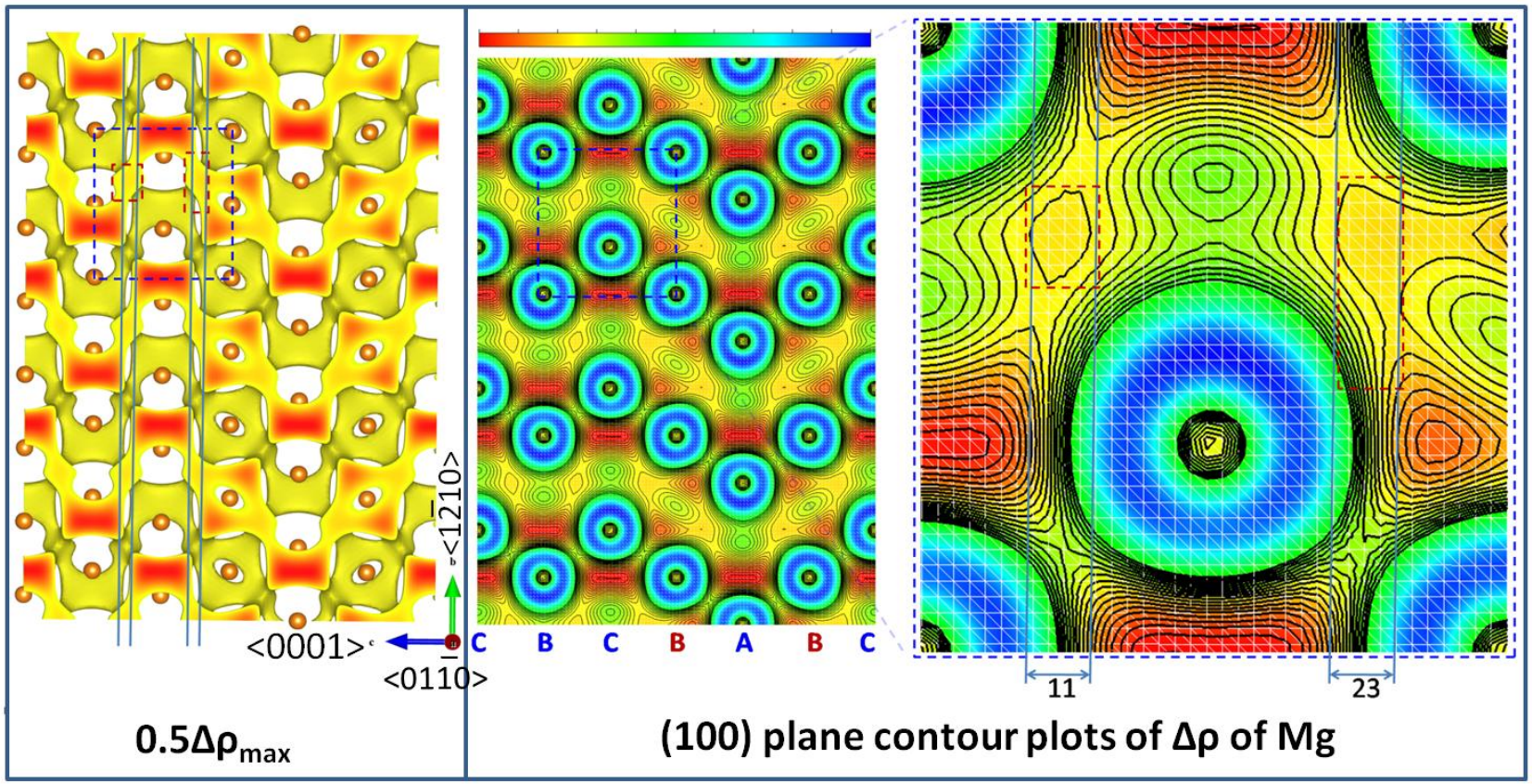

Figure 7.4. Chemical bond strength characterized by the deformation electron density (Δρ) of Mg with 6H in views of the isosurface and the contour plots.

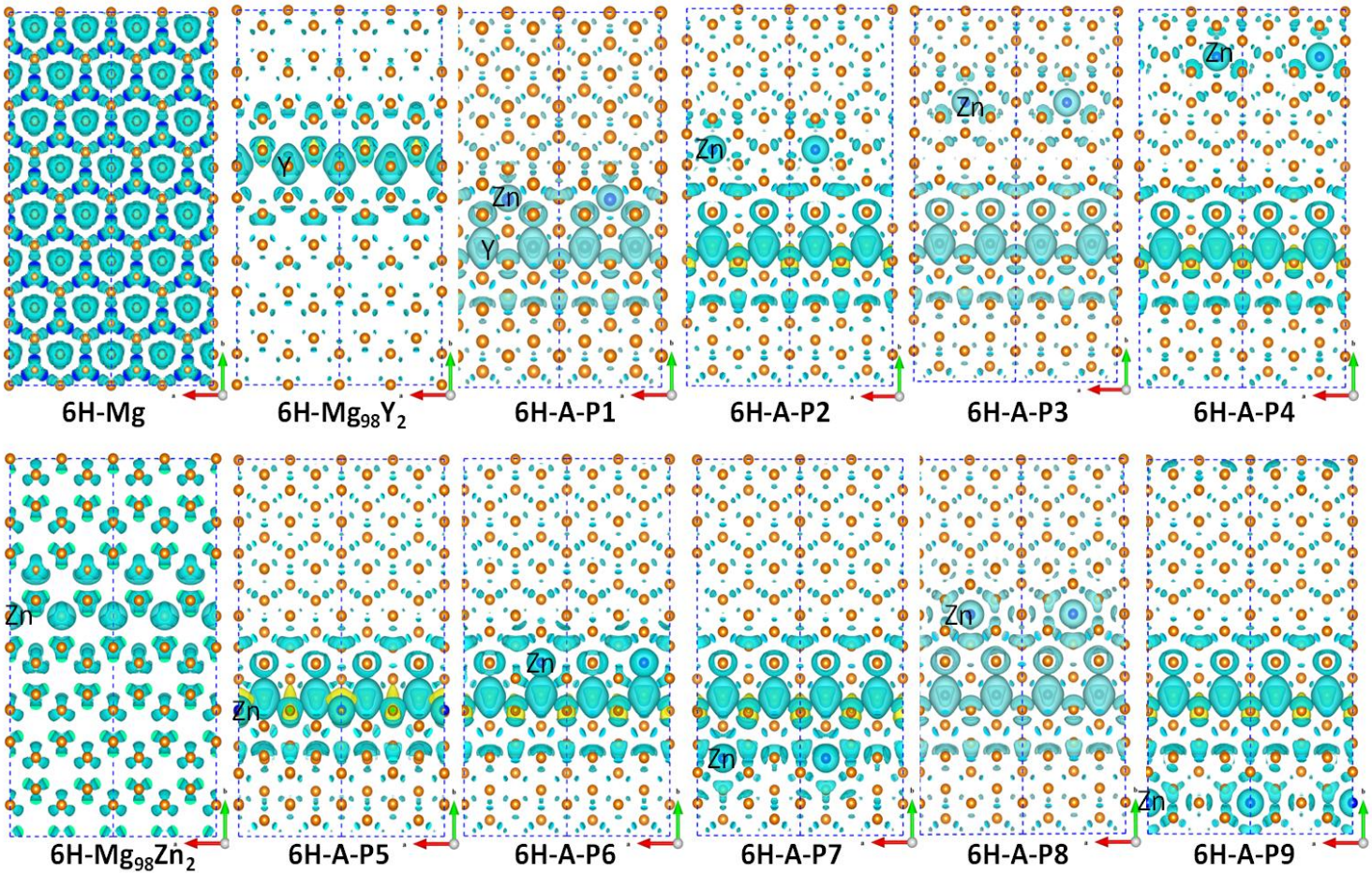

Figure 7.5 $(001)_{s.c.}$ plane view of $-\Delta\rho_{max}$ isosurface plots of Mg, $Mg_{98}Zn_2$ with Zn cluster in 2B layer, $Mg_{98}Y_2$ with Y array in A layer and $Mg_{97}Zn_1Y_2$ with possible positions of Zn (P1-P9) for a fixed position of Y.

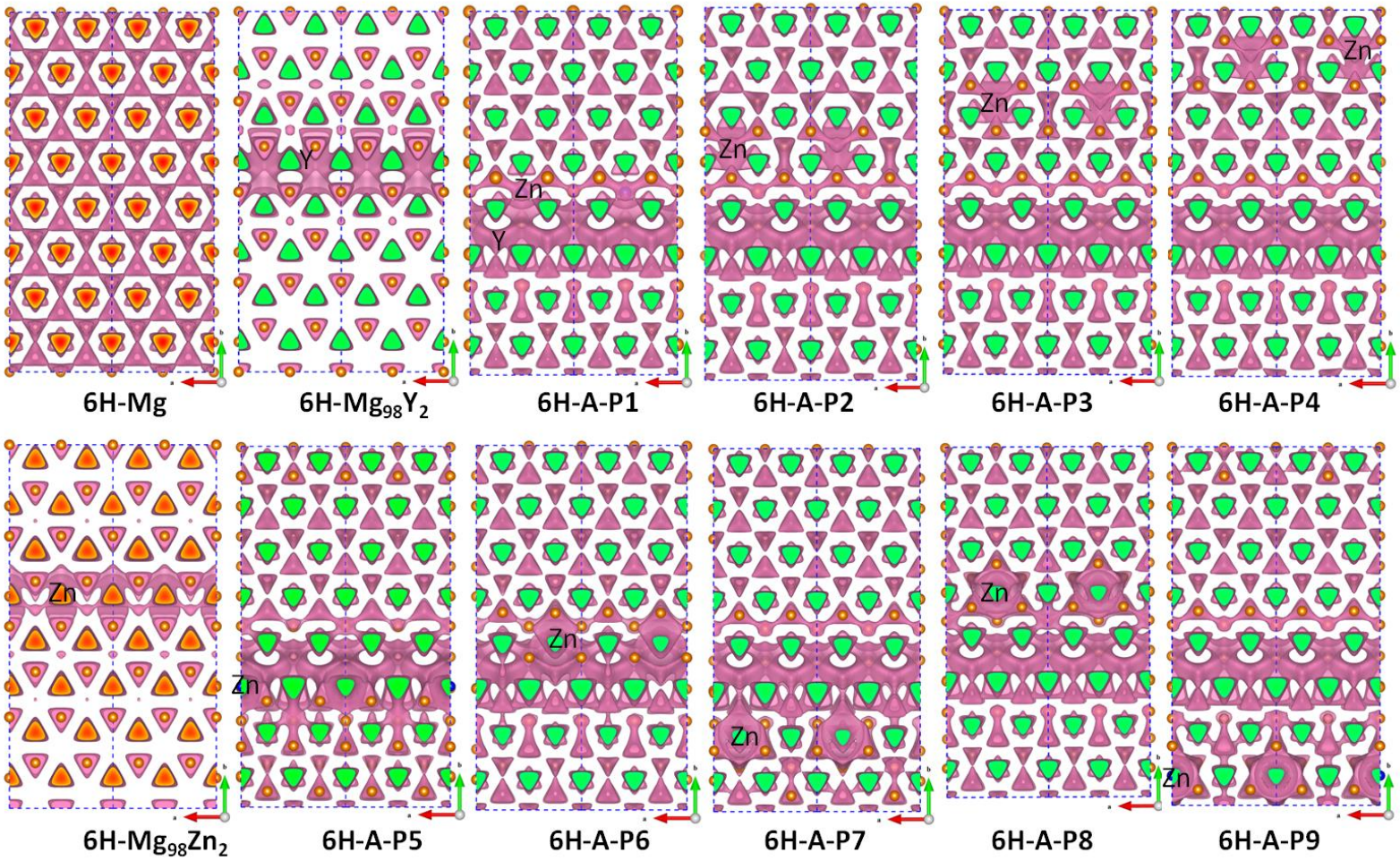

Figure 7.6 $(001)_{s.c.}$ plane view of $0.5\Delta\rho_{max}$ isosurface plots of Mg, $Mg_{98}Zn_2$ with Zn cluster in 2B layer, $Mg_{98}Y_2$ with Y array in A layer and $Mg_{97}Zn_1Y_2$ with possible positions of Zn (P1-P9) for a fixed position of Y.

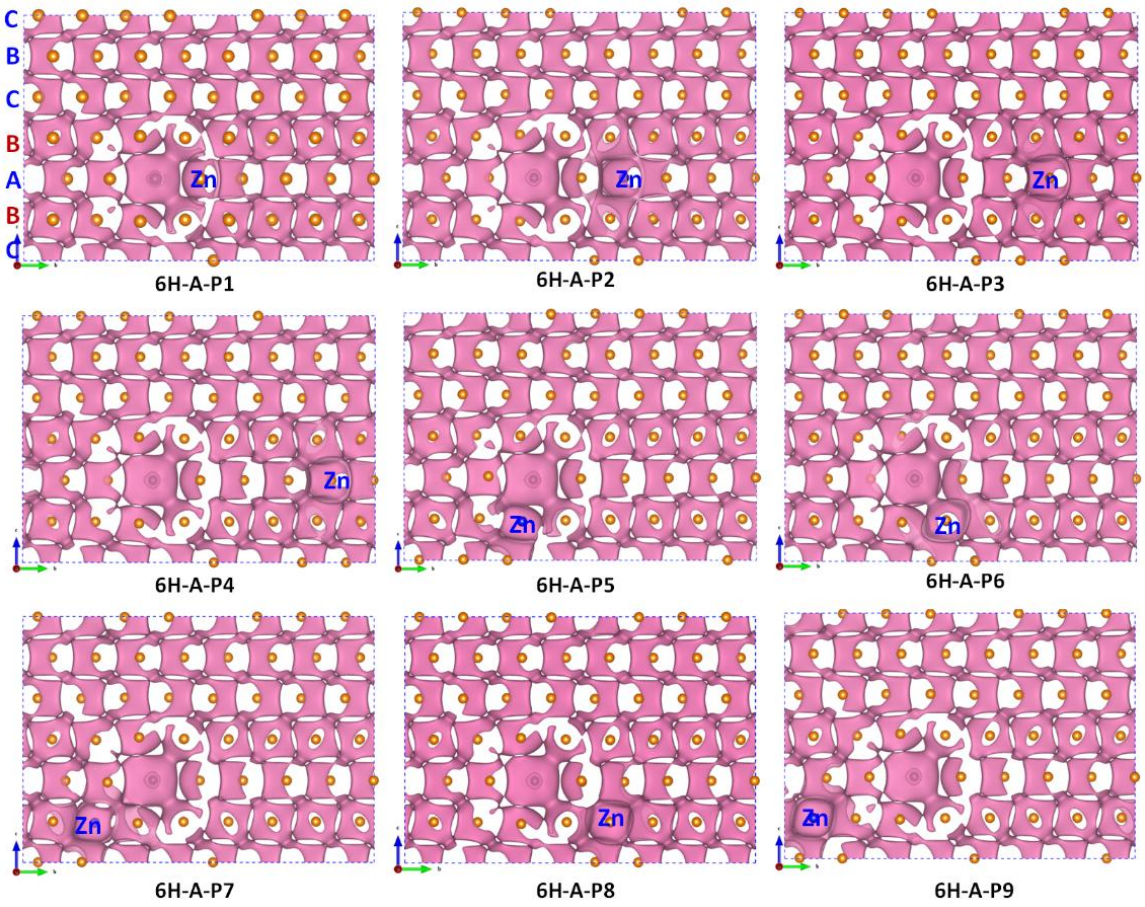

Figure 7.7 $(100)_{s.c.}$ plane view of $0.4\Delta\rho_{max}$ isosurface plots of $Mg_{97}Zn_1Y_2$ with possible positions of Zn (P1-P9) for a fixed position of Y.

A quantitative description of contribution of alloying elements Zn and Y to the bond strength of $Mg_{97}Zn_1Y_2$ with 6H LPSO along prismatic plane is shown in Figure 7.8, whose crystal structure is present in Figure 7.2. In view of ELF, it also can be seen that the charge is accumulated on site of the atomic array of Y, shown in Figure 7.8(a). Particularly, the charge of the basal plane around the Y atomic array is enhanced significantly. Hence, we would expect to reveal the strong interactions between alloying elements and the fault layers in 6H LPSO of $Mg_{97}Zn_1Y_2$ alloy. Three lines along [0001] with different distance to the Y atomic array and Zn are selected, labeled as S1, S2 and S3 in Figure 7.8(a). Since those lines are crossing the A layer instead of B or C, the value of ELF for the Mg-Mg bond in non-fault planes will be smaller than that of the typical covalence bond (0.6 - 1), shown in Figure 7.8(b). Moreover, the bond strength of Mg matrix around the Y/Zn atomic array would be dramatically decreased in the prismatic plane. For example, for these two fault layers separated by A Layer, the bond strength of Mg matrix in the prismatic plane is decreased obviously by the formation of fault (displayed by line profile of S2), which could be further reduced by the segregation of Zn in the 1^{st} nearest neighbor of Y atomic array (displayed by line profile of S1), shown in Figure 7.8(b). Thus, it can be concluded that the strengthen mechanism of Zn and Y to $Mg_{97}Zn_1Y_2$ alloy is that the basal plane of Mg is strengthened due to the formation of stronger chemical bond between atomic array and Mg matrix. On the contrary, the weakened bond strength of Mg matrix in the prismatic plane by the fault layers and alloying elements indicates a possible non-basal slip system could occur during deformation, which could improve the ductility of Mg alloys.

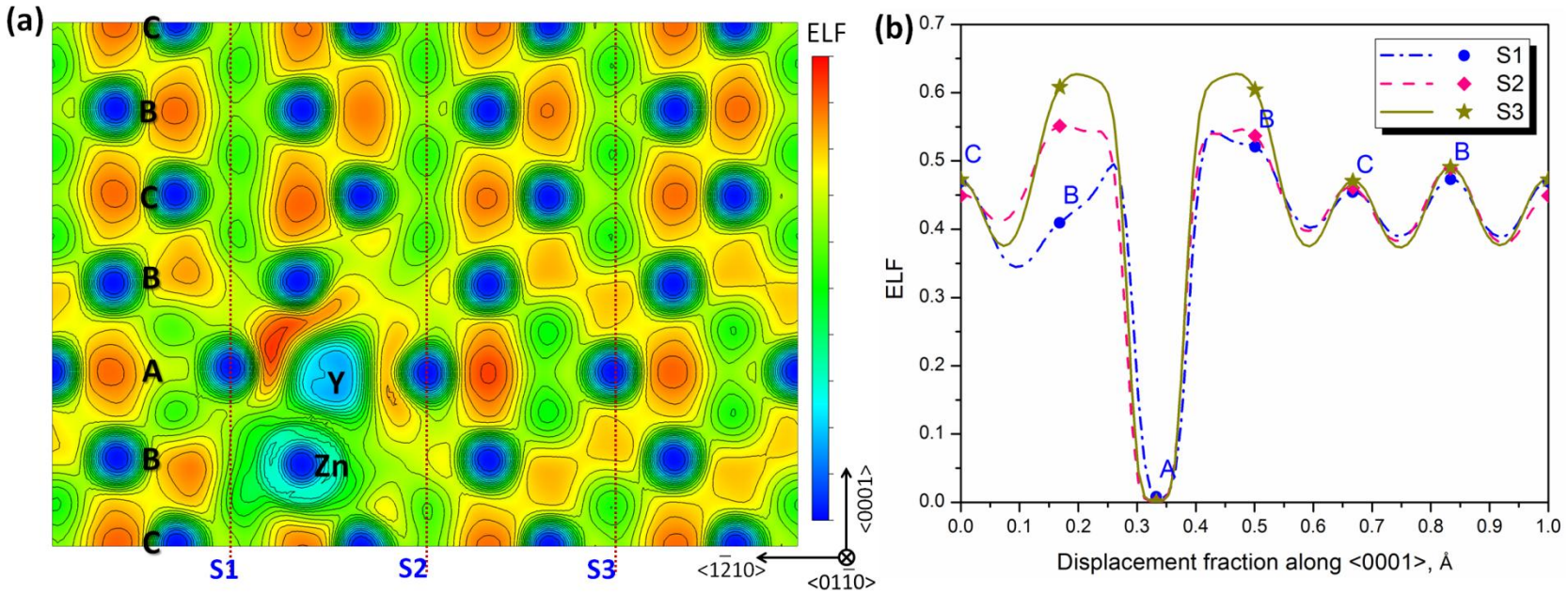

Figure 7.8. Chemical bond strength characterized by electron localization function (ELF) of Mg97Zn2Y1 with 6H-A-P5 configuration, (a) (100) plane contour plot of ELF; (b)the corresponding line profiles of ELF with those listed in (a).

7.3.3 Simulated HRTEM image and electron diffraction pattern of atomic array in 6H

In order to verify the validation of the proposed atomic array model in $Mg_{97}Zn_1Y_2$ alloy, the first-principles simulated HRTEM image are presented for the comparation with experimentally observed contrast feature [33, 120, 184], shown in Figure 7.9. Based on the atomic positions shown as the insert picture in Figure 7.9, their charge redistribution caused by alloying elements can be determined efficiently and directly through FP calculations. Thus, the contrast feature of alloying elements in $Mg_{97}Zn_1Y_2$ alloy by applying the atomic array model in the simulated HRTEM can be obtained, which confirms the previous HRTEM observed one (Zn and Y forms by occupying every $A\dot{B}$ layers in the 6H LPSO of $Mg_{97}Y_2Zn_1$ (at%) alloy) [33, 120] and theoretical calculation [185]. Similarly, the assumed $Mg_2Si_2Al_7$ with Si_2 pillars have been successfully applied in the study of nanoprecipitates hardening AlMgSi alloys, in which pillarlike silicon double columns are observed by atomic-resolution electron microscopy [125].

Since the electron diffraction pattern is sensitive to the composition and the lattice strain of the system [23], it is used to finally estimate the morphology of ordered alloying element in 6H LPSO based on the local strain. Figure 7.10 shows the simulated selected area electron diffraction patterns of $Mg_{98}Zn_2$ and $Mg_{98}Y_2$ with atomic array and atomic cluster in 6H LPSO. It can be seen that more extra diffraction spots and streaks appears along $[0001]_{LPSO}$. Comparing the electron diffraction patterns of atomic clusters shown in

Figure 7.10(b) and (d), more diffraction spots along $[11\bar{2}0]_{LPSO}$ will be strengthened by the atomic array of alloying elements in $[10\bar{1}0]_{LPSO}$ view of Figure 7.10(a) and (c), presenting the different local lattice strain caused by alloy elements via these two models.

Figure 7.11 presents simulated selected area electron diffraction patterns of $Mg_{97}Zn_1Y_2$ with atomic array of Y and Zn in 6H LPSO of $Mg_{97}Zn_1Y_2$, matching with experimental observations of $Mg_{97}Zn_1Y_2$ with 6H LPSO [33, 122]. Extra diffraction spots arising from the fault layers and atomic array of alloying element are indicated by arrows. It is necessary to point out that the composition of the sample used by Ping et al.[186], is Mg-2.4RE-0.4Zn-0.6Zr (wt %), alloying elements of which disperse like disks within 10nm in diameter and 1 nm in thickness. Examinations of electron diffraction pattern shown in Figure 7.11(c) indicate an ordered structure probably existing in the disk-like regions, which is Zn may occupy the neighboring sites of RE atoms based on observations by 3D atomic probe [186]. Hence, it can be seen that the disk-like ordered structure of alloying elements result in the strengthened diffraction spots spread along $[11\bar{2}0]$ in Figure 7.11(c-1) and along $[01\bar{1}0]$ in Figure 7.11(c-2). It is easy to understand the formation of atomic array of Y atoms with Zn locating at their first nearest neighbor site causes the strengthened diffraction spots spread along $[11\bar{2}0]$ shown in Figure 7.11(a-1) and Figure 7.11(b-1). The weaken streaks in these predicted electron diffraction patterns indicate the local order structure in the 6H and the difference to experimental observed ones are due to their different compositions.

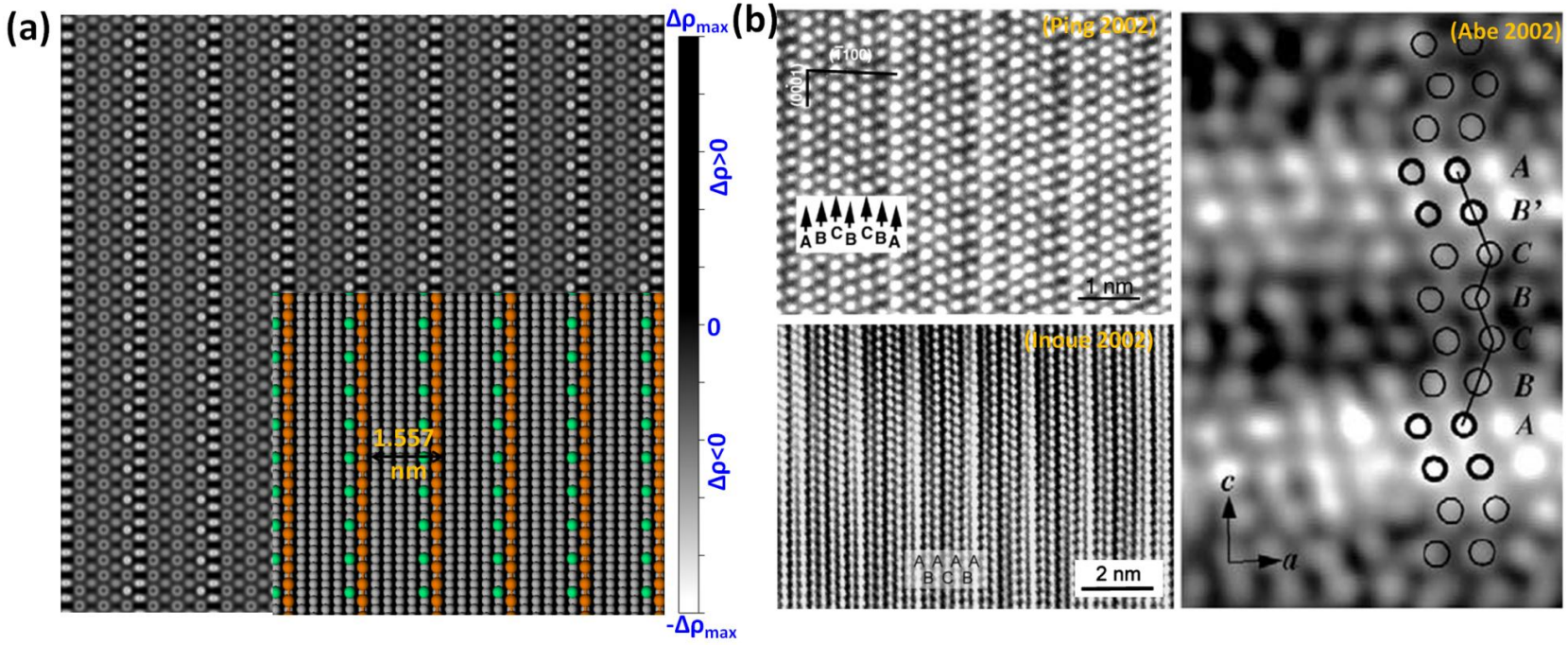

Figure 7.9. Crystal structure morphology of 6H LPSOs in $Mg_{98}Zn_2Y_1$ (at %), (a) simulated HRTEM image with together with the atomic positions in the insert picture and (b) experimental observed HRTEM and HAADF-STEM images by Ping [120], Inoue [23] and Abe [33].

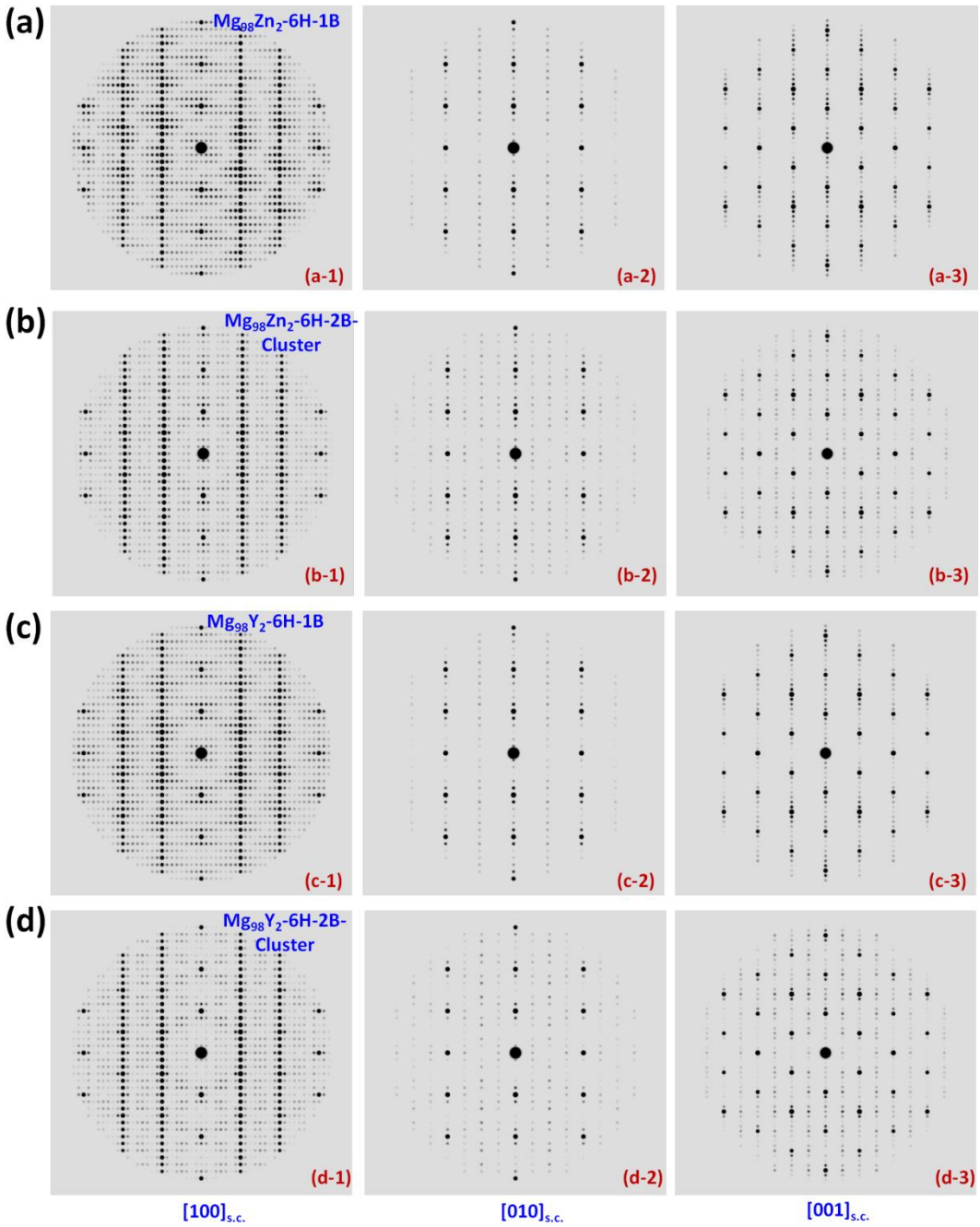

Figure 7.10. Simulated selected area electron diffraction patterns of $Mg_{98}Zn_2$ (a-b) and $Mg_{98}Y_2$ (c-d) with atomic array and atomic cluster in 6H LPSO. The electron bean directions are parallel to $<100>_{S.C.} \| <10\bar{1}0>_{LPSO}$, $<010>_{S.C.} \| <11\bar{2}0>_{LPSO}$ and $[001]_{S.C.} \| [0001]_{LPSO}$.

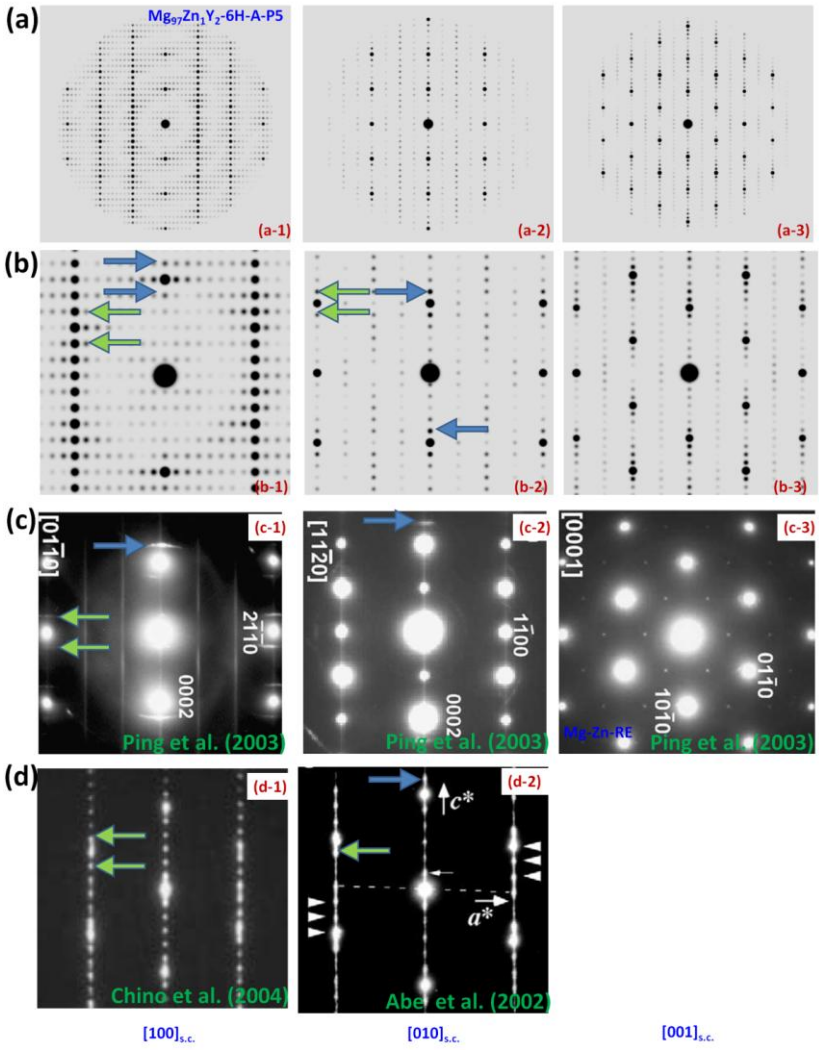

Figure 7.11. Simulated selected area electron diffraction patterns of $Mg_{97}Zn_1Y_2$ with atomic array in 6H LPSO (Fig. a-b), comparing with experimental observations of nanoprecipitates in Mg-Zn-RE-Zr alloy by Ping [120] (Fig. c) and 6H LPSO in $Mg_{97}Zn_1Y_2$ by Chino[122] and Abe [33] (Fig. d). The diffraction patters in (b) are the corresponding enlarged part of (a). The electron bean directions are parallel to $<100>_{S.C.} \| <10\bar{1}0>_{LPSO}$, $<010>_{S.C.} \| <11\bar{2}0>_{LPSO}$ and $[001]_{S.C.} \| [0001]_{LPSO}$. Extra diffraction spots arising from the fault layers and atomic array are indicated by arrows.

7.3.4 Elastic properties of atomic array in 6H LPSO

Table 7.2 summarized elastic properties of Mg, $Mg_{98}Zn_2$, $Mg_{98}Y_2$, and $Mg_{97}Zn_1Y_2$ alloys with and without atomic array in 6H LPSO. The predicted bulk modulus (B) of HCP Mg derived from elastic constant calculated by Equation 2.12 matches well with experimental measurements [180], which will be increased from 36.24GPa to 36.80 GPa by forming 6H LPSO. However, the shear modulus (G) is dramatically decreased from 21.20 GPa to 18.87 GPa by forming 6H LPSO in Mg. Comparing to the ***B*** and ***G*** of solution phase $Mg_{98}X_2$ (no bonds from between alloying element X), through forming atomic array of Y and Zn in HCP and 6H LPSO, ***B*** will be increased in $Mg_{98}Y_2$ and decreased in $Mg_{98}Zn_2$ while ***G*** increased in both. It is worth to mention that ***B*** of $Mg_{97}Zn_1Y_2$ with atomic array of Y/Zn (6H-A-P5) in 6H LPSO is enhanced while G is dramatically decreased comparing to that of HCP Mg matrix. Based on the classification introduced by Pugh [187], metals having a B/G ratio greater than 1.75 are ductile whereas less than 1.75 are considered brittle [188]. The ductility of $Mg_{97}Zn_1Y_2$ with atomic array of Y/Zn (6H-A-P5) in 6H LPSO will be increased since the B/G ratio is changed from 1.71 of HCP Mg to 1.95 of Mg with 6H LPSO and further reaching at 2.09 of $Mg_{97}Zn_1Y_2$. Moreover, through forming atomic array of Y and Zn, the Young's modulus (E) of HCP Mg is reduced from 53.21 GPa to 47.37 GPa of $Mg_{98}Y_2$ (6H-A), 45.47 GPa of $Mg_{98}Y_2$ (6H-1B) and 46.36 of $Mg_{97}Zn_1Y_2$. The predicted Young's modulus of $Mg_{97}Zn_1Y_2$ in this work agrees well with previous experimental result [189], listed in Table 7.2.

Table 7.2. Elastic properties of Mg, $Mg_{98}Zn_2$, $Mg_{98}Y_2$, and $Mg_{97}Zn_1Y_2$ alloys with and without atomic array in 6H LPSO

	Structure	C11	C12	C13	C33	C44	B	G	E	υ	B/G	Remark
Mg	HCP	65.90	24.78	18.05	73.45	17.70	36.24	21.20	53.21	0.26	1.71	
		67.5	24.76	24.1	72.4	23.97	39.3	22.8	57.3	0.23	1.72	[190]
		63.5	25.9	21.7	66.5	18.4	36.9	19.4	49.5	0.28	1.90	Exp. (0K) [180]
		59.4	25.6	21.4	61.6	16.4	35.2	17.4	44.8	-	2.02	Exp. (298K) [180]
		59.5	25.9	21.8	61.6	16.4	35.6	17.3	44.6	-	-	Exp. (298K) [179]
	6H	59.35	21.63	25.93	66.10	19.30	36.80	18.87	48.33	0.28	1.95	
Y	HCP	62.24	26.74	22.63	67.46	14.27	37.38	17.52	45.46	0.30	2.13	1.04 at%
		66.29	31.01	19.09	77.74	18.25	38.80	20.27	51.79	0.28	1.91	2.77 at%
		59.5	27.3	21.6	64.5	19.0	36.1	18.3	47.1	0.28	1.97	2.77 at% Ref: [188]
	HCP-Array	52.45	29.00	24.75	70.70	16.70	38.04	17.86	46.33	0.30	2.13	2.08 at%
	6H-A	54.65	28.18	23.93	73.00	17.05	37.96	18.33	47.37	0.29	2.07	2.08 at%
Zn	HCP	60.11	25.36	22.89	62.55	13.62	36.10	16.59	43.15	0.30	2.18	1.04 at%
		65.23	23.78	16.08	73.57	15.92	35.14	20.25	50.97	0.26	1.73	2.77 at%
		62.3	25.5	23.1	66.2	14.1	37.1	17.3	44.8	0.30	2.15	2.77 at% Ref: [188]
									46.5			Exp. [191]
	HCP-Array	55.20	23.20	25.43	61.25	21.50	35.63	18.82	48.01	0.28	1.89	2.08 at%
	6H-1B	55.60	23.60	24.83	64.70	19.75	35.71	17.65	45.47	0.29	2.02	2.08 at%
Zn+Y	6H-A-P5	53.45	28.15	23.88	71.90	16.80	37.54	17.91	46.36	0.29	2.09	Mg97Zn1Y2 at%
									45			Exp.[189]

Note: Voigt's approach

7.4. Results and Discussions on $Mg_{97.5}Gd_{1.67}TM_{0.83}$ (TM=Zn and Zr)

7.4.1. Applications of atomic array and atomic cluster of Gd and TM in 6H and 10H LPSOs

Based on the excess energy of binary Mg-10G (wt %) discussed in Chapter 6, it has shown that the fault layer and its first nearest neighbor layer of 6H LPSO prefer to be enriched of Gd atoms. Atomic array of Gd atoms locating at A layer (configuration P8 shown in Figure 6.4(c)) and atomic cluster occupying two 1B layer (configuration P7 shown in Figure 6.4(b)) are applied to discussing the contributions of selected alloying element (TM =Zn and Zr) to the formability of 6H in $Mg_{97.5}Gd_{1.67}TM_{0.83}$ alloys. The supercells of $Mg_{97.5}Gd_{1.67}TM_{0.83}$ are generated by substituted one Mg atom by TM in Mg-10Gd, which is occupying the first nearest neighbor position of Gd atoms. Similarly, the energetic favorable configuration of Gd in 10H (10H-P8 shown in Figure 6.6(a)) is chosen in the study of $Mg_{97.5}Gd_{1.67}TM_{0.83}$ alloy. Because it is identical between configurations of 10H-P7 and 10H-P8 (shown in Figure 6.15) for having the same bond structures and energies, which is due to Gd atoms segregate at two separate fault layers.

Figure 7.1 shows energies of 6H and 10H LPSO of $Mg_{97.5}Gd_{1.67}TM_{0.83}$ (TM=Zn and Zr) with various configurations as a function of volume fitted by four parameters Birch-Murnaghan equation of state (EOS). Hence, the equilibrium properties predicted by first-principles EOS can be obtained, including lattice parameters (a and C_{LPSO}), equilibrium volume (V_0), energy (E_0), bulk modulus (B_0) and its derivative of pressure (B_0'), summarized in Table 7.3. The interfacial energy of LPSO, γ_{LPSO}, is defined as,

Equation 7.4 $$\gamma_{LPSO} = \frac{1}{A}(E_{LPSO} - E_{Bulk})$$

where E_{sf} and E_{Bulk} are the total energies of supercells with and without LPSOs, respectively, and *A* is the area of the basal plane with fault layers. Moreover, the morphologies of alloying elements are same in the supercell with and without LPSOs. It can be seen that with the addition of Zn and Zr, the interfacial energy of 6H and 10H can be decreased significantly when forming the cluster between TM and Gd, indicating the formability of 6H and 10H will be increased in Mg-Gd-Zr and Mg-Gd-Zn alloys. For example, the interfacial energy of 6H in is decreased from 44.6 mJ/m^2 of Mg to 13.17 mJ/m^2 of $Mg_{98.33}Gd_{1.67}$, to 16.3 mJ/m^2 of $Mg_{97.5}Gd_{1.67}Zn_{0.83}$ and to 16.79 mJ/m^2 of $Mg_{97.5}Gd_{1.67}Zr_{0.83}$. Meanwhile, the interfacial energy of 10H in is decreased from 98.2 mJ/m^2 of Mg to 22.04 mJ/m^2 of $Mg_{98.33}Gd_{1.67}$, to 25.38 mJ/m^2 of $Mg_{97.5}Gd_{1.67}Zn_{0.83}$ and to 17.74 mJ/m^2 of $Mg_{97.5}Gd_{1.67}Zr_{0.83}$. It will be more efficient alloying Zr into Mg-Gd to form 10H LPSO than alloying Zn since the interfacial energy of 10H in $Mg_{97.5}Gd_{1.67}Zr_{0.83}$ is much smaller than that of $Mg_{97.5}Gd_{1.67}Zn_{0.83}$.

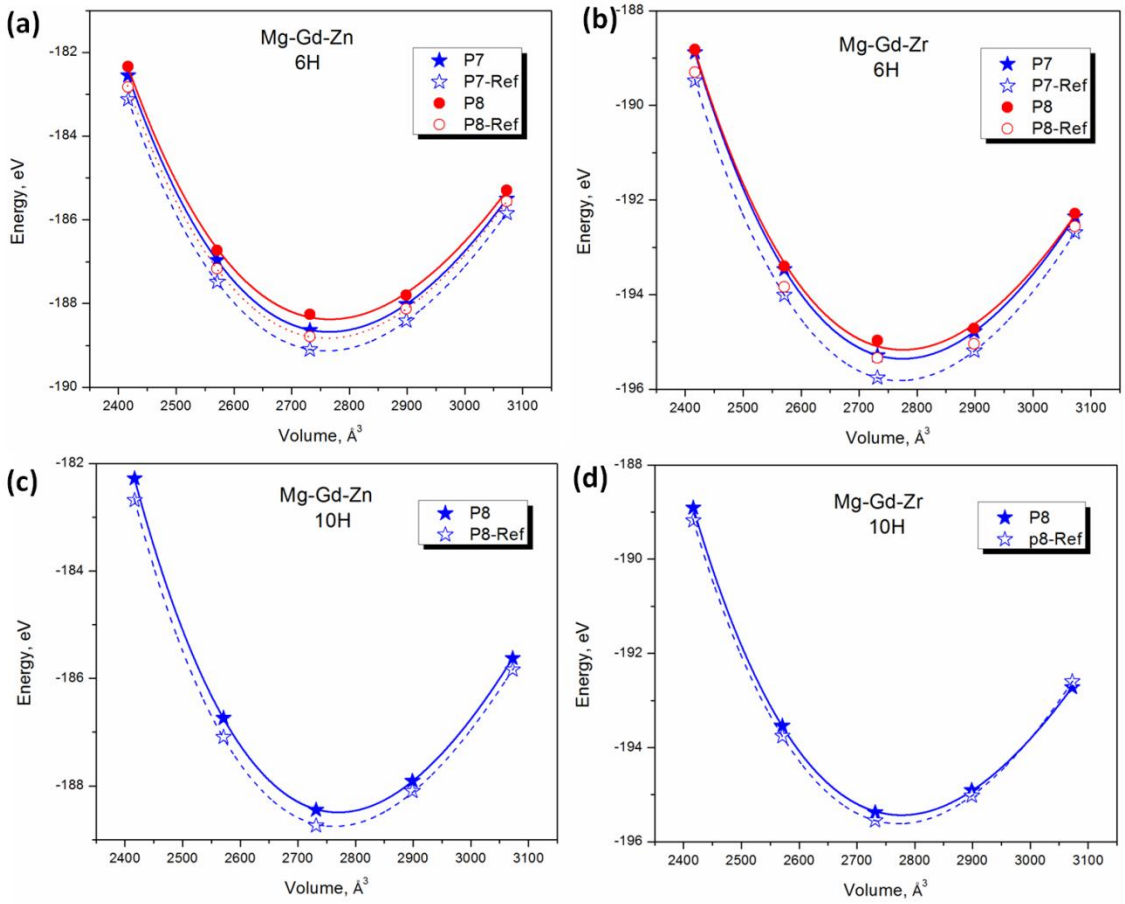

Figure 7.12. Energy as a function of volume fitted by four parameters Birch-Murnaghan equation of state, (a) and (b) configuration P7 and P8 together with their reference states in 6H LPSO of $Mg_{97.5}Gd_{1.67}Zr_{0.83}$ and $Mg_{97.5}Gd_{1.67}Zr_{0.83}$; (c) and (d) configuration P8 together with its reference states in 10H LPSO of $Mg_{97.5}Gd_{1.67}Zr_{0.83}$ and $Mg_{97.5}Gd_{1.67}Zr_{0.83}$.

Table 7.3. Energies and properties of $Mg_{97.5}Gd_{1.67}TM_{0.83}$ (TM=Zn and Zr) with atomic array and atomic clusters in 6H and 10H

Composition Configuration #		Lattice Parameter		V_0 Å3/atom	E_0 eV/atom	B_0 GPa	B_0'	γ_{LPSO} mJ/m^2
		a Å	C_{LPSO} Å					
Gd-6H	**P7**	3.226	15.473	23.067	-1.57217	34.4	5.10	13.17
	Ref	3.226	15.425	23.004	-1.57525	36.3	4.37	-
	P8	3.244	15.677	23.143	-1.57183	34.3	4.45	82.50
	P9	3.241	15.697	23.176	-1.57162	34.9	4.07	87.99
	Ref	3.236	15.646	23.085	-1.57496	34.4	4.94	-
Gd-Zn-6H	**P7**	3.202	15.571	21.601	-1.47405	35.6	4.11	16.30
	Ref	3.164	15.501	21.565	-1.47758	35.9	4.13	-
	P8	3.186	15.717	21.611	-1.47172	34.7	4.14	102.20
	Ref	3.175	15.683	21.575	-1.47522	35.8	4.00	-
Gd-Zr-6H	**P7**	3.176	15.609	21.676	-1.52625	35.7	4.03	16.79
	Ref	3.185	15.581	21.637	-1.52982	36.0	4.03	-
	P8	3.187	15.699	21.682	-1.52476	34.3	4.28	83.21
	Ref	3.180	15.660	21.648	-1.52762	34.6	4.31	-
Gd-10H	**P7**	3.216	26.008	23.149	-1.57356	35.8	3.88	22.04
	P8	3.218	25.986	23.149	-1.57350	35.9	3.84	22.69
	Ref	3.233	25.938	23.123	-1.57541	33.6	5.18	-
Gd-Zn-10H	**P8**	3.224	25.967	21.641	-1.47262	34.0	4.76	25.38
	Ref	3.251	25.897	21.590	-1.47462	33.8	5.28	-
Gd-Zr-10H	**P8**	3.217	26.055	21.695	-1.52685	33.9	5.02	17.74
	Ref	3.245	25.933	21.660	-1.52825	35.6	4.24	-
Mg-10H		3.198	25.917	22.950	-1.51976	35.5	4.00	98.2
Mg-6H		3.197	15.549	22.944	-1.51949	35.6	3.96	44.6
Mg-HCP		3.195	5.179	22.904	-1.52387	35.9	3.87	-

7.4.2. Simulated electron diffraction patterns of atomic array and atomic cluster in 6H and 10H LPSO

Figure 7.13 shows the simulated electron diffraction patterns of $Mg_{98.33}Gd_{1.67}$ with atomic array and atomic cluster in 6H and 10H LPSOs. In views of $[10\bar{1}0]_{LPSO}$ and $[11\bar{2}0]_{LPSO}$, it can be seen that more extra diffraction spots and streaks appears along $[0001]_{LPSO}$, which is caused by the solute atoms and fault layers in 6H and 10H. The weak streaks shown in the view of $[11\bar{2}0]_{LPSO}$ indicate local order structure in the 6H and 10H LPSOs. With the formation of atomic array of Gd in 6H, more diffraction spots along $[11\bar{2}0]_{LPSO}$ will be strengthened, shown in Figure 7.13(b). On the contrary, the formation of atomic cluster of Gd in 6H and 10H LPSOs contributes to the highlighted spots along $[0001]_{LPSO}$. Hence, the obvious difference in the electron diffraction pattern between atomic array and atomic cluster could be conveniently estimated by the experiments. As shown in Figure 7.13(c) and (d), the electron diffraction of configurations of 10H-P7 and 10H-P8 are same, confirming that they are identical since Gd atoms segregated at two separated fault layers. The difference between 10H-P7 and 10H-P8 is the distance of two Gd atoms along $[0001]_{LPSO}$ is different, contributing limited change in the total energy and lattice stain.

Figure 7.14 and Figure 7.15 shows the simulated electron diffraction patterns of $Mg_{97.5}Gd_{1.67}Zn_{0.83}$ and $Mg_{97.5}Gd_{1.67}Zr_{0.83}$ with atomic array and atomic cluster in 6H and 10H LPSOs. It can be seen that the intensity of some spots of $Mg_{98.33}Gd_{1.67}$ shown in Figure 7.13 will be decreased by alloying Zn, indicating the reduction of lattice strain

caused by the segregation of Gd with Zn located at its first neighbor. Moreover, streaks caused by of atomic array of Zn in 6H of $Mg_{97.5}Gd_{1.67}Zn_{0.83}$ in the view of $[11\bar{2}0]_{LPSO}$ are much clear than that of $Mg_{98.33}Gd_{1.67}$. On the contrary, in the view of $[11\bar{2}0]_{LPSO}$, intensity of streaks caused by of atomic array of Zr in 6H of $Mg_{97.5}Gd_{1.67}Zr_{0.83}$ is weaker than that of $Mg_{98.33}Gd_{1.67}$, presenting the decreased local lattice strain around atomic array. Therefore, the formation energy of atomic array in 6H of $Mg_{97.5}Gd_{1.67}Zr_{0.83}$ is smaller than that of $Mg_{97.5}Gd_{1.67}Zn_{0.83}$, listed in Table 7.3.

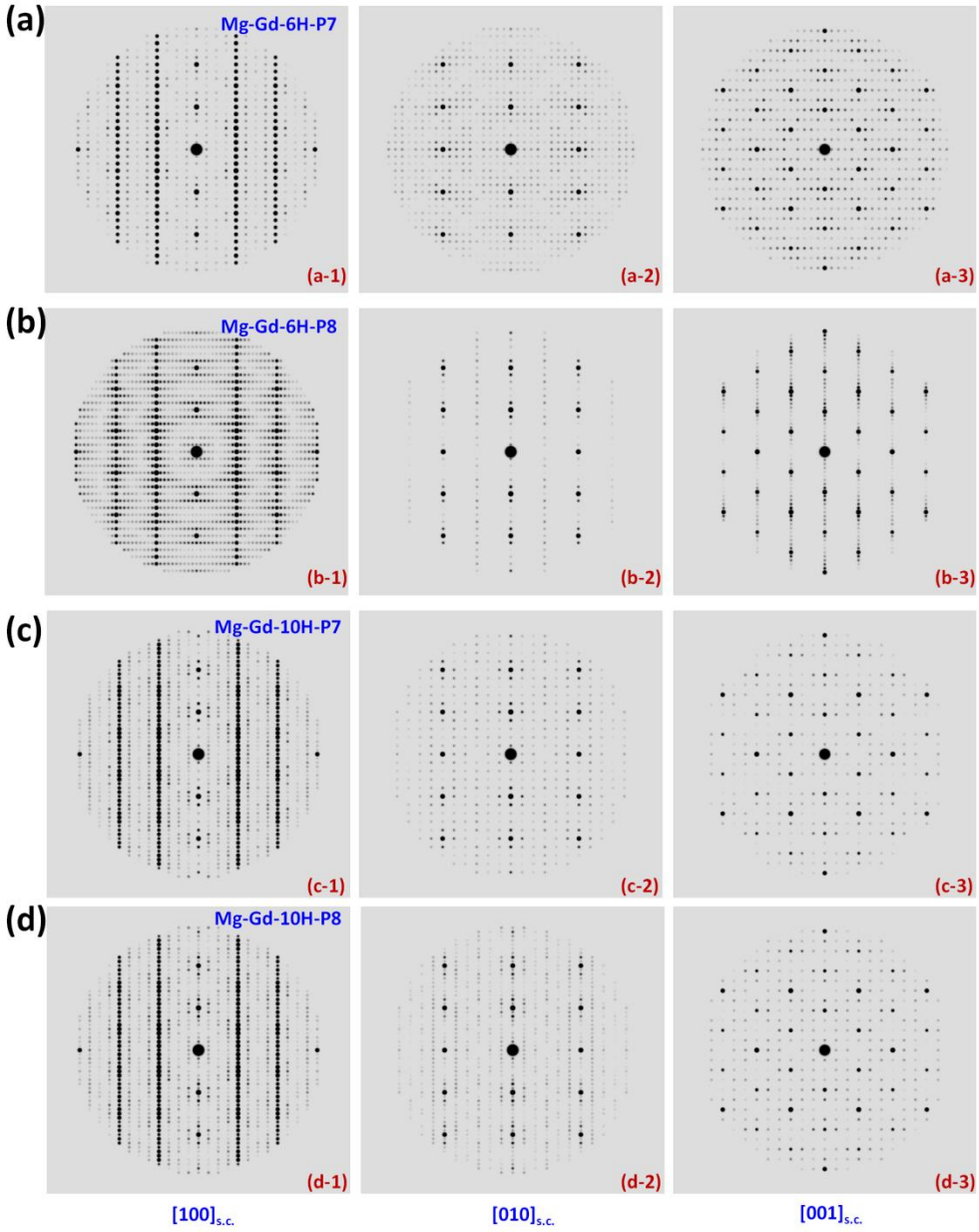

Figure 7.13. Simulated selected area electron diffraction patterns of $Mg_{98.33}Gd_{1.67}$ with atomic array and atomic cluster in 6H and 10H LPSOs, (a) atomic cluster of Gd in 6H; (b) atomic array of Gd in 6H; (c) and (d) Gd segregated in two separated fault layers. The electron bean directions are parallel to $<100>_{S.C.} \| <10\bar{1}0>_{LPSO}$, $<010>_{S.C.} \| <11\bar{2}0>_{LPSO}$ and $[001]_{S.C.} \| [0001]_{LPSO}$.

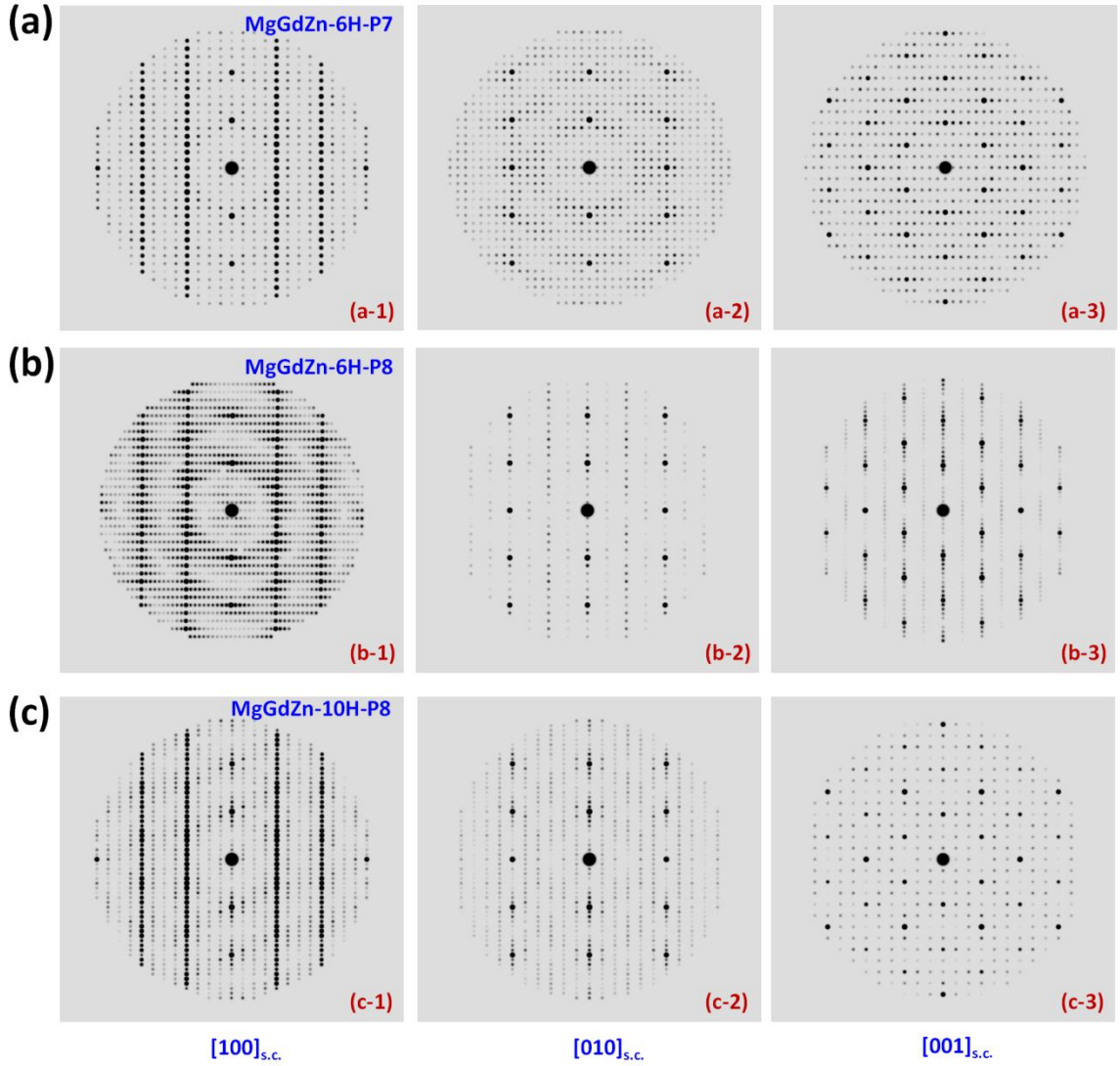

Figure 7.14. Simulated selected area electron diffraction patterns of $Mg_{97.5}Gd_{1.67}Zn_{0.83}$ with atomic array and atomic cluster in 6H and 10H LPSOs, (a) atomic cluster of Gd in 6H; (b) atomic array of Gd in 6H; (c) Gd segregated in two separated fault layers. The electron bean directions are parallel to $<100>_{S.C.} \| <10\bar{1}0>_{LPSO}$, $<010>_{S.C.} \| <11\bar{2}0>_{LPSO}$ and $[001]_{S.C.} \| [0001]_{LPSO}$.

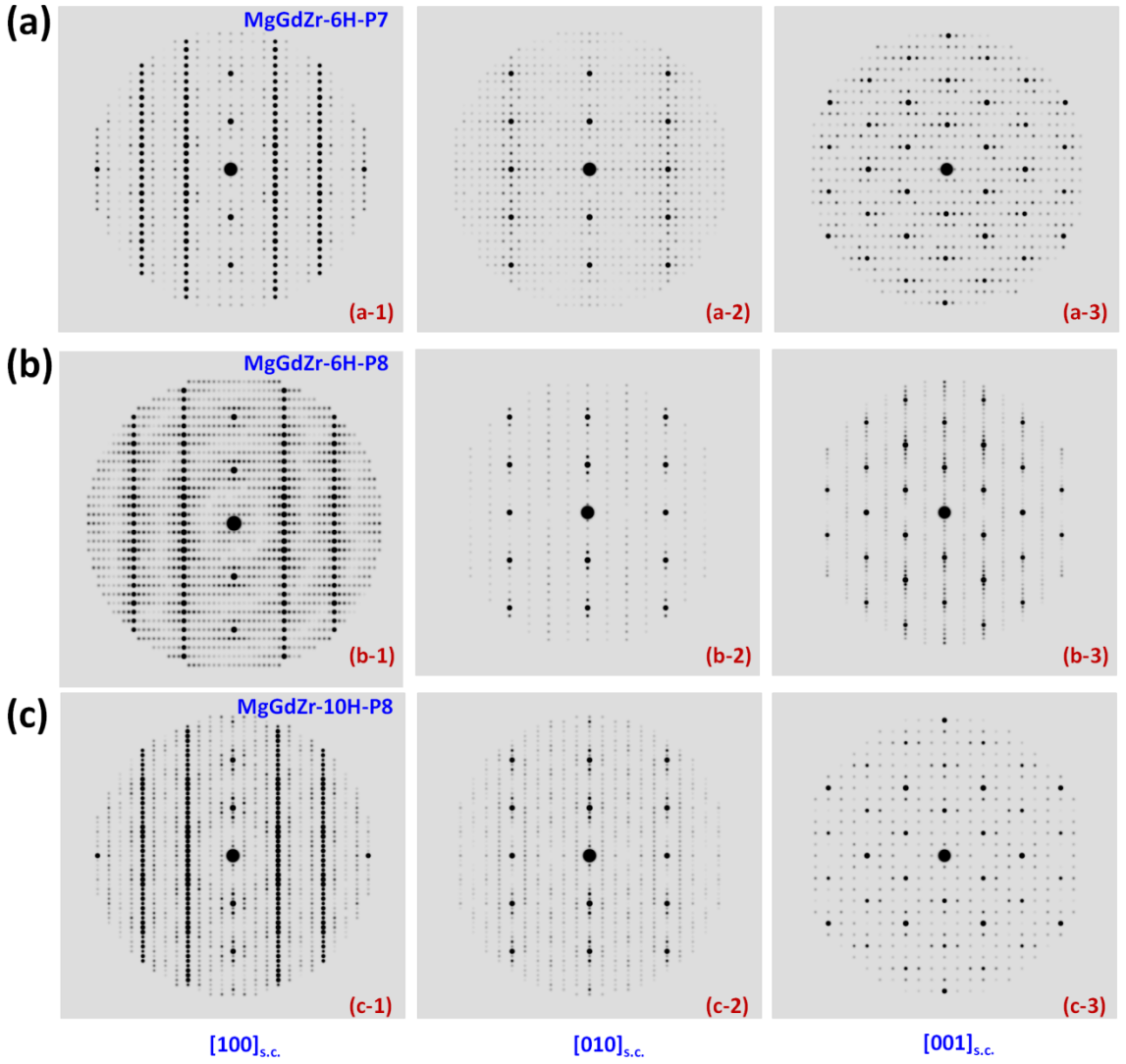

Figure 7.15. Simulated selected area electron diffraction patterns of $Mg_{97.5}Gd_{1.67}Zr_{0.83}$ with atomic array and atomic cluster in 6H and 10H LPSOs, (a) atomic cluster of Gd in 6H; (b) atomic array of Gd in 6H; (c) Gd segregated in two separated fault layers. The electron bean directions are parallel to $<100>_{S.C.} \| <10\bar{1}0>_{LPSO}$, $<010>_{S.C.} \| <11\bar{2}0>_{LPSO}$ and $[001]_{S.C.} \| [0001]_{LPSO}$.

7.4.3. Bond structure and strength affected by solute atoms and fault layers

In the view of the deformation electron density, bond structure and strength of $Mg_{97.5}Gd_{1.67}TM_{0.83}$ alloys affected by the solute atoms (Zn and Y) and the fault layers in 6H and 10H LPSOs and are captured. Isosurfaces of the deformation electron density ($\Delta\rho$=0.0021 $e^{-}Å^{3}$) of atomic cluster of Gd-TM in 6H and 10H LPSOs of $Mg_{97.5}Gd_{1.67}TM_{0.83}$ (TM=Zn and Zr) are shown in Figure 7.16. It can be seen that the deformation electron density of atomic cluster of Gd-TM is significantly denser than that of surrounding Mg atoms, whose deformation electron densities are further decreased. This is because (i) more electrons should locate at the position of atomic clusters of alloying elements since they always have more electrons for the valence, for example, according to the electronic configurations of solute atoms in the first-principles calculations, 12 electrons are used for the valance of Zn ($3d^{10}4s^{2}$) and Zr ($4s^{2}4p^{6}4d^{2}5s^{2}$); and (ii) contributions of solute atoms and fault layers to the redisctribution of electrons result in the electron density change. The enhanced electrons along the basal plane caused by atomic cluster of Gd-TM and the reduced electrons in the prismatic and pyramidal planes indicate the bonds are strengthened along basal plane but weakened along prismatic and pyramidal planes, shown in Figure 7.16. When the solute atoms of Gd forming an atomic array with TM locating the first nearest neighbor site, the bond morphology will be significantly changed, comparing with that of atomic cluster of Gd-TM. Moreover, the bond strength along prismatic plane is dramatically decreased by the formation of atomic array in 6H of $Mg_{97.5}Gd_{1.67}Zn_{0.83}$ and $Mg_{97.5}Gd_{1.67}Zr_{0.83}$. shown in Figure 7.17.

Figure 7.18 shows deformation electron density isosurface ($\Delta\rho$=0.0021 $e^{-}Å^{3}$) of atomic cluster of Gd-TM in 10H of $Mg_{97.5}Gd_{1.67}TM_{0.83}$ (TM=Zn and Zr). Since more valence electrons existing in Zn and Zr than the matrix, it can be seen that the electron redistribution range affect by solute atoms is significantly enlarged by the formation of Gd-TM atomic cluster in the fault layers. Moreover, solute atom of Zr attracts more electrons than Zn, presenting a the stronger pinning effect and improved thermal stability of LPSOs [38].

It is worth to mention that the directional bond will result in the elastic anisotropy, and thus hinders the anisotropic of deformation behavior. With the formation of fault layers in the matrix of Mg, the rod-type directional bonds transfer into tetrahedrons, which are the typical FCC-type chemical bonds [61]. Furthermore, the inhomogeneous electron distribution in the fault layers of LPSOs could be introduced by the interactions among solute atoms and fault layers. Since it is more difficult for the electrons to readapt during breaking rod-type directional bonds than the spherical ones [63], the redistribution of electrons characterized by the change of bond morphology implicates the directionality of the bonds crossing the fault layers of LPSOs and the dependency of formation energy of defects on composition [64]. Therefore, the segregation behavior of solute atoms and their contributions to the energy, bond structure and strength, and elastic properties can be captured conveniently, providing a qualitative description of the strengthen mechanism in the development of advanced Mg alloys.

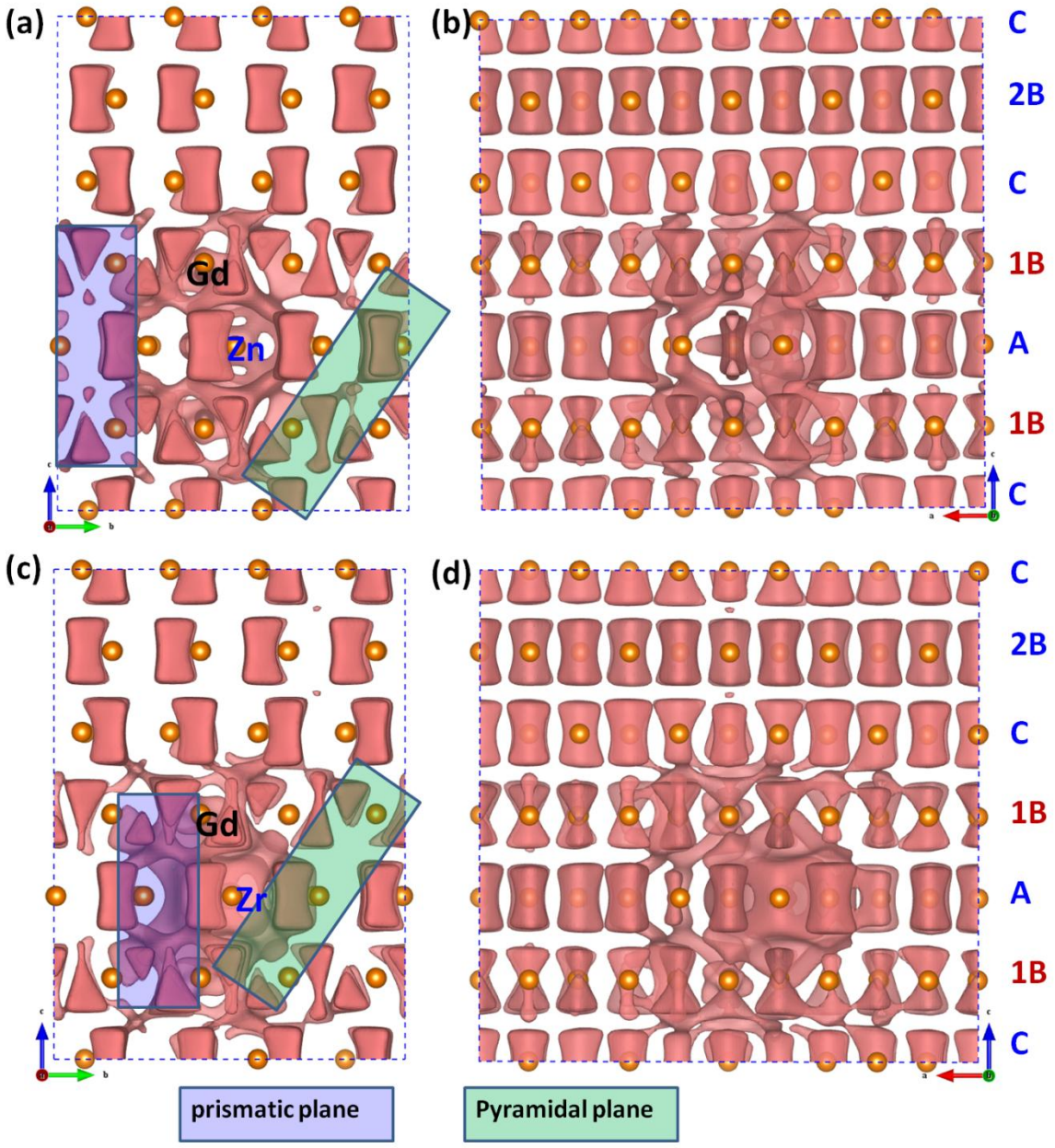

Figure 7.16. Deformation electron density isosurface ($\Delta\rho$=0.0021 $e^{-}Å^{3}$) of atomic cluster of Gd-TM in 6H of $Mg_{97.5}Gd_{1.67}TM_{0.83}$ (TM=Zn and Zr), (a) and (c) in the $(100)_{s.c.}$ view; (b) and (d) in the $(010)_{s.c.}$ view.

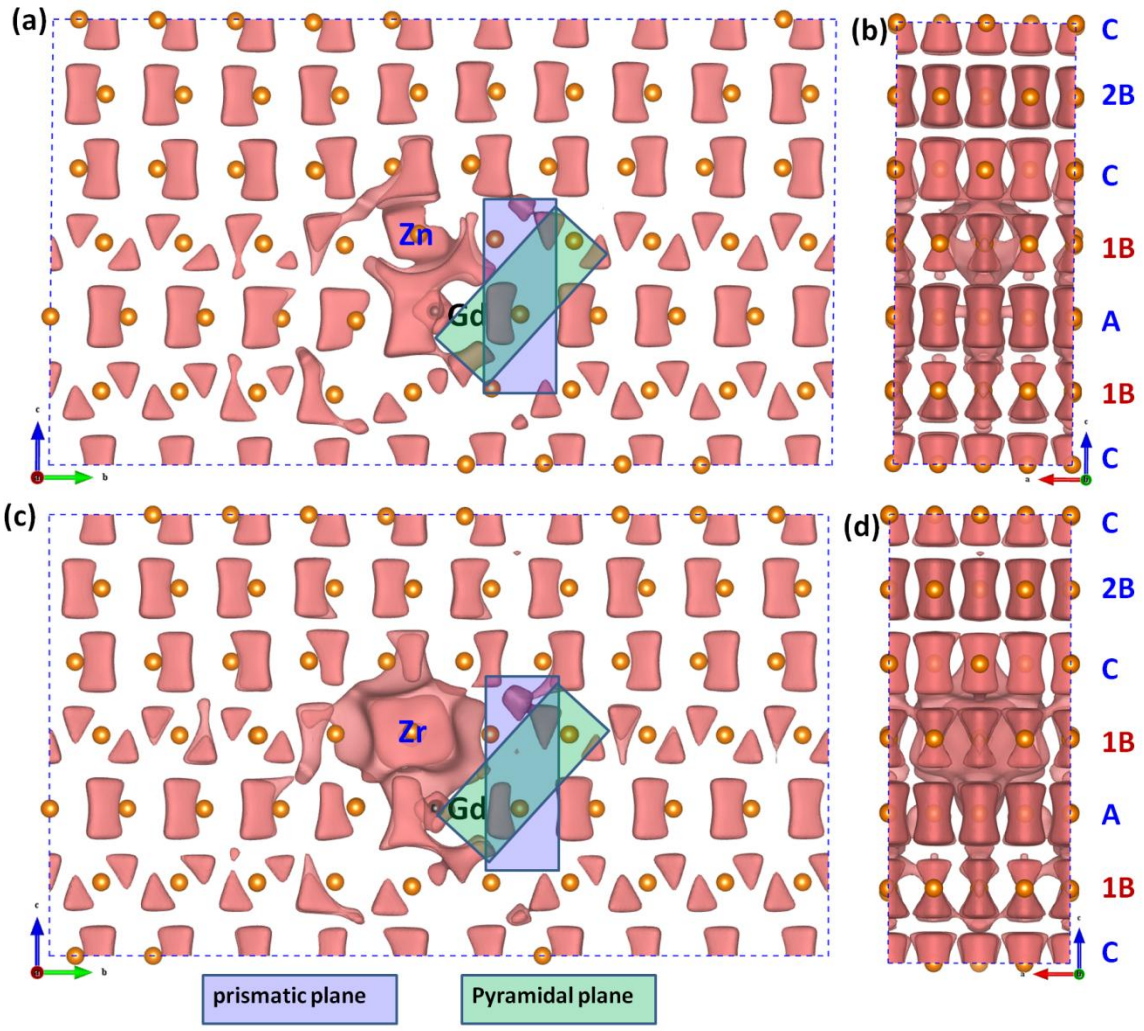

Figure 7.17. Deformation electron density isosurface ($\Delta\rho$=0.0021 $e^{-}Å^{3}$) of atomic array of Gd-TM in 6H of $Mg_{97.5}Gd_{1.67}TM_{0.83}$ (TM=Zn and Zr), (a) and (c) in the $(100)_{s.c.}$ view; (b) and (d) in the $(010)_{s.c.}$ view.

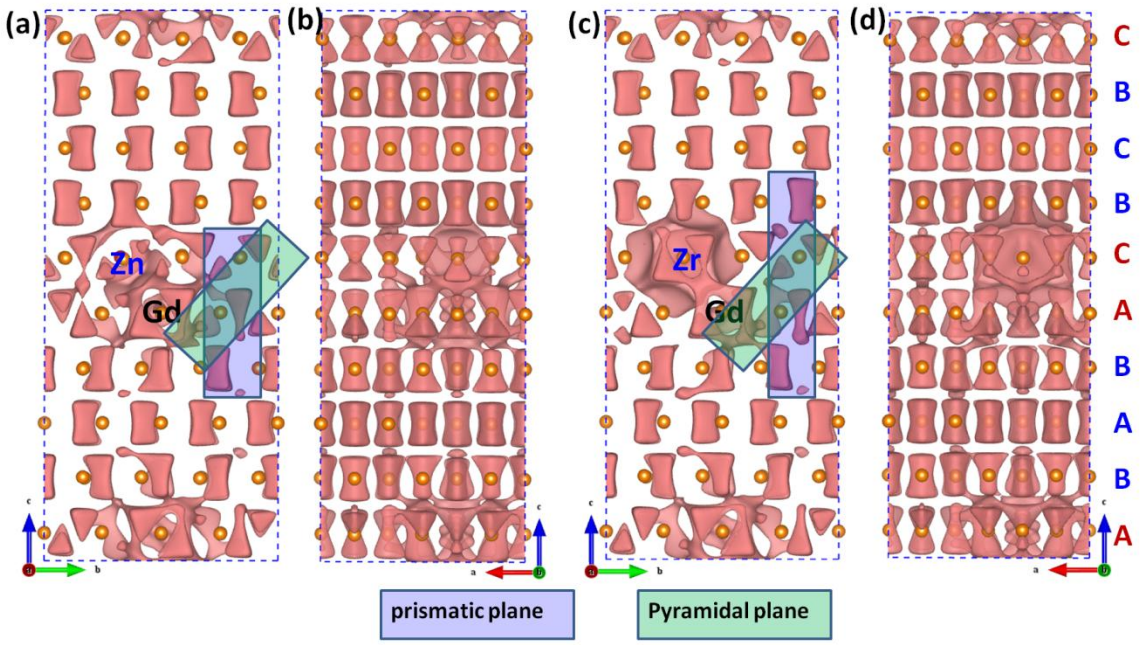

Figure 7.18. Deformation electron density isosurface ($\Delta\rho$=0.0021 $e^{-}Å^{3}$) of atomic cluster of Gd-TM in 10H of $Mg_{97.5}Gd_{1.67}TM_{0.83}$ (TM=Zn and Zr), (a) and (c) in the (100)s.c. view; (b) and (d) in the (010)s.c. view.

7.5. Conclusion

In this work, contributions of alloying elements of Zn and Y to the electronic structure and the elastic properties of $Mg_{97}Zn_1Y_2$ alloy have been investigated via first-principles calculations. Segregation behavior of the alloying elements (Zn or/and Y) in 6H LPSOs of $Mg_{98}Zn_2$, $Mg_{98}Y_2$, and $Mg_{97}Zn_1Y_2$ has been estimated through the proposed atomic array and atomic cluster models. In the view of excess energy caused by the contributions of alloying elements and fault layers, the energetic favorable configurations of 6H LPSO in $Mg_{98}Zn_2$, $Mg_{98}Y_2$ and $Mg_{97}Zn_1Y_2$ have been presented. With the formation of atomic array of Y forming with Zn occupying its 1st neighbor, the ductility of $Mg_{97}Zn_1Y_2$ will be increased since the bulk modulus/shear modulus ratio (B/G) is changed from 1.95 of Mg to 2.09. The validation of the proposed atomic array model in $Mg_{97}Zn_1Y_2$ alloy is further confirmed by the simulated HRTEM image.

Atomic array and atomic cluster of Gd atoms are applied to discussing the contributions of selected alloying element (TM =Zn and Zr) to the formability of 6H and 10H LPSO in $Mg_{97.5}Gd_{1.67}TM_{0.83}$ alloys. It can be seen that with the addition of Zn and Zr, the interfacial energy of 6H and 10H can be decreased significantly when forming the cluster between TM and Gd, indicating the formability of 6H and 10H will be increased in Mg-Gd-Zr and Mg-Gd-Zn alloys. In 10H LPSO, it will be more efficient alloying Zr into Mg-Gd to form 10H LPSO than alloying Zn since the interfacial energy of 10H in $Mg_{97.5}Gd_{1.67}Zr_{0.83}$ is much smaller than that of $Mg_{97.5}Gd_{1.67}Zn_{0.83}$.

Moreover, in terms of deformation electron density and electron localization function, the strengthen mechanism of RE and TM to Mg-TM-RE alloys is that the basal

plane of Mg is strengthened due to the formation of stronger chemical bond between atomic array/cluster and Mg matrix. On the contrary, the weakened bond strength of Mg matrix in the prismatic plane by the fault layers and alloying elements indicates a possible non-basal slip systems could occur during deformation, which could improve the ductility of Mg alloys. The directional bond will result in the elastic anisotropy, and thus hinders the anisotropic of deformation behavior.

Chapter 8

Conclusion and Future Work

8.1. Conclusion

In this dissertation, contributions of stacking faults, LPSOs and alloying elements to the formation energy, elastic, electronic and phonon properties of Mg and Mg alloys are investigated through the first-principles calculations. A brief introduction of first-principles calculations, yielding the energy of stacking faults and LPSOs, characterizing their electronic structures and presenting their effect on the phonon and elastic properties of Mg and Mg alloys, is discussed. Atomic array and atomic cluster models for the arrangement of alloying elements in LPSOs of Mg alloys are proposed, comparing with previous works reported in the literature. The main contributions of the present work include:

(i) In pure Mg, the connections among stacking faults and LPSOs are discussed. Three typical basal-plane stacking faults, i.e., growth fault, deformation fault and extrinsic fault, are investigated. Through the electron localization morphology, electronic structures of these three stacking faults are revealed in terms of deformation electron density and electron localization function. These results yield a quantitative description of charge transfer between atoms in and out of the

stacking faults. We also obtain a brief physical correlation between stacking fault energy and the difference of $\Delta\rho$ and ELF between fault and the regular planes. Furthermore, through detailed investigations of deformation electron density, we show that the electron structures of 10H, 14H, 18R and 24R LPSO structures in Mg originate from those of deformation stacking faults in Mg, and their formation energies can be scaled with respect to formation energy and the number of layers of deformation stacking faults, while the electron structure and formation energy of the 6H LPSO structure are between those of deformation and growth stacking faults. In the end, effects of fault layers in stacking faults and LPSOs on the local phonon density of states and Debye temperatures are discussed together with their specific electronic structures. Moreover, the simulated images of high resolution transmission electron microscopy compare well with experimentally observed ones, and the simulated diffraction patterns display the classic character of the superlattices of stacking faults and LPSOs. Contributions of each individual atomic layer to the thermal dynamic properties of stacking faults and LPSOs have been qualitatively and quantitatively described by the Helmholtz energy, vibrational entropy and Debye temperature.

(ii) In the binary Mg-X alloys, contributions of alloying elements to the energy and the bond structure of stacking faults and LPSOs are investigated. In view of electron localization morphology, the bonding structure of Mg around the fault plane can be recognized as the HCP-FCC transform in the short-range. Together with the specific electron structure of each alloying element, it has been confirmed that the bond strength of the fault planes are strengthened around the

effected zone of alloying elements, while that of prismatic and pyramidal plane will be weakened by the electron redistributions effected by the contributions of alloying elements and fault layers in stacking faults and LPSOs.

(iii) In the ternary Mg-TM-RE alloys, contributions of alloying elements and fault layers to the energy, electronic structure and elastic properties of 6H and 10H LPSOs are discussed through our proposed atomic array and atomic cluster models. For example, with the formation of atomic array of Y forming with Zn occupying its 1st neighbor, the ductility of $Mg_{97}Zn_1Y_2$ will be increased based on the criteria proposed by Pugh [187]. In terms of deformation electron density and electron localization function, the strengthen mechanism of alloying elements in Mg alloys is that the basal plane of Mg is strengthened due to the formation of stronger chemical bonds between the atomic array and Mg matrix. With the addition of TMs into Mg alloys with LPSOs, the excess energy will be reduced to make the structure more stable than that of without TM in Mg alloys.

(iv) With the guidance of the electronic structure characterized by the deformation electron density and electron localization function, we can see that (a) the bond strength affected by alloying elements and fault layers can be conveniently estimated, supporting fundamental information to strengthen mechanism of Mg alloys; (b) the simulated images of high resolution transmission electron microscopy and diffraction patterns could show the experimental comparable character of the superlattices of stacking faults and LPSOs, estimating the accuracy of the proposed models and the predicted results.

This work enables quantitative investigations of the segregation behavior of solute atoms in stacking faults and LPSOs. Contributions of solute atoms and fault layers in stacking faults and LPSOs to the energy, bond structure and strength, and elastic properties of Mg alloys are discussed, providing a qualitative description of the strengthening mechanism in the development of advanced Mg alloys.

8.2. Future work

Since works focusing on the segregating behavior of alloying elements are important to optimize the microstructure and to improve the mechanical properties of Mg alloys, it is necessary to apply the proposed atomic array and atomic cluster models into the development of advanced Mg alloys.

(i) According to the concentration of alloying elements, length of the atomic array displaying short range order can be estimated via inserting Mg atom, which could optimize the concentration of solute atoms in the enrichment planes. Incorporating with the ANNNI model mentioned in Chapter 2, energies of stacking faults and LPSOs in Mg alloys with various concentrations of solute atoms can be captured conveniently.

(ii) Vibrational entropy stabilized stacking faults and LPSOs could be studied in Mg alloys through investigating the phonon properties via the supercell approach. Through combining contributions of thermal electron and lattice vibrations, the Helmholtz energy at finite temperatures can be predicted. Hence, the stability of stacking faults and LPSOs of Mg alloys can be compared, presenting the thermal stability of

stacking faults and LPSOs in Mg alloys. Effects of alloying elements on the formability of various LPSOs will be studied.

Bibliography

[1] Shang S, Zhang H, Ganeshan S, Liu ZK. Jom 2008;60:45.
[2] Datta A, Waghmare UV, Ramamurty U. Acta Mater. 2008;56:2531.
[3] Foley DC, Al-Maharbi M, Hartwig KT, Karaman I, Kecskes LJ, Mathaudhu SN. Scripta Mater. 2011;64:193.
[4] Shang SL, Wang WY, Wang Y, Du Y, Zhang JX, Patel AD, Liu ZK. J. Phys.: Condes. Matter 2012;24:155402.
[5] Hartford J, von Sydow B, Wahnstrom G, Lundqvist BI. Phys. Rev. B 1998;58:2487.
[6] Chetty N, Weinert M. Phys. Rev. B 1997;56:10844.
[7] Argon AS, Moffatt WC. Acta Metall. Mater. 1981;29:293.
[8] Sastry DH, Prasad YVR, Vasu KI. Scripta Matall. Mater. 1969;3:927.
[9] Suzuki M, Kimura T, Koike J, Maruyama K. Mater. Sci. Eng. A 2004;387-389:706.
[10] Bernstein N, Tadmor EB. Phys. Rev. B 2004;69:094116.
[11] Lu K, Lu L, Suresh S. Science 2009;324:349.
[12] Zhao YH, Zhu YT, Liao XZ, Horita Z, Langdon TG. Appl. Phys. Lett. 2006;89:121906.
[13] Zhu YT, Liao XZ, Wu XL. Prog. Mater. Sci. 2010;57:1.
[14] Li Y, Kong QP. Phys. Status Solidi A-Appl. Res. 1989;113:345.
[15] Guo Z, Miodownik AP, Saunders N, Schille JP. Scripta Mater. 2006;54:2175.
[16] Gotsis HJ, Papaconstantopoulos DA, Mehl MJ. Phys. Rev. B 2002;65:134101.
[17] Tang P-Y, Wen L, Tong Z-F, Tang B-Y, Peng L-M, Ding W-J. Comput. Mater. Sci. 2011;50:3198.
[18] Wen L, Chen P, Tong ZF, Tang BY, Peng LM, Ding WJ. Eur. Phys. J. B 2009;72:397.
[19] Itoi T, Gonda K, Hirohashi M. Wear 2011;270:606.
[20] Wang Y, Chen LQ, Liu ZK, Mathaudhu SN. Scripta Mater. 2010;62:646.
[21] Dai Y, Li JH, Liu BX. J. Phys.: Condes. Matter 2009;21:385402.
[22] Hu WY, Zhang BW, Huang BY, Gao F, Bacon DJ. J. Phys.: Condes. Matter 2001;13:1193.
[23] Inoue A, Matsushita M, Kawamura Y, Amiya K, Hayashi K, Koike J. Mater. Trans. 2002;43:580.
[24] Chen B, Lin DL, Zeng XQ, Lu C. J. Alloy. Compd. 2007;440:94.
[25] Kawamura Y, Yamasaki M. Mater. Trans. 2007;48:2986.
[26] Onorbe E, Garces G, Perez P, Adeva P. J. Mater. Sci. 2012;47:1085.
[27] Yamasaki M, Hashimoto K, Hagihara K, Kawamura Y. Acta Mater. 2011;59:3646.
[28] Nie JF. Metall. Mater. Trans. A 2012;43:3891.
[29] Egusa D, Abe E. Acta Mater. 2012;60:166.
[30] Leng Z, Zhang JH, Zhang ML, Liu XH, Zhan HB, Wu RZ. Mater. Sci. Eng. A 2012;540:38.
[31] Yamasaki M, Anan T, Yoshimoto S, Kawamura Y. Scripta Mater. 2005;53:799.
[32] Itoi T, Seimiya T, Kawamura Y, Hirohashi M. Scripta Mater. 2004;51:107.
[33] Abe E, Kawamura Y, Hayashi K, Inoue A. Acta Mater. 2002;50:3845.
[34] Jian WW, Cheng GM, Xu WZ, Yuan H, Tsai MH, Wang QD, Koch CC, Zhu YT, Mathaudhu SN. Mater. Res. Lett. 2013;1:61.
[35] Hui X, Dong W, Chen GL, Yao KF. Acta Mater. 2007;55:907.
[36] Itoi T, Inazawa T, Yamasaki M, Kawamura Y, Hirohashi M. Mater. Sci. Eng. A 2012.
[37] Leyson GPM, Hector LG, Curtin WA. Acta Mater. 2012;60:5197.
[38] Nie JF, Zhu YM, Liu JZ, Fang XY. Science 2013;340:957.

[39] Onorbe E, Garces G, Perez P, Adeva P. J. Mater. Sci. 2012;47:1085.
[40] Rao JC, Song M, Furuya K, Yoshimoto S, Yamasaki M, Kawamura Y. J. Mater. Sci. 2006;41:2573.
[41] Zhang JS, Chen CJ, Que ZP, Cheng WL, Xu JD, Kang JJ. Mater. Sci. Eng. A 2012;552:81.
[42] Yokobayashi H, Kishida K, Inui H, Yamasaki M, Kawamura Y. Acta Mater. 2011;59:7287.
[43] Li RG, Nie JF, Huang GJ, Xin YC, Liu Q. Scripta Mater. 2011;64:950.
[44] Ozaki T, Kuroki Y, Yamada K, Hoshikawa H, Kamado S, Kojima Y. Mater. Trans. 2008;49:2185.
[45] Xu C, Zheng MY, Xu SW, Wu K, Wang ED, Kamado S, Wang GJ, Lv XY. Mater. Sci. Eng. A 2012;547:93.
[46] Homma T, Kunito N, Kamado S. Scripta Mater. 2009;61:644.
[47] Anyanwu IA, Kamado S, Kojima Y. Mater. Trans. 2001;42:1206.
[48] Xu C, Zheng MY, Xu SW, Wu K, Wang ED, Kamado S, Wang GJ, Lv XY. J. Alloy. Compd. 2012;528:40.
[49] Zhang JH, Leng Z, Liu SJ, Li JQ, Zhang ML, Wu RZ. J. Alloy. Compd. 2011;509:7717.
[50] Peng QM, Dong HW, Wang LD, Wu YM, Wang LM. Mater. Sci. Eng. A 2008;477:193.
[51] Xu SW, Kamado S, Honma T. Mater. Sci. Eng. A 2011;528:2385.
[52] Homma T, Hirawatari S, Sunohara H, Kamado S. Mater. Sci. Eng. A 2012;539:163.
[53] Xu SW, Oh-ishi K, Kamado S, Takahashi H, Homma T. Mater. Sci. Eng. A 2012;542:71.
[54] Xu SW, Oh-Ishi K, Kamado S, Uchida F, Homma T, Hono K. Scripta Mater. 2011;65:269.
[55] Car R, Parrinello M. Phys. Rev. Lett. 1985;55:2471.
[56] Hohenberg P, Kohn W. Phys. Rev. 1964;136:B864.
[57] Kohn W, Sham LJ. Phys. Rev. 1965;140:1133.
[58] Birch F. Phys. Rev. 1947;71:809.
[59] Birch F. J. Geophys. Res. 1978;83:1257.
[60] Shang SL, Saengdeejing A, Mei ZG, Kim DE, Zhang H, Ganeshan S, Wang Y, Liu ZK. Comput. Mater. Sci. 2010;48:813.
[61] Nakashima PNH, Smith AE, Etheridge J, Muddle BC. Science 2011;331:1583.
[62] Midgley PA. Science 2011;331:1528.
[63] Ogata S, Li J, Yip S. Science 2002;298:807.
[64] Qi Y, Mishra RK. Phys. Rev. B 2007;75:224105.
[65] Momma K, Izumi F. J. Appl. Crystallogr. 2008;41:653.
[66] Momma K, Izumi F. J. Appl. Crystallogr. 2011;44:1272.
[67] Gemming T, Mobus G, Exner M, Ernst F, Ruhle M. J. Microsc.-Oxf. 1998;190:89.
[68] Deng B, Marks LD. Acta Crystallogr. Sect. A 2006;62:208.
[69] Meyer JC, Kurasch S, Park HJ, Skakalova V, Kunzel D, Gross A, Chuvilin A, Algara-Siller G, Roth S, Iwasaki T, Starke U, Smet JH, Kaiser U. Nat. Mater. 2011;10:209.
[70] Shibata N, Findlay SD, Azuma S, Mizoguchi T, Yamamoto T, Ikuhara Y. Nat. Mater. 2009;8:654.
[71] Mogck S, Kooi BJ, De Hosson JTM, Finnis MW. Phys. Rev. B 2004;70:245427.
[72] Mogck S. TEM studies of interfaces in multicomponent systems (Chapter6). 2004.
[73] Stadelmann PA. Ultramicroscopy 1987;21:131.
[74] Silvi B, Savin A. Nature 1994;371:683.
[75] Santos JC, Tiznado W, Contreras R, Fuentealba P. J. Chem. Phys. 2004;120:1670.
[76] Espinosa-Garcia WF, Ruiz-Tobon CM, Osorio-Guillen JM. Physica B 2011;406:3788.
[77] Liu ZK, Zhang H, Ganeshan S, Wang Y, Mathaudhu SN. Scripta Mater. 2010;63:686.

[78] Shang SL, Wang Y, Liu ZK. Appl. Phys. Lett. 2007;90:101909.
[79] Ganeshan S, Shang SL, Zhang H, Wang Y, Mantina M, Liu ZK. Intermetallics 2009;17:313.
[80] Zhang H, Shang SL, Wang Y, Saengdeejing A, Chen LQ, Liu ZK. Acta Mater. 2010;58:4012.
[81] Shang SL, Wang J, Wang Y, Du Y, Liu ZK. Comput. Mater. Sci. 2011;50:2096.
[82] Wrobel J, Hector Jr LG, Wolf W, Shang SL, Liu ZK, Kurzydlowski KJ. J. Alloy. Compd. 2012;512:296.
[83] Zhang H, Shang S-L, Wang Y, Chen L-Q, Liu Z-K. Intermetallics 2012;22:17.
[84] Shang SL, Wang Y, Kim D, Liu ZK. Comput. Mater. Sci. 2010;47:1040.
[85] Arroyave R, Liu ZK. Phys. Rev. B 2006;74:174118.
[86] Creuze J, Berthier F, Tetot R, Legrand B, Treglia G. Phys. Rev. B 2000;61:14470.
[87] Wang Y, Wang JJ, Wang WY, Mei ZG, Shang SL, Chen LQ, Liu ZK. J. Phys.: Condes. Matter 2010;22:202201.
[88] Wang Y, Wang JJ, Saal JE, Shang SL, Chen LQ, Liu ZK. Phys. Rev. B 2010;82:172503.
[89] Wang Y, Zacherl CL, Shang SL, Chen LQ, Liu ZK. J. Phys.: Condes. Matter 2011;23.
[90] Kresse G, Furthmuller J. Phys. Rev. B 1996;54:11169.
[91] Kresse G, Furthmuller J. Comput. Mater. Sci. 1996;6:15.
[92] Parlinski K, Li ZQ, Kawazoe Y. Phys. Rev. Lett. 1997;78:4063.
[93] Vitos L, Korzhavyi PA, Johansson B. Phys. Rev. Lett. 2006;96:117210.
[94] Denteneer PJH, Vanhaeringen W. J. Phys. C: Solid State Phys. 1987;20:L883.
[95] Vitos L, Korzhavyi PA, Johansson B. Nat. Mater. 2003;2:25.
[96] Sandlobes S, Friak M, Zaefferer S, Dick A, Yi S, Letzig D, Pei Z, Zhu LF, Neugebauer J, Raabe D. Acta Mater. 2012;60:3011.
[97] Gebhardt T, Music D, Ekholm M, Abrikosov IA, Vitos L, Dick A, Hickel T, Neugebauer J, Schneider JM. J. Phys.: Condes. Matter 2011;23.
[98] Abbasi A, Dick A, Hickel T, Neugebauer J. Acta Mater. 2011;59:3041.
[99] Vitos L, Abrikosov IA, Johansson B. Phys. Rev. Lett. 2001;87:156401.
[100] Faulkner JS. Prog. Mater. Sci. 1982;27:1.
[101] Vitos L. Computational Quantum Mechanics for Materials Engineers - The EMTO Method and Applications: Springer, 2007.
[102] Ruban AV, Simak SI, Shallcross S, Skriver HL. Phys. Rev. B 2003;67:214302.
[103] Shang SL, Wang Y, Kim DE, Zacherl CL, Du Y, Liu ZK. Phys. Rev. B 2011;83:144204.
[104] Jiang C, Wolverton C, Sofo J, Chen L-Q, Liu Z-K. Phys. Rev. B 2004;69:214202.
[105] Shin D, Arr 贸 yave R, Liu Z-K, Van de Walle A. Phys. Rev. B 2006;74:024204.
[106] Pekguleryuz MO, Kainer KU, Kaya AS, editors. Fundamentals of Magnesium Alloy Metallurgy: Woodhead Publishing Limited, 2013.
[107] Zunger A, Wei SH, Ferreira LG, Bernard JE. Phys. Rev. Lett. 1990;65:353.
[108] Suzuki H. Sci. Rep. Res. Tohoku A 1952;4:455.
[109] Koizumi Y, Nukaya T, Suzuki S, Kurosu S, Li YP, Matsumoto H, Sato K, Tanaka Y, Chiba A. Acta Mater. 2012;60:2901.
[110] Saka H. Philos. Mag. A 1983;47:131.
[111] Mendis BG, Jones IP, Smallman RE. Journal of Electron Microscopy 2004;53:311.
[112] Kaneko Y, Kaneko K, Nohara A, Saka H. Philos. Mag. A 1995;71:399.
[113] Zhu YM, Morton AJ, Weyland M, Nie JF. Acta Mater. 2010;58:464.
[114] Yang Z, Chisholm MF, Duscher G, Ma X, Pennycook SJ. Acta Mater. 2013;61:350.
[115] Suzuki M, Kimura T, Koike J, Maruyama K. Scripta Mater. 2003;48:997.
[116] Tane M, Nagai Y, Kimizuka H, Hagihara K, Kawamura Y. Acta Mater. 2013.

[117] Yamasaki M, Hagihara K, Inoue S-i, Hadorn JP, Kawamura Y. Acta Mater. 2013;61:2065.
[118] Saal JE, Wolverton C. Scripta Mater. 2012;67:798.
[119] Ma SY, Liu LM, Wang SQ. J. Mater. Sci. 2013;48:1407.
[120] Ping DH, Hono K, Kawamura Y, Inoue A. Philos. Mag. Lett. 2002;82:543.
[121] Zhu YM, Morton AJ, Nie JF. Acta Mater. 2010;58:2936.
[122] Chino Y, Mabuchi M, Hagiwara S, Iwasaki H, Yamamoto A, Tsubakino H. Scripta Mater. 2004;51:711.
[123] Zhu YM, Morton AJ, Nie JF. Acta Mater. 2012;60:6562.
[124] Zhu YM, Morton AJ, Nie JF. Acta Mater. 2010;58:2936.
[125] Chen JH, Costan E, van Huis MA, Xu Q, Zandbergen HW. Science 2006;312:416.
[126] Chen P, Li DL, Yi JX, Tang BY, Peng LM, Ding WJ. J. Alloy. Compd. 2009;485:672.
[127] Yang S, Kiraly B, Wang WY, Shang S, Cao B, Zeng H, Zhao Y, Li W, Liu Z-K, Cai W, Huang TJ. Adv. Mater. 2012;24:5598.
[128] Reboredo FA, Pizzagalli L, Galli G. Nano Lett. 2004;4:801.
[129] Peng XH, Nayak SK, Alizadeh A, Varanasi KK, Bhate N, Rowland LB, Kumar SK. J. Appl. Phys. 2007;102:024304.
[130] Fan TW, Zhang Q, Tang BY, Peng LM, Ding WJ. Eur. Phys. J. B 2012;82:143.
[131] Smith AE. Surf. Sci. 2007;601:5762.
[132] Wang Y, Curtarolo S, Jiang C, Arroyave R, Wang T, Ceder G, Chen LQ, Liu ZK. CALPHAD 2004;28:79.
[133] Kresse G, Joubert D. Phys. Rev. B 1999;59:1758.
[134] Wang Y, Perdew JP. Phys. Rev. B 1991;44:13298.
[135] Methfessel M, Paxton AT. Phys. Rev. B 1989;40:3616.
[136] Blöchl PE, Jepsen O, Andersen OK. Phys. Rev. B 1994;49:16223.
[137] Couret A, Caillard D. Acta Metall. Mater. 1985;33:1447.
[138] Fan TW, Tang BY, Peng LM, Ding WJ. Scripta Mater. 2011;64:942.
[139] Han J, Su XM, Jin ZH, Zhu YT. Scripta Mater. 2011;64:693.
[140] Wang H-Y, Zhang N, Wang C, Jiang Q-C. Scripta Mater. 2011;65:723.
[141] Blaha P, Schwarz K, Dederichs PH. Phys. Rev. B 1988;38:9368.
[142] Wu L, Zhu Y, Vogt T, Su H, Davenport JW, Tafto J. Phys. Rev. B 2004;69:064501.
[143] Althoff JD, Allen PB, Wentzcovitch RM, Moriarty JA. Phys. Rev. B 1993;48:13253.
[144] Pynn R, Squires GL. Proc. Roy. Soc. Lond. A. 1972;326:347.
[145] Shang S-L, Wang Y, Du Y, Liu Z-K. Intermetallics 2010;18:961.
[146] Pomrehn GS, Toberer ES, Snyder GJ, van de Walle A. Phys. Rev. B 2011;83:094106.
[147] Hashimoto M, Ishida Y, Yamamoto R, Doyama M. J. Phys. F: Metal Phys. 1980;10:1109.
[148] van de Walle A, Ceder G. Phys. Rev. B 2000;61:5972.
[149] Gupta M, Sharon NML. Magnesium, Magnesium alloys, and Magnesium Composites. New Jersey: John Wiley & Sons, Inc, 2011.
[150] Zhang J, Dou Y, Liu G, Guo Z. Comput. Mater. Sci. 2013;79:564.
[151] Muzyk M, Pakiela Z, Kurzydlowski KJ. Scripta Mater. 2012;66:219.
[152] Zhang Q, Fan TW, Fu L, Tang BY, Peng LM, Ding WJ. Intermetallics 2012;29:21.
[153] Zhang Q, Fu L, Fan TW, Tang BY, Peng LM, Ding WJ. Physica B 2013;416:39.
[154] Li XQ, Schonecker S, Zhao JJ, Johansson B, Vitos L. Phys. Rev. B 2013;87:214203.
[155] Tang PY, Tang BY, Peng LM, Ding WJ. Mater. Chem. Phys. 2012;131:634.
[156] Blochl PE, Jepsen O, Andersen OK. Phys. Rev. B 1994;49:16223.
[157] Fan TW, Zhang Q, Tang BY, Peng LM, Ding WJ. Eur. Phys. J. B 2011;82:143.
[158] Harris J. Phys. Rev. B 1985;31:1770.

[159] Farid B, Heine V, Engel GE, Robertson IJ. Phys. Rev. B 1993;48:11602.
[160] Fabris S, Elsasser C. Acta Mater. 2003;51:71.
[161] Jian WW, Cheng GM, Xu WZ, Koch CC, Wang QD, Zhu YT, Mathaudhu SN. Appl. Phys. Lett. 2013;103:133108.
[162] Couret A, Caillard D. Acta Metall. Mater. 1985;33:1455.
[163] Wang WY, Shang SL, Wang Y, Darling KA, Mathaudhu SN, Hui XD, Liu ZK. Chem. Phys. Lett. 2012;551:121.
[164] Zhang S, Han Q, Liu ZK. Philos. Mag. 2007;87:147.
[165] Lu G-H, Zhang Y, Deng S, Wang T, Kohyama M, Yamamoto R, Liu F, Horikawa K, Kanno M. Phys. Rev. B 2006;73:224115.
[166] Chen P, Li DL, Yi JX, Tang BY, Peng LM, Ding WJ. J. Alloy. Compd. 2009;485:672.
[167] Yi JX, Tang BY, Chen P, Li DL, Peng LM, Ding WJ. J. Alloy. Compd. 2011;509:669.
[168] Okuda H, Horiuchi T, Tsukamoto T, Ochiai S, Yamasaki M, Kawamura Y. Scripta Mater. 2013;68:575.
[169] Matsuda M, Ii S, Kawamura Y, Ikuhara Y, Nishida M. Mater. Sci. Eng. A 2005;393:269.
[170] Shao XH, Yang ZQ, Ma XL. Acta Mater. 2010;58:4760.
[171] Matsuda M, Ii S, Kawamura Y, Ikuhara Y, Nishida M. Mater. Sci. Eng. A 2004;386:447.
[172] Pan FS, Luo SQ, Tang AT, Peng J, Lu Y. Prog. Nat. Sci. 2011;21:485.
[173] Kohn W, Sham L. Phys. Rev. 1965;140:1133.
[174] Arslan I, Stach EA. Nat. Mater. 2012;11:908.
[175] Van Aert S, Batenburg KJ, Rossell MD, Erni R, Van Tendeloo G. Nature 2011;470:374.
[176] Van Dyck D, Chen FR. Nature 2012;486:243.
[177] Guillaume S-O, Zheng B, Charlier J-C, Henrard L. Phys. Rev. B 2012;85:035444.
[178] Karen P, Kjekshus A, Huang Q, Karen VL. J. Alloy. Compd. 1999;282:72.
[179] Wazzan AR, Robinson LB. Phys. Rev. 1967;155:586.
[180] Slutsky LJ, Garland CW. Phys. Rev. 1957;107:972.
[181] Iikubo S, Matsuda K, Ohtani H. Phys. Rev. B 2012;86:054105.
[182] Wang WY, Shang SL, Mei Z-G, Wang Y, Darling K, Kecskes LJ, Mathaudhu SN, Hui XD, Liu Z-K.(To be published).
[183] Yamada K, Okubo Y, Kamado S, Kojima Y. Precipitate microstructures of high strength Mg-Gd-Y-Zn-Zr alloys. In: Nogami M, Jin R, Kasuga T, Yang W, editors. Aicam 2005, vol. 11-12. Stafa-Zurich: Trans Tech Publications Ltd, 2006. p.417.
[184] Inoue A, Kawamura Y, Matsushita M, Hayashi K, Koike J. J. Mater. Res. 2001;16:1894.
[185] Wang Y-F, Wang Z-Z, Yu N, Zeng X-Q, Ding W-J, Tang B-Y. Scripta Mater. 2008;58:807.
[186] Ping DH, Hono K, Nie JF. Scripta Mater. 2003;48:1017.
[187] Pugh SF. Philos. Mag. 1954;45:823.
[188] Ganeshan S, Shang SL, Wang Y, Liu ZK. Acta Mater. 2009;57:3876.
[189] Kawamura Y, Hayashi K, Inoue A, Masumoto T. Mater. Trans. 2001;42:1172.
[190] Ouyang YF, Tao XM, Zeng FJ, Chen HM, Du Y, Feng YP, He YH. Physica B 2009;404:2299.
[191] Hardie D. Acta Metall. 1971;19:719.

VITA

(William) Yi Wang was born to parents Xiuying Ge and Xiuliang Wang in Hebei province, China in 1982. He graduated from the Hebei United University with a B.S. degree in Materials Science and Engineering in 2005. Since 2006, he joined the State Key Laboratory for Advanced Metals and Materials at the University of Science and Technology Beijing (USTB) being a graduate student. In 2009, he was exchanged from USTB to the Pennsylvania State University (PSU) under the finical support of China Scholarship Council and the project from U.S. Army Research Laboratory. During his study at PSU, he obtained a M.S. degree in Materials Science and Engineering in December 2012. He was awarded the Scholarship and the Poster Award from Gordon Research Conference in July 2010, the Scholarship from the 1st TMS - Integrated Computational Materials Engineering (ICME) conference in July 2011, the 2nd place of 10th Material Science and Engineering Award for the Graduate Poster Competition at PSU in April 2012, the CALPHAD Scholarship from CALPHAD XLI Conference in June 2012, the ACerS Nuclear & Environmental Technology Division (NETD) Travel Grant and Graduate Excellence in Materials Science (GEMS) Diamond Award at MS&T'12 meeting in October 2012, the TMS LMD best graduate poster award at TMS 2013 Annual Meeting, the Bayer Travel Fund - International Travel Grants for iMATSE Graduate Students at PSU and the Stiftelsen för Tillämpad Termodynamik grant from KTH Royal Institute of Technology in March 2013.

He authored or co-authored about 15 publications during his PhD study at PSU and some of them are listed below:

1. **W. Y. Wang**,* H. Z. Fang, S. L. Shang, H. Zhang, Y. Wang, X. Hui, S. Mathaudhu and Z. K. Liu, Atomic structure and diffusivity in liquid $Al_{80}Ni_{20}$ by ab initio molecular dynamics simulations. **Physica B: Condensed Matter**, **2011**, 406:3089-3097.
2. **W. Y. Wang**,* S. L. Shang, H. Z. Fang, H. Zhang, Y. Wang, S. N. Mathaudhu, X. Hui and Z. K. Liu, Effect of composition on atomic structure, diffusivity and viscosity of liquid Al-Zr alloys. **Metallurgical Materials Transaction A**, **2012**, 43:3417-3480.
3. **W. Y. Wang**,* S. L. Shang, Y. Wang, K. A. Darling, S. N. Mathaudhu, X. Hui* and Z. K. Liu,* Electron localization morphology of the basal-plane stacking faults in Mg: A first-principles study. **Chemical Physics Letters, 2012**, 551:121-125.
4. S. K. Yang, B. Kiraly, **W. Y. Wang**, S. L. Shang, B. Q. Cao, H. B. Zeng, Y. H. Zhao, W. Z. Li, Z. K. Liu, W. P. Cai,* and T. J. Huang,* Fabrication and characterization of beaded SiC quantum rings with anomalous red spectral shift. **Advanced Materials, 2012**, 24:5598-5603.
5. **W. Y. Wang,*** S. L. Shang, Y. Wang, K. A. Darling, L. J. Kecskes, S. N. Mathaudhu, X. Hui and Z. K. Liu,* Electronic structure of long periodic stacking orders in Mg: A first-principles study. **Journal of Alloys and Compounds**, **2014**, 586:656-662.
6. **W. Y. Wang**,* S. L. Shang, Y. Wang, Z. G. Mei, K. A. Darling, L. J. Kecskes, S. N. Mathaudhu, X. Hui and Z. K. Liu, Effects of alloying elements on stacking faults energies and electronic structures of binary Mg alloys: A first-principles study. **Materials Research Letters, 2014**, 2:29-36.
7. **W. Y. Wang**,* X. Hui, Y. Wang, S. L. Shang, K. A. Darling, L. J. Kecskes, S. N. Mathaudhu and Z. K. Liu,*. Atomic array nanoprecipitates of solute atoms in 6H long periodic stacking order of $Mg_{97}Zn_1Y_2$ alloy. (To be submitted)